Axion Quark Nugget Dark Matter Model: Developments in Model Building and Observations

by

Shuailiang Ge

B.Sc., Shandong University, Weihai, 2015

A THESIS SUBMITTED IN PARTIAL FULFILLMENT
OF THE REQUIREMENTS FOR THE DEGREE OF

DOCTOR OF PHILOSOPHY

in

The Faculty of Graduate and Postdoctoral Studies
(Physics)

THE UNIVERSITY OF BRITISH COLUMBIA
(Vancouver)

July 2021

The following individuals certify that they have read, and recommend to the Faculty of Graduate and Postdoctoral Studies for acceptance, the thesis entitled:

Axion Quark Nugget Dark Matter Model: Developments in Model Building and Observations

submitted by **Shuailiang Ge** in partial fulfillment of the requirements for the degree of **Doctor of Philosophy** in **Physics**.

Examining Committee:

Ariel Zhitnitsky, Department of Physics and Astronomy, UBC
Supervisor

Ludovic Van Waerbeke, Department of Physics and Astronomy, UBC
Supervisory Committee Member

Gary Hinshaw, Department of Physics and Astronomy, UBC
University Examiner

Roman Krems, Department of Chemistry, UBC
University Examiner

Robert Brandenberger, McGill University
External Examiner

Additional Supervisory Committee Members:

Jeremy Heyl, Department of Physics and Astronomy, UBC
Supervisory Committee Member

Janis McKenna, Department of Physics and Astronomy, UBC
Supervisory Committee Member

Abstract

The axion quark nugget (AQN) model was initially proposed with the motivation to explain the observed similarity between the visible and dark matter abundances in the Universe. AQNs are dense objects made of standard model quarks in color superconducting (CS) phase. AQNs can be made of matter as well as antimatter. Matter AQNs and antimatter AQNs together form the dark matter, while the disparity between them will lead to the observed matter-antimatter asymmetry. Thus, the similarity between visible and dark matter abundances can be naturally explained since they have the same origin in the AQN framework.

This thesis focuses on recent developments in model building and some potential observational evidence of AQNs. First, we show how the coherent nonzero axion field in the early Universe generates the disparity between matter and antimatter AQNs. Then, we calculate the real-time evolution of an AQN from its initial state as a closed axion domain wall with baryon charge trapped inside to its final CS state. Next, we show that for the most part of axion parameter space, AQNs are the dominant part of dark matter compared to the contribution of the free axions from the misalignment mechanism. After that, we calculate the size distribution of AQNs based on percolation theory. We also demonstrate that after formation, the size distribution can survive the subsequent evolution in the early Universe. Finally, we study potential observational evidence of the AQN model, focusing on the following two phenomena: the impulsive radio events in quiet solar corona recorded by the Murchison Widefield Array and the seasonal variation of the near-Earth X-ray background observed by the XMM-Newton observatory.

Lay Summary

More than 80 percent of the matter in the Universe is hidden in the form of dark matter. What is the nature of dark matter? This remains unknown. This thesis is about a dark matter model known as the axion quark nugget (AQN) model. This model can not only explain dark matter but also solve another fundamental problem: Why is there more matter than antimatter in the Universe? In this thesis, we present the recent developments in building the AQN model, including the formation, evolution, and size distribution of AQNs. Also, we discuss some observed astrophysical phenomena that could be induced by AQNs.

Preface

This thesis contains the materials of my research papers that have been published or posted on arXiv [1–5] during my PhD studies:

- Chapter 3.2 is adapted from the published paper [1] (S. Ge, X. Liang, and A. Zhitnitsky, "Cosmological CP-odd axion field as the coherent Berry's phase of the Universe", Physical Review D 96, 063514 (2017)). My supervisor, A. Zhitnitsky, proposed the fundamental idea of this project. I worked closely with X. Liang on the details and we did the numerical calculations and analytical calculations. The manuscript of this publication was written by all authors collaboratively.

- Chapter 4 is adapted from the published paper [2] (S. Ge, X. Liang, and A. Zhitnitsky, "Cosmological axion and a quark nugget dark matter model", Physical Review D 97, 043008 (2018)). A. Zhitnitsky initiated the project and built the big picture. I worked closely with X. Liang on the details and we did the numerical calculations and analytical calculations. The manuscript of this publication was written by all authors collaboratively.

- Chapter 3.3, Chapter 5 and Appendix A are adapted from the published paper [3] (S. Ge, K. Lawson, and A. Zhitnitsky, "Axion quark nugget dark matter model: Size distribution and survival pattern", Physical Review D 99, 116017 (2019)). I was in charge of the real-time evolution of AQNs and the size distribution of AQNs. A. Zhitnitsky and K. Lawson analyzed the survival pattern of AQNs. The manuscript of this publication was written by all authors collaboratively.

- Chapter 6 and Appendix B are adapted from the published paper [4] (S. Ge, M. S. R. Siddiqui, L. Van Waerbeke, and A. Zhitnitsky, "Impulsive radio events in quiet solar corona and axion quark nugget dark

matter", Physical Review D 102, 123021 (2020)). I did the numerical simulations. I developed the Monte Carlo code based on N. Raza's code which was originally written for his work [6]. I thank N. Raza for providing his original code. L. Van Waerbeke provided the platform for me to do the numerical simulations. Also, L. Van Waerbeke and M. S. R. Siddiqui assisted me in running codes in the platform. The main part of the publication was written by A. Zhitnitsky. I wrote the appendix and generated all the plots with relevant analysis. L. Van Waerbeke revised the manuscript of this publication, and M. S. R. Siddiqui also proofread it.

- Chapter 7, Appendix C, Appendix D and Appendix E are adapted from the paper [5] (S. Ge, H. Rachmat, M. S. R. Siddiqui, L. Van Waerbeke, and A. Zhitnitsky, "X-ray annual modulation observed by *XMM-Newton* and axion quark nugget dark matter", arXiv:2004.00632, (2020)) which has been submitted for publication and now is under peer-review. A. Zhitnitsky and L. Van Waerbeke initiated the project and built the big picture. I did the analytical calculations and numerical calculations, which were achieved with the inspiration and assistance from the numerous discussions with A. Zhitnitsky, L. Van Waerbeke, H. Rachmat and M. S. R. Siddiqui. I prepared the first daft which was then revised and expanded by A. Zhitnitsky and L. Van Waerbeke. Also, H. Rachmat and M. S. R. Siddiqui proofread the manuscript of this publication.

All of my contributions above were done under the guidance of my supervisor, Professor Ariel Zhitnitsky. I also benefited a lot from the collaboration with Professor Ludovic Van Waerbeke for Refs. [4, 5] (the works presented in chapter 6 and chapter 7).

Besides, Chapter 2 reviews the generic features of the AQN model mainly based on the introductory part of Refs. [1–5]. Chapter 3.1 reviews the AQN formation that was studied in Ref. [7] authored by Xunyu Liang and Ariel Zhitnitsky, as a background material for Chapter 3.

Table of Contents

List of Figures

Acknowledgements

First of all, I would like to thank my supervisor, Professor Ariel Zhitnitsky, for bringing me the opportunities to carry out research in this fascinating field. Thank you for your guidance and support with enormous knowledge and patience during my PhD studies, and also for the encouragement on my independent research.

I would like to thank Kyle Lawson, Xunyu Liang, Hikari Rachmat, Md Shahriar Rahim Siddiqui, and Ludovic Van Waerbeke, for our fruitful collaboration. Especially, I would like to thank Professor Ludovic Van Waerbeke for valuable discussions and for his expertise in astronomy.

I would like to thank Professor Jeremy Heyl and Professor Janis McKenna for their assistance and support as supervisory committee members during my PhD process.

Also, I am very lucky to have made many great friends in Vancouver. Thank you all for the great times we spent together in this beautiful city!

Finally, I wish to express my gratitude to my parents and my sister. Your unconditional love and support, across the Pacific Ocean, help me to be who I am today.

献给我的父母

To my parents

Chapter 1

Introduction

Dark matter accounts for about a quarter of the total mass-energy in the Universe. The existence of dark matter is supported by evidence from the observations of galaxy rotation curves, gravitational lensing, cosmic microwave background (CMB), etc. [11, 12]. However, the nature of dark matter remains unknown. There are many dark matter candidates arising in different models and theories, including weakly interacting massive particles (WIMPs), QCD axions, sterile neutrinos, primordial black holes, to name a few. In this thesis, we focus on the axion quark nugget (AQN) dark matter model. The AQN model was initially proposed in Ref. [13], and has been developed subsequently in model building and in the identification of potential observational signatures. Before moving on to the AQN model, it is worth briefly reviewing the related term, QCD axion.

QCD axion was proposed to solve the strong CP problem through the known Peccei-Quinn mechanism [14, 15]. In the QCD Lagrangian, there is a topological term,

$$\mathcal{L}_\theta = \theta \frac{g_s^2}{32\pi^2} \tilde{G}^{a\mu\nu} G^a_{\mu\nu}, \tag{1.1}$$

where $G^a_{\mu\nu}$ is the gluon field strength, and $\tilde{G}^{a\mu\nu} = \frac{1}{2}\varepsilon^{\mu\nu\sigma\tau} G^a_{\sigma\tau}$ is its dual. θ is called theta vacuum. Eq. (1.1) arises due to the non-trivial topological configuration of QCD vacuum.[1] This term violates parity (P) symmetry

[1] Besides, another source can affect θ, which is from the quark sector. The complex quark mass matrix M can be transformed to a real diagonal matrix by chiral rotation of quark fields. The induced chiral anomaly changes θ by $\arg \mathrm{Det} M$. In fact, the sum of the two sources for θ (rather than the two components individually) is an observable. See e.g., Refs. [16, 17] for more details.

and time reversal (T) symmetry, thus CP symmetry, with the strength proportional to θ. θ is an angular parameter, which in general can be a value between 0 and 2π. The CP-violating effects generated by this term include the neutron electric dipole moment, $d_n \approx 2.4 \times 10^{-16}\theta$ e cm. The measurement of d_n puts a strong constraint on the value of θ: the measurement result $|d_n| < 3 \times 10^{-26}$ e cm implies that $\langle\theta\rangle \lesssim 10^{-10}$; see e.g., a recent review, Ref. [17]. Why is θ so small instead of being a natural $\mathcal{O}(1)$ value? This is coined as the strong CP problem. The PQ mechanism is an elegant solution to the strong CP problem, with θ settling down at $\theta = 0$ *dynamically* and thus becoming a boson field, the axion. The original proposal of the axion in the Peccei-Quinn-Weinberg-Wilczek (PQWW) model [14, 15, 18, 19] has been ruled out by experiments. But there are other possibilities, known as the invisible axion models. The two available benchmark models are the Kim-Shifman-Vainshtein-Zakharov (KSVZ) axion model [20, 21] and the Dine-Fischler-Srednicki-Zhitnitsky (DFSZ) axion model [22, 23]. We refer the readers to Refs. [16, 17, 24] for a review of these axion models.

In addition to solving the strong CP problem, the extra benefit of the axion is that it may explain dark matter. Note that the terminology axion in this thesis means QCD axion only, not the axion-like particles. The couplings of axion with the standard model are suppressed by the decay constant f_a which is very large with a typical value $f_a \sim 10^{10}$ GeV. This makes axions behave as dark matter and evade detection of various experiments so far. Axion dark matter can be generated from the misalignment mechanism and the decay of topological defects (axion strings and axion domain walls) in the early Universe. The present-day axion abundance Ω_a of the Universe is sensitive to the axion mass m_a. The misalignment mechanism predicts $\Omega_a \sim m_a^{-7/6}$ (see e.g., Ref. [24] or eq. (4.12) below in chapter 4 for more details). In addition, there are many uncertainties in computing the axion abundance from the decay of topological objects, and the result is also sensitive to the axion mass. We refer the readers to Refs. [17, 24, 25] for a review of axion cosmology and also Ref. [26] for a review of axion detection methods.

AQNs are formed from the dynamics of the axion topological defects in the early Universe. To be more specific, the collapse of closed axion domain walls with standard model quarks trapped inside leads to the formation of AQNs. Squeezed by closed axion domain walls, quarks (and gluons) inside will finally become stable in a color superconducting (CS) phase in nuclear density [13]. An AQN is macroscopically large with the typical parameters: $R \sim 10^{-5}$ cm

and $B \sim 10^{25}$, where R is the AQN radius and B is the baryon charge carried by an AQN. AQNs are good dark matter candidates due to their small cross-section-to-mass ratio $\sigma/M \sim \rho_{\rm AQN}^{-2/3} m_p^{-1/3} \cdot B^{-1/3} \sim 10^{-10}$ cm^2/g where $\rho_{\rm AQN}$ is the AQN mass density ($\sim$ nuclear density) and m_p is the proton mass. A distinctive feature of the AQN model is that AQNs can be made of matter (quarks) as well as *antimatter* (antiquarks) [13, 27]. This feature makes the AQN model able to resolve the problem of matter-antimatter asymmetry observed in the Universe. Matter AQNs and antimatter AQNs together constitute dark matter, while the disparity between them leads to the matter-antimatter asymmetry. The disparity between matter and antimatter AQNs is of *order one* (specifically, the coherent nonzero axion field $\theta(t)$ in the early Universe results in this disparity, which gives that more antiquarks are trapped inside antimatter AQNs than quarks trapped inside matter AQNs [1]).[2] This scenario thus naturally explains the similarity between the abundances of dark matter and visible matter, i.e.,

$$\Omega_{\rm DM} \sim \Omega_{\rm visible}, \tag{1.2}$$

since now dark matter and visible matter have the same origin in the AQN model. This is also the original motivation of proposing this model [13, 27]. We will review more details of the AQN features in a separate chapter (chapter 2).

Although AQNs behave as dark matter, they will inevitably generate some observational signals due to their interactions with visible matter. Such signals will be relatively more evident in regions/epochs where matter density is large, such as the early Universe and the Galactic Center or when AQNs hit the Sun or the Earth. As we will review in chapter 2, the AQN-induced effects do not violate various current observations. Instead, such effects could potentially explain a number of cosmological and astrophysical puzzles, which we list in chapter 2.

This thesis mainly discusses the recent developments in model building

[2] One comment is that the formation and survival efficiency of closed axion domain walls could actually be very small (it only requires that the closed walls that will finally become AQNs account for $\gtrsim 10^{-8}$ of the total wall area [7]). This is because the closed walls are initially formed at a higher temperature (above QCD transition temperature$\sim$ 170 MeV) when the baryons/antibaryons abundance is much higher than later at $T_{\rm form} \approx 40$ MeV when the AQN formation is completed. Therefore, a small efficiency at initial temperature could be able to lead to an disparity of order one at the end of AQN formation.

and some potential observational evidence of AQNs. The thesis structure goes as follows. In chapter 2, we review the basic features, observational signatures and constraints of the AQN model, and also the crucial ingredients of the AQN formation. The details of the AQN formation will be presented in chapter 3. In chapter 3, we first review the AQN formation that has been studied in Ref. [7]. Then, we study the AQN formation in the background of the coherent nonzero axion field $\theta(t)$. The CP-violating effects generated by the coherent nonzero $\theta(t)$ will finally lead to an order-of-one disparity between matter AQNs and antimatter AQNs [1]. Furthermore, we resolve a multi-scale problem that arises in numerical computations of the AQN formation due to the presence of drastically different scales (QCD scale $\Lambda_{\rm QCD}$ and the axion scale m_a) in the system. We finally get the *real-time* evolution of AQNs from the initial state as closed axion domain walls (with baryon charge induced on the wall) to the final CS state [3].

In chapter 4, we study the contribution of the AQNs to dark matter in the background of axion cosmology, where we take into account the contribution of axions from misalignment mechanism [2]. We find that for the most part of the axion parameter space, AQNs are the dominant contribution to dark matter.

In chapter 5, we study the size distribution and the survival pattern of AQNs [3]. Using percolation theory, we find that the size distribution of AQNs follows a power-law. Furthermore, the size distribution can survive the subsequent evolution in the early Universe. The size distribution of AQNs is consistent with the energy distribution of solar nanoflares, which also follows a power-law. This supports the proposal [6, 28, 29] that the AQN model could explain the "solar corona heating mystery" with the solar nanoflare events identified as the annihilation events of AQNs that impact the Sun.

Finally, in chapter 6 and chapter 7, we discuss two phenomena that could be potentially explained by the AQN model [4, 5]. In chapter 6, we show that the impulsive radio events recorded by Murchison Widefield Array [9] from quiet solar corona could be induced by the annihilation events of AQNs impacting the Sun. In chapter 7, we show that the seasonal variation of the near-Earth X-ray background in 2-6 keV energy range recorded by the XMM-Newton observatory [10] could be explained by the AQN interactions with the Earth. We conclude the thesis in chapter 8.

Chapter 2

Review of the Axion Quark Nugget (AQN) Model

We review the AQN model in this chapter, including the original motivation, basic features, observational signatures, and observational constraints of the model, and also the crucial ingredients related to the AQN formation. This chapter is mainly based on the introductory part of Refs. [1–5]. (AQN papers in recent years, e.g., Refs. [1–7, 28–42], usually incorporate a similar review as the introductory part.)

2.1 Original motivation and basic features

As we have mentioned in the Introduction, the axion quark nuggets (AQNs) are dense objects made of standard model quarks and gluons in CS phase in nuclear density [13]. AQNs carry a large number of baryon charge, B. There are several constraints on the parameter B, which will be reviewed later in chapter 2.2. The typical baryon charge carried by an AQN is $B \sim 10^{25}$, and the typical mass of an AQN can be estimated as $M \sim m_p B \sim 10$ g where m_p is the proton mass. Using the typical nuclear density, the typical radius of an AQN is thus $R \sim 10^{-5}$ cm, which indicates that AQNs are macroscopically large objects.

The idea that dark matter is in the form of composite objects consisting of standard model quarks in a novel phase dates back to the models of strange quark matter with different names: quark nuggets [43], strangelets [44] and nuclearities [45]; see also Ref. [46] for a review. The AQN model which was

originally proposed in Ref. [13] distinguishes itself from the old well-studied models [43–46] in the following aspects:

1. AQNs are formed from the collapse of the closed axion domain walls which are copiously produced during the epoch of QCD transition in the early Universe. The closed axion domain wall is the shell of an AQN, acting as an additional stabilization factor that makes the AQN stable. This will be discussed in chapter 2.3 and chapter 3 in detail. This fact solves several problems arising in the older models. The formation of nuggets in old models [43–46] requires the QCD phase transition to be first-order. However, QCD transition is known by now to be a crossover rather than the first-order phase transition. In comparison, the AQN model does not require the first-order QCD phase transition because the closed axion domain wall works as the squeezer. In addition, even if the nuggets in old models can be formed, it is likely that they eventually evaporate in a Hubble timescale. AQNs do not suffer from the fast evaporation because they are in CS phase that is drastically different from the hadronic phase, which is realized with the external pressure from the axion domain-wall shell. In comparison, nuggets in older models are stable with zero external pressure.

2. AQNs can be made of not only matter but also *antimatter* (antiquarks) [13, 27]. This feature is important in the AQN framework because it provides a solution to the problem of the matter-antimatter asymmetry observed in the Universe, in addition to explaining dark matter. It naturally answers why the visible and dark matter abundances are at the same order of magnitude, $\Omega_{\rm DM} \sim \Omega_{\rm visible}$. These important points are elaborated below.

The original motivation of the AQN dark matter model is to explain the observed similarity between visible and dark matter abundances, eq. (1.2) (i.e., $\Omega_{\rm DM} \sim \Omega_{\rm visible}$). We argue below that this similarity is a very generic feature in the AQN framework.

In the AQN framework, dark matter consists of matter AQNs and antimatter AQNs. They are formed as a consequence of the dynamics of closed axion domain walls in the early Universe which can trap either quarks or antiquarks inside. However, due to the global CP-violating effects induced by the misalignment angle of the coherent axion field $\theta \neq 0$ in the early Universe, there will be a disparity between matter and antimatter AQNs,

i.e., they trap different amounts of quarks and antiquarks. This is dubbed as the CP-violating *charge separation process*. The disparity between matter and antimatter AQNs is always an order-of-one effect and insensitive to the model parameters, which will be demonstrated analytically and numerically in chapter 3 and chapter 4. The charge separation process should be contrasted with the conventional "baryogenesis" process which normally assumes that the Universe starts in a neutral phase with the net baryon charge being zero and then evolves into a state with a net positive baryon charge through the so-called "baryogenesis" process. The baryogenesis is replaced by the charge separation process in the AQN framework where the Universe remains neutral in baryon charge at all times.

The result of the CP-violating charge separation process is that there are more antibaryons stored in antimatter AQNs than baryons stored in matter AQNs, so there are fewer free antibaryons than free baryons in the cosmic plasma. Then, after the annihilation of these free particles and anti-particles in the plasma, only the extra baryons survive and comprise the visible matter today. In other words, the unobserved antibaryons are stored in the extra antimatter AQNs. These words can be expressed as the following simple relations:

$$\begin{aligned} \Omega_{\rm DM} &= \Omega_- + \Omega_+, \\ \Omega_{\rm visible} &= \Omega_- - \Omega_+. \end{aligned} \tag{2.1}$$

where $+$ and $-$ represents matter AQNs and antimatter AQNs respectively. Therefore, the dark matter problem and the matter-antimatter asymmetry problem turn out to be two sides of the same coin, which can be simultaneously resolved in the AQN framework. Furthermore, since visible and dark mater have the same origin in the AQN framework, it is natural to expect that they have similar abundances, $\Omega_{\rm DM} \sim \Omega_{\rm visible}$, which is clearly indicated by eq. (2.1). Of course, this pattern will be destroyed if the two components, Ω_+ and Ω_- are very close to each other, which implies that $\Omega_{\rm DM} \gg \Omega_{\rm visible}$. However, as we will show in chapter 3, the disparity between matter and antimatter AQNs is an $\mathcal{O}(1)$ value, naturally generated by the coherent nonzero axion field $\theta(t)$, which means $\Omega_- \sim \Omega_+ \sim \Omega_- - \Omega_+$. Therefore, the relation $\Omega_{\rm DM} \sim \Omega_{\rm visible}$ holds as a consequence of eq. (2.1).

To be more specific, the observed $\Omega_{\rm DM} \simeq 5\Omega_{\rm visible}$ implies the disparity between matter and antimatter AQNs is $\Omega_+/\Omega_- \simeq 2/3$. This $\mathcal{O}(1)$ disparity is not sensitive to many model parameters, as we will demonstrate in chapter 3 and chapter 4. In comparison, the conventional axion contribution to dark

matter from misalignment mechanism [47–49] scales as $\Omega_a \sim m_a^{-7/6}$ which is sensitive to the axion mass; see eq. (4.12) in chapter 4 for more details. This implies that Ω_a quickly drops if m_a deviates (towards a larger value) from the value at which Ω_a saturates dark matter. The AQN framework does not reject Ω_a as part of dark matter. For most of the axion parameter space, the AQN part $\Omega_\pm$ is the dominant contribution to dark matter. The relation between Ω_a and $\Omega_\pm$ as a function of m_a will be studied in detail in chapter 4.

Another important parameter is the baryon-to-photon ratio observed in the present Universe

$$\eta_{b/\gamma} \equiv \frac{n_b - n_{\bar{b}}}{n_\gamma} \simeq \frac{n_b}{n_\gamma} \approx 6 \times 10^{-10}. \tag{2.2}$$

For a baryon symmetric Universe, baryons and antibaryons will annihilate until $T \simeq 22$ MeV when they freeze out with the relic abundance, $n_b/n_\gamma = n_{\bar{b}}/n_\gamma \simeq 10^{-19}$, which is about nine orders of magnitude smaller than the observed n_b/n_γ. In order to avoid this annihilation catastrophe, there should be a mechanism operating in an earlier stage. The conventional mechanism, baryogenesis, requires the generation of net baryon charge. In comparison, the AQN solution is that different amounts of baryons and antibaryons are hidden in form of AQNs as mentioned above. The plasma of free baryons/antibaryons can continue to interact with the AQN baryons/antibaryons until the AQN formation is completed at $T_{\rm form}$ as the CS phase is built. Thus, AQNs decouple from the plasma and the asymmetry between matter and antimatter AQNs, and therefore, the asymmetry between baryons and antibaryons outside in the plasma, become concrete since $T_{\rm form}$.[3] The asymmetry is preserved until today and becomes the observed $\eta_{b/\gamma}$ whose value is determined by the temperature at which the asymmetry is formed,

[3]Although the asymmetry between matter AQNs (Ω_+) and antimatter AQNs (Ω_-) only becomes concrete after $T_{\rm form}$, it is actually generated in an earlier stage when the coherent axion field $\theta(t)$ is nonzero. $\theta(t)$ decreases to nearly zero soon after the QCD transition $T_c \simeq 170$ MeV, but AQNs continue to evolve until $T_{\rm form}$, independently of the earlier stage when the nonzero θ is present as the source of asymmetry. The observed baryon-to-photon ratio requires that $T_{\rm form} \approx 40$ MeV, that is, the previous accumulated asymmetry becomes much more apparent at this temperature, as all antibaryons outside are annihilated away while baryons still remain in the cosmic plasma. There will be no much annihilation between visible baryons and antimatter AQNs after this temperature, as we have discussed in Ref. [3] (see also chapter 5.2). For $T > T_{\rm form}$, the annihilation between baryons and antibaryons is very efficient.

$\eta_{b/\gamma} \sim (m_p/T_{\rm form})^{3/2} \cdot \exp(-m_p/T_{\rm form})$ where m_p is the proton mass; see e.g., Ref. [27, 50]. Using the observed value of $\eta_{b/\gamma}$, eq. (2.2), we can derive that $T_{\rm form} \approx 40$ MeV. However, a small change of $T_{\rm form}$ will result in a very large change of $\eta_{b/\gamma}$ because of the exponential dependence, which means that we cannot theoretically calculate the value of $\eta_{b/\gamma}$ with any precision in the AQN framework.

We emphasize that $T_{\rm form} \approx 40$ MeV is *not* theoretically derived from the side of AQN model. Instead, it is an observation value, precisely determined by the baryon-to-photon ratio, eq. (2.2). In fact, in order to compare the theoretical prediction with the observation eq. (2.2), $T_{\rm form}$ has to be theoretically calculated with high precision (such a theoretical calculation in AQN model is impracticable). Otherwise, a small deviation will result in a large fluctuation of $\eta_{b/\gamma}$ because of the exponential dependence. Nevertheless, $T_{\rm form} \approx 40$ MeV is a very reasonable value in the AQN model, because it has a typical QCD scale, and it is close to the critical temperature of the formation of CS phase, $T_{\rm CS} \simeq 0.6\Delta \simeq 60$ MeV (see e.g., Ref. [51]) where $\Delta \sim 100$ MeV is the energy gap of the CS phase.

Unlike conventional dark matter candidates, e.g., WIMPs, the presence of the antimatter in the antimatter AQNs makes them strongly interacting with the baryonic matter. Intuitively, such a model would strongly contradict observations. However, detailed studies show that the model does not violate any known observational constraints on dark matter or antimatter. Below, we list the main features of AQNs that make them good candidates for cold dark matter [52]:

1. The typical baryon charge carried by an AQN is huge, $B \sim 10^{25}$,[4] which implies that the number density of AQNs is extremely low.

2. AQNs have nuclear densities, so the ratio of the AQN's cross-section to its mass is low, $\sigma/M \sim 10^{-10}$ cm^2/g, which is far below the astrophysical and cosmological limits that $\sigma/M < 1$ cm^2/g. This makes AQNs qualify as dark matter candidates.

3. AQNs are stable objects over the cosmological timescale. They can survive the unfriendly environment of the early Universe, pre-and post-BBN (Big Bang Nucleosynthesis) epochs, and most of them can also

[4] B here is in the average sense based on the observational constraints which will be discussed in chapter 2.2. The entire B distribution (and thus the average B) can be fixed if we identify the solar nanoflares as AQN-annihilation events in the Sun.

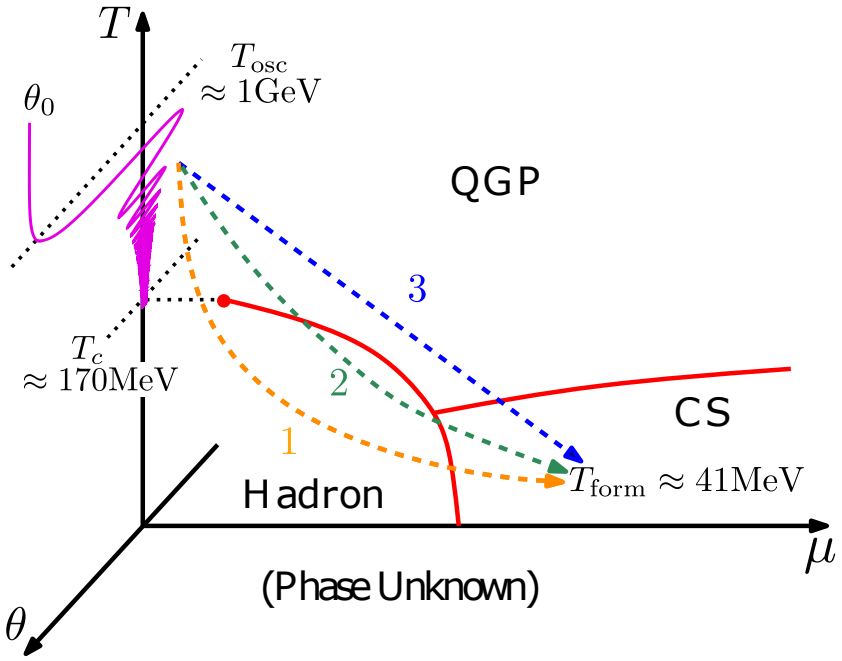

Figure 2.1: This diagram incorporates many important ingredients of the AQN framework with the QCD phase diagram. The solid oscillating line represents the misalignment mechanism with the initial misalignment angle θ_0 staring at $T_{\rm osc}$ when the axion mass effectively turns on. The three dashed lines represent possible paths of the AQN formation. The phase diagram is actually much more complicated as it depends on the third essential parameter, θ, which is nonzero in the early Universe. The phase at nonzero θ is not shown because it is largely unknown. This figure is taken from Refs. [1–3, 7].

survive the violent environment during structure formation and star formation epochs; the survival pattern of AQNs will be discussed in detail in chapter 5.

4. AQNs have considerable binding energy due to the large gap ($\Delta \sim$ 100 MeV) in CS phase, so the baryons or antibaryons locked inside AQNs cannot participate in BBN that happens around $T \sim 1$ MeV. Thus, the conventional BBN scenario holds with possible tiny corrections at the order of 10^{-10}, which could provide a solution to the "Primordial Lithium Puzzle"[35].

5. In the AQN framework, AQNs do not affect the conventional scenario of structure formation because they completely decouple from photons due to the small ratio σ/M.

6. Also, AQNs do not change the conventional analysis of CMB. Instead, the small corrections to radiations provided by the presence of AQNs may solve the tension of the stronger than anticipated 21 cm absorption features observed by EDGES, as discussed in Ref. [31].

In summary, different from conventional dark matter candidates which are "dark" because they (usually assumed to be new fundamental fields) couple weakly to standard model particles, AQNs are "dark" because of their small cross-section-to-mass ratio, $\sigma/M \sim B^{-1/3}$. Nevertheless, the interactions between AQNs and visible matter will inevitably generate some observational signatures, especially in the regions/epochs where matter is dense such as the early Universe and the Galactic Center, or when AQNs hit the Sun or the Earth. The induced phenomena do not violate any current observational constraints but instead may account for some unexplained astrophysical puzzles and mysteries. In the following text, we list the astrophysical puzzles and mysteries that could possibly be explained within the AQN framework. We also overview the observational constraints put on the parameter space of AQN mass.

2.2 Observational signatures and constraints

An antimatter AQN will emit radiation when it collides with a baryon if they can successfully annihilate. Such events are actually very infrequent because the number density of AQNs is very low. Incoming baryons can only excite the surface of an AQN to emit radiation, while most of the mass remains dark, hidden inside the AQN. This implies that the AQN model with a larger average baryon charge, $\langle B \rangle$, will actually generate weaker emissions. Obviously, the strength of emissions also depends on the environment. There will be more emissions in dense regions such as the center of the Milky Way. The interactions between antimatter AQNs and the visible baryonic matter in the center of the Milky Way lead to electromagnetic signatures, which may explain various emission excesses in different frequency bands from radio to γ-ray wavelengths, including the well-known 511 keV line, if AQNs carry a baryon charge $\langle B \rangle \sim 10^{25}$. We refer the readers to Refs. [53–58] for further

details.

In addition, the AQN model may explain some other naively unrelated phenomena. We list them here with the corresponding AQN papers that contain more details: the "primordial lithium puzzle" [35]; the "solar corona heating mystery" [6, 28, 29]; the recent EDGES observations [31]; the annual modulation of the near-Earth X-ray background in 2-6 keV observed by XMM-Newton observatory [5]; the annual modulation observed by DAMA/LIBRA experiment [30]; the fast radio bursts [33]; the infrasound and seismic acoustic waves generated by AQN annihilation events in the Earth's atmosphere [39]; the mysterious bursts observed by Telescope Array experiment [40, 42].

Next, we overview the observational constraints on the AQN model. The IceCube Observatory's non-detection of a non-relativistic magnetic monopole [59] can be used to constrain the AQN model. This is likely to be the strongest constraint. Although AQNs and magnetic monopoles interact with matter in very different ways, they both can generate electromagnetic and hadronic cascades along their path impacting the Earth. Such cascades can be detected by the detector, the non-detection of which thus puts a constraint on the AQN flux, $\Phi_{\rm AQN} \lesssim 1/({\rm km}^2{\rm yr})$. With the local dark matter density, $\rho_{\rm DM} \sim 0.3\ {\rm GeV/cm}^3$, assumed to be saturated by AQNs, this constraint on flux can be translated into the constraint on the baryon charge averaged over all AQNs:

$$\langle B\rangle \gtrsim 3\times 10^{24} \qquad \text{(constraint from direct (non)observation of IceCube).} \tag{2.3}$$

More details can be found in Appendix A of Ref. [36]. A constraint similar to eq. (2.3) is given in Ref. [60] based on the Antarctic Impulsive Transient Antenna, despite that it depends on details of the AQN emissivity. The same paper also gives a constraint from the total geothermal energy budget of the Earth, which sets $\langle B\rangle > 2.6\times 10^{24}$.[5]

In Ref. [62], the authors use the Apollo data (collected by seismometers implanted on the Moon) to constrain strange quark nuggets. When macro

[5]In addition, there is a constraint on the mass of macro dark matter (e.g., AQNs), $M \gtrsim 55$ g (which corresponds to $B \sim 10^{25}$), derived in Ref. [61] from the non-detection of etching tracks in ancient mica. It is slightly above the lower bound (2.3), but it will not strongly constrain the allowed window (2.5), because AQNs actually have a mass distribution (as we will discuss below; see eq. (2.6)) and large AQNs as the dominant portion of the total dark matter mass are well above the lower bound (2.3).

dark matter candidates pass through the Moon, they could generate seismic waves that could be detected by the Apollo seismometers. The Apollo data (~ 2500 seismic events per year and $\sim 10^{17}$ ergs total seismic energy per year) could be used to constrain the mass and abundance of strange quark nuggets [62]. The result is that the strange quark nuggets' abundance in the mass range of 10 kg to 1 ton must be at least one order of magnitude smaller than would fully account for local dark matter [62]. The same result can be applied to AQNs, which implies that the majority (at least 90%) of AQNs much be lighter than 10 kg, so we have

$$\langle B\rangle \lesssim 10^{28} \qquad \text{(constraint from Apollo data)}. \tag{2.4}$$

In comparison, the authors Ref [63] did another analysis about whether such macro dark matter can generate detectable seismic waves. They showed that Apollo data cannot be used to constrain macro dark matter with a density roughly equal to or higher than the nuclear density, such as AQNs. This is mainly because the size of such dense dark matter candidates is small and cannot generate long-wavelength seismic waves strong enough (much weaker than the assumption made by the previous paper, Ref. [62]) to be detected by the Apollo seismometers. Thus, there is no constraint on $\langle B\rangle$ as eq. (2.4) based on Ref. [63].

Combining together eq. (2.3) and the analyses related to Apollo data, we get the window of AQNs that can saturate dark matter:

$$3\times 10^{24} \lesssim \langle B\rangle \lesssim \begin{cases} 10^{28}, \text{ based on Ref. [62]}, \\ \text{(no upper limit)}, \text{ based on Ref. [63]}. \end{cases} \tag{2.5}$$

In addition, the authors of Ref. [64] have discussed various constraints on the macro dark matter made of antimatter. The AQN model with the window (2.5) is consistent with many constraints presented in their paper, including the CMB and BBN constraints but in tension with the constraint from "human detector".[6] The explanation for this tension is given in Ref. [4]

[6]When a macro dark matter "particle" passes through a human body, it could result in death or serious injury similar to a gunshot injury [65]. Furthermore, an antimatter macro could generate additional injury through radiation when it passes through a human body [64]. The null observation of such events in a large population can be used to constrain macro dark matter, as discussed in Ref. [64, 65]. However, these constraints have been criticized in Ref. [4]; see also the text below.

(see footnote 3 in Ref. [4] for details) with the basic points as follows: due to the internal structure of (antimatter) AQNs, their annihilation with baryons is not similar to $p\bar{p}$ process that was assumed in Ref. [64]; the typical X-ray energy assumed to be $\sim$1 keV in Ref. [64] is lower than that in the AQN model [39], and higher energy X-rays have a longer mean-free path so the majority of emissions will be deposited in the air outside the human body; the typical AQN radius is 10^{-5} cm which is not likely to make a gunshot injury, with the majority of energy deposited in the form of X-rays over the centimeter scale [39]. It may result in death after a long time delay, so the cause of death would be hard to be identified, in contrast with the assumption in Ref. [64].

As we mentioned above, the AQN model may explain various emission excesses in different frequency bands in the galactic spectrum if AQNs carry a baryon charge $\langle B\rangle \sim 10^{25}$ [53–58]. This value of $\langle B\rangle$ is consistent with the window eq. (2.5). Another self-consistency check can be found in the proposal that the AQN model may solve the "solar corona heating mystery" [6, 28, 29], as we will discuss below.

When antimatter AQNs hit the Sun, they will get completely annihilated in the transition region of the Sun. The total annihilation energy is not sensitive to the details of the AQN model but can be estimated based on the local dark matter density $\rho_{\rm DM} \sim 0.3$ GeV/cm^3. The result of the total annihilation energy is very close to the observed EUV (extreme ultraviolet) luminosity $\sim 10^{27}$ erg/s [28]. It is believed that the EUV emission is powered by the impulsive heating events known as nanoflares, but the physical origin of the nanoflares is not known yet. The similarity between the total annihilation energy and the observed EUV emission motivated the identification of solar nanoflares as AQN annihilation events [28]. The energy of nanoflares W is connected to the AQN baryon charge through the simple relation $W = 2m_p c^2 B$. The energy distribution of nanoflares, dN/dW, has been modeled as a power-law distribution by people in the community of solar physics (see e.g., Refs. [66, 67]). The baryon charge distribution of AQNs, dN/dB, should follow the same distribution, so we have [28]

$$dN \propto W^{-\alpha} dW \propto B^{-\alpha} dB \tag{2.6}$$

where dN is the number of nanoflare events (per unit time) with the energy between W and $W + dW$. The slope α varies for different models. Analysis in Ref. [66] favors $\alpha \approx 2.5$, while Ref. [67] considered a broken power-law

with $\alpha = 1.2$ for small energies and $\alpha = 2.5$ for large energies. The energy range of nanoflares is usually characterized by 10^{21} erg $\lesssim W \lesssim 10^{26}$ erg, which corresponds to $3 \times 10^{23} \lesssim B \lesssim 3 \times 10^{28}$ based on the relation $W = 2m_p c^2 B$. This largely overlaps with the window eq. (2.5), which should be considered as a highly non-trivial self-consistency check of the AQN framework.

In chapter 5, we will study the baryon charge distribution of AQNs, dN/dB, from the theoretical side. The result shows that dN/dB follows a power-law distribution, which supports the proposal of identifying solar nanoflares as AQN annihilation events. In addition, the annihilation of AQNs in the Sun will be studied in chapter 6 where we show that AQN annihilation events will generate impulsive radio signals that can explain the observations by MWA [9].

2.3 Crucial ingredients of the AQN formation

We have reviewed the motivation, basic features, observational signatures, and observational constraints of the AQN model. Now, we are in a position to discuss how AQNs are formed in the early Universe. In the following text, we review the crucial ingredients related to the AQN formation while leaving the details of analyses and simulations of AQN formation in chapter 3.

2.3.1 $N_{\rm DW} = 1$ axion domain walls

The first important ingredient of the AQN formation is the existence of axion domain walls that are formed in the early Universe. The general case of the formation of axionic topological defects will be briefly reviewed in chapter 2.3.3, while in this part, we focus on the possibility of the formation of $N_{\rm DW} = 1$ axion domain walls in the *pre-inflationary* scenario.

If the Peccei-Quinn (PQ) phase transition occurs *before* inflation, the axion field θ will get homogenized by the inflation. As a consequence, θ is uniform everywhere, and there is only a single physical vacuum. Therefore, it is normally assumed that the prerequisite for the formation of domain walls is that the PQ phase transition occurs *after* inflation (post-inflationary scenario). This argument holds for the domain walls of the types $N_{\rm DW} > 1$ whose formation requires the presence of physically *different vacua*. However, $N_{\rm DW} = 1$ domain walls are special in the sense that θ interpolates between one

and the same physical vacuum. This special characteristic makes it possible that $N_{\rm DW}=1$ domain walls can form even if the PQ phase transition occurs before inflation (pre-inflationary scenario) [1, 7].[7] This can be argued from the following aspects.

First, we start with the expression of the vacuum energy, which is known as [68, 69][8]

$$E_{\rm vac}=\min_k(\theta+2\pi k)^2+\mathcal{O}(1/N_c). \tag{2.7}$$

θ in this context stands for the axion field; k represents different branches of the unique physical vacuum. In order to satisfy the required 2π periodicity, $E_{\rm vac}(\theta)=E_{\rm vac}(\theta+2\pi)$, the k different branches must be present at each point in space and cannot be removed away by the inflation. Therefore, $N_{\rm DW}=1$ domain walls can form as θ interpolates between different branches, $k=0$ and $k=1$. Second, the interpolation between one and the same physical vacuum is identical to the creation of solitons in $1+1$ dimensional sine-Gordon model.[9] Due to bosonization, the sine-Gordon soliton can be identified with the ψ fermion of the Thirring Model [70, 71]. The production of ψ fermions at nonzero temperature is permitted obviously, which implies the existence of the sine-Gordon solitons in the dual picture, and this is irrelevant to whether the PQ symmetry breaking occurs before the inflation or not. The second argument is based on an exactly solvable model when a soliton interpolating between different sectors can be presented as the local field which knows nothing about the topological sectors. Nevertheless, the results should be the same, which implies that the interpolation between different branches must be present everywhere in space irrespective of inflation. Otherwise,

[7] We emphasize that pre- (post-) inflationary scenario corresponds to *PQ phase transition* occurring before (after) inflation. PQ phase transition corresponds to the spontaneous symmetry breaking of the PQ symmetry and it leads to the formation of axion strings. In comparison, the symmetry breaking leading to the formation of axion domain walls happens much later, which is always after the inflation. In the pre-inflationary scenario, domain walls are not accompanied by strings because strings have been blown away by inflation. This should be contrasted with the conventional picture of string-wall network considered in the literature for the post-inflationary scenario. More discussions can be found in chapter 2.3.3.

[8] Though this expression is derived in the large-N_c limit where N_c is the number of colors, it still holds for finite N_c, as explained in Ref. [7].

[9] The Lagrangian for the sine-Gordon model is $\mathcal{L}_{\rm sG}(x,t)=\frac{1}{2}(\partial_\mu\phi)^2+m_a^2f_a^2\cos(\phi/f_a)$. The time-independent soliton solution has the configuration $\phi(x)=4f_a\tan^{-1}[\exp(m_ax)]$. Extending the soliton solution trivially in the other two spatial dimensions, we get a domain wall.

some fundamental features of QFT will be broken.

In summary, both the arguments of the vacuum structure and the soliton-ψ duality supports the formation of $N_{\rm DW} = 1$ axion domain walls even in the pre-inflationary scenario.

The final comment is that we can also check the formation of such walls from the perspective of energy. The energy barrier in the sine-Gordon potential is $\sim \Lambda_{\rm QCD}$. The temperature of cosmic plasma at this moment is also at the same order of magnitude, so the temperature fluctuation can overcome the barrier and make the axion field interpolate between $\theta = 0$ and 2π which are separated by the barrier $\sim \Lambda_{\rm QCD}$. This should be contrasted with the formation of axion strings which can only be formed at a much higher temperature at PQ phase transition.

2.3.2 Local spontaneous symmetry breaking of baryon charge

Many years after the idea of axion domain walls were proposed [72, 73], it was realized that they generally demonstrate a sandwich substructure on the QCD scale $\Lambda_{\rm QCD}^{-1} \simeq$ fm. This is supported by the large-N_c analysis of QCD with the inclusion of the η' (eta' meson) field [74], which showed the existence of the axion-η' wall: the axion domain wall with the scale $\sim m_a^{-1}$ has a much smaller η' structure $\sim \Lambda_{\rm QCD}^{-1}$ sandwiched inside. This substructure plays an important role in the AQN model, because quarks are actually squeezed by the η' field (rather than the axion field). The axion field and η' field are linked with each other so they are very stable an cannot untwist themselves. Similar structures are also supported by the analysis of supersymmetric models with a similar θ vacuum [75], and the explicit construction of domain walls in CS phase [76]. In addition to these known substructures, another substructure with a similar QCD scale that carries baryon charge has been studied in Ref. [7]. Due to this additional substructure, quarks or antiquarks will be trapped in the core of a domain wall. This will be discussed in detail in chapter 3.1 based on Ref. [7], from which we will see that the baryon charge trapped in the vicinity of the domain wall is

$$B_{\rm wall} = Ng \int \frac{d^2x_\perp d^2k_\perp}{(2\pi)^2} \frac{1}{\exp\left(\frac{\epsilon-\mu}{T}\right)+1}. \tag{2.8}$$

N is the baryon number induced on the domain wall per degree of freedom, and it can be any positive or negative integers. $g \simeq N_c N_f$ is the degeneracy factor in the CS phase. μ is the chemical potential of baryon charge in the vicinity of the wall.

The QCD substructure with $N \neq 0$ only slightly lifts the axion domain-wall tension with a correction factor $\sim \Lambda_{\rm QCD}/f_a \ll 1$, so carrying nonzero baryon charge can be a generic feature of the axion domain walls. Furthermore, as we will see in chapter 3.1, the QCD substructure is formed topologically, so the trapped baryon charge is protected by topology and thus cannot easily leave the system.

The sign of N (i.e., quarks or antiquarks) is chosen randomly. As a result, baryon and antibaryon charges are separated on the scale of the wall's correlation length, $\xi(T) \sim m_a^{-1}(T)$. This is coined as the *local spontaneous breaking of C symmetry*. If the external environment is CP even (as in the case $\theta = 0$), the sign of baryon charge will be chosen randomly with *equal probability*, and the evolution of matter AQNs and antimatter AQNs will be symmetric with each other, which results in an equal number of baryons/antibaryons carried by matter/antimatter AQNs.

2.3.3 Kibble-Zurek mechanism

Topological defects will form during a cosmological phase transition induced by a symmetry breakdown, which is known as the Kibble-Zurek mechanism [77, 78]. Due to this mechanism, symmetry breakdowns of the axion field in the early Universe will generate various types of topological defects known as strings and domain walls [72, 73]. When the Universe cools down to the temperature $T_s \sim f_a$, the PQ symmetry, $U(1)_{\rm PQ}$, spontaneously breaks, and the axion strings form. Later, when the temperature further drops to the scale $T_{\rm osc} \sim 1$ GeV, the axion mass effective turns on induced by non-perturbative QCD effects (see Refs. [24, 25] for a review). The nonzero axion mass explicitly breaks $U(1)_{\rm PQ}$ with $N_{\rm DW}$ degenerate vacua, which leads to the formation of axion domain walls. With the axion mass increasing rapidly with the cosmological temperature dropping down, the symmetry breaking becomes more pronounced, and therefore, the domain wall formation becomes more efficient. Finally, the axion mass acquires its asymptotic value at the QCD transition temperature, $T_c \sim 170$ MeV, when the chiral condensate forms (see e.g., Ref. [79]); see also Fig. 2.1. In general, we should expect that the axion domain walls can form at any time between T_c and $T_{\rm osc}$. The

temperature-dependence of axion domain-wall formation will be discussed in detail in chapter 5.

In our case, the axion domain walls are the type $N_{\rm DW} = 1$ which are formed in the pre-inflationary scenario, as we have discussed in chapter 2.3.1. In this scenario, the pre-existing strings that are formed at $T_s \sim f_a$ will be "blown" away by the inflation, so they are not in the system when the domain walls form. The domain wall network is dominated by a very large, highly folded wall with a very complicated topology. In addition to this main wall, there are some walls in the closed form [80] (see also Ref. [81] where closed domain walls have been observed in simulation with the strings present). Normally, these closed walls are considered to collapse with the energy released in the form of free axions and gravitational waves [25], and they play no important role due to their small wall area in comparison with the large main wall. However, as we have discussed in chapter 2.3.2, the axion domain walls carry quarks. The collapse of a closed domain wall will be balanced by the Fermi pressure exerted by the quarks trapped inside. This will be discussed in detail in chapter 3. We will see that the closed walls with quarks/antiquarks trapped inside will finally evolve into matter/antimatter AQNs.

2.3.4 Color superconductivity

The existence of the CS phase in QCD is crucial for the stability of AQNs. In astrophysics, a CS phase could be realized in the interiors of neutron stars, in the collapse of massive stars, and in the collision of neutron stars, etc. See Refs. [51, 82] for a review. Similarly, a CS state could form inside an AQN when the Fermi pressure inside balances the domain wall tension, as we will see in chapter 3. The domain wall tension here plays the role of the gravitational collapse in the case of neutron stars.

The superconducting phases have a large binding energy $\Delta \sim 100$ MeV, so the quarks inside AQNs can hardly participate in processes like BBN in the early Universe at $T \sim 1$ MeV long after the AQN formation, as we have reviewed in chapter 2.1.

2.3.5 Coherent CP-odd axion field

As we discussed in chapter 2.3.2, baryon charge and antibaryon charge will be separated as a result of axion domain walls trapping (anti)quarks with

the sign chosen randomly. If the external environment is CP-even as in the case $\theta = 0$, matter/antimatter AQNs will finally carry an equal number of baryons/antibaryons. However, the axion field can be nonzero in the early Universe, with the initial value θ_0 being any value between 0 and 2π known as the *misalignment angle*. In the pre-inflationary scenario, the misalignment angle gets homogenized by inflation and thus is coherent at the scale of the whole Universe. At $T_{\rm osc}$, the axion field starts to oscillate as a response to the effectively turning on of the axion mass. The oscillation of the coherent axion field is (see e.g., the review paper [25])

$$\theta(t) \simeq \frac{C}{f_a\sqrt{m_a(t)}}\frac{1}{t^{3/4}}\cos\left(\int^t dt'\omega_\theta(t')\right), \quad \omega_\theta^2(t) = m_a^2(t) + \frac{3}{16t^2} \tag{2.9}$$

where C is a constant. The nonzero θ will generate CP-odd effects, so the charge separation process discussed in chapter 2.3.2 will be asymmetric. Moreover, $\theta(t)$ is uniform in the entire Universe so that the asymmetry will be coherent over this large scale. Instead, if $\theta(t)$ is space-dependent and assumes arbitrary values in the Universe as in the post-inflationary scenario, the asymmetric effects can be totally canceled out over a large scale of space. This is the exact reason why we require the pre-inflationary scenario.

The coherent $\theta(t)$ will finally lead to an asymmetry between matter and antimatter AQNs, that is, more *antiquarks* are trapped inside antimatter AQNs than *quarks* trapped inside matter AQNs. The magnitude of the asymmetry is $\mathcal{O}(1)$. This will be discussed in detail in chapter 3.2. Also, the AQN model assumes that the Universe is neutral in baryon charge at all times. As a consequence, in the cosmic plasma outside AQNs, there are fewer free antiquarks than free quarks. After the annihilation in the cosmic plasma, only the excess of quarks survives as the visible matter today. Thus, the AQN model can explain not only the dark matter problem but also the observed matter-antimatter asymmetry with the conventional baryogenesis mechanism replaced by the CP-asymmetric baryon charge separation process, as we have reviewed in chapter 2.1. In summary, matter and antimatter AQNs together account for dark matter, and the difference between them results in visible matter. The AQN model naturally explains the similarity between abundances of visible matter and dark matter, $\Omega_{\rm visible} \sim \Omega_{\rm DM}$, since the asymmetry between matter AQNs and antimatter AQNs is order-of-one in magnitude, which will be demonstrated in chapter 3.2.

Chapter 3

AQN Formation

In this chapter, we are going to discuss the dynamics of closed axion domain walls with the initial nonzero baryon charge induced in the vicinity of the wall, which, as we will see, leads to the formation of AQNs. Also, we will study the effect of the coherent CP-odd axion field on the AQN formation, which turns out to generate an asymmetry between matter and antimatter AQNs.

3.1 Review of the AQN formation

In this part, we review the AQN formation based on Ref. [7] which has studied how baryon charge is initially induced in the vicinity of axion domain walls and how the system (a closed axion domain wall with the induced baryon charge) evolves.

As we have briefly mentioned in chapter 2.3.2, the QCD substructure of baryon charge is induced in the vicinity of axion domain walls in a way similar to that of the η' field [74]. In both cases, the substructures arise as a result of nontrivial boundary conditions that the vacuum states are physically the same but topologically distinct at the two sides of a wall. This can be described more quantitatively (see below) with the technique used in Refs. [83, 84] which studied the generation of the magnetic field in the domain wall background. The interaction between pseudo-scalar fields and fermions can be described by

$$\mathcal{L}_4 = \overline{\Psi}(i\partial\!\!\!/ - m_{\text{eff}} \mathrm{e}^{i(\theta-\phi_{\eta'})\gamma_5} - \mu\gamma_0)\Psi. \tag{3.1}$$

$\phi_{\eta'}$ represents the eta' meson, which is a pseudo-scalar. It enters the Lagrangian in the combination $\theta - \phi_{\eta'}$ as required by the low-energy effective potential (see e.g., Refs. [74, 76, 84]). θ is the QCD topological angle and can be understood as the dynamical axion field. The interaction between it and Ψ in eq. (3.1) is generated through a chiral rotation to cancel the QCD topological term.

For simplicity, in eq. (3.1), we omitted the color and flavor indices of Ψ. $m_{\rm eff}$ should be treated as an effective mass that describes the interaction of Ψ in all phases during evolution, including the initial quark-gluon plasma (QGP) phase, the hadronic phase, and the final CS phase. For the purpose of this chapter, the exact history of $m_{\rm eff}(T)$ is not needed. Instead, it can be assumed to be the QCD energy scale, $m_{\rm eff} \sim \Lambda_{\rm QCD}$, to simplify the analysis. μ is the chemical potential of Ψ trapped by the wall.

Same as Refs. [83, 84], "thin-wall" approximation can be adopted here ($\partial_x = \partial_y = 0$), which simplifies eq. (3.1) to a Lagrangian of a $1+1$ dimensional fermionic system. Such a system can be further transformed into a bosonic system using the well-known *bosonization* procedure [70, 71],[10] which gives

$$\mathcal{L}_2 = \frac{1}{2}(\partial_\mu \theta_1)^2 + \frac{1}{2}(\partial_\mu \theta_1)^2 + U(\theta_1, \theta_2) + \frac{\mu}{\sqrt{\pi}}\partial_z(\theta_1 + \theta_2). \tag{3.2}$$

with the effective potential

$$U(\theta_1, \theta_2) = -m_{\rm eff} m_0[\cos(2\sqrt{\pi}\theta_1 - \phi_{\eta'} + \theta)] - m_{\rm eff} m_0[\cos(2\sqrt{\pi}\theta_2 + \phi_{\eta'} - \theta)] \tag{3.3}$$

θ_1, θ_2 are the bosonic fields. m_0 is at the same order of magnitude as $m_{\rm eff}$, i.e., $m_0 \sim m_{\rm eff} \sim \Lambda_{\rm QCD}$. The potential is minimized when the terms inside the cosine functions take the values that are integer times of 2π. The two sides of a domain wall can pick up different integers, just like the formation of the axion domain wall itself. $U(\theta_1, \theta_2)$ can be minimized for the following

[10] A well-known example of bosonization is the equivalence between the sin-Gordon model and Thirring model in $1+1$ dimension [70, 71], as mentioned in chapter 2.3.1. The bosonization dictionary is known to be

$$\overline{\Psi}_{(j)} i\hat{\gamma}^\mu \partial_\mu \Psi_{(j)} \to \frac{1}{2}(\partial_\mu \theta_j)^2, \qquad \overline{\Psi}_{(j)} \hat{\gamma}_\mu \Psi_{(j)} \to \frac{1}{\sqrt{\pi}} \epsilon_{\mu\nu} \partial^\nu \theta_j,$$
$$\overline{\Psi}_{(j)} \Psi_{(j)} \to -m_0 \cos(2\sqrt{\pi}\theta_j), \qquad \overline{\Psi}_{(j)} i\hat{\gamma}_5 \Psi_{(j)} \to -m_0 \sin(2\sqrt{\pi}\theta_j).$$

boundary conditions[11]

$$\begin{aligned} 2\sqrt{\pi}\theta_1(z=+\infty)-2\sqrt{\pi}\theta_1(z=-\infty)=2\pi n_1,\\ 2\sqrt{\pi}\theta_2(z=+\infty)-2\sqrt{\pi}\theta_2(z=-\infty)=2\pi n_2, \end{aligned} \tag{3.4}$$

where n_1 and n_2 are integers. Such boundary conditions imply that the domain wall carries the baryon charge N,

$$N=\int d^3x\overline{\Psi}\gamma_0\Psi=\int dz\left[\overline{\Psi}_{(1)}\hat{\gamma}_0\Psi_{(1)}+\overline{\Psi}_{(2)}\hat{\gamma}_0\Psi_{(2)}\right]=-(n_1+n_2), \tag{3.5}$$

which is calculated for the one-particle Dirac equation. The baryon charge N is nonzero as long as n_1+n_2 is nonzero. This is generally true as the integers n_1 and n_2 are randomly picked up, so it is a generic phenomenon that axion domain walls carry a certain amount of baryon charge. We emphasize that there is no preferences for the boundary conditions (3.4); they are determined randomly by uncorrelated patches picking up different values. These boundary conditions correspond to the vacuum states with the lowest energy at large distances. The result is that a wall could carry zero baryon charge, but more generally it will carry nonzero baryon charge. This is also physically allowed since this QCD substructure with nonzero baryon charge only lifts the wall tension very slightly due to the fact that $\Lambda_{\rm QCD}\ll f_a$, which therefore does not suppress the formation rate of such walls.

Furthermore, the baryon charge $B_{\rm wall}$ carried by a domain wall in three dimensions can be recovered by multiplying N by an appropriate statistical factor in the vicinity of the wall,

$$B_{\rm wall}=Ng\int\frac{d^2x_\perp d^2k_\perp}{(2\pi)^2}\frac{1}{\exp\left(\frac{\epsilon-\mu}{T}\right)+1}, \tag{3.6}$$

where $g\simeq N_cN_f$ is the degeneracy factor, ϵ is the energy, and μ is the chemical potential of the baryon charge. T is the temperature when the axion walls are initially formed, $T\sim 200$ MeV. But it evolves with time, keeping thermal equilibrium with the cosmological temperature (see below) until $T_{\rm form}\sim 40$ MeV when the AQN formation is completed.

The evolution of a *closed* axion domain wall that initial carries the baryon

[11] These boundary conditions are not complete because the role of θ and $\phi_{\eta'}$ are neglected. However, they are good enough for the purpose of showing the possibility that axion domain walls can carry baryon charge.

charge $B_{\rm wall}$, eq. (3.6), is dominated by the effective Lagrangian:

$$\mathcal{L} = \frac{1}{2}\cdot 4\pi R^2(t)\sigma_a \cdot \dot{R}^2(t) - 4\pi\sigma_a R^2(t) + \frac{4\pi R^3(t)}{3}[P_{\rm in}(\mu) - P_{\rm out}(t)]. \quad (3.7)$$

The closed wall is assumed to be spherically symmetric with the radius, $R(t)$, evolving with time. $\sigma_a = 8 f_a m_a^2$ is the well-known axion domain wall tension. $\mu(t)$ implicitly depends on time. The expressions of pressure terms are:

$$P_{\rm out} \simeq \frac{\pi^2 g^{\rm out}}{90} T_{\rm out}^4, \qquad g^{\rm out} \simeq \frac{7}{8} 4N_c N_f + 2(N_c^2 - 1), \quad (3.8)$$

$$P_{\rm in}(\mu) = P_{\rm in}^{\rm (Fermi)}(\mu) + P_{\rm in}^{\rm (bag\ constant)}(\mu), \quad (3.9)$$

$$P_{\rm in}^{\rm (Fermi)}(\mu) = \frac{g^{\rm in}}{6\pi^2}\int_0^\infty \frac{k^3 dk}{\exp\left(\frac{\epsilon(k)-\mu}{T}\right)+1}, \qquad g^{\rm in} \simeq 2N_c N_f, \quad (3.10)$$

$$P_{\rm in}^{\rm (bag\ constant)}(\mu) \simeq -E_B \cdot \Theta(\mu - \mu_1)(1 - \mu_1^2/\mu^2). \quad (3.11)$$

We take the outside pressure $P_{\rm out}$ as the pressure exerted by QGP outside the closed wall for simplicity. $P_{\rm in}^{\rm (Fermi)}$ is the Fermi pressure exerted by the trapped quarks. The pressure comes from the quarks in the *bulk* inside the closed wall. These quarks are accumulated as a consequence of keeping chemical equilibrium with the baryon charge initially induced in the vicinity of the wall, $B_{\rm wall}$. Such chemical equilibrium will be built very quickly, which will be discussed below (see also eq. (3.18)). $P_{\rm in}^{\rm (bag\ constant)}(\mu)$ is the pressure due to the famous bag constant from the MIT bag model, where $E_B \sim (150\ {\rm MeV})^4$ and $\mu_1 \sim 330$ MeV [13]. Θ is the unit step function. $g^{\rm out}$ and $g^{\rm out}$ are the degeneracy factors. It is assumed that the inside and outside of the closed wall are in thermal equilibrium with each other at all times, $T_{\rm out} \simeq T_{\rm in} \equiv T$. This assumption will be justified as *a posteriori*. The flux exchange between the inside and outside regions is so efficient that the baryon charge inside the closed wall will be refreshed very quickly, so the thermal equilibrium is easily maintained, which will be seen later. The same argument goes for the chemical potential μ as well. The chemical equilibrium is maintained in the entire volume of the closed wall, i.e., μ in the bulk always keeps the same as that in the vicinity of the wall. But unlike T, μ evolves independently from the chemical potential outside (QGP or hadronic phase). μ increases rapidly due to the contraction of the closed wall and could finally settle down in CS phase, which will be seen later.

The equation of motion from eq. (3.7) is

$$\sigma_a \ddot{R}(t) = -\frac{2\sigma_a}{R(t)} - \frac{\sigma_a \dot{R}^2(t)}{R(t)} + \Delta P(\mu) - 4\eta \frac{\dot{R}(t)}{R(t)} \tag{3.12}$$

where $\Delta P = P_{\rm in} - P_{\rm out}$. The additional term, $4\eta\frac{\dot{R}(t)}{R(t)}$, is added to account for the friction from the surroundings, where the shear viscosity $\eta \sim m_\pi^3$ (π is the pion mass) has the conventional QCD scale [85]. This term is dissipative, so it cannot be directly incorporated into the Lagrangian, eq. (3.7). Eq. (3.12) is analogous to the classical Rayleigh–Plesset equation in fluid mechanics. The coefficient of $4\eta\frac{\dot{R}(t)}{R(t)}$ is chosen the same as that in the Rayleigh–Plesset equation when the viscosity, the tension term $\frac{2\sigma_a}{R(t)}$ and the pressure difference ΔP enter the equation of motion in the combination as shown in eq. (3.12).

The form of eq. (3.12) implies that the closed wall oscillates with time, with the oscillation amplitude gradually decreasing due to the viscous term. Assuming the stable radius is $R_{\rm form}$, the oscillation amplitude $\delta R \equiv R(t) - R_{\rm form}$ tends to vanish as t approaches $t_{\rm form}$. Taylor expanding eq. (3.12) at $R = R_{\rm form}$ to get[12]

$$\begin{aligned} &\frac{d^2\delta R}{dt^2} + \frac{2}{\tau_R}\frac{d\delta R}{dt} + \omega_R^2 \cdot \delta R = 0, \\ &\tau_R = \frac{\sigma_a}{2\eta} R_{\rm form}, \qquad \omega_R^2 = -\frac{1}{\sigma_a}\frac{d\Delta P}{dR}\bigg|_{R_{\rm form}} - \frac{2}{R_{\rm form}^2} \sim \frac{1}{R_{\rm form}^2}. \end{aligned} \tag{3.13}$$

This differential equation represents a damped oscillator where ω_R and τ_R are identified as the frequency and damping time respectively, and

$$\omega_R \tau_R \sim \frac{\sigma_a}{2\eta} \sim \frac{m_\pi}{m_a} \sim \frac{\Lambda_{\rm QCD}}{m_a} \sim 10^{10}, \tag{3.14}$$

where the expressions $\eta \sim m_\pi^3$, $\sigma_a \simeq m_\pi^4/m_a$ and $m_a \sim 10^{-4}$ eV were used. $\omega_R\tau_R \gg 1$ means the oscillation is under-damped and the system will become

[12]Besides, the relation $2\sigma_a/R_{\rm form} = \Delta P(R_{\rm form})$ is used, which is inferred from eq. (3.12) with $\dot{R} = \ddot{R} = 0$ at $R = R_{\rm form}$. Here, ΔP (which also occurs in eq.(3.13)) depends on $\mu(t)$ and thus implicitly depends on R. More details can be found in the original paper, Ref. [7]. Near the formation point, the closed wall oscillates at a speed close to the speed of light, so approximately $\omega_R \sim 1/R_{\rm form}$. This is also confirmed by analyzing the implicit $\Delta P(R)$ in Ref. [7].

stable after $\# \sim 10^{10}$ oscillations. Eq. (3.13) has the solution,

$$\begin{aligned} R(t) &= R_{\rm form} + (R_0 - R_{\rm form}) {\rm e}^{-t/\tau_R} \cos\left(\sqrt{1 - 1/(\omega_R \tau_R)^2} \cdot \omega_R t\right) \\ &\simeq R_{\rm form} + (R_0 - R_{\rm form}) {\rm e}^{-t/\tau_R} \cos\left(\omega_R t\right). \end{aligned} \tag{3.15}$$

To get a more precise result of the system's evolution, eq. (3.12) needs to be solved directly, which can only be accomplished numerically. To numerically solve the evolution of eq. (3.12), we need an extra equation that relates $\mu(t)$ to $R(t)$. Such an equation is the conservation of the baryon charge accumulated in the vicinity of the wall,

$$\dot{B}_{\rm wall}(t) = 0. \tag{3.16}$$

Note that $\int d^2x_\perp = 4\pi R^2(t)$ in the expression of $B_{\rm wall}(t)$. $B_{\rm wall}$ is conserved because this part of charge is well protected by topology. Although $B_{\rm wall}$ is conserved, baryon charge in the bulk can accumulate with μ increasing. The source of the baryon charge accumulated in the bulk is due to the net flux, $\Delta\Phi \equiv \Phi_\Rightarrow - \Phi_\Leftarrow$, where $\Phi_\Rightarrow$ and $\Phi_\Leftarrow$ are respectively the incoming and outgoing flux of quarks.[13] $\Delta\Phi$ is tiny for a small μ ($\Delta\Phi = 0$ at $\mu = 0$). On the contrary, the average flux $\langle\Phi\rangle \equiv \Phi_\Rightarrow + \Phi_\Leftarrow$ is always large, which can be estimated as

$$\langle\Phi\rangle \sim \frac{g^{\rm in}}{(2\pi)^3} \int \frac{v_z d^3k}{\exp\left(\frac{k-\mu}{T}\right) + 1} \sim {\rm fm}^{-3} \tag{3.17}$$

A large $\langle\Phi\rangle$ implies that the particle exchange is very efficient between inside and outside of the system. The total number of particles exchanged per oscillation period of the system can be estimated as follows,

$$\frac{2\pi}{\omega_R} \cdot 4\pi R_{\rm form}^2 \cdot \langle\Phi\rangle \sim R_{\rm form}^3 {\rm fm}^{-3}. \tag{3.18}$$

This implies the particles can be entirely refreshed within ∼one cycle of the system's oscillation. This is the reason why the system is always in thermal

[13] The fluxes in both directions are not zero. The quarks inside are not absolutely trapped but they can exchange with the outside plasma. The key point is that the thermal equilibrium and chemical equilibrium are maintained over the scale of the entire AQN volume, so the net baryon charge will gradually accumulate inside the nugget with a preference depending on the sign of chemical potential. We refer the readers to Appendix A of Ref. [7] for more details.

equilibrium and chemical potential equilibrium.

By numerically solving the differential equations (3.12) and (3.16), one can get how a closed axion domain wall with baryon charge trapped inside evolves. The numerical computation in Ref. [7] has shown that when the closed wall finally becomes stable, the chemical potential could be large, locating in a CS phase. However, the numerical solution suffers from a multi-scale problem represented by eq. (3.14). The differential equations have to be solved for $\# \sim 10^{10}$ oscillations to reach the final stable state, which makes the numerical solution extremely time-consuming and thus impractical for traditional numerical methods. Ref. [7] made a compromise by artificially increasing the viscosity η by 10^8 times to relieve the discrepancy between scales, and assumed that this would make the system's evolution 10^8 times faster. This multi-scale problem is finally resolved by a novel numerical method named the envelope-following method, and the details will be presented in chapter 3.3. As we will see, our result in chapter 3.3 confirms the feature mentioned above that a formed AQN could be in a CS phase.

3.2 AQN formation: asymmetry between matter and antimatter AQNs

The section (chapter 3.2) is adapted from Ref. [1]. As we have briefly reviewed in chapter 2.3, the nonzero axion field, which is coherent in the entire Universe, eq. (2.9), is one of the crucial ingredients for the AQN model. It produces CP-violating processes which will finally lead to a large disparity of order one between matter and antimatter AQNs. This will be studied in detail in this part. In chapter 3.2.1, we present some qualitative explanations of how a relatively small $\theta(t)$ may produce a large disparity between matter and antimatter AQNs. In chapter 3.2.2, we develop some equations to analyze the disparity quantitatively. In chapter 3.2.3, we numerically solve the formation of matter and antimatter AQNs with the θ effects included to see the generation of the disparity.

3.2.1 CP-violating effects

In this part, we present the generic qualitative analysis that does not depend on detailed dynamical computations of the model. When we studied the evolution of AQNs in chapter 3.1, we did not distinguish one species of AQNs

(i.e., matter AQNs or antimatter AQNs) from the other. Indeed, the same arguments hold for the other species of AQNs by flipping the sign of μ in the Lagrangian (3.2), $\mu \to -\mu$, which is equivalent to flipping the sign of $\theta_{1,2}$. One can restore the original form of the Lagrangian by flipping the sign of the axion field, θ (and also the η' field, $\phi_{\eta'}$) [7]. This argument based on symmetry indicates that as long as the pseudoscalar field θ fluctuates around zero, i.e., $\langle\theta\rangle = 0$, like conventional pseudoscalar fields (π and η' mesons, for example), the system will be CP invariant, and the matter and antimatter AQNs will be equal in size and number density.

However, an important feature of the axion field, eq. (2.9), is that its oscillating amplitude decreases with time, so we have $\langle\theta\rangle \neq 0$, and the system violates CP-symmetry. Many strong processes, such as annihilation, evaporation, scattering, transmission and reflection coefficients, and viscosity, etc., taking place inside and outside the closed wall, which are slightly different for matter and antimatter AQNs. In particular, a slight difference between the ground states represented by the θ-dependent condensate $\left\langle \det \bar{\Psi}_L^f \Psi_R^f \right\rangle$, which can generate differences in the processes mentioned above. As a consequence, when θ is positive, the accumulation of one species of quarks (i.e., quarks or antiquarks) inside closed axion domain walls will be favored; when θ is negative, the accumulation of the other species of quarks will be favored, instead. This is the generation of the disparity between matter and antimatter AQNs.

It is hard to calculate these CP-violating QCD effects explicitly as they require the ability to solve the many-body effects in an unfriendly configuration where θ, μ, and T are nonzero when even the phase diagram is still not available; see Fig. 2.1. However, we expect the final disparity between matter and antimatter AQNs to be proportional to $\theta(t)$, the axion field value at the moment of the formation of axion domain walls. This is because $\theta(t)$ finally decreases to nearly zero after many oscillations and the average of axion field during this time interval is $\langle\theta\rangle \sim \theta(t)/2$. The time when domain walls form could be very close to the QCD transition point, T_c. Thus, numerically $\theta(t)$ could be very small, $|\theta(t)/\theta_0| \sim 10^{-2}$-$10^{-3}$. θ_0 is the initial misalignment angle and is naturally an $\mathcal{O}(1)$ value. Naively, we may think that this small factor can only lead to a minor disparity $\lesssim 10^{-2}$. However, while this coupling is indeed small in the QCD scale, it is nevertheless effectively long-range and long-lasting, in contrast with conventional random QCD processes. As a result, we expect these coherent CP-violating effects will produce a large $\mathcal{O}(1)$ disparity between matter and antimatter AQNs. These coherent CP-violating effects occur in the entire volume of a closed

wall so that the disparity can be expressed as

$$\Delta B \sim \theta(t) V, \qquad |\theta(t)/\theta_0| \sim 10^{-2}\text{–}10^{-3}, \tag{3.19}$$

where ΔB is the difference of baryon charge accumulated by matter and antimatter AQNs. This expression should be compared with the scale of the local spontaneous symmetry of baryon charge as discussed in chapter 2.3.2, where $B_{\text{wall}} \sim S$.

The axion field is coherent in the entire Universe (i.e., θ is uniform in the entire Universe for a given time), so the disparity between matter and antimatter AQNs will not be washed out by the spatial variation of θ. This is the reason why we require the pre-inflationary scenario in the AQN framework.

Next, we develop the method to quantitatively analyze the disparity between matter and antimatter AQNs in the background of the coherent axion field.

3.2.2 Quantitative analysis

We can quantify the relation (3.19) as

$$B_\theta^{\pm} = \pm g^{\text{in}} A V \int \frac{d^3k}{(2\pi)^3} \frac{1}{\exp\left(\frac{\epsilon-\mu}{T}\right)} \tag{3.20}$$

where B_θ^+ and B_θ^- are respectively the baryon charge *correction* to a matter AQN and an antimatter AQN induced by the coherent axion field, eq. (2.9), so we have $\Delta B = \left|B_\theta^+ - B_\theta^-\right|$. The quantity A is parameterized as $A \sim \Delta\theta$ where $\Delta\theta$ can be understood as the change of the coherent axion field amplitude after each axion field oscillation.[14] Thus, eq. (3.20) should be understood as the baryon charge correction per axion field oscillation, and ΔB here is the disparity between matter and antimatter AQNs generated per axion field oscillation. The disparity for each oscillation will be accumulated, so the total disparity gradually increases with time. This can be described by an effective A, which increases with time, representing the accumulation of all corrections generated in the past oscillations. From now on, to discuss the final disparity between matter and antimatter AQNs, the parameter A and

[14] $\Delta\theta$ is defined as a positive value which is the amount of the axion amplitude reduction after each oscillation.

thus eq. (3.20) should be understood in the sense of accumulation. Later, we will see in chapter 3.2.3 where numerical results are presented, A is explicitly parameterized as a specific function that increases with time.

Many other factors can affect A. In writing down eq. (3.20), we assumed that most quarks in volume V move coherently during evolution. The quark coherence may not be so perfect, and only a portion of the quarks inside can move coherently as a macroscopic system. It is challenging to calculate the resulting suppression factor because the system is now formulated in terms of a single macroscopic variable, $R(t)$. We assume that the uncertainties of this suppression factor and other correction factors mentioned previously in chapter 3.2.1 can be effectively absorbed into the numerical coefficient of A. As we will see below, the disparity between matter and antimatter AQNs is of order one, and it is robust as long as A is not exceedingly small.

Next, we discuss the backreaction of the coherent quark fields on the background axion field. Eq. (3.20) was derived by considering the coherently moving quarks inside a closed wall in the background of the axion field. This approximation is only justified when the effect induced by the background field is sufficiently small. Formally, the effect eq. (3.20) should be much smaller than the baryon charge eq. (3.6) that is initially induced in the vicinity of the walls due to the local spontaneous symmetry breaking of the baryon charge. Such a condition must be imposed on our system to avoid any complications related to the backreaction of the coherent quark field on the background axion field. This condition can be expressed as

$$\left|\frac{B_\theta^\pm}{B_{\rm wall}}\right| = \frac{ART}{3\pi}\frac{I_3(\tilde{\mu})}{I_2(\tilde{\mu})} \lesssim 1 \tag{3.21}$$

where the symbols I_n are the Fermi integrals defined as follows,

$$I_n(\tilde{\mu}) = \int_0^\infty dx \frac{x^{n-1}}{\mathrm{e}^{x-\tilde{\mu}}+1}. \tag{3.22}$$

In writing down eq. (3.21), we have re-expressed $B_{\rm wall}$ and $B_\theta^\pm$ as[15]

$$B_{\rm wall} = \frac{g^{\rm in}ST^2}{2\pi} I_2(\tilde{\mu}), \qquad B_\theta^\pm = \frac{g^{\rm in}AVT^3}{2\pi^2} I_3(\tilde{\mu}). \tag{3.23}$$

[15]The induced baryon number N in the expression of $B_{\rm wall}$ eq. (2.8) can be taken as 2 [7] which means that a unit baryon charge is induced for each spin state in addition to the principal degenerate factor, so we have $Ng = g^{\rm in}$. This will simplify our analysis.

where $\tilde{\mu} \equiv \mu/T$.

We can also understand the condition (3.21) in the way that $B_\theta^\pm$ should be small enough so it will not violate the original boundary conditions that determine the sign of $B_{\rm wall}$. The expression of $B_\theta^\pm/B_{\rm wall}$ is exact in eq. (3.21), but it is not technically useful for us to carry out further analysis because it depends on R, μ, and T. To make it technically handleable, we can simplify eq. (3.21) as

$$\left|\frac{B_\theta^\pm}{B_{\rm wall}}\right| = a(t)\cdot\left(\frac{RT}{R_0T_0}\cdot\frac{2}{3}\frac{I_3(\tilde{\mu})}{I_2(\tilde{\mu})}\right)\sim a(t), \qquad a(t)\equiv\frac{AR_0T_0}{2\pi}. \tag{3.24}$$

In approximating $B_\theta^\pm/B_{\rm wall}$ as a, we used the relation that the oscillating R is at the same order of magnitude of R_0 on average, which is confirmed later in numerical simulations in chapter 3.2.3 and also chapter 3.3. $T = T_0$ is due to the simplification adopted in this section that T is constant during the formation of nuggets. Also, the ratio of the two Fermi integral can be well approximated as $I_3(\tilde{\mu})/I_2(\tilde{\mu}) \sim 3/2 + 2/3\sqrt{I_2(\tilde{\mu})}$ for small $\tilde{\mu}$ ($\tilde{\mu} \lesssim 10$), so the combination $2/3\cdot I_3(\tilde{\mu})/I_2(\tilde{\mu}) \sim 1$ if we neglect the second term.

The dimensionless parameter $a(t)$ does not depend on R, μ and T. The condition (3.21) now becomes $a(t) \lesssim 1$. $a(t)$ captures the feature of A, which is monotonically increasing with time, representing the accumulation of baryon charge corrections generated by the background axion field. By monitoring the value of $a(t)$, we know whether the expression of $B_\theta^\pm$ and thus our analysis is valid or not. Our analysis breaks down when $a(t)$ becomes close to 1.

The equation of motion of AQN is still eq. (3.12), which is assumed to be unaltered by the inclusion of the background axion field. We need an extra constraint on the relation between $R(t)$ and $\mu(t)$ to solve the AQN formation. Analogous to eq. (3.16), we have

$$\frac{d}{dt}(B_{\rm wall} + B_\theta^\pm) = 0 \tag{3.25}$$

$B_{\rm wall}$ is the topologically trapped baryon charge due to nontrivial boundary conditions as discussed in chapter 3.1. $B_\theta^\pm$ can be regarded as an effective modification to the boundary conditions (3.5) to change the value of $B_{\rm wall}$, but we require it not to flip the sign of $B_{\rm wall}$, which is guaranteed by the condition (3.21). Although $B_{\rm wall} + B_\theta^\pm$ is conserved, baryon charge will ac-

cumulate in the in the bulk of an AQN (note that $B_\theta^\pm$ is only the *correction* to the bulk charge, but not represents the bulk charge itself). The source of the charge accumulation is the net flux $\Delta\Phi \equiv \Phi_\Rightarrow - \Phi_\Leftarrow$ as we discussed in chapter 3.1.

$B_{\rm wall} + B_\theta^\pm$ is conserved, which is always equal to the initial value, so we have

$$B_{\rm wall} + B_\theta^\pm = B_{\rm wall}\left[1 \pm a \cdot \frac{RT}{R_0 T_0} \cdot \frac{2}{3}\frac{I_3(\tilde{\mu})}{I_2(\tilde{\mu})}\right] = \frac{g^{\rm in} S_0 T_0^2}{2\pi} I_2(0), \tag{3.26}$$

Note that we used the condition that a is initially zero since it represents an accumulative effect. From eq. (3.26) we get

$$\left(\frac{R^\pm}{R_0}\right)^2 \frac{T^2}{T_0^2}\frac{I_2(\tilde{\mu})}{I_2(0)}\left[1 \pm a \cdot \frac{R^\pm T}{R_0 T_0} \cdot \frac{2}{3}\frac{I_3(\tilde{\mu})}{I_2(\tilde{\mu})}\right] = 1 \tag{3.27}$$

where we have added the subscript '$\pm$' to R to indicate the difference between matter and antimatter AQNs explicitly. Since we are only interested in a sufficiently small a, we Taylor expand this equation in terms of a and keep the terms up to the first order, then we get

$$\begin{aligned} \frac{R^\pm}{R_0} &= \frac{T_0}{T}\sqrt{\frac{I_2(0)}{I_2(\tilde{\mu})}} \mp \left(\frac{T_0}{T}\sqrt{\frac{I_2(0)}{I_2(\tilde{\mu})}}\right)^2 \cdot \frac{1}{3} a \frac{T}{T_0}\frac{I_3(\tilde{\mu})}{I_2(\tilde{\mu})} \\ &\simeq \frac{\langle R\rangle}{R_0} \mp \left(\frac{\langle R\rangle}{R_0}\right)^2 \cdot \frac{1}{3} a \frac{T}{T_0}\frac{I_3(\tilde{\mu})}{I_2(\tilde{\mu})} \end{aligned} \tag{3.28}$$

where $\langle R\rangle$ is the radius averaged between matter and antimatter AQNs,[16]

$$\frac{\langle R\rangle}{R_0} \equiv \frac{1}{R_0}\cdot\frac{1}{2}(R^+ + R^-) \simeq \frac{T_0}{T}\sqrt{\frac{I_2(0)}{I_2(\tilde{\mu})}}. \tag{3.29}$$

[16] We have neglected the difference between $\tilde{\mu}^+$ and $\tilde{\mu}^-$. Indeed, the difference is small, $\Delta\tilde{\mu} \ll \langle\tilde{\mu}\rangle$, as the chemical potential $\langle\tilde{\mu}\rangle \equiv \langle\mu\rangle/T$ becomes larger and larger with time. In comparison, ΔR and R are at the same order of magnitude, which is the main source of the disparity between matter and antimatter AQNs.

The difference between the radii of matter and antimatter AQNs is

$$\Delta R = |R^+ - R^-| \simeq R_0 \cdot \left(\frac{\langle R\rangle}{R_0}\right)^2 \cdot \frac{2}{3} a \frac{T}{T_0} \frac{I_3(\tilde{\mu})}{I_2(\tilde{\mu})}, \tag{3.30}$$

so we get

$$\frac{\Delta R}{\langle R\rangle} \simeq \frac{\langle R\rangle}{R_0} \cdot \frac{2}{3} a \frac{T}{T_0} \frac{I_3(\tilde{\mu})}{I_2(\tilde{\mu})} \simeq \frac{2}{3} a \cdot \frac{\langle R\rangle}{R_0} \frac{I_3(\tilde{\mu})}{I_2(\tilde{\mu})} \tag{3.31}$$

where we used the constant-temperature simplification, $T = T_0$. As we will see from numerical result in chapter 3.2.3, we have $\langle R_{\rm form}\rangle / R_0 \simeq 0.6$ for $T_0 = 200$ MeV. Substituting it back to eq. (3.29), we can get the value of $I_2(\tilde{\mu}_{\rm form})$ and further $I_3(\tilde{\mu}_{\rm form})/I_2(\tilde{\mu}_{\rm form}) \simeq 2.5$, so we get

$$\frac{\Delta R_{\rm form}}{\langle R_{\rm form}\rangle} \simeq a_c. \tag{3.32}$$

where the critical parameter a_c should be regarded as the final value of a when the coherent axion field decreases to nearly zero soon after the QCD transition temperature and the disparity between matter and antimatter AQNs stops increasing. If we assume $a_c \lesssim 1$, then the condition (3.21) is always satisfied during the AQN evolution, which validates our analysis.

Next, the baryon charge difference between matter and antimatter AQNs can be estimated as

$$\frac{\Delta B_{\rm form}}{\langle B_{\rm form}\rangle} \simeq 3 \frac{\Delta R_{\rm form}}{\langle R_{\rm form}\rangle} \simeq 3 a_c. \tag{3.33}$$

We see that even for a_c as small as 0.1-0.2, the final disparity between matter and antimatter AQNs represented by eq. (3.33) is relatively large, which is of order one. The above analysis does not depend on the axion mass m_a, which implies that the final disparity represented by eq. (3.33) is insensitive to m_a.

Next, we are going to solve the evolution of the disparity numerically with $a(t)$ modeled as a specific function that increases from 0 to a_c. We will see that the numerical result supports our quantitative analysis here about the disparity between matter and antimatter AQNs, eq. (3.32).

3.2.3 Numerical results

In the background of the coherent axion field, the form of the Lagrangian (3.7) that dominates the evolution of AQN in chapter 3.1 remains unchanged, so the corresponding equation of motion (3.12) is the same for both matter and antimatter AQNs. The modification, $B_\theta^\pm$, brought by the coherent axion field, is included in the equation of the baryon charge conservation, eq. (3.25). The main goal of this section is to solve the equations (3.12) and (3.25) numerically to obtain the evolution of the disparity between matter and antimatter AQNs as a support to the analysis result (3.32).

In this section, we choose the initial temperature $T_0 = 200$ MeV (which is above the QCD transition temperature T_c) as an example to demonstrate the disparity between matter and antimatter AQNs. The coherent axion field $\theta(t)$ (2.9) is nonzero at T_0 and quickly drops to nearly zero after T_c, so we expect the disparity is mainly accumulated during the evolution stage from T_0 to T_c.

Before $\sim T_c$, it is known that the axion mass $m_a(T)$ experiences very sharp changes with the temperature, $m_a(T) \sim T^{-\beta}$ with $\beta \simeq 4$ (see e.g., Ref. [25] for a review). Nevertheless, the axion mass does not vary much during a single axion oscillation. For the numerical computations in this section, similar to the constant-temperature simplification $T = T_0$, we assume that the axion mass is a constant. These assumptions are justified only if the typical time scale of the relevant processes such as the AQN oscillation period is much shorter than the time scale of the external parameters ($m_a(T)$, T, etc.) varying. We first compare the oscillation periods of an AQN and the coherent axion field by computing $\omega_R(t)/\omega_\theta(t)$.

From eq. (2.9), we know $\omega_\theta(t) \simeq m_a(t)$ which is a good approximation near T_c with $m_a(t)t \gg 1$ long after the axion mass effectively turning on at $T_{\rm osc} \sim 1$ GeV. The exact relation between m_a with T or t can be found in the literature, see e.g. Refs. [25, 79, 86, 87]. The AQN oscillation frequency $\omega_R(t)$ can be computed based on the numerical solution of eq. (3.12) for a few consecutive oscillations of $R(t)$ for different values of the temperature.[17] The corresponding $\omega_R(T)/\omega_\theta(T)$ as a function of temperature is shown in Fig. 3.1 where we choose the temperature range as 170 MeV $\leq T \leq$ 500 MeV, with $m_a \simeq 10^{-4}$ eV. We see that this ratio is always much larger than unity,

[17] Note that $\omega_R(t)$ is different from ω_R calculated in eq. (3.13) with assuming the smallness of the oscillations which is correct at the final stage of the evolution. However, here we care about the oscillation frequencies in the initial stage above T_c when $\theta(t)$ is relevant.

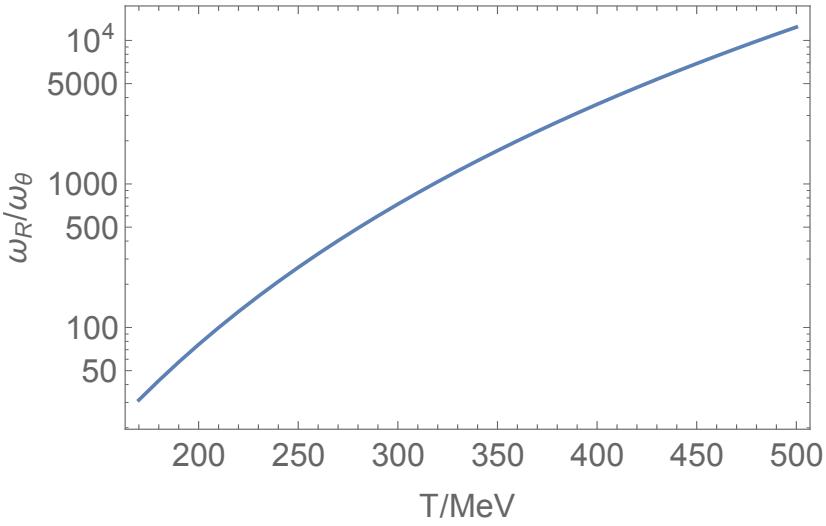

Figure 3.1: This plot shows that ω_R/ω_θ is always much larger than unity in the temperature range that we are interested in. It essentially shows that an AQN makes a large number of oscillations while the axion field $\theta(t)$ slowly varies. This figure is taken from Ref. [1].

even in the vicinity of the QCD transition at $T_c \sim 170$ MeV. $\omega_R(T) \gg \omega_\theta(T)$ means that for an AQN making a large number of oscillations, the coherent axion field varies only slightly.

The cosmological temperature-time relation is $T \sim t^{-1/2}$. During a single *axion* oscillation period, $\delta t \sim \omega_\theta \sim m_a^{-1}(t)$, the corresponding temperature variation is very tiny, $\delta T/T \sim \delta t/t \sim [m_a(t)t]^{-1} \ll 1$. The corresponding axion mass variation is also very tiny, $\delta m_a/m_a \sim \beta \cdot (\delta T/T) \ll 1$. During a single AQN oscillation period, which is much shorter than an axion oscillation period, the temperature and axion mass variations are even smaller. These arguments unambiguously show that our adiabatic approximation that treats $m_a(T)$ and T as constants is justified.

Next, we come back to numerically solve the evolution of the disparity between matter and antimatter AQNs. As we have discussed in chapter 3.2.2, $a(t)$ monotonically increases with time from 0 at T_0 to its final value a_c soon after T_c when the coherent axion field almost vanishes. Also, as we have argued in chapter 3.2.2, it is hard to calculate $a(t)$ from first principles because it requires the ability to solve the many-body effects in the background of nonzero μ, T and θ but even the QCD phase diagram is not clearly known

yet. Instead, we model $a(t)$ as a function which captures the essential features $a(t)$. Such a function can be

$$a(t) = a_c \tanh\left(\frac{t}{t_c}\right). \tag{3.34}$$

a_c and t_c are two free parameters. We impose $a_c \lesssim 1$ so that the expression $B_\theta^\pm$ (3.20) is valid. t_c controls the rate of $a(t)$ changing with time.

Now, with eq. (3.34) implemented into the equation of baryon charge conservation, eq. (3.25), we can solve it together with the equation of motion eq. (3.12). The numerical result is presented in Fig. 3.2 where we choose $m_a = 10^{-4}$ for illustrative purposes. In Fig. 3.2a, we plotted two subfigures for $a_c = (0.1, 0.5)$ respectively. The parameter t_c is rescaled by R_0 and we set it to be $t_c/R_0 = 10^{-2}$, which represents a relatively fast increase of $a(t)$ from the initial value 0 to the final value a_c, based eq. (3.34). Fig. 3.2b is the same as Fig. 3.2a but with a different parameter $t_c/R_0 = 10^0$ which is chosen to represent a relatively slow increase of $a(t)$, as a comparison with Fig. 3.2a. In each subfigure, the blue and orange lines represent the evolution of $R^-(t)$ (antimatter AQN) and $R^+(t)$ (matter AQN) respectively. The difference between the two lines represent the accumulated disparity.

Comparing Fig. 3.2a with Fig. 3.2b, we see that changing t_c does not affect the final disparity, i.e., the rate at which $a(t)$ increases does not affect the final disparity. This is consistent with our analysis result in chapter 3.2.2 that the disparity only depends on a_c, but not depends on how $a(t)$ increases, fast or slow. From all plots in Fig. 3.2, we see that the disparity is determined by a_c rather than other parameters. For $a_c = 0.1$, we see that $\Delta R_{\rm form} = \left|R^+_{\rm form} - R^-_{\rm form}\right| \approx 0.06$ and $\langle R_{\rm form}\rangle = 1/2 \cdot (R^+_{\rm form} + R^-_{\rm form}) \approx 0.6$; for $a_c = 0.5$, we see that $\Delta R_{\rm form} \approx 0.3$ and $\langle R_{\rm form}\rangle \approx 0.6$. These results verify the analysis result eq. (3.33), that is, $\Delta R_{\rm form}/\langle R_{\rm form}\rangle \approx a_c$.

We also notice that the oscillations shown in Fig. 3.2 are very sharp. However, this seemingly cuspy behavior is in fact quite smooth in comparison the QCD scale. To see this, we zoom in the first few oscillations of R^+ in one subfigure ($t_c/R_0 = 10^{-2}, a_c = 0.5$) of Fig. 3.2 as an example and show it in Fig. 3.3. We see that the duration of the cusp is $\delta t_{\rm cusp} \sim 10^{-3} R_0 \sim 10^{-3} m_a^{-1}$, which is much longer than the QCD scale $\delta t_{\rm cusp} \gg \Lambda_{\rm QCD}^{-1}$.

In the numerical computations in Ref. [7], the viscosity term that enters the equation of motion (3.12) was set as $\eta = 1 \cdot m_\pi^3$. Such η has been computed in different models under different conditions [85, 88]. It is known

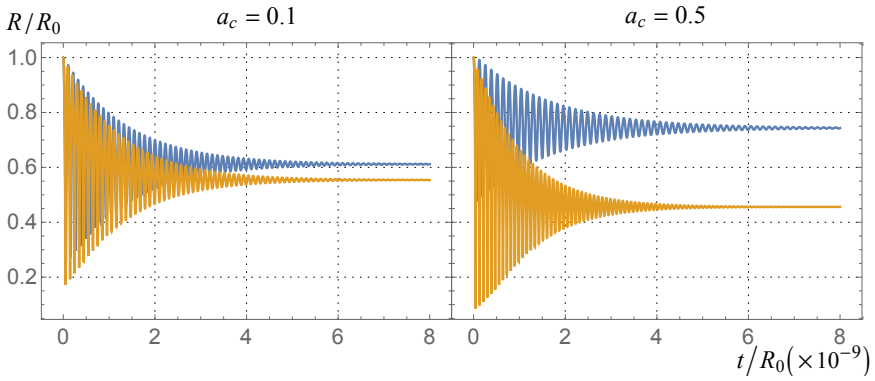

(a) $t_c/R_0 = 10^{-2}$

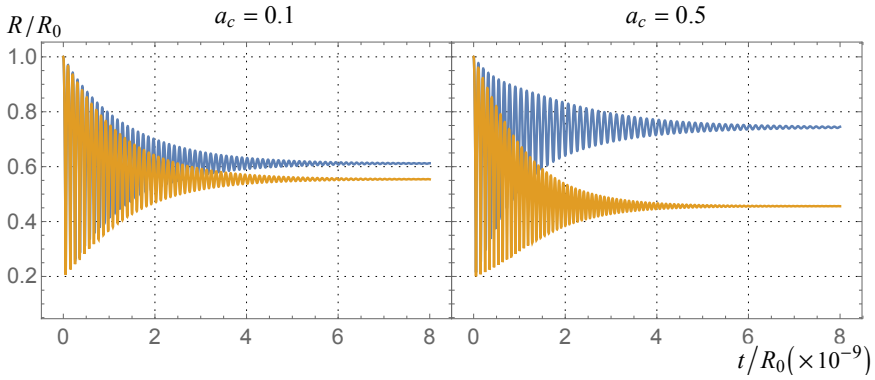

(b) $t_c/R_0 = 10^{0}$

Figure 3.2: Numerical solutions of a matter/antimatter AQN evolving in the coherent $\theta(t)$ background. The blue and orange lines represent $R^-(t)$ and $R^+(t)$ respectively. All four subfigures are calculated with $m_a = 10^{-4}$ eV, and R_0 is chosen as m_a^{-1}. The numerical values of a_c that we use in calculating each subfigure can be seen in the upper edge of the graph. In panel (a), we choose $t_c/R_0 = 10^{-2}$, which represents a relatively fast increase of $a(t)$ from 0 to a_c, based on eq. (3.34). Fig. 3.2a is adapted from Ref. [1]. As a comparison, in panel (b), we choose $t_c/R_0 = 10^0$ which represents a relatively slow increase of $a(t)$ from 0 to a_c.

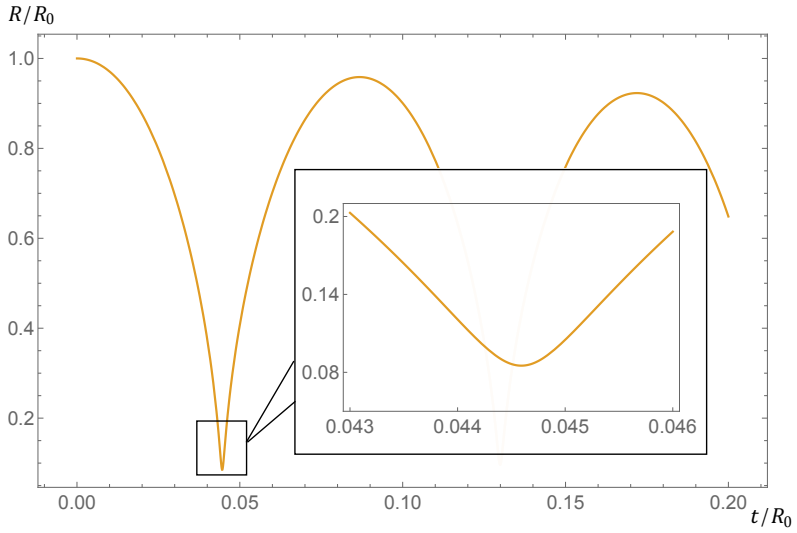

Figure 3.3: The fist few oscillation of R^+ in one subfigure ($t_c/R_0 = 10^{-2}, a_c = 0.5$) of Fig. 3.2. We choose this as an example to show that there is no cuspy problem. This figure is taken from Ref. [1].

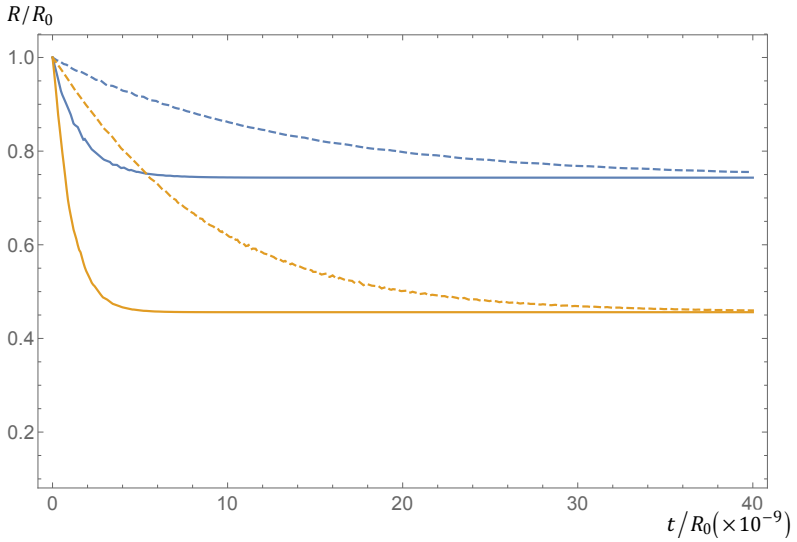

Figure 3.4: Dependence on viscosity η. Amplitudes of R^-(blue) and R^+ (orange) are plotted. The solid lines correspond to $\eta = 8.4 m_\pi^3 (\times 10^9)$ and the dashed lines correspond to $\eta = m_\pi^3 (\times 10^9)$. Here, the parameter $m_a = 10^{-4}$ eV and $t_c/R_0 = 10^{-5}$ are chosen. This figure is taken from Ref. [1].

that the viscosity is in fact somewhat larger in the region of sufficiently high temperature. The holographic arguments [89] suggest that η could be one order of magnitude larger than conventional perturbative QCD predictions (we use the factor 8.4 in our numerical computations). To see how the value of η affects our result, in Fig. 3.4 we plot our numerical result with $\eta = m_\pi^3$ and $8.4m_\pi^3$ respectively. We see that the final disparity is insensitive to η.

We conclude chapter 3.2 as follows. The presence of a global coherent axion field θ will generate a significant disparity, eq. (3.33), between matter and antimatter AQNs. The disparity is the accumulation of all the CP-violating effects generated by $\theta(t)$ during a large number of oscillations with the amplitude gradually decreasing, as shown in eq. (2.9). The magnitude of the final disparity is order one, supported by both quantitative analysis and numerical computations under the condition (3.21) that the backreaction effects are small. This is even true for a small θ, because the asymmetry effects are generated over the scale of the entire volume of a closed wall, $\sim \theta V$ (see eq. (3.19)). It can easily grow to a large value in comparison with the original baryon charge $B_{\rm wall}$ which is only proportional to the surface area of the closed wall. The $\mathcal{O}(1)$ disparity is not sensitive to many parameters of the system but only depend on a_c, which effectively models the change of the coherent axion field from its initial value when axion domain walls form and closed walls start to evolve to its final nearly zero value soon after T_c. The robust $\mathcal{O}(1)$ disparity between matter and antimatter AQNs unambiguously supports the basic claim that the relation $\Omega_{\rm DM} \sim \Omega_{\rm visible}$ is a very natural outcome of the AQN framework.

3.3 AQN formation: real-time evolution

This section (chapter 3.3) is adapted from Ref. [3]. The main goal of this section is to resolve the multi-scale problem that arises in numerically simulating the AQN evolution that has been briefly mentioned at the end of chapter 3.1.[18] We will eventually present the full evolution of an AQN from initial temperature T_0 to its formation temperature $T_{\rm form}$ without artificially

[18] In numerical computations in chapter 3.2.3, η has also been artificially rescaled to a large number (10^9 times larger) [1]. This does not affect any important results we care about in chapter 3.2.3, such as the final disparity and formation radius. The rescaling just changes the time scale [1]. It is the goal of present section (chapter 3.3) to study the real time scale of AQN formation.

increasing the viscosity η by 10^8 times. This is coined as the "real-time evolution" in contrast with the case that the artificially enlarged η makes the evolution $\sim 10^8$ times faster in Ref. [7]. The real-time evolution of an AQN is accomplished with a novel numerical method named the *envelope-following* method, which will be discussed in detail later in this section. Other improvements compared to Ref. [7] include the cosmological time-dependent temperature $T(t)$ instead of a constant temperature and a temperature-dependent axion mass $m_a(t)$ instead of a constant axion mass, etc.

We first review the multi-scale problem and introduce some new elements meanwhile. Because now we adopt $m_a(T)$ as a function of cosmological temperature (time), the equation of motion (3.12) should be modified as

$$\sigma_{\rm eff}\ddot{R}(t) = -\frac{2\sigma_{\rm eff}}{R(t)} - \frac{\sigma_{\rm eff}\dot{R}^2(t)}{R(t)} + \Delta P(\mu) - 4\eta\frac{\dot{R}(t)}{R(t)} - \dot{\sigma}_{\rm eff}\dot{R}(t). \tag{3.35}$$

The difference is that there we have an extra term $\dot{\sigma}_{\rm eff}\dot{R}(t)$. This term occurs because the tension $\sigma_{\rm eff}$ itself is a function of time, $\sigma_{\rm eff}(t) = \kappa \cdot 8f_a^2 m_a(t)$ (see eq. (3.37) below for the explicit expression of m_a(t)). Note that the domain wall tension σ_a used in previous sections is replaced by the effective wall tension $\sigma_{\rm eff} = \kappa \cdot \sigma_a$. The phenomenological parameter κ accounts for the difference between the wall tension of an AQN $\sigma_{\rm eff}$ and that of a planar domain wall σ_a [2]. In general, the $\sigma_{\rm eff}$ is smaller than σ_a with $0 < \kappa < 1$, which will be discussed in detail in chapter 4.[19]

Using the approximation of small-amplitude oscillation that has been discussed in chapter 3.1, the equation of motion can be analytically solved,

[19]There are two main reasons for the difference between $\sigma_{\rm eff}$ and σ_a. We briefly summarize the two reasons here. The first reason is that AQNs with baryon charge accumulated inside will finally become stable in CS phase. Thus, in our case, the axion domain wall solution interpolates between topologically distinct vacuum states in hadronic (outside the AQN) and CS (inside) phases, in contrast to a conventional axion domain wall which interpolates between distinct hadronic vacuum states. The chiral condensate may or may not be formed in CS phase, which could strongly make the topological susceptibility in the CS phase much smaller than in the conventional hadronic phase. The second reason is that $\sigma_a = 8f_a^2 m_a$ is derived using the thin-wall approximation, which could be badly violated in the case of the closed domain wall when the radius and the width of the wall are at the same order of magnitude. This effect is expected to reduce the domain wall tension drastically.

which gives

$$\omega_R \sim \frac{1}{R_{\rm form}}, \qquad \tau_R \sim \frac{\sigma_{\rm eff}}{2\eta} R_{\rm form}, \qquad \omega_R \tau_R \sim \frac{\sigma_{\rm eff}}{2\eta} \sim \frac{\Lambda_{\rm QCD}}{m_a} \tag{3.36}$$

where ω_R is the oscillation frequency and τ_R is the damping time that represents the time scale when the formation is completed. This is a highly nontrivial parameter as it represents a combination of very different scales. Indeed, the viscosity η along any path in the QCD phase diagram always assumes $\Lambda_{\rm QCD}$ scale, $\eta \sim m_\pi^3$ (of course, it is not known exactly in different phases). The axion scale enters through $\sigma_{\rm eff} = \kappa \cdot 8 f_a^2/m_a \sim \kappa \cdot m_\pi^4/m_a$. Finally, the cosmological scale enters as the formation effectively starts at $T \simeq T_c \simeq 170$ MeV and ends at $T \simeq T_{\rm form}$ which represents a very long cosmological journey with typical time scale $t \sim T^{-2} \sim 10^{-4}$ seconds.

It is a highly nontrivial observation that all these drastically different scales nevertheless lead to a consistent picture. Indeed, a typical time for a single oscillation is $\omega_R^{-1} \sim 10^{-14}$ s for the axion mass $m_a \sim 10^{-4}$ eV, while the number of oscillations is very large which is of order $\omega_R \tau_R \sim 10^{10}$. Therefore, a complete formation of the AQN occurs on a time scale 10^{-4} s corresponding to the cosmological scale when the temperature drops to ~ 40 MeV. This scale is known from completely different arguments related to the estimate of the baryon-to-photon ratio, eq. (2.2); see e.g., Ref. [50].

Unfortunately, we could not directly numerically test this amazing "conspiracy of scales" in Refs. [1, 7]. $\omega_R \tau_R$ is very large due to the drastically different scales, $\Lambda_{\rm QCD}$ and m_a. The AQN formation will be complete after $\# \sim \omega_R \tau_R$ oscillations, which makes it extremely time-consuming and thus impractical to be solved using traditional numerical methods.[20] This is why the numerical analyses in Ref. [7] adopted a technical trick that the viscosity η was artificially rescaled to $\sim 10^8$ times larger to make the equation of motion solvable.

The main goal of this section is to overcome this technical difficulty by adopting a new numerical method—coined as the *envelope-following* method—which can solve our system successfully while allowing the viscosity term to keep its real physical magnitude, $\eta \sim m_\pi^3$, when the parameter $\omega_R \tau_R \sim 10^{10}$

[20] Of course, our case is by no means special in this respect: it is a common problem in any numerical study when some parameters assume extremely large/small values. This is obviously the case in any numerical studies related to axion physics because of the drastic separation of scales; see, e.g., Refs. [90–92].

assumes its very large physical value. The motivation of using the envelope-following method and how it works are briefly explained as follows.

We notice that although an AQN is oscillating very fast during evolution, the amplitude of oscillation is decreasing very slowly for each given cycle. The peaks of oscillations in fact form a "smooth" line which we call an *envelope*. We realize that if we can find a way to solve the envelope numerically, it is unnecessary to know the full details of all oscillations. The envelope-following method turns out to be very beneficial for our study of the AQN oscillations. The method is efficient in solving highly oscillatory ordinary differential equations, which was illustrated in Ref. [93]. We briefly summarize the basic idea here.

We start with the initial conditions $R = R_0, \dot{R} = 0$ (and $\mu = \mu_0 \simeq 0$) which correspond to the first peak of R oscillations and we label this peak as point a. Then we numerically solve the equation of motion (3.35) (with the constraint from the conservation of the wall baryon charge, eq. (3.16) or eq. (3.25)) until we get the next peak b of R oscillations, which should be slightly smaller than the first peak. This step is very fast since we solve the equations just for one oscillation. Joining points a and b, we get a secant line. This secant line is then used to project the solution to point a', which is many oscillations away. Starting with a' as the new peak, we solve the differential equations until we get the next peak b', etc. We repeat the above procedure of drawing the secant line, projecting the solution, and finding the next peak. After several projections, we get the upper envelope of R oscillations. Using the same method, we can find the lower envelope of R oscillations and also the envelopes of μ oscillations. We should point out that, although the details of oscillations are not important for us, we can recover them locally if we substitute the corresponding envelope information into the differential equations as the initial conditions.

To numerically solve the equation of motion (3.35), we also need to know how the effective domain wall tension $\sigma_{\text{eff}} = \kappa \cdot 8 f_a^2 m_a(t)$ evolves as a function of time. One of the most updated results for the axion mass $m_a(T)$ is based on high-temperature lattice QCD [79]. The topological susceptibility of QCD, $\chi(T)$, is plotted in Figure 2 in Ref. [79] as a function of the cosmological temperature T. The data points of the figure is also provided in Table 9 in the Supplementary Information of the same paper, by fitting which we get

the expression of $\chi(T)$ as

$$\frac{\chi(T)}{\mathrm{MeV}^4} = 3.27\times10^7\Theta[T-150\mathrm{MeV}] + \Theta[150\mathrm{MeV}-T]\frac{3.94\times10^{24}}{(T/\mathrm{MeV})^{7.85}}, \quad (3.37)$$

where Θ is the unit step function. Then we can get the axion mass using the relation

$$m_a(T) = \frac{\chi^{1/2}(T)}{f_a}. \quad (3.38)$$

Eqs. (3.37) and (3.38) explicitly show that before the QCD transition, the axion mass increase rapidly with the exponent $\beta = 7.85/2 = 3.925$ as the cosmological temperature decreases (see e.g., Refs. [25, 86, 87] for similar results). Then the axion acquires its asymptotic mass near the QCD transition and remains constant after that.

The cosmological time-temperature relationship is also useful in our numerical calculations, which in the radiation-dominated era is well known as

$$\frac{T(t)}{1\mathrm{MeV}} \simeq 1.56 g_\star^{-1/4}(T)\left(\frac{1\mathrm{sec}}{t}\right)^{1/2}, \quad (3.39)$$

where $g_\star(T)$ is the effective degrees of freedom of all relativistic particles at temperature T. Since the major part of the AQN evolution is after the QCD transition, we treat $g_\star(T)$ as a constant for simplicity with $g_\star = 17.25$ (see e.g. [94]) as in the hadronic phase.

Now we are ready to solve the equation of motion (3.35) numerically. The numerical result is shown in Fig. 3.5.[21] As we can see from Fig. 3.5, the basic results of the real-time evolution confirm the main features of the AQN model, which can be summarized as follows:

1. The AQN completes its evolution by oscillating a large number of times, $\omega_R\tau_R \sim 10^{10}$, before it assumes its final configuration with size R_{form}

[21] We have ignored the effect of the background coherent axion field on the AQN evolution. This means that we used the conservation of the wall baryon charge (3.16), $\dot{B}_{\mathrm{wall}}(t) = 0$, instead of eq. (3.25) in solving the equation of motion. This simplification is good enough for our purpose in this section to show the validity of the envelope-following method and verify the final CS state of AQNs. In addition, we assign a group of reasonable values to the parameters of the system with $\kappa = 0.04$, $f_a = 10^{10}$ GeV, $T_0 = 200$ MeV and $R_0 = 6\times10^{-4}$ cm. Of course, these parameters can vary within a certain range, but it is not the subject of the present work to numerically study how these parameters taking different values will affect the AQN evolution.

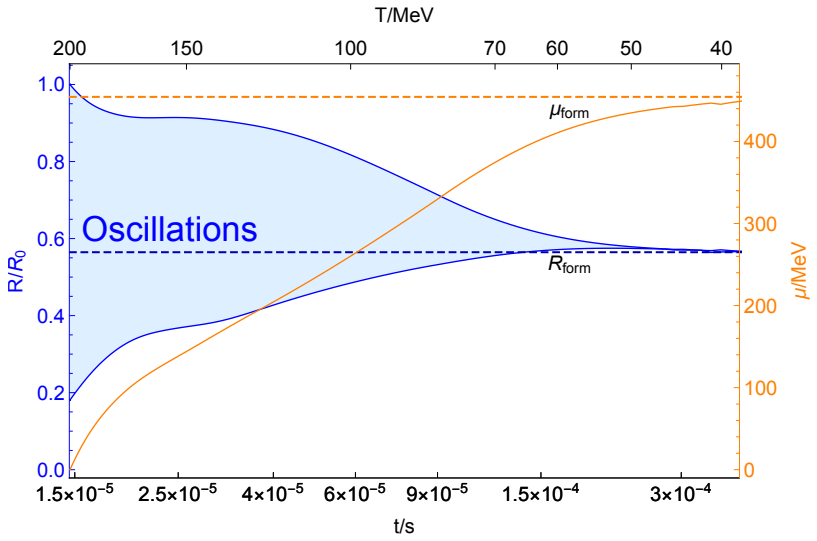

Figure 3.5: An AQN's real-time evolution. The two solid blue lines represents respectively the upper envelope and the lower envelope of R oscillations. The shaded light blue region represents the numerous oscillations. The solid orange line represents the lower envelope of μ oscillations (we did not show the upper envelope and shaded region for μ oscillations for legibility purpose). The dashed blue line and dashed orange line represents respectively $R_{\rm form}$ and $\mu_{\rm form}$ which are derived by simple analytical arguments; see eqs. (3.42) and (3.43). We see that they match the numerical result of AQN evolution pretty well. This figure is taken from Ref. [3].

at $T_{\rm form}$ around 40 MeV.[22] Therefore, the "conspiracy of scales" phenomenon mentioned above has been explicitly tested.

2. The chemical potential inside the AQN indeed assumes a sufficiently large value $\mu_{\rm form} \gtrsim 450$ MeV during this long evolution. This magnitude

[22] This does not mean we can obtain $T_{\rm form}$ with high precision from the side of AQN model. As we have discussed in chapter 2 (see the text below eq. (2.2)), to compare the theoretical prediction with the observed baryon-to-photon ratio, $\eta_{b/\gamma}$, $T_{\rm form}$ has to be determined with high precision because $\eta_{b/\gamma}$ depends on $T_{\rm form}$ very sensitively. To get $T_{\rm form}$ high precisely, we have to take all the ingredients (including the omitted ones such as the effects of annihilation events during AQN formation) into simulation with high precision, which is an extremely difficult task. Nevertheless, the simulation here shows that $T_{\rm form}$ is indeed in the appropriate range, ~ 40 MeV.

is consistent with the formation of a CS phase. Therefore, the original assumption about the CS phase used in the construction of the AQN is justified as *a posteriori*.

Note that in Fig. 3.5, we also present the value of $R_{\rm form}$ and $\mu_{\rm form}$, which are derived by the following simple analytical arguments. We start with the baryon charge in the vicinity of the wall of an AQN, eq. (3.6). The AQN starts evolution at T_0 with the initial chemical potential of the baryon charge being approximately zero, $\mu_0 \simeq 0$. Eq. (3.6) with a zero chemical potential can be calculated as

$$B_{\rm wall}(T = T_0) \simeq \frac{\pi^2}{6} g^{\rm in} R_0^2 T_0^2. \tag{3.40}$$

Then the AQN completes its formation at $T_{\rm form}$ as it stops oscillating with $\dot{R}(t) \simeq 0,\ \ddot{R}(t) \simeq 0,\ \dot{\mu}(t) \simeq 0$. All features of the AQN (radius, chemical potential, etc.) should remain almost constant after the formation point $T = T_{\rm form}$ until the very end $t \to \infty$ ($T \to 0$). Thus, with $R_{\rm form} \simeq R(T = 0)$ and $\mu_{\rm form} \simeq \mu(T = 0)$ we get

$$B_{\rm wall}(T = 0) \simeq g^{\rm in} \cdot 4\pi R_{\rm form}^2 \cdot \int_0^{\mu_{\rm form}} \frac{d^2 k_\perp}{(2\pi)^2} \simeq g^{\rm in} R_{\rm form}^2 \mu_{\rm form}^2. \tag{3.41}$$

According to eq. (3.16), $B_{\rm wall}$ is conserved during evolution. Therefore, by equating (3.40) with (3.41) we arrives at

$$\frac{R_{\rm form}^2}{R_0^2} = \frac{\pi^2}{6} \cdot \frac{T_0^2}{\mu_{\rm form}^2}. \tag{3.42}$$

Also, with all the derivative terms vanishing after $T_{\rm form}$, the equation of motion (3.35) can be simplified as

$$R_{\rm form} \simeq R(T = 0) \simeq \frac{2\sigma_{\rm eff}(T = 0)}{\Delta P(T = 0)}, \tag{3.43}$$

where the pressure difference $\Delta P(T = 0)$ is determined by the inside pressure eq. (3.9) and the outside pressure eq. (3.8),

$$\Delta P(T = 0) \simeq \frac{g^{\rm in} \mu_{\rm form}^4}{24\pi^2} - E_B \left(1 - \frac{\mu_1^2}{\mu_{\rm form}^2}\right). \tag{3.44}$$

The above analysis implies that we can get $R_{\rm form}$ and $\mu_{\rm form}$ directly by solving eqs. (3.42) and (3.43) without even numerically computing the AQN evolution, and they are completely determined by the initial parameters, R_0 and T_0. In Fig. 3.5, we plotted the analytical result of $R_{\rm form}$ and $\mu_{\rm form}$ corresponding to the same R_0 and T_0 as shown in footnote 21. We see that they match the numerical result pretty well and thus verify the validity of the envelope-following method.

In summary, we used an approach coined as the envelope-following method to overcome a common numerical problem with the drastic separation of scales in the system. In our case, the scales are the QCD scale $\Lambda_{\rm QCD}$, the axion scale m_a, and the cosmological time scale $t \sim 10^{-4}$ s. The results support our original assumptions that the chemical potential inside the AQN indeed assumes a sufficiently large value $\mu_{\rm form} \gtrsim 450$ MeV after this long cosmological evolution. This magnitude is consistent with the formation of a CS phase, as shown in the QCD phase diagram. Also, the AQNs complete their formation precisely in the region of $T_{\rm form} \approx 40$ MeV, which determines the present value of the baryon-to-photon ratio, eq. (2.2). These results represent a highly nontrivial consistency check of the AQN framework when the three drastically different scales "conspire" to produce a self-consistent picture.

3.4 Conclusion

We conclude this chapter as follows. We first reviewed the AQN formation based on Ref. [7]. Axion domain walls are initially formed during the QCD epoch with some baryon charge induced in the vicinity of walls. Closed walls could evolve into stable objects called AQNs after numerous oscillations, dominated by the equation of motion (3.12). We also demonstrated that the CP-violating effects due to the coherent CP-odd axion field will generate an $\mathcal{O}(1)$ disparity between matter and antimatter AQNs, which is not sensitive to many parameters of the model. Finally, we resolved the multi-scale problem that arose in numerical simulations of the AQN formation with the novel numerical method, envelope-following method, the result of which confirms the basic features of the AQN formation temperature and chemical potential, $T_{\rm form} \sim 40$ MeV and $\mu_{\rm form} \gtrsim 450$ MeV, which is consistent with the formation of a CS phase. This result shows that the drastically different scales in the system nevertheless lead to a consistent picture in the AQN framework.

In this chapter, we focused on the formation of a single AQN. However,

AQNs can have different masses, which are determined by different initial conditions of closed axion domain walls. We will study the size distribution of AQNs in chapter 5. In addition, after formation at $T_{\rm form} \sim 40$ MeV, antimatter AQNs are subject to the annihilation events with baryons from the surrounding cosmic plasma. We will study the AQN evolution after $T_{\rm form}$ in the same chapter.

In chapter 4 below, we are going to study the disparity between matter and antimatter AQNs (represented by the parameter c) from the observational side, in the context of axion cosmology where free axions from misalignment mechanism also contribute to dark matter.

Chapter 4

AQNs and Free Axions as Dark Matter

The AQN model does not reject the conventional source of dark matter from the axions generated by the misalignment mechanism. In fact, the oscillating coherent axion field, eq. (2.9), plays a dual role: in addition to generating the asymmetry between matter AQNs and antimatter AQNs as we have discussed in chapter 3.2, it also produces non-thermal axions, which is known as the misalignment mechanism [47–49]. We call these axions the "free axions" in comparison with the axion field in the form of domain wall as the shell of an AQN. In this chapter, we are going to study the relation between AQNs and free axions as two sources of dark matter in the AQN framework. This chapter is adapted from Ref. [2].

4.1 Abundances of AQNs and free axions

We first start with the simple case that dark matter is fully saturated by AQNs. From eq. (2.1), we get

$$\Omega_{\rm DM} \simeq \left(\frac{1+c}{1-c}\right)\Omega_{\rm visible}, \qquad c \equiv \left|\frac{B_{\rm nuggets}}{B_{\rm antinuggets}}\right|. \tag{4.1}$$

The relation between $\Omega_{\rm DM}$ and $\Omega_{\rm visible}$ is now expressed in terms of the parameter c which describes the disparity between matter and antimatter AQNs. $B_{\rm nuggets}$ and $B_{\rm antinuggets}$ can be understood as the baryon charge stored in all matter AQNs and antimatter AQNs respectively. Some effects

have been ignored in deriving this relation. First, the contribution from free axions to dark matter was ignored. Second, the mass of closed axion domain wall as the shell of an AQN was ignored when calculating the AQN mass, so the ratio c is defined in the way that only the baryon part of an AQN accounts for the total AQN mass. Third, energy per baryon charge for CS phase (AQNs) and hadronic phase (visible matter) was assumed to be the same, but in fact there are corrections to the AQN energy due to the CS energy gap and the bag-constant term which will be discussed in chapter 4.2. In spite of these simplifications, this relation (4.1) represents a very generic consequence of the framework that $\Omega_{\rm DM} \sim \Omega_{\rm visible}$ as long as the asymmetry between matter AQNs and antimatter AQNs (i.e., c) is of order one which has been verified in chapter 3.2. As defined in eq. (4.1), the range of c is $0 < c < 1$.

Now we want to generalize the relation (4.1) by accounting for all these (previously neglected) effects. The corresponding modifications do not affect the basic qualitative claim $\Omega_{\rm DM} \sim \Omega_{\rm visible}$, but may change some numerical factors (e.g., c, as we will see in chapter 4.3), which is precisely the main objective of the studies in this chapter.

Traditionally, the axion is regarded as one of the leading candidates for dark matter; see e.g., Ref [24] for a review. It is normally assumed that free axions are generated through the misalignment mechanism or as a result of the decay of topological defects. However, in the AQN framework, AQNs generated in the same QCD epoch as free axions enter the game and can be the dominant part of dark matter as we will see. We now proceed with our definitions and notations of these contributions: the contribution from the conventional axion production reviewed in Ref. [24] and the contribution from AQNs. As usual, we use the ratio of different component densities to critical density today to mark their proportions:

$$\Omega_i = \rho_i/\rho_{\rm cr}, \qquad i = b, \pm, a, \tag{4.2}$$

where label i stands for different species: b for baryon (i.e., visible matter); $+$ for matter AQN and $-$ for antimatter AQN; a for free axions. $\rho_{\rm cr}$ is the critical density of the Universe today. Then we have

$$\Omega_{\rm DM} : \Omega_b = (\Omega_+ + \Omega_- + \Omega_a) : \Omega_b \approx 5 : 1, \tag{4.3}$$

where $\Omega_{\rm DM}$ is represented by two parts, the axion contribution, $\Omega_{\rm DM}({\rm axion}) \equiv$

$\Omega_{\rm a}$, and the AQN's contribution $\Omega_{\rm DM}({\rm nugget}) \equiv (\Omega_+ + \Omega_-)$.

Next, to describe the difference between matter AQNs and antimatter AQNs, we define the following parameters:

$$c_\Omega \equiv \frac{\Omega_+}{\Omega_-} = \frac{N_+ E_+}{N_- E_-} = \frac{N_+ \epsilon_+ B_+}{N_- \epsilon_- B_-} = \frac{N_+}{N_-} c_\epsilon \cdot c, \tag{4.4}$$

where

$$c_\epsilon \equiv \frac{\epsilon_+}{\epsilon_-}, \qquad c \equiv \frac{B_+}{B_-}, \qquad 0 < c < 1, \tag{4.5}$$

and $N_\pm$ is the number density of matter/antimatter AQNs in the Universe today; $E_\pm$, $B_\pm$ and $\epsilon_\pm = E_\pm/B_\pm$ are respectively the energy, baryon number and energy density per baryon charge for a single matter/antimatter AQN. In these relations, both baryon charges B_+ and B_- are defined to be positive numbers. The definition of c in eq. (4.5) thus coincides with the definition given in eq. (4.1).

As we have already mentioned, a number of important numerical factors were neglected in deriving eq. (4.1). We can now formalize these effects in a very precise way using our definitions, eqs. (4.4) and (4.5). In particular, $\epsilon_\pm$ is the energy per baryon charge in CS phase which is not the same as in hadronic phase, i.e., $\epsilon_\pm \neq m_p/3$. Furthermore, $E_\pm$, which was previously estimated as $E_+ = E_- = B \cdot m_p$ (see eq. (4.15)), now includes the contribution from the surrounding axion domain wall, and obviously has a much more complicated structure. In addition, we previously ignored the contribution of free axions by assuming $\Omega_a = 0$. This will be recovered with an explicit expression for the contribution of free axions.

To simplify our analysis, we want to make a technical assumption that $N_+ \simeq N_-$ in eq. (4.4). It does not affect any of our conclusions as we argue below. The basic justification for this assumption is as follows: the initial distributions of the matter AQNs and antimatter AQNs (i.e., closed axion domain walls) are the same. It is just their evolution in the background of the coherent CP-odd axion field that generates the asymmetry between them as argued in chapter 3.2. The result in chapter 3.2 shows that matter/antimatter AQNs are only different in $B_\pm$ carried by a single AQN, but their number densities N_+ and N_- remain the same. This information is coded in equations (4.4) and (4.5) by the relation $B_+ \neq B_-$.

Substituting $N_+ = N_-$ into eq. (4.4), we arrive at the desired expression

$$c_\Omega = c_\epsilon \cdot c. \tag{4.6}$$

This equation has obvious physical meaning and essentially states that the relative contribution of the matter/antimatter AQNs to Ω_{DM} is proportional to the difference of the corresponding baryon charges parameterized by c, and it is also proportional to the difference of their energy densities parameterized by c_ϵ.

Now we want to derive an equation, similar to eq. (4.1), which accounts for a number of the effects which were previously ignored. With this purpose, we express the baryon number conservation in the following form

$$B_- - B_+ \simeq \frac{1}{N_\pm}\frac{3\rho_b}{m_p}, \tag{4.7}$$

where m_p is the mass of a single baryon charge and can be approximated by the proton mass. The coefficient 3 in eq. (4.7) corresponds to our normalization of the baryon charge in the present work. This normalization is consistent with our definition of μ corresponding to the quark (rather than baryon) chemical potential, which implies that $B_\pm$ count for the number of quarks in the system, rather than the baryon charges.

With these comments in mind and using eqs. (4.2), (4.4) and (4.7), we arrive at the following relation

$$\frac{\Omega_+}{\epsilon_+}\left(\frac{1}{c} - 1\right) = \frac{\Omega_-}{\epsilon_-}(1-c) = \frac{3\Omega_b}{m_p}. \tag{4.8}$$

The coefficient $c \in (0,1)$ in these relations satisfies the same constraint as in our simplified treatment of the problem presented in eq. (4.1). Therefore,

$$0 < c < 1. \tag{4.9}$$

Our next step is to rewrite the eqs. (4.3) and (4.4) in the following convenient form:

$$\Omega_+ = c_\Omega \cdot \frac{\Omega_{\rm DM} - \Omega_a}{1 + c_\Omega}, \qquad \Omega_- = \frac{\Omega_{\rm DM} - \Omega_a}{1 + c_\Omega}. \tag{4.10}$$

The last step to achieve our goal is to use eqs. (4.8) and (4.6) to arrive at the

final expressions which will be used in our numerical studies in chapter 4.3:

$$\frac{1-c}{1+c_\epsilon c} = \frac{3\epsilon_-}{m_p} \cdot \frac{\Omega_b}{\Omega_{\rm DM} - \Omega_a}, \tag{4.11a}$$

$$c_\epsilon \cdot \frac{1-c}{1+c_\epsilon c} = \frac{3\epsilon_+}{m_p} \cdot \frac{\Omega_b}{\Omega_{\rm DM} - \Omega_a}. \tag{4.11b}$$

Eq. (4.11) is a generalization of our previous simplified expression (4.1). It accounts for a number of numerical effects mentioned previously. Eq. (4.11) obviously reduces to our previous expression, eq. (4.1), in the limit when $\Omega_a = 0$ and matter and antimatter AQNs have the same energies, i.e., $\epsilon_+ = \epsilon_- = m_p/3$ such that $c_\epsilon = 1$.

While the numerical estimates for parameters $\epsilon_\pm$ entering eq. (4.11) will be discussed in detail in next chapter 4.2, the rest of this section is devoted to a short overview of known estimates of the parameter Ω_a which also enters eq.(4.11).

The corresponding computations of Ω_a have been carried out in a number of papers. In what follows we limit ourselves by reviewing the estimates of Ω_a resulted from the misalignment mechanism [47–49], while leaving out the contribution related to the decay of the topological defects.[23] We emphasize that we do not exclude the corresponding contribution related to the topological defects because they are unimportant. Rather, we omit them because their role is largely unknown under present circumstances when the PQ symmetry is broken before inflation in the AQN framework. In addition, even in a different scenario when the PQ symmetry is broken after inflation, the question of whether it saturates the observed dark matter density remains controversial as mentioned in footnote 23. Thus, we leave out this contribution to simplify our notations and our analysis as the focus of this chapter is the AQN contribution to $\Omega_{\rm DM}$ rather than the direct axion production represented by Ω_a. In other words, Ω_a contribution is kept in our formulas

[23]There is a number of uncertainties and remaining discrepancies in the corresponding estimates. We shall not comment on these subtleties by referring to the original papers [81, 90, 91, 95, 96]. According to the computations presented in Ref. [91], the axion contribution to $\Omega_{\rm DM}$ as a result of the decay of the topological objects can saturate the observed dark matter density today if the axion mass is in the range $m_a = (2.62 \pm 0.34) \times 10^{-5}$ eV (a more recent simulation gives $m_a = (2.52 \pm 1.10) \times 10^{-5}$ eV [97]), while the earlier estimates suggest that the saturation occurs at a larger axion mass. One should also emphasize that the computations in Refs. [81, 90, 91, 95–97] have been performed with the assumption that PQ symmetry is broken after inflation.

for normalization purposes to illustrate the significance (or insignificance) of the AQN contribution to $\Omega_{\rm DM}$ as a function of parameters. The contribution to Ω_a due to the decay of the topological objects can always be incorporated into our formulas once the uncertainties of this contribution are better understood.

For the misalignment production of free axions, we adopt the general formula as presented in Ref. [24],[24]

$$\Omega_a h^2 \approx 2\times 10^4 \left(\frac{f_a}{10^{16}\ {\rm GeV}}\right)^{7/6} \left(\theta_0^2+\frac{H_I^2}{(2\pi f_a)^2}\right) F_{\rm anh}\left(\sqrt{\theta_0^2+\frac{H_I^2}{(2\pi f_a)^2}}\right), \tag{4.12}$$

with

$$F_{\rm anh}(x) = \left[\ln\left(\frac{e}{1-x^2/\pi^2}\right)\right]^{7/6}, \tag{4.13}$$

where H_I is the inflationary Hubble scale and $F_{\rm anh}(x)$ is the correction factor due to the anharmonic cosine part in the axion potential [24, 98]. The parameter θ_0 is the initial misalignment angle and $H_I/(2\pi f_a)$ is the backreaction contribution to this homogeneous field displacement due to the isocurvature perturbations. The parameter f_a and the axion mass m_a are not independent parameters, as their product is fixed by the topological susceptibility of QCD, $\chi = f_a^2 m_a^2$. Using the recent value $\chi \simeq 0.0216\ {\rm fm}^{-4} \simeq 3.2\times 10^7\ {\rm MeV}^4$ (see eq. (3.37) for details) at zero temperature [79], we have the present-day value of axion mass:

$$m_a \simeq 5.7\times 10^{-4}\ {\rm eV}\left(\frac{10^{10}\ {\rm GeV}}{f_a}\right). \tag{4.14}$$

This completes our short overview of Ω_a contribution entering our basic formula (4.11).

Chapter 4.2 is mainly devoted to the estimates of $\epsilon_\pm$ which, along with Ω_a, also enter our basic formula (4.11). Then in chapter 4.3, using the results of

[24]One comment on the power 7/6. The number density of misalignment axions is $n_a = 1/2\cdot m_a(t_{\rm osc})\cdot(f_a\theta_0)^2$ which is determined by the initial (dimensional) amplitude, $f_a\theta_0$, of axion oscillations at $t_{\rm osc}$ ($t_{\rm osc}$ is determined by $m_a(t_{\rm osc})\cdot t_{\rm osc}=1$). n_a is conserved per co-moving volume (see e.g., Ref. [25]), so the present-day abundance is $\rho_a \sim m_a\cdot m_a(t_{\rm osc})(f_a\theta_0)^2\cdot(T_{\rm now}/T_{\rm osc})^3$. Using the relations $m_a(T)\sim f_a^{-1}T^{-\beta}$ where $\beta\approx 4$ (see eq. (3.38)) and $T\sim t^{-1/2}$, we then get $\rho_a \propto f_a^{\beta'}$ with the exponent $\beta'\approx 7/6$.

chapter 4.1 and chapter 4.2, we do a numerical analysis to study the allowed window and constraints related to the phenomenological parameters of the AQN framework.

We conclude this section with the following generic comment. The AQN contribution given by $\Omega_{\pm}$ and the direct axion production represented by Ω_a always accompany each other during relaxation of the dynamical axion field during the QCD epoch. These contributions to $\Omega_{\rm DM}$ represent complementary mechanisms and cannot be formally separated (e.g., by variation of a free parameter of the system such as f_a), as the closed $N_{\rm DW} = 1$ axion domain walls, which are responsible for the AQN formation, can be produced irrespective of whether the PQ scale is above or below the inflationary scale H_I, as reviewed in chapter 2.

4.2 Internal structure of an AQN

For a stable AQN that has already been formed and settles down in CS phase after $T_{\rm form}$, the energy per baryon charge of the AQN $\epsilon_{\pm}$ can be simply estimated as follows:

$$M \sim B \cdot m_p, \qquad \epsilon_{\pm} \sim \frac{M}{B} \sim m_p. \tag{4.15}$$

However, as we have mentioned, in writing this expression, we have neglected the difference of the CS energy density from the hadronic energy density. Also, we have neglected the contribution from the closed axion domain wall as the shell. The main goal of this section is to give a more precise description of eq. (4.15) through studying the internal structure of an AQN, with the above effects included. But as will see below, these effects will not significantly change the basic relation (4.15), and eq. (4.15) is a very good approximation.

To accomplish the goal of incorporating the above effects, we consider two drastically different models. Considering two different models can help us to test the sensitivity (or non-sensitivity) of our framework to different phenomenological parameters effectively describing the strongly coupled QCD. For simplicity and without loss of generality, we assume that the CS phase assumes the simplest possible structure in the form of the color flavor locked (CFL) phase without any additional complications such as the possible meson condensation.

The first model largely follows the original work, Ref. [13]. However,

the difference with the previous analysis is that, as the first paper on the subject, Ref. [13] was mostly dealing with fundamental and basic questions on principle possibility to stabilize the AQNs by the axion domain walls. The goal of the present studies is quite different as we want to produce some quantitative results on the parameters entering the basic eq. (4.11).

The model [13] considers the equilibrium between the Fermi pressure, the domain wall surface tension, the "bag constant" pressure $\sim E_B$, and finally, the quark-quark interaction related to the CS gap. The energy of a stabilized AQN can be represented in the following form

$$E^{(1)} = 4\pi\sigma_{\rm eff}R^2 + \frac{g\mu^4}{6\pi}R^3 - \frac{3\Delta^2\mu^2}{\pi^2}V + E_B\Theta(\mu-\mu_1)\left(1-\frac{\mu_1^2}{\mu^2}\right)V, \quad (4.16)$$

while the AQN's baryon number can be estimated as follows

$$B = gV\int_0^\mu \frac{d^3p}{(2\pi)^3} = \frac{2g}{9\pi}\mu^3R^3, \quad (4.17)$$

where our normalization corresponds to $B = 1$ per single quark degree of freedom in order to remain consistent with notations of chapter 4.1. Since we are describing a stable AQN, the chemical potential μ and the radius R are in fact $\mu_{\rm form}$ and $R_{\rm form}$ of chapter 3. The entire AQN is in chemical equilibrium so that we can calculate the total baryon charge carried by an AQN in such a way, eq. (4.17); see also eq. (5.2) in chapter 5.

The domain wall tension $\sigma_{\rm eff}$ entering (4.16) requires some additional comments. First of all, the effective domain wall tension $\sigma_{\rm eff}$ should not be confused with the conventional surface tension $\sigma_a \simeq 8f_a^2m_a$, which normally enters the computations [81, 90, 91, 95, 96] of the axion production due to the decay of the topological defects.

There are two main reasons for this important difference. First of all, the axion domain wall solution in our case interpolates between topologically distinct vacuum states in hadronic and CS phases, in contrast to a conventional axion domain wall which interpolates between topologically distinct hadronic vacuum states. The chiral condensate may or may not be formed in CS phase. It strongly affects the topological susceptibility in CS phase which could be much smaller than in the conventional hadronic phase. The well-known manifestation of this difference is the expected smallness of the η' mass in CS phase in comparison with the hadronic phase. One should

emphasize that the 2π periodicity of the axion θ and the Nambu-Goldstone fields η' still holds in the presence of the chemical potential μ in dense matter CS phases [76]. Therefore, the topological reason for the mere existence of the axion domain wall still persists, while the numerical value of the tension $\sigma_{\rm eff}$ will deviate from its conventional expression σ_a computed in the hadronic phase.

The second reason for strong deviation of the $\sigma_{\rm eff}$ from conventional expression for σ_a is that formula $\sigma_a \simeq 8 f_a^2 m_a$ was derived assuming the thin-wall approximation when the domain wall is assumed to be almost flat, i.e., a typical curvature of the domain wall structure is much smaller than its width. This approximation is obviously badly violated because the axion domain wall width is of order m_a^{-1}, while the typical curvature is comparable with the width of the domain wall as these two parameters are related in our framework, $R \sim m_a^{-1}$. The physical consequence of this relation is that the axion field strongly overlaps within the AQN's volume. This effect is expected to drastically reduce the domain wall tension.[25]

To account for these complicated QCD effects, we define $\sigma_{\rm eff} \equiv \kappa \cdot \sigma_a$, with an unknown phenomenological parameter, $0 < \kappa < 1$, which accounts for the physics mentioned above. In particular, the violation of the thin-wall approximation was modeled in Ref. [7] by introducing a suppression factor $\exp(-R_0/R_{\rm form})$. The corresponding suppression could be quite strong and can be as small as 10^{-5} assuming a typical formation radius $R_{\rm form} \sim 0.1 R_0$ as studied in Ref. [7]. In what follows we treat κ as a free phenomenological parameter.

Our goal now is to minimize the expression (4.16). To achieve this goal we introduce two dimensionless variables x and σ_0 as

$$x \equiv R\frac{E_B^{1/4}}{B^{1/3}} = \frac{E_B^{1/4}}{\mu}\left(\frac{8\pi}{2g}\right)^{\frac{1}{3}}, \qquad \sigma_0 \equiv \frac{\sigma_{\rm eff}}{B^{1/3}E_B^{3/4}} = \frac{8\chi}{E_B^{3/4}}\frac{1}{\kappa^{-1}B^{1/3}m_a}, \quad (4.18)$$

where we express σ_0 in terms of the topological susceptibility, $\chi = f_a^2 m_a^2$.

[25] The corresponding large modifications can be understood from a simple model when the domain wall is bent, allowing a strong overlap between opposite sides of the wall. The effective domain wall tension obviously receives the modifications as a result of this bending geometry when the axion field configuration deviates from a simple well-known 1D solution.

Then, the energy per baryon charge is

$$\epsilon^{(1)}_{\rm tot}(x) \equiv \frac{E^{(1)}}{B} = \epsilon_{\rm DW} + \epsilon^{(1)}_{\rm QCD}(x), \qquad \epsilon_{\rm DW}(x) = \frac{32\pi\chi}{E_B^{1/2}} \frac{x^2}{\kappa^{-1} B^{1/3} m_a},$$
$$\epsilon^{(1)}_{\rm QCD}(x) = \frac{3}{4}\left(\frac{9\pi}{2g}\right)^{\frac{1}{3}} \frac{E_B^{\frac{1}{4}}}{x} - \frac{18\Delta^2}{g E_B^{\frac{1}{4}}}\left(\frac{2g}{9\pi}\right)^{\frac{1}{3}} x + \frac{4\pi}{3} E_B^{\frac{1}{4}} \theta(x_1 - x)\left(1 - \frac{x^2}{x_1^2}\right) x^3. \tag{4.19}$$

The equilibrium point can be found using the condition $\partial\epsilon_{\rm tot}/\partial x = 0$ at $x = x_{\rm eq}$, and the solution can be well approximated from numerical computation as

$$\epsilon^{(1)}_{\rm tot} \simeq -0.57 m_\pi + \frac{3.51 m_\pi}{(\kappa^{-1} B^{\frac{1}{3}} \frac{m_a}{m_\pi})^{0.310}}, \quad \text{within } 0.2 \lesssim \kappa^{-1} B_\pm^{\frac{1}{3}} m_a/m_\pi \lesssim 0.95. \tag{4.20}$$

In this expression, $\epsilon_\pm$ are distinguished from each other implicitly by replacing B with $B_\pm$ characterized by the parameter c.

This solution eq. (4.20) has accuracy up to 0.6% comparing to the exact numerical solution within the range specified. Within this range, the contribution of the closed domain wall as the shell accounts for only $\sim 1/3$ of the total energy, $\epsilon_{\rm DW} \simeq 1/3 \cdot \epsilon_{\rm tot}$; see the Appendix of Ref. [2] for more numerical details. This means the contribution of the domain-wall shell is subdominant. Besides, the CS energy gap $\Delta \simeq 100$ MeV and $E_B^{1/4} \simeq 150^{1/4}$ MeV are considerably smaller than $\mu \gtrsim 450$ MeV (see chapter 3.3). Thus, we conclude that the second term in eq. (4.16), which represents the contribution of the baryon part, is dominant in comparison with other terms, i.e., the first term (contribution of the domain-wall shell contribution) and the latter two terms (contributions of the CS gap and the bag constant terms). This verifies that the simple relation eq. (4.15) is a good approximation which only differs from the precise expression (4.16) by a few subdominant numerical factors.

In addition to the first model eq. (4.16) from Ref. [13], we introduce the second model based on the ideas of the old constituent quark model being applied to the dense matter systems [99],

$$E^{(2)} = B M_q + 4\pi\sigma_{\rm eff} R^2. \tag{4.21}$$

M_q is the effective constituent quark mass in CS phase with a typical QCD

scale. The energy per baryon charge, $E^{(2)}/B$, is

$$\epsilon_{\rm tot}^{(2)} \simeq M_q + \left(\frac{376{\rm MeV}}{\mu}\right)^2 \frac{m_\pi}{\kappa^{-1} B^{\frac{1}{3}} \frac{m_a}{m_\pi}}, \tag{4.22}$$

M_q and μ are not completely free parameters according to various phenomenological models for dense phases. Similar to the previous studies of this model in neutron star physics, we adopt the following numerical values [99]: $(M_q,\ \mu) \simeq (200, 400)$ and $(160, 500)$ MeV respectively.

$\epsilon_\pm$ in both models depends on the same parameter $\kappa^{-1} B^{1/3} m_a$, which is a highly nontrivial feature. Despite that the two models are built based on fundamentally different principles, we will see in the following section that they produce similar results.

4.3 Confronting the model with observations

In previous sections, we introduced a number of phenomenological parameters describing the AQN model and the related axion physics. Eq. (4.20) or eq. (4.22) is used to fit the parameters $\epsilon_\pm$ and further c_ϵ. Eq. (4.12) is used to fit the abundance of free axions, Ω_a. With these equations substituted into the basic formula (4.11), we can express the key parameter c as a function of the physically observable parameters, B, θ_0, m_a and H_I. The main goal of this section is to study the value of c with the above parameters varying within the allowed parameter space that is consistent with all known observations. c, defined in eq. (4.5), which describes the disparity between matter and antimatter AQNs, is a key parameter in our model. As we argued in chapter 3.2, the magnitude of the disparity is $\mathcal{O}(1)$ as a result of interaction with the coherent CP-odd axion field. This coefficient, in principle, is calculable from the first principles along with other parameters of the model as all fields, coupling constants and interactions are represented by the standard model physics accompanied by the axion field $\theta(x)$ with a single additional fundamental parameter f_a. However, such computations presently are not feasible as even the QCD phase diagram at $\theta \neq 0$ is not yet understood; see Fig. 2.1.

However, the value of c can be studied from the observational side repre-

sented by eq. (4.11). We represent our numerical results about c and related physics in chapters 4.3.2 and 4.3.3. However, first of all, in chapter 4.3.1, we overview the known constraints on relevant parameters.

4.3.1 Constraints on the parameter space

We start with eq. (4.9). This should not be considered as a constraint on c as it essentially represents our convention that we define the visible matter as the baryons with positive baryon charge. Therefore, the absolute value of the baryon charge hidden in the antimatter AQNs B_- must be greater than the baryon charge B_+ hidden in the matter AQNs (as a result of the global conservation of the baryon charge which is assumed to be zero at all times). This leads to the formal relation $c < 1$ which reflects our convention. The parameter c is obviously a positively defined parameter as $B_\pm$ are both defined positive here, which is explicitly represented by eq. (4.5).

Another constraint in our model arises in computing the energy per baryon charge of an AQN, which is $0.2 \lesssim \kappa^{-1} B^{1/3} m_a/m_\pi \lesssim 0.95$ following from eq. (4.20). This constraint is related to our studies of the stability of the AQNs in CS phase; see more details in chapter 4.2.[26] In addition, there are some constraints on B as we reviewed in chapter 2; see eq. (2.5).[27]

We next consider the classical window[28] for axion mass, see e.g., the

[26]To be more specific, the chemical potential decreases with the parameter $\kappa^{-1} B^{1/3} m_a$ increasing. This can be seen from the AQN properties at the equilibrium point $x = x_{\rm eq}$ where $\partial \epsilon_{\rm tot}/\partial x = 0$. Numerically, $\kappa^{-1} B^{1/3} m_a/m_\pi \gtrsim 0.95$ corresponds to $\mu \lesssim 330$ MeV where the AQNs are not in CS phase. Besides, $\kappa^{-1} B^{1/3} m_a$ cannot be too small, required by the condition of AQN stability that $3\epsilon_{\rm QCD}/m_p \lesssim 1$ which numerically gives a lower limit ~ 0.2. We refer the readers to the Appendix of Ref. [2] for more technical details. So we take $0.2 \lesssim \kappa^{-1} B^{1/3} m_a/m_\pi \lesssim 0.95$ for both the conditions of CS phase and stability are satisfied. In comparison, the two conditions are always satisfied in model 2, since the parameters M_q and μ are fixed at appropriate values.

[27]The baryon charge B that enters the basic formula (4.11) is in fact the average baryon number $\langle B \rangle$, which can be seen from our definition of $\Omega_\pm = N_\pm B_\pm$. This means that we have assumed that all AQNs are identical, which can greatly simplify our analysis. The size distribution of AQNs will be discussed in chapter 5.

[28]For the main purposes of this paper, we will only consider "the classical axion window", where the initial misalignment angle θ_0 is not fine-tuned. Note that while the upper bound is a very solid constraint as it is given by stellar physics (e.g., see review [100]), the lower bound on the axion mass in eq. (4.23) should be treated as an order of magnitude estimate provided that θ_0 is not fine-tuned. If the fine tuning is allowed, θ_0 may assume an arbitrarily small value, in which case the corresponding lower bound on m_a is shifted.

review paper [102]:

$$10^{-6}\ \text{eV} \lesssim m_a \lesssim 10^{-2}\ \text{eV}. \tag{4.23}$$

By using the relation (4.14), this window for m_a can be expressed in terms of the corresponding classical window for f_a:

$$5.7\times 10^{8}\ \text{GeV} \lesssim f_a \lesssim 5.7\times 10^{12}\ \text{GeV}. \tag{4.24}$$

One should emphasize that the constraint (4.23) or equivalently (4.24) is the commonly accepted axion window, and it is not, by any means, originated from our analysis of the AQN model. Nevertheless, all our constraints depend on m_a as it explicitly enters the eq. (4.20).

From these discussions it is clear that the axion mass m_a plays a dual role in our analysis because it enters the formulas related to the physics of the AQNs as eq. (4.20) states. It also enters the expression (4.12) for Ω_a. This unambiguously implies that the remaining portion of the dark matter represented by the AQN contribution (4.10) also becomes (implicitly) highly sensitive to m_a through the dependence of the axion portion of the dark matter represented by Ω_a.

As we argue below, for values of κ in the range $10^{-4} \lesssim \kappa \lesssim 10^{-2}$, the constraints (4.20), (4.23) and (2.5) become mutually compatible, which we consider as a highly nontrivial consistency check as all the parameters entering these relations have been constrained by very different physics related to independent observations, experiments and analysis.

The next constraint to consider is related to the analysis of the inflationary scale H_I and the related constraints on the tensor-to-scalar ratio and the isocurvature perturbations. The basic assumption of the AQN model is that PQ symmetry breaking occurs before inflation, in which case

$$f_a > H_I/2\pi, \tag{4.25}$$

see e.g. Ref [24] for a review. This assumption plays a crucial role in our analysis in chapter 3 because the CP-odd axion field must be coherent on enormous scale of the entire Universe to separate the baryon charges on this gigantic scale with the same sign of θ. Precisely this coherent axion field generates the disparity between the matter and antimatter AQNs which

The only exclusion interval in this case $6\times 10^{-13}\text{eV} < m_a < 2\times 10^{-11}\text{eV}$ is obtained from the black hole superradiance effects [101].

eventually leads to the generic and fundamental prediction $\Omega_{\rm DM} \sim \Omega_{\rm visible}$ of this entire framework.

It is known that the inflationary Hubble scale is tied to the value of the tensor-to-scalar ratio r_T which measures H_I. Assuming the simplest single field inflationary model, the non-observation of the tensor modes ($r_T < 0.12$) imposes the upper limit for the inflation scale, see Refs. [24, 103]:

$$H_I/2\pi \lesssim 1.4 \times 10^{13}\ \text{GeV}. \tag{4.26}$$

An important comment here is that (4.26) is a highly model-dependent result and varies from one inflationary model to another. It is presented here exclusively for illustrative purposes to provide some orientation for the relevant scales of the problem.

The isocurvature perturbations related to the axion field provide another independent constraint on H_I. We recall that the amplitude for the isocurvature power spectrum is determined by the following expression (see the original papers [104–108] and the review article [24]):

$$A_I = \left(\frac{\Omega_a}{\Omega_{\rm DM}}\right)^2 \cdot \left(\frac{H_I}{\pi\phi_i}\right)^2, \quad \phi_i \equiv f_a\theta_0. \tag{4.27}$$

The corresponding isocurvature amplitude is strongly constrained by a CMB analysis, $A_I/A_s < 0.038$, where A_s is the conventional amplitude for the scalar power. It is normally assumed that the non-observation of the isocurvature perturbation provides a strong constraint on axion properties in a scenario where the PQ symmetry is broken before inflation. Our original comment here is that the axion contribution represented by Ω_a in eq. (4.27) to the dark matter density $\Omega_{\rm DM}$ could be numerically quite small in the AQN model as the AQNs in most cases play the dominant role by saturating the dark matter density. Such a scenario drastically alleviates some severe constraints on parameters in a conventional analysis where one normally assumes that the axions saturate the dark matter density.

We conclude this part with the following remark. The conventional analysis on the relation between dark matter axions, inflationary scale, isocurvature perturbations very often assumes that the axions saturate the dark matter density. It should be contrasted with our AQN model where the axions themselves with the same f_a may contribute very little to $\Omega_{\rm DM}$, as the dominant contribution may come from the AQNs which always satisfy

the relation $\Omega_{\rm DM} \sim \Omega_{\rm visible}$ irrespective of many parameters in axion physics which have been demonstrated in chapter 3. It may alleviate some severe constraints on the parameters (such as H_I, f_a, r_T, θ_0) which other models normally face.

4.3.2 Numerical plots

The goal of this part is to analyze the dependence of the internal (with respect to the AQN model) parameter c from external parameters of the system such as B, θ_0, m_a, H_I which are well-defined observables irrespective of the specific features of the AQN model. As the parameter c cannot be negative or larger than one, the corresponding plots provide us with information on the typical values of the external parameters B, θ_0, m_a, H_I when the AQN model is self-consistent with all presently available constraints.

We start our analysis by plotting in Fig. 4.1a the parameter c as a function of m_a and B, where we fix specific values for parameters $\kappa = 10^{-4}$ and $H_I/2\pi = 5.7 \times 10^8$ GeV and $\theta_0 = 10^{-3}$ to simplify the arguments and analysis. We also plotted the $f_a = H_I/2\pi$ with a red solid line to localize the physical parameter space and remove unphysical (within the AQN model) solutions. We also plotted (in green and blue dashed lines) the region in parameter space where the condition (4.20) is satisfied and our computations in the CS phase are justified. For this specific choice of the parameters one can explicitly see that parameter c is constrained in a parallelogram with the range $0.4 \lesssim c \lesssim 0.6$. This region of the parameter space satisfies all internal and external constraints listed chapter 4.3.1.

From the same plot one can also identify the allowed region of the baryon charge B for a given axion mass m_a. One should emphasize that the dark matter density in Fig. 4.1a for $\theta_0 = 10^{-3}$ is entirely saturated by the AQNs, as the direct axion production is strongly suppressed by the small initial misalignment angle, $\theta_0 = 10^{-3}$. To see the role of the free axions, one can choose $\theta_0 = 10^0$, as shown in Fig. 4.1b. In this case, free axions saturate the dark matter density, $\Omega_{\rm DM} = \Omega_a$, at small axion masses $m_a \simeq 10^{-5}$ eV, as shown by the solid yellow line. When the choice of θ_0 changes from 10^{-3} to 1, the corresponding allowed region for the AQN parameter space (B, m_a) will be modified accordingly as the allowed region for the AQNs obviously shrinks when the contribution of free axions starts to play an essential role.

The key observation here is that there will always be a region (B, m_a) when the total dark matter density assumes its observational value through

the parameter c which determines the AQN contribution to $\Omega_{\rm DM}$. The corresponding contribution varies to accommodate the related free axion portion Ω_a as the total dark matter density $\Omega_{\rm DM}$ in Fig. 4.1 is fixed and assumes its observational value.

In Fig. 4.2, we wish to demonstrate the sensitivity of the allowed region (B, m_a) with respect to the parameter $H_I/2\pi$ constrained by eq. (4.26), so we choose different values of $H_I/2\pi$.

We want to demonstrate the corresponding sensitivity to $H_I/2\pi$ by showing that there is not any dependence on H_I for a sufficiently small $H_I/2\pi \simeq 10^{10}$ GeV as shown in Fig. 4.2a. In all respects, the plot is very much the same as the one shown in Fig. 4.1a. In both cases, the dark matter density is dominated by the AQNs, and the allowed region (B, m_a) is not sensitive to the $H_I/2\pi$ as long as the Hubble parameter is sufficiently small. However, when $H_I/2\pi$ becomes close to $f_a \sim 10^{11}$ GeV, the window for c is shifted a little bit (but still largely overlaps with the region $0.4 \lesssim c \lesssim 0.6$) as shown in Fig. 4.2b to accommodate the conventional contribution of the free axions. The main point is that there will always be a region (B, m_a) when the total dark matter density assumes its observational value.

Our next task is to analyze the sensitivity of our results to the QCD parameters related to CS properties of the AQNs. To accomplish this goal we plot the parameter c in Fig. 4.3 as a function of m_a and B using $\epsilon^{(2)}_{\rm tot}$ for model 2, eq. (4.22). The corresponding plot for $(M_q, \mu) = (200, 400)$ MeV is shown in Fig. 4.3a, while the plot for $(160, 500)$ MeV is shown in Fig. 4.3b.

The main conclusion is that the model 2 (which is based on fundamentally different building principles than model 1) with various parameters produces nevertheless quantitatively similar results as model 1 analyzed above and shown in Fig. 4.1a. This conclusion essentially implies that our phenomenological results are not very sensitive to the specifics of the QCD parameterization of the system describing the dense CS phase of matter in a strongly coupled regime. Therefore, we treat our results as the solid consequences of the AQN framework.

As an additional note, the parameter c_Ω as defined by eqs.(4.4) and (4.6), which describes the mass difference between matter and antimatter AQNs (in contrast to parameter c, which describes the baryon charge difference) is numerically very close to parameter c studied above. Specifically, one can show that for model 1 that is represented by eq. (4.20), the parameter $c_\Omega \simeq 1.17c$ is within 15% accuracy for the region $0.4 \lesssim c \lesssim 0.6$ which

dominates the parametrically allowed region as discussed in the preceding paragraphs. Therefore, we do not show the plots for c_Ω as a function of external parameters because they are very similar to the plots for c presented and discussed above.

4.3.3 No fine-tuning problem

As we mentioned in chapter 4.1, the free axions themselves may not saturate the total dark matter. In contrast, the AQN formation always generates a large contribution $\Omega_{\rm DM} \sim \Omega_{\rm visible}$, which always accompanies the conventional production of free axions. This property of the AQN model is demonstrated in Fig. 4.4, where we plot Ω_a/Ω_{DM} as a function of m_a and the combined parameter $\phi \equiv \sqrt{\theta_0^2 + (H_I/(2\pi f_a))^2}$. The function $\phi(\theta_0, H_I)$ enters formula (4.12) for Ω_a and counts together the initial homogeneous displacement contribution and the backreaction contribution to the free axions. Fig. 4.4 explicitly shows that m_a and ϕ have to be highly fine-tuned to make Ω_a saturate $\Omega_{\rm DM}$ exactly, shown as a bright green solid line. In other words, for a specific magnitude of m_a, there is a single value of ϕ when the total dark matter density assumes its observable value. Once these two parameters, m_a and ϕ, slightly deviate from the appropriate values, Ω_a strongly deviates from $\Omega_{\rm DM}$.

This conventional fine-tuning scenario should be contrasted with the results of the AQN framework when Ω_a may contribute very little to $\Omega_{\rm DM}$. Nevertheless, the $\Omega_{\rm DM}$ assumes its observation value as a result of an additional contribution from AQNs which always accompanies the production of free axions and is always at the magnitude of order one, as we have already emphasized. In other words, the AQNs play the role of the "remaining" DM density which, in fact, could be the dominant portion of $\Omega_{\rm DM}$. As we have seen in chapter 4.3.2, for a specific magnitude of m_a, there is a large window of ϕ corresponding to different values of the parameter $c \in (0, 1)$ when the dark matter density assumes its observable value constituted of free axions as well as AQNs. Therefore, the fine-tuning problem does not even occur in the AQN scenario, as the insufficient part on the left from the green solid curve in Fig. 4.4 will be fulfilled by the contribution of AQNs. The white region in Fig. 4.4 is excluded because the requirement $\Omega_a \leq \Omega_{\rm DM}$ is violated.

As the final technical remark, we also notice from Fig. 4.4 that for the most part of the parameter space, we have $\Omega_a \lesssim 0.2\Omega_{\rm DM}$. To make the above

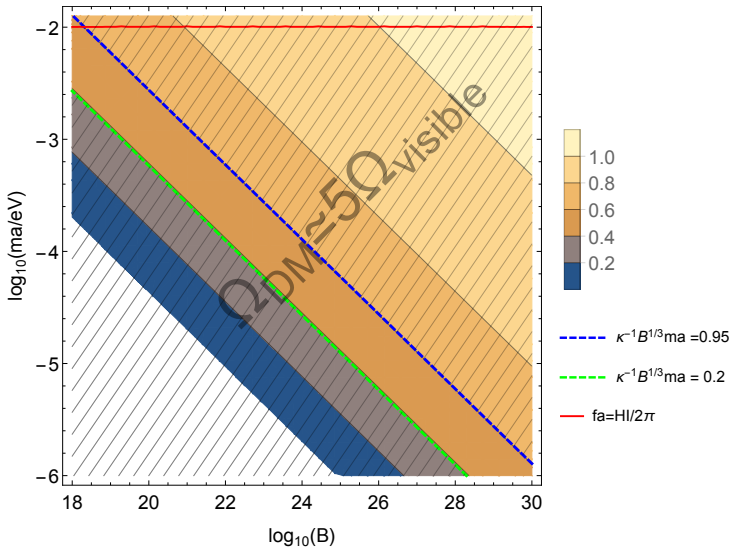

(a) $H_I/2\pi = 5.7 \times 10^8$ GeV, $\theta_0 = 10^{-3}$

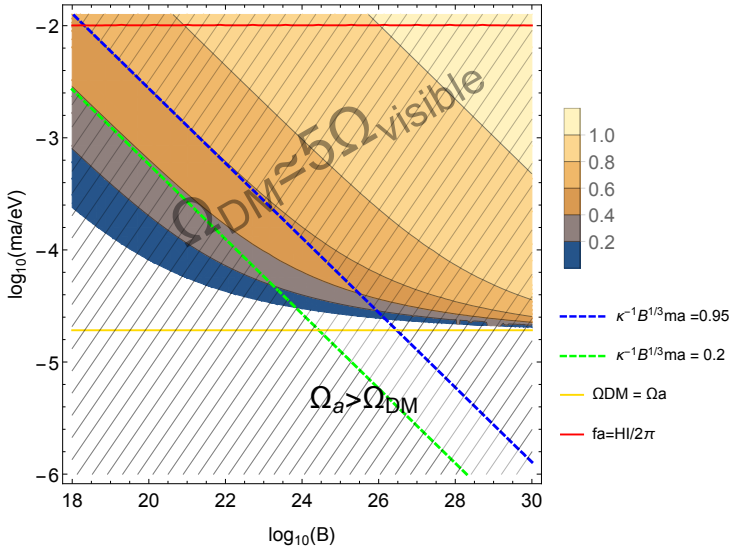

(b) $H_I/2\pi = 5.7 \times 10^8$ GeV, $\theta_0 = 10^0$

Figure 4.1: Contour plots of c as a function of m_a and B for $\theta_0 = 10^{-3}$ and 10^0 respectively with the fixed values $H_I/2\pi = 5.7 \times 10^8$ GeV and $\kappa = 10^{-4}$. The color bar shows values of the parameter $c \sim 1$. This is plotted with dark matter assumed to be saturated by AQNs and free axions and $\Omega_{\rm DM} \simeq 5\Omega_{\rm visible}$ (same for Figs. 4.2 and 4.3). Here, B is for antimatter AQNs (same for other figures in this chapter). This figure is taken from Ref. [2].

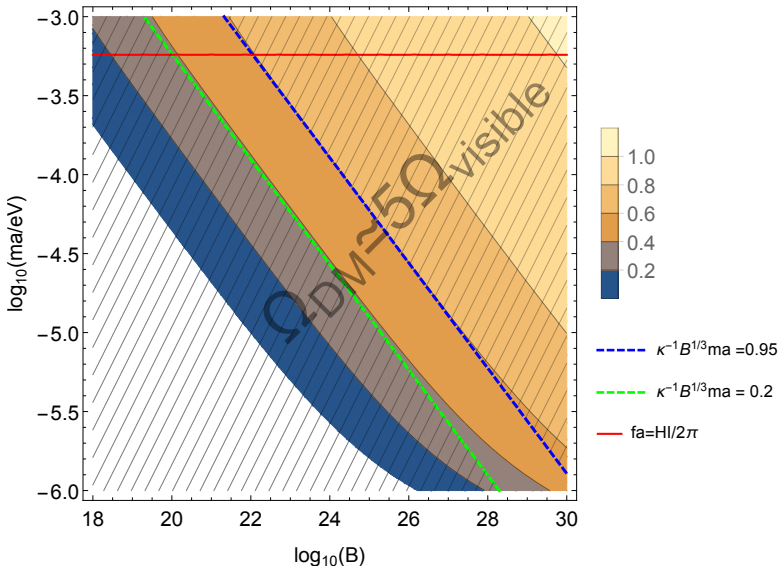

(a) $H_I/2\pi = 10^{10}$ GeV, $\theta_0 = 10^{-1}$

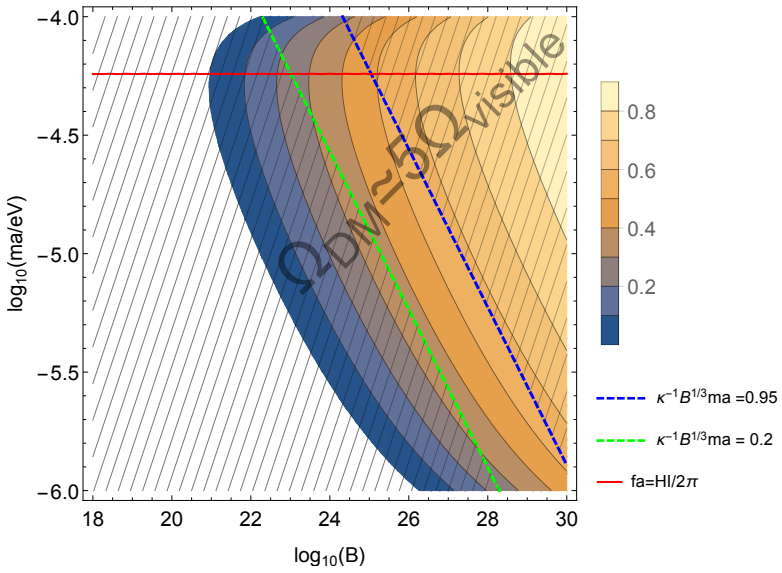

(b) $H_I/2\pi = 10^{11}$ GeV, $\theta_0 = 10^{-1}$

Figure 4.2: Contour plots of c as a function of m_a and B for $H_I/2\pi = 10^{10}$ GeV and 10^{11} GeV respectively with the fixed value $\theta_0 = 10^{-1}$ and $\kappa = 10^{-4}$. The color bar shows values of the parameter $c \sim 1$. This figure is taken from Ref. [2].

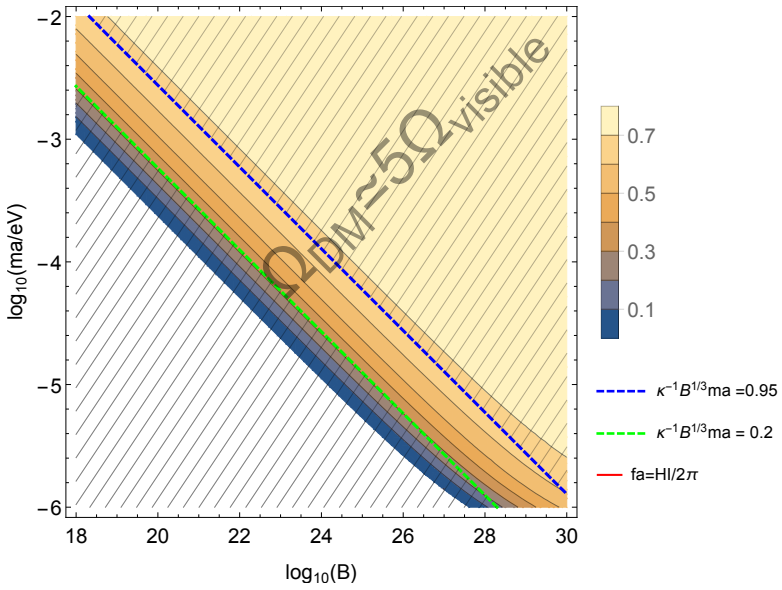

(a) $H_I/2\pi = 5.7\times 10^8$ GeV, $\theta_0 = 10^{-1}$

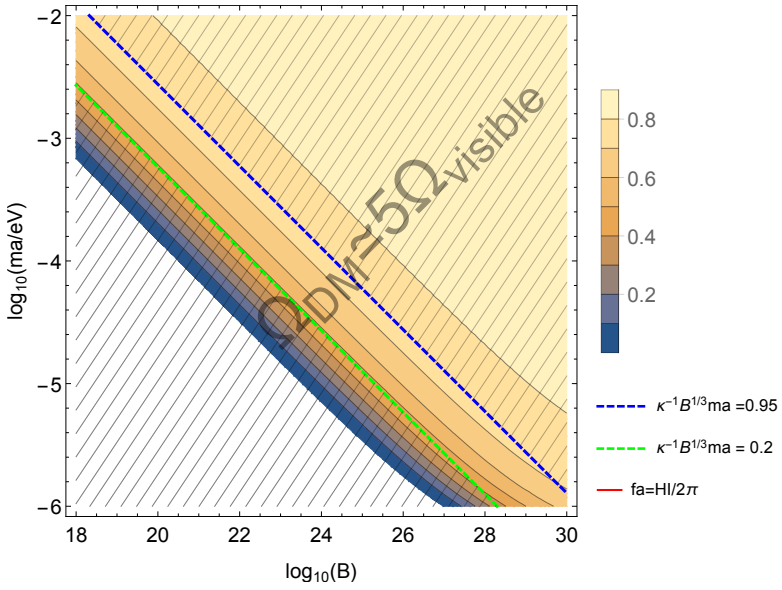

(b) $H_I/2\pi = 5.7\times 10^8$ GeV, $\theta_0 = 10^{-1}$

Figure 4.3: Model 2: contour plots of c as a function of m_a and B for specific values of H_I, θ_0, and $\kappa = 10^{-4}$. (a): $(M_q, \mu) = (200, 400)$ MeV. (b): $(M_q, \mu) = (160, 500)$ MeV. The color bar shows values of the parameter $c \sim 1$. This figure is taken from Ref. [2].

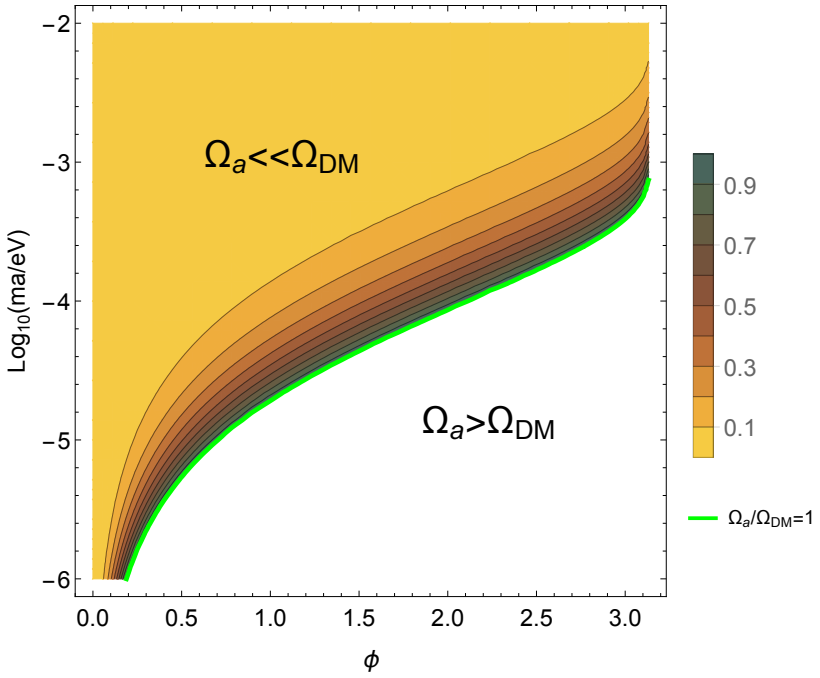

Figure 4.4: Contour plots of $\Omega_a/\Omega_{\rm DM}$ as a function of m_a and ϕ (see the definition of ϕ in the first paragraph of chapter 4.3.3). The color bar shows values of $\Omega_a/\Omega_{\rm DM}$. This figure is taken from Ref. [2].

statement more precise, we plot in Fig. 4.5 the ratio $\Omega_a/\Omega_{\rm DM}$ as a function of c and the parameter $\kappa^{-1}B^{1/3}m_a/m_\pi$ determined by the QCD physics as given by eq. (4.20). The white region in Fig. 4.5 stands for the excluded region of parameters (c, $\kappa^{-1}B^{1/3}m_a$). This plot shows that the parameter c cannot be very close to $\sim$1 for the allowed QCD window $0.2 \lesssim \kappa^{-1}B^{1/3}m_a/m_\pi \lesssim 0.95$. This property, in fact, can be understood analytically from eq. (4.1) or its generalized version eq. (4.11) where $c \to 1$ implies $\Omega_{\rm DM} \gg \Omega_{\rm visible}$, which violates the observable relation $\Omega_{\rm DM} \simeq 5\Omega_{\rm visible}$. The main conclusion drawn from this plot is that the allowed parameter space where Ω_{DM} assumes its observable value is very large and perfectly consistent with the QCD constraints related to parameters c and $\kappa^{-1}B^{1/3}m_a/m_\pi$.

This result is another manifestation of the basic consequence of the AQN framework when the relation $\Omega_{\rm DM} \sim \Omega_{\rm visible}$ is not sensitive to the details of the system but rather represents a direct outcome of this proposal. This fundamental result is essentially incorporated into the initial building principle

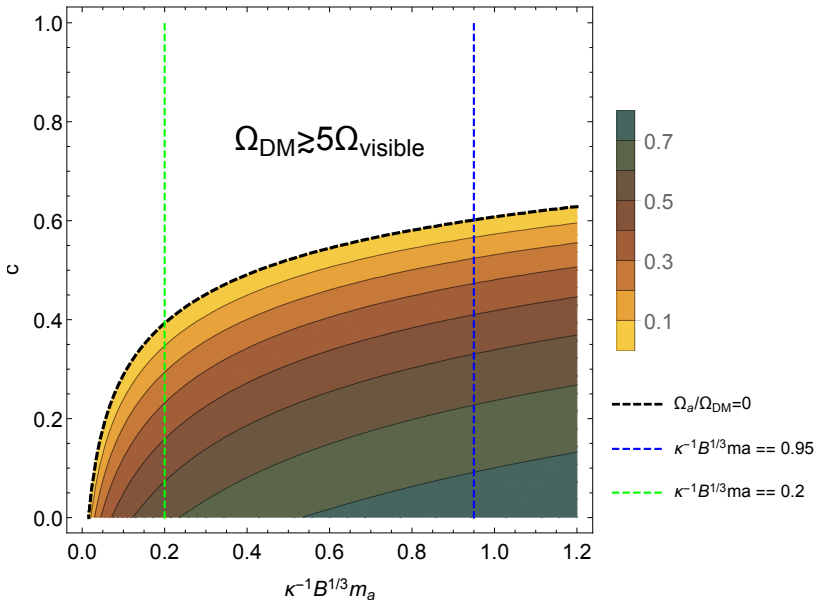

Figure 4.5: Contour plots of $\Omega_a/\Omega_{\rm DM}$ as a function of c and $\kappa^{-1}B^{1/3}m_a$. The color bar shows values of $\Omega_a/\Omega_{\rm DM}$. This figure is taken from Ref. [2].

of the entire framework, and cannot disappear as a result of some additional technical details and modifications.

4.4 Conclusion

In this chapter, we have extracted the key element of the AQN framework, the coefficient c, which describes the disparity between matter and antimatter AQNs, as defined by eq. (4.1) or its generalized version eq. (4.11), from the observational constraints in a quantitative way. Precisely this asymmetry eventually determines the dark matter density (within this framework) we observe today as a result of the charge separation mechanism replacing the conventional baryogenesis scenario as discussed in chapter 2. For most of the parameter space of the axion mass m_a, the initial misalignment angle θ_0, and the inflationary scale H_I (pre-inflationary scenario), the contribution of free axions Ω_a is only a small portion of the observed dark matter density, as the remaining dominant portion of dark matter is contributed by AQNs. Therefore, the fundamental relation (1.2), i.e., $\Omega_{\rm DM} \sim \Omega_{\rm visible}$, is always satisfied in the AQN framework with c roughly in the range $(0.4, 0.6)$. The reason

why $c \equiv B_+/B_-$ is not exactly 2/3 is due to the small contribution of Ω_a to $\Omega_{\rm DM}$ and the corrections to the AQN mass as shown in eq. (4.16) beyond the simple relation $M \sim m_p B$.

We should point out that all AQNs are assumed to have a single mass in this chapter, which greatly simplifies the analysis. Including a size distribution of AQNs may change some numerical factors but will not affect the main conclusion of this chapter. However, the size distribution of AQNs itself is very important, because it is crucial for understanding many AQN-related observational signatures as we have reviewed in chapter 2; see also chapter 6. Moreover, the solar nanoflares are identified as the AQN annihilation events in the Sun. It is thus crucial to theoretically derive the size distribution of AQNs and check if it is consistent with the energy distribution of nanoflares. This is the content of next chapter.

Chapter 5

Size Distribution of AQNs and Survival Pattern

In this chapter, we study the AQN size distribution from the theoretical side.[29] In the AQN framework, solar nanoflares are identified as the AQN annihilation events in the Sun to explain the solar corona heating mystery, as we have reviewed in chapter 2. Based on the simple relation, $W = 2m_p c^2 B$ (W is the nanoflare energy), the AQN size and nanoflare energy should follow the same distribution (i.e., eq. (2.6)):

$$dN \sim W^{-\alpha} dW \sim B^{-\alpha} dB. \tag{5.1}$$

The main motivation of this chapter is to check if the AQN size distribution is consistent with the energy distribution of solar nanoflares. Furthermore, we will discuss the survival pattern of the AQN size distribution during the long evolution after the formation temperature $T \sim 40$ MeV. This chapter is adapted from Ref. [3].

[29] Since the size is connected to mass and baryon charge through the simple relation $M = m_p B = \rho V$ (we neglect the corrections (e.g., the axion domain-wall shell) to AQN mass which are less important compared to the mass of baryon part as we have discussed in chapter 4), the terms "size/mass/baryon charge distributions" have the same physical meaning.

5.1 Size distribution of AQNs

5.1.1 Basic idea

As we have demonstrated in chapter 3.3, the final properties of an AQN, $R_{\rm form}$ and $\mu_{\rm form}$, are determined by the initial conditions R_0 and T_0 via the relations (3.42) and (3.43). The entire volume of an AQN is in chemical equilibrium, i.e., the bulk of the AQN keeps the same chemical potential as the vicinity of the wall. Thus, the total baryon charge carried by a stable AQN can be calculated as

$$B \simeq g^{\rm in} \cdot \frac{4\pi}{3} R_{\rm form}^3 \cdot \int_0^{\mu_{\rm form}} \frac{d^3k}{(2\pi)^3} \simeq \frac{2}{9\pi} g^{\rm in} R_{\rm form}^3 \mu_{\rm form}^3. \tag{5.2}$$

This is calculated in the $T \to 0$ limit, which is justified as the AQN remains almost unchanged after formation, i.e., $R_{\rm form} \simeq R(T=0)$ and $\mu_{\rm form} \simeq \mu(T=0)$. Then, using eq. (3.42), we further have

$$B \simeq K \cdot R_0^3 T_0^3, \qquad K \equiv \frac{\pi^2}{27\sqrt{6}} g^{\rm in} \tag{5.3}$$

where the constant K is introduced for convenience. This relation implies that the final baryon charge B of a stable AQN is completely determined by the initial size R_0 and the initial temperature T_0 of the closed domain wall such that $B \propto (R_0 T_0)^3$.

As we will see later, the initial conditions of closed walls, R_0 and T_0, are not fixed. Instead, they have distributions that follow certain probability densities. Closed walls with different R_0 and T_0 will finally evolve into AQNs carrying different amounts of baryon charge. By mapping the initial distributions of R_0 and T_0 onto B via eq. (5.3), we can get the baryon charge distribution of AQNs, dN/dB. We start with the following equation

$$dN = N_0 \cdot P \cdot f(R_0, T_0) \cdot dR_0 dT_0, \tag{5.4}$$

where dN is the number of closed domain walls with the initial radius in the range $(R_0, R_0 + dR_0)$ and the initial temperature in the range $(T_0, T_0 + dT_0)$; $f(R_0, T_0)$ is a two-parameter distribution function which represents the probability density of a closed domain wall with R_0 and T_0 in the above

ranges. The factor N_0 is the total number of closed walls that form in the early Universe, while P is a normalization factor to make the probability density $f(R_0, T_0)$ normalized to one, i.e.,

$$\iint P \cdot f(R_0, T_0) \cdot dR_0 dT_0 = 1. \tag{5.5}$$

To simplify our analysis we assume that all initial closed walls will eventually become the stable AQNs. We clarify this assumption later in the text when we compare the prediction of our construction with observational constraints. As the next step, we use the eqs. (5.3) and (5.4) to represent the number of stable AQNs with the baryon charge *less* than B as follows:

$$N(B) = \iint_{K \cdot R_0^3 T_0^3 \leq B} N_0 \cdot P \cdot f(R_0, T_0) \cdot dR_0 dT_0, \tag{5.6}$$

where $K \cdot R_0^3 T_0^3 \leq B$ constraints the parameter space of the integration.

From eq. (5.6), we can further calculate the baryon charge distribution, dN/dB, which is the main topic of this section. Obviously, the distribution $f(R_0, T_0)$ which depends on T_0 and R_0 in a very nontrivial way plays a crucial rule in our calculations of the $dN(B)/dB$ distribution. The study of the function $f(R_0, T_0)$ can be approximately separated into two distinct pieces: one part describes the R_0 dependence, while the T_0 distribution can be incorporated separately. These will be studied in detail in the following text.

5.1.2 Initial size distribution

As discussed in chapter 2, in the AQN model, we require the pre-inflationary scenario that the PQ symmetry breaking occurs before inflation. $N_{\rm DW} = 1$ axion domain walls can still form in this scenario with the axion field θ interpolating between $k = 0$ ($\theta = 0$) and $k = 1$ ($\theta = 2\pi$) branches. Although $k = 0$ and $k = 1$ branches correspond to the same unique physical vacuum, they effectively act as two different vacua with the same energy. The domain walls can interpolate between these (physically identical but topologically distinct) vacua, similar to a model with $V(\theta) \sim \cos\theta$ potential, when $\theta = 0$ and $\theta = 2\pi$ correspond to one and the same physical vacuum. Therefore, the $N_{\rm DW} = 1$ axion domain walls in this scenario can be treated as Z_2 domain walls which greatly simplifies the analysis.

The closed Z_2 domain walls have been observed in the simulations of Z_2-wall system [80]. In our case, this means that closed $N_{\rm DW}=1$ axion domain walls can form, and they are the sources of AQNs. Furthermore, this analogy will provide us with more useful information about the initial size distribution of these closed bubbles. The Ref. [80] pointed out that the probability of forming a closed Z_2 domain wall with the initial radius $R_0 \gg \xi$ (where ξ is the correlation length of the topological defects) is exponentially suppressed, $\sim \exp\left(-R_0^2/\xi^2\right)$. The procedure in Ref. [80] to derive this relation is briefly reiterated as follows.

To simulate the Z_2 system in three dimensions, we first divide a big cubic volume into many small cubic cells, each of which has length ξ. Then, to each cell a number $+1$ or -1 is assigned at random with equal probability $p=0.5$. This is the simulation of the phenomenon that different patches (with volume $\sim \xi^3$) of the space during the phase transition will settle randomly with equal probability in one of the two vacua ($\theta=0$ and $\theta=2\pi$ in the case of $N_{\rm DW}=1$ axion domain walls). The domain walls lie on the boundaries between cells of opposite sign. Two neighboring cells are connected if they have the same sign. Many connected cells can form a cluster with the same sign. The size s of a cluster is defined as the number of cells in the cluster. We then can look for the size distribution of $+1$-clusters (Of course, the size of -1-clusters will follow the same distribution). It turns out that this is a typical problem of *percolation theory*, which deals with the statistics of the clusters at different values of p. See Refs. [109, 110] for a review of the percolation theory.[30]

In our case where $p=0.5$ in three dimensions, the size distribution of the finite clusters is known from percolation theory [109]:

$$n_s \propto s^{-\tau} \exp\left(-\lambda s^{2/3}\right), \tag{5.7}$$

where n_s is the number density of finite clusters as a function of the cluster size s (the number of the cells inside a cluster). Although the distribu-

[30] In percolation theory, there is a percolation threshold p_c, at which an infinite cluster first appears on an infinite lattice. $p_c=0.31$ in three dimensions for a cubic lattice. In our case where the probability of a cell picking $+1$ is $p=0.5$, we have one infinite $+1$-cluster ($p>p_c$) and one infinite -1-cluster ($1-p>p_c$). In the language of domain walls, it can be interpreted as the system being dominated by one infinite wall of very complicated topology [80]. In addition to this infinite domain wall, there are some closed domain walls (finite clusters) and they satisfy the size distribution (5.7). The structure and dynamics of the infinite domain wall are less important for our present work which focuses on the closed domain walls.

tion (5.7) is derived for large clusters $s \gg 1$ [109], it turns out that this relation can be extrapolated down to $s = 1$ as a very good approximation [111]. As a consequence, we adopt eq. (5.7) for the whole spectrum $s \geq 1$ for further calculations. The two coefficients τ and λ are p-dependent. According to the Ref. [111], λ has a typical value ~ 10 and τ ranges from 1.5 to 2.2 based on the three dimensional lattice simulations. Discussing the exact values of τ and λ at $p = 0.5$ is beyond the scope of this work. Instead, we simply adopt $\lambda = 10$ and $\tau = 2$ for further calculations.[31] However, as we will see, the shape of the baryon charge distribution $dN(B)/dB$ for AQNs is not sensitive to the precise numerical values of τ and λ.

The result (5.7) can be translated into the language of domain walls straightforwardly: The probability of forming a closed bubble with radius R_0 decreases exponentially when R_0 increases, which can be formally expressed as

$$\frac{dN}{dR_0} \propto \xi^{-1} \left(\frac{R_0}{\xi}\right)^{2-3\tau} \cdot \exp\left[-\lambda \left(\frac{R_0}{\xi}\right)^2\right]. \tag{5.8}$$

To derive this distribution as a function of R_0 from eq. (5.7), we used the relations $s \simeq R_0^3/\xi^3$ and $n_s = 1/V \cdot dN/ds$ (we get rid of the simulation volume V which is a constant in eq. (5.8)). The parameter ξ is the correlation length of topological defects as mentioned above, which is also set as the length of a single cell. The smallest cluster is a cell ($s \geq 1$) implying that the lowest bound of the radius of closed bubbles is $R_0 \gtrsim \xi$. Since the relation (5.7) is applicable for all finite clusters $s \geq 1$ as mentioned above, we adopt eq. (5.8) as the size distribution of all closed bubbles $R_0 \gtrsim \xi$.

It is very instructive to consider an oversimplified case where there is no initial temperature distribution. It can be realized if all the closed bubbles form at the same moment (at the same temperature). In this case the distribution $f(R_0, T_0)$ does not depend on T_0 and, according to eq. (5.8), can be written as $f(R_0) = dN/dR_0 \propto \xi^{-1}(R_0/\xi)^{2-3\tau} \exp[-\lambda(R_0/\xi)^2]$. Using

[31] λ can also be calculated using the relation $\lambda^{-1} \simeq |p - p_c|^{-1/\sigma_p}$ where λ^{-1} is the crossover size (see e.g. Refs. [109, 112, 113]). This relation is valid for $|p - p_c| \ll 1$. The parameter $\sigma_p = 0.45$ in 3D [110]. We then get $\lambda \approx 0.025$ for $|p - p_c| \ll 1$ satisfied. In addition, $\tau = -1/9$ for $p > p_c$ is obtained in a field theoretical formulation of percolation problem [114]. However, the exact values of λ and τ are not important for us, since they do not affect the slope of the distribution $dN(B)/dB$ as we will see in chapter 5.1.4.

eq. (5.3), this R_0 dependence can be translated into dN/dB distribution:

$$\frac{dN}{dB} = \frac{dN}{dR_0}\frac{dR_0}{dB} \propto \frac{1}{B_{\rm min}}\left(\frac{B}{B_{\rm min}}\right)^{-\tau} \exp\left[-\lambda\left(\frac{B}{B_{\rm min}}\right)^{\frac{2}{3}}\right], \tag{5.9}$$

where $B_{\rm min} \equiv K \cdot \xi^3 T_0^3$.[32] In this oversimplified model where there is no T_0 distribution, we find that dN/dB is greatly suppressed by the exponential factor $\sim \exp\left[-\lambda(B/B_{\rm min})^{2/3}\right]$. This essentially implies that the distribution strongly peaks at $B \approx B_{\rm min}$, while larger bubbles are strongly suppressed.

As we will discuss in next part, the T_0 dependence drastically and qualitatively changes this simplified picture. The key element is that the closed bubbles initially form at different temperatures between T_c and $T_{\rm osc}$. The correlation length $\xi \sim m_a^{-1}$, which is inversely proportional to the axion mass m_a, drastically changes during this evolution because of the dramatic changes of the axion mass in this interval.

These profound changes completely modify the basic features of the distribution function $f(R_0, T_0)$, which is the subject of the following subsection. As we shall see below, the baryon charge distribution satisfies a power-law $dN/dB \propto B^{-\alpha}$ when T_0 dependence is properly incorporated, rather than following the exponential behavior eq. (5.9). This power law is consistent with the parameterization eq. (5.1) which has been postulated to fit the observations. Furthermore, the power-law behavior $dN/dB \propto B^{-\alpha}$ is not very sensitive to the parameters of coefficients τ and λ, and therefore, represents a very robust consequence of the framework.

[32] We want to emphasize that although our discussions in this chapter can give the shape of the AQN size distribution, it cannot predict precisely the value of $B_{\rm min}$. This is because there are other uncertainties, especially the uncertainty of the phenomenological parameter κ in chapter 4.2 which was introduced to account for the suppression of closed-wall tension compared to the flat-wall tension, that can strongly affect the final stable AQN size and further the stable B (see eq. (4.20)). But we expect that the effect of κ will shift the sizes of all AQNs proportionally and thus will not affect the shape of AQN size distribution. Instead, the best prediction for the value of $B_{\rm min}$ comes from the observational constraints (especially via matching the energy window of solar nanoflares with the AQN size distribution), which implies $B_{\rm min} \sim 3 \times 10^{24}$; see the discussions in chapter 2.2 and also chapter 6.1 below.

5.1.3 Initial temperature distribution and the correlation length $\xi(T)$

As we discussed in chapter 2, the closed axion domain walls could form anywhere between $T_{\rm osc}$ and T_c where $T_{\rm osc} \sim 1$ GeV is the temperature when the axion mass effectively turns on and $T_c \sim 170$ MeV is the QCD transition temperature. At $T_{\rm osc}$, as the axion mass effectively turns on, the potential term $V_a \sim m_a(T)^2 f_a^2 \cdot (1-\cos\theta)$ comes to play a role of explicitly breaking the PQ symmetry, which leads to the formation of axion domain walls. But the walls are very "shallow" at $T_{\rm osc}$ (recall that the wall tension is $\sigma_a \simeq 8 f_a^2 m_a(T)$) because $m_a(T)$ is small. $m_a(T)$ increases abruptly with time and acquires its asymptotic maximum value around T_c (see e.g., Ref. [79] for the evolution of axion mass), so the walls become much more profound at this temperature. We do not have much information about when the closed walls are stable enough to start their evolution to form AQNs, but without losing generality we can study this by assigning a probability distribution to it. It is hard to calculate this T_0 distribution exactly. It is known, though, that normally the temperature dependence enters implicitly through the correlation length $\xi(T)$ which is highly sensitive to the temperature.

To account for the corresponding modifications, we adopt the conventional assumption that the correlation length is a few times the domain wall width, $\xi(T) \sim m_a^{-1}(T)$. The axion mass is known to be a temperature-dependent function before it reaches its asymptotic value near T_c because it is proportional to the topological susceptibility; see eq. (3.37). At sufficiently high temperature $T \gg T_c$, one can use the instanton liquid model [86, 87] to estimate the power-law $m_a(T) \propto T^{-\beta}$. When the temperature is close to $T \simeq T_c$, one should use the lattice results to account for a proper temperature scaling of the axion mass. See eq. (3.37) for the full expression of $m_a(T)$ where $\beta = 3.925$. We then can approximate the correlation length in the entire interval as

$$\xi(T_0) = \xi_{\rm min} \cdot \left(\frac{T_0}{T_c}\right)^{\beta}, \qquad T_c \lesssim T_0 \lesssim T_{\rm osc} \tag{5.10}$$

where $\xi_{\rm min} \equiv \xi(T_0 = T_c)$ is the minimal correlation length. The same $\xi_{\rm min}$ also serves as the minimal radius that closed bubbles could have because $R \gtrsim \xi$.

In what follows we also assume the following simple model to account for

the temperature variation of the dN/dT_0 distribution:[33]

$$\frac{dN}{dT_0} \propto \frac{1}{T_c}\left[\frac{\xi(T_0)}{\xi(T_c)}\right]^{\delta} \propto \frac{1}{T_c}\left[\frac{T_0}{T_c}\right]^{\beta\delta}, \qquad T_c \lesssim T_0 \lesssim T_{\rm osc} \tag{5.11}$$

where δ is a free parameter adjustable to shape different T_0 distributions. This parameterization has the advantage of producing a simple final expression for the baryon number distribution while still capturing the essentials of the temperature dependence. The constant $1/T_c$ has no special physical meaning but is introduced to balance the units of the right-hand side and the left-hand side of the relation. Perhaps the simplest case is $\delta = 0$, in which case T_0 is a uniformly distributed, i.e., the probability of forming closed walls is uniform between $T_{\rm osc}$ and T_c. One should emphasize that $\delta = 0$ case is still not reduced to the oversimplified example mentioned at the end of the previous subsection. This is because the temperature dependence not only explicitly enters through (5.11), but it also enters implicitly through the temperature dependence of the correlation length $\xi(T)$ in eq. (5.8).

For positive $\delta > 0$, the AQNs tend to form close to the point $T_{\rm osc}$, while for negative $\delta < 0$, AQNs tend to form when the tilt becomes much more pronounced close to the QCD transition temperature T_c. A sufficiently large numerical value of $|\delta| > 1$ with any sign corresponds to a very sharp (almost explosive for $|\delta| \gg 1$) increase of the probability for the axion bubble formation at $T \simeq T_{\rm osc}$ or at $T \simeq T_c$ depending on the sign of δ. On the other hand, $|\delta| \sim 0$ corresponds to a very smooth behavior in the entire temperature interval (5.11). We, of course, do not know any properties of the distribution (5.11) in strongly coupled QCD when $\theta \neq 0$. Therefore, we proceed with our computations with arbitrary δ and make comments on the obtained properties of the baryon distribution dN/dB as a function of the unknown parameter δ in the following chapter 5.1.4.

Combining the T_0 distribution (5.11) with the R_0 distribution (5.8), and substituting eq. (5.10) into eq. (5.8), we arrive at the following two-parameter

[33] One subtlety is that the effect of the expansion of the Universe between $T_{\rm osc}$ and T_c is also included in the model (5.11), since N is defined as the number of closed domain walls rather than the number density.

distribution function,

$$f(R_0,T_0) = \frac{1}{\xi_{\min} T_c}\cdot\left(\frac{T_0}{T_c}\right)^{3\beta(\tau-1)+\beta\delta}\cdot\left(\frac{R_0}{\xi_{\min}}\right)^{2-3\tau} \times \exp\left[-\lambda\left(\frac{R_0}{\xi_{\min}}\right)^{2}\left(\frac{T_c}{T_0}\right)^{2\beta}\right], \qquad T_c \lesssim T_0 \lesssim T_{\rm osc}, \quad R_0 \gtrsim \xi(T_0). \tag{5.12}$$

Notice that here we use "=" rather than "$\propto$". This is because we have an extra factor P in eq. (5.4) which serves as the normalization factor, and the constant multipliers in $f(R_0,T_0)$ can be collected and included in P.

With this expression for $f(R_0,T_0)$ and the basic eq. (5.6), we can now proceed with our calculation of the baryon charge distribution dN/dB. The corresponding results will be discussed in the next subsection.

5.1.4 The dN/dB distribution: results

Substituting eq. (5.12) into eq. (5.6), one can explicitly compute the function $N(B)$ and the distribution dN/dB. In what follows it is convenient to introduce the following dimensionless variables: the baryon charge $b = B/B_{\min}$ of an AQN measured from its minimum value $B_{\min} = K\xi_{\min}^3 T_c^3$; the relative size $r = R_0/\xi_{\min}$ of an AQN measured from its minimum size $\xi_{\min}$; the relative temperature $u = T_0/T_c$ measured in unit of T_c. In terms of these dimensionless variables, the desired distribution dN/dB can be represented as follows

$$\frac{dN}{dB} = \frac{N_0 P}{3B_{\min}}\cdot\left(\frac{1}{b}\right)^{\tau}\cdot\int_1^{b^{\frac{1}{3(\beta+1)}}} du\ \left[u^{3(\beta+1)(\tau-1)+\beta\delta}\mathrm{e}^{-\lambda b^{2/3}u^{-2(\beta+1)}}\right], \tag{5.13}$$

See Appendix A with all technical details.

One can easily estimate the integral (5.13) by observing that it is saturated for very large $b \gg 1$ by $u_{\rm sat}$ of order

$$u_{\rm sat} \sim \left[\lambda b^{2/3}\right]^{\frac{1}{2(\beta+1)}} \sim b^{\frac{1}{3(\beta+1)}}, \qquad b \gg 1 \tag{5.14}$$

when the exponential factor in eq. (5.13) assumes a value of order one. Substituting the expression back into eq. (5.13), one arrives at the following

asymptotic behavior for the distribution:

$$\frac{dN}{dB} \propto B^{-\alpha}, \quad B \gg B_{\rm min}, \tag{5.15}$$

where the final result is expressed in terms of the physical baryon charge B rather than the dimensionless parameter b. The parameter α here is defined precisely in the same way as it was defined in the observational fitting formula (5.1). As we can see from the plots in Appendix A, the power-law distribution is exact as long as B is not very close to $B_{\rm min}$ (within $\sim 1.5 B_{\rm min}$). In other words, the condition $B \gg B_{\rm min}$ is easily satisfied for $B \gtrsim 1.5 B_{\rm min}$.

The exponent α entering (5.15) can be approximated in the limit $B \gg B_{\rm min}$ as follows

$$\alpha \approx 1 - \frac{\beta\delta + 1}{3(\beta + 1)} \sim 1 - \frac{\delta}{3}, \tag{5.16}$$

where in the last step we ignored the factors of order one in comparison with the known (and very large) value of $\beta \simeq 4$ to simplify the qualitative discussions below. The approximate analytical formula (5.15) at very large $B \gg B_{\rm min}$ is in perfect agreement with the numerical analysis presented in Appendix A.

The behavior (5.15) is an amazingly simple and profoundly important result. Indeed, it shows that the exponential suppression is replaced by the algebraic decay (5.15) which is consistent with the observational fitting formula (5.1). The "technical" explanation of why this happens is that the integral (5.13) is saturated by $u_{\rm sat}$ when the exponential factor in eq. (5.13) assumes a value of order one. In terms of the physical parameters, it is related to the fact that exponential suppression (5.12) due to the large size R_0 is effectively removed by a strong temperature dependence with a very large β. Integration over the entire temperature interval eventually leads to the algebraic decay (5.15).

Another important property of eq. (5.15) is that the final result of the slope α is not very sensitive to the parameters λ and τ. Of course, the total normalization factor is very sensitive to these parameters, as discussed in Appendix A. The slope α is also not very sensitive to the well-known parameter $\beta \approx 4$ as long as it is relatively large. α is mostly determined by δ which may have any sign and effectively describes the temperature interval where the bubbles are produced with the highest efficiency. The fitting models (5.1) based on observations can be reproduced with a negative

$\delta < 0$. As we previously mentioned, a negative δ corresponds to a preference for bubble formation close to T_c where the axion potential tilt becomes much more pronounced. Specifically, a model with $\alpha \simeq 2$ corresponds to $\delta \simeq -3$ (strongly peaks at $T \simeq T_c$), while another model with $\alpha \simeq 1.2$ corresponds to a more smooth distribution of dN/dB over the entire temperature interval with $\delta \simeq -1$ which is a mild preference for the bubble formation at $T \simeq T_c$.

The last comment we want to make is about the largest possible size of AQNs. According to percolation theory, there is no upper limit on the size of finite clusters (closed domain walls). However, the shape of large clusters may not be perfectly spherical while our computations are based on the assumption of exact spherical symmetry of the formed bubbles. Furthermore, the radius for non-symmetric bubbles is defined in an average sense for large closed clusters; see e.g., Ref. [110] for more details. The deviation from the ideal spherical shape makes the large collapsing closed domain walls fragment into smaller pieces with high probability, and thus could significantly suppress the possibility of forming large AQNs.[34] The detailed calculation of the suppression effect from the irregular shape for large clusters is hard to carry out and also well beyond the scope of the present work. However, we may introduce a cutoff $B_{\rm cut}$ to roughly account for this extra suppression. Above $B_{\rm cut}$, no AQNs can form from the collapse of closed axion domain walls. This parameter turns out to be useful when we later calculate the total number of AQNs.

We see that it is actually difficult to theoretically calculate the maximum size of AQN. Instead, the best prediction for this maximum value comes from the observational constraints, especially via matching the energy window of solar nanoflares with the AQN size distribution, as we have mentioned in footnote 32 for the case of $B_{\rm min}$. Based on our review of the observational constraints in chapter 2.2 (see also chapter 6.1 below), we have roughly $B_{\rm max} \sim 10^{28}$.

We conclude this section with the following remark. The main result of our analysis is expressed as eq. (5.15) with the slope (5.16). This formula represents the baryon charge distribution of AQNs immediately after the formation period is complete, $T_{\rm form} \approx 40$ MeV, when the baryon-to-photon ratio, eq. (2.2), assumes its present value. This "primordial" distribution of AQNs is subject to modifications from the long evolution in hot cosmic

[34] Ref. [115] presents a similar argument when the author discussed the possibility of domain wall membranes (e.g., closed domain walls) collapsing into black holes.

plasma after $T_{\rm form}$. This problem of the "survival" of the primordial AQNs is the subject of the next section.

5.2 Survival of the primordial distribution

After AQNs have formed at $T_{\rm form} \approx 40$ MeV, the process of "charge separation" is essentially complete. AQNs are surrounded by the cosmic plasma consisting of exclusively protons, neutrons, electrons and positrons. A matter AQN will attract electrons from the plasma.[35] As the consequence, an electrosphere forms as the surface layer of the AQN. Similarly, an antimatter AQN has an electrosphere consisting of positrons rather than electrons. We refer the reader to the original papers [53–58] for the properties of electrosphere and the induced astronomical phenomena. The electrosphere contributes negligibly to the total mass, so the mass distribution of AQNs remains essentially identical to the above primordial distribution, eq. (5.15). Since the cosmic plasma already possesses the required baryon asymmetry, only antimatter AQNs are subject to annihilation from free protons in plasma soon after $T_{\rm form}$, while matter AQNs experience only elastic scattering and thus remain almost unchanged. Thus, AQNs in the following text actually refer to antimatter AQNs for the study of the subsequent evolution.

We divide the subsequent evolution after $T_{\rm form}$ into several stages depending on the densities of electrons, positrons and protons in the cosmic plasma, which will be discussed in the following subsections. In all stages, we expect the scattering rate of protons on an AQN and thus the annihilation rate scale with the cross section of the AQN, so any change of the primordial mass distribution should behave as $\Delta M/M \sim \sigma/M \sim B^{-1/3}$.

5.2.1 Pre-BBN evolution

This stage corresponds to $T > 1$ MeV. The plasma is dominated by electrons and positrons which are as abundant as photons, $n_e \simeq n_{e^+} \simeq n_\gamma \sim T^3$. As long as electrons and positrons are relativistic and this relation holds, all long-range interactions are effectively screened, and we should rigidly take the AQN size as the cross section entering the calculation of collision rate.

[35] This is because an AQN in CS state, say, the most symmetric color-flavor-locking phase, is not charge neutral due to finite volume effects; see Ref. [53] and the references therein.

The collision rate between an AQN and baryons (protons) in the surrounding plasma is

$$\Gamma_{\rm col} = 4\pi R^2 n_b v_b = 4\pi R^2 \frac{2\zeta(3)}{\pi^2}\eta_{b/\gamma}T^3\sqrt{\frac{2T}{m_p}} \tag{5.17}$$

where the baryon number density in plasma, n_b, is approximated as $n_b \sim \eta_{b/\gamma}T^3$ with $\eta_{b/\gamma}$ as the baryon-to-photon ratio. The total number of collisions is saturated by the highest temperature $T_{\rm form} \approx 40$ MeV when the collision rate is largest, and can be estimated as

$$N_{\rm col} \simeq \int_0^{T_{\rm form}} \Gamma_{\rm col} \approx 3\times 10^{25}\left(\frac{T_{\rm form}}{40\ {\rm MeV}}\right)^{1.5}\left(\frac{R}{10^{-5}{\rm cm}}\right)^2 \tag{5.18}$$

$R \sim 10^{-5}$ cm is the typical radius of a formed AQN. While the number of collisions is comparable with the typical total baryon charge $B \sim 10^{25}$ of a baryon charge, only a small portion $\kappa_{\rm ann} \ll 1$ of collisions will result in annihilation, as we argue below.

The first suppression factor of annihilation comes from the sharp boundary between the CS phase inside and the hadronic phase outside, $\kappa_{\rm anni,1} \sim (T/\Lambda_{\rm QCD})^3$, where $\Lambda_{\rm QCD}$ is the typical strength of the sharp boundary "potential" and the temperature T is the typical energy of the incoming three quarks in a proton. This suppression factor is a generic quantum-mechanical feature in the scattering of a particle on a sharp potential. Another suppression factor comes from the strong mismatch between the wave functions of the hadronic quarks and CS antiquarks, $\kappa_{\rm anni,2} \sim 1/N!$ where $N = 3$ for a proton. It also depends on the overlapping features of the wave functions from the two phases. We refer the readers to Appendix C in Ref. [3] for more details. We have $\kappa_{\rm anni}(T) = \kappa_{\rm anni,1}\cdot\kappa_{\rm anni,2} \lesssim 10^{-3}$ for $T = 40$ MeV. This order-or-magnitude analysis of $\kappa_{\rm anni}$ shows that the pre-BBN environment does not change the AQN's primordial distribution eq.(5.15), due to the tiny number of annihilation events, $\kappa_{\rm anni}\cdot N_{\rm col}/B \ll 1$.

5.2.2 Post-BBN evolution

When T drops below 1 MeV, n_e and n_{e^+} in the plasma decreases exponentially. The electrosphere can no longer capture positrons from the plasma sufficiently fast to balance its loss. Instead, the electrosphere starts to capture protons from the plasma for the requirement of screening. This effect

becomes more pronounced as T drops to $T_* \approx 20$ keV when n_e and n_{e^+} become equal to the proton density in the plasma, n_b.[36] In this section, we are going to study how this new feature affects the annihilation of AQNs with protons.

We start with the basic features of the AQN's electrosphere. The number density of positrons, n, in electrosphere distributes as follows [57],[37]

$$n(z) = \frac{T}{2\pi\alpha}\frac{1}{(z+\bar{z})^2}, \qquad \bar{z}^{-1} = \sqrt{2\pi\alpha}\cdot m_e \cdot \left(\frac{T}{m_e}\right)^{1/4} \tag{5.19}$$

where z is the distance from the AQN's quark surface. In $T \neq 0$ environment, the electrosphere will be ionized with the loosely bound positrons stripped off, resulting in a net negative charge [28],[38]

$$Q \simeq 4\pi R^2 \int_{z_1}^{\infty} n(z)dz \sim \frac{4\pi R^2}{2\pi\alpha}\cdot\left(T\sqrt{2m_e T}\right) \tag{5.20}$$

Consequently, protons in plasma will be collected by electrosphere at T_* to screen the charge Q. The proton density distribution in electrosphere, n_p, can be calculated using the same Thomas-Fermi method in Ref. [58] for positrons. We have [35]:

$$n_p(z) = \frac{T}{2\pi\alpha}\frac{1}{(z+\bar{z}_p)^2}, \qquad \bar{z}_p^{-1} = \sqrt{2m_e T} \tag{5.21}$$

which is similar to eq. (5.19) but with a different constant, $\bar{z}_p$, obtained by matching the charge, $Q = \int_0^\infty n_p(z)dz$. The density distributions eq. (5.19) and eq. (5.21) are 1D approximations only valid for $z \ll R$. However, we

[36] AQNs at $T_* \approx 20$ keV has been discussed in Ref. [35] for their effects on BBN nuclei, which can solve the "primordial lithium puzzle".

[37] The structure of electrosphere will also be discussed in chapter 7 but in a totally different context of AQNs impacting and crossing the Earth. The temperature of electrosphere in the context of chapter 7 is much higher, $T \sim 200$-500 keV, so the positron distribution in the electrosphere will be modified by a few factors there. In comparison, the temperature we are discussing here is below 20 keV, so we can use the positron distribution, eq. (5.19) (which was derived in Ref. [57] in the context of $T \sim$ eV) as a good approximation for our purpose here.

[38] We assume that positrons with the energy $p^2/(2m_e) < T$ will be stripped off by the nonzero temperature. The positions of these positrons are mostly at the outer region of the electrosphere, $z \gtrsim z_1 \simeq (2m_e T)^{-1/2}$ [28].

expect the results of Q and further $\bar{z}_p$ will not be significantly altered by 3D corrections, because the main contribution to Q comes from the region $z \ll R$.

At large distances, $r \gtrsim R$, we assume a simple power-law scaling of $n_p(r)$ [35]:

$$n_p(r) = n_0 \left(\frac{R}{r}\right)^p, \qquad n_0 \equiv n_p(z=0) = \frac{T}{2\pi\alpha} \cdot 2m_e T. \tag{5.22}$$

This assumption is consistent with the numerical studies in Ref. [58] with $p \simeq 6$ for positrons. It is also consistent with the conventional $T = 0$ Thomas-Fermi model (see Ref. [35] and references therein). Then, the effective radius of an AQN capturing protons, $R_{\rm cap}$, can be obtained by matching eq. (5.22) with the proton density in plasma, i.e., $n_p(R_{\rm cap}) = n_b$. This gives[39]

$$R_{\rm cap} \sim \left(\frac{n_0}{\eta_{b/\gamma} n_\gamma}\right)^{1/p} R \sim 10^{12/p} \cdot \left(\frac{20\ {\rm keV}}{T}\right)^{\frac{1}{p}} R. \tag{5.23}$$

We see that $R_{\rm cap} \sim 10^2 R$ at $T = T_*$ for the typical value of the exponent, $p = 6$.

To calculate the collision rate in this stage, we replace $4\pi R^2$ in eq. (5.17) with the effective cross section $4\pi R_{\rm cap}^2$. Then, similar to eq. (5.18), we get the total number of collisions:

$$N_{\rm col}(T) \simeq \int_0^{T_*} dT\ \frac{dt}{dT} \Gamma_{\rm col}(T) \sim 10^{24} \left(\frac{T}{20\ {\rm keV}}\right)^{\left(\frac{3}{2}-\frac{2}{p}\right)} \left(\frac{R}{10^{-5}{\rm cm}}\right)^2. \tag{5.24}$$

where we used $p = 6$ in calculating the first factor 10^{24}. While the number of collisions in the $T \lesssim T_*$ regime is slightly smaller than that in the pre-BBN period, eq. (5.18), the annihilation probability of these low-energy protons is much larger. This is because these protons are electromagnetically bounded by the AQN and they spend an extended amount of time near the AQN quark surface. They have a larger opportunity to overlap with the CS quark modes and thus annihilate.

[39] This equation breaks down when $R_{\rm cap}$ is sufficiently large. The power-law scaling is replaced by an exponential scaling due to Debye screening which numerically becomes operational at $\sim 10 R_{\rm cap}$ for $T \sim 20$ keV [35]. The distribution of proton cloud may significantly deviate from the power-law. But for our purpose to simply determine the scale of $R_{\rm cap}$, the simple expression eq. (5.22) should be good enough.

Even if the total 10^{24} collisions all result in annihilation, it is still small compared with the typical baryon charge carried by an AQN, $B \sim 10^{25}$. Thus, we conclude that the majority of AQNs will survive the post-BBN evolution and the primordial baryon charge distribution, eq. (5.15), will not be significantly affected.

A thoughtful reader may put forward the following question: on the one hand, AQNs with $B > 10^{24}$ can survive the pre- and post-BBN evolution in the hot and dense plasma. On the other hand, all AQNs will get completely annihilated when they hit the Sun to account for the "solar corona mystery" [6, 28, 29]. How can these two claims be consistent? The main reason of the drastic enhancement of the annihilation rate in solar corona is that AQNs propagates with supersonic speeds ($v > v_\odot \sqrt{2GM_\odot/R_\odot} \sim 600$ km/s due to the strong gravitational force from a mass $M_\odot$ localized over a relatively small distance $R_\odot$) in the ionized plasma with a very large Mach number, $M_{\rm mach} = v/c_s \simeq 10$, where $c_s \simeq \sqrt{T/m_p}$ is the speed of sound in the solar atmosphere. It is well known that such a body will inevitably generate a shock wave and an accompanying temperature discontinuity with turbulence in the vicinity of the moving body. As a result of this complicated non-equilibrium dynamics, the effective cross section and the subsequent annihilation could be drastically enhanced in the course of the shock-wave propagation as a huge number of ions are captured from the solar plasma due to the long-range Coulomb interaction. We also refer the readers to chapter 6 for more details about the AQN evolution in solar plasma which is drastically different from its evolution in the early Universe discussed here.

5.2.3 Post-recombination evolution

When the temperature drops to the recombination scale, $T \simeq 0.3$ eV. The universe becomes neutral and the AQN cross section no longer receives the boost from electromagnetic effects as eq. (5.23). This implies the collision rate is much lower after recombination and thus the AQN mass distribution remains unchanged. In this stage, the rare annihilation events of AQNs with the surrounding baryons are negligible compared with the dominant CMB radiation. Nevertheless, they will leave some imprints that can be observed today [31], due to the specific features of the spectrum of the AQN annihilation events that the low-energy tail has a spectrum $\sim \nu$ in contrast with the CMB black-body spectrum $\sim \nu^2$ at $\nu \ll T$.

Because AQNs of all sizes can get completely annihilated in the Sun, one may wonder whether the structure formation and star formation epochs will deplete all AQNs. The analysis of AQN evolution in the structure formation epoch is simple, because the typical particle velocity in the gas in this stage is at the same order of magnitude as the speed of sound, $v_b \sim c_s \sim 10^2$ km/s and thus the AQN annihilation does not receive any enhancement from Mach number. Basically, we should use the same formula, eq. (5.17), to compute the collision rate but with a much smaller $n_b \sim 1$ cm^3 and v_b, so we get a much smaller collision rate and the total number of collisions is much smaller compared with $B \sim 10^{25}$. Thus, the structure formation epoch will not change the primordial mass distribution of AQNs.

Next, we analyze the AQN evolution in the star formation epoch which can be divided into two stages: the initial stage of star formation characterized by density ranging from $n_p \sim 10^{15}$ to 1 cm^3 depending on the size of the infall cloud; the final stage when the stars assume their final form as the Sun. We start with the final stage. In this stage, AQNs captured by a star will get completely annihilated, the same as what happens in the Sun. The capture impact parameter, $b_{\rm cap}$, is

$$b_{\rm cap} \simeq R_\star \sqrt{1+\gamma_\star}, \qquad \gamma_\star \equiv \frac{2GM_\star}{R_\star v}. \tag{5.25}$$

where $v \sim 10^{-3}c$ is the typical AQN (dark matter) velocity far away from the star. Then, the rate of a star consuming AQNs can be estimated as

$$\frac{dM_{\rm ann}}{dt} \sim 4\pi b_{\rm cap}^2 v \rho_{\rm DM} \simeq 3 \cdot 10^{30} \left(\frac{v}{10^{-3}c}\right) \frac{m_p}{\rm s}, \tag{5.26}$$

where solar parameters were used and $\rho_{\rm DM}$ is assumed to be saturated by AQNs. Then, the total mass consumed by a star during its lifetime (approximated as the Hubble time, H^{-1}) is

$$M_{\rm ann} \leq \frac{dM_{\rm ann}}{dt} \cdot H^{-1} \sim 10^{48} m_p \sim 10^{21} {\rm kg} \tag{5.27}$$

which is tiny compared with the star mass $M_\star \sim M_\odot \sim 10^{30}$ kg. Given that dark matter is 5 times larger than visible matter in abundance, we conclude that all stars consume only a tiny portion of all AQNs.

For the initial stage of star formation, AQNs experience annihilation

events as they pass through the infall cloud, which can be estimated as

$$N_{\rm col} \sim \pi R^2 n_b L_{\rm infall} \sim 10^9 \cdot \left(\frac{n_b}{1\ {\rm cm}^3}\right) \cdot \left(\frac{L_{\rm infall}}{10^6\ {\rm AU}}\right) \tag{5.28}$$

where AQNs enter the large region $L_{\rm infall} \sim 10^6$ AU where $n_b \sim 1$ cm^3 [116]. Eq. (5.28) is tiny compared with $B \sim 10^{25}$. Even in the case that AQNs enters a small region $L_{\rm infall} \sim 10^{-1}$ AU with much high density $n_b \sim 10^{15}$ cm^3, the total number of collisions is still tiny, $N_{\rm col} \sim 10^{17}$, let alone this is only possible for a small portion of AQNs flux.

We conclude this section that the violent environments of structure formation and star formation after the recombination epoch will not change the primordial mass distribution of AQNs.

5.2.4 Present-day mass distribution

Based on our discussions in previous sections, we conclude that AQN evolution after $T_{\rm form}$ will not change the primordial mass distribution of AQNs. Thus, the present-day mass distribution of AQNs is the same as eq. (5.15), which we rewrite here as

$$\frac{dN}{dB} = N_0 \left(\frac{B_{\rm min}}{B}\right)^{\alpha}. \tag{5.29}$$

As we have discussed in chapter 5.1.4 and Appendix A, the power-law relation is exact as long as B is not very close to $B_{\rm min}$. We assume that dark matter is saturated by AQNs, then the normalization factor N_0 can be fixed by[40]

$$\rho_{\rm DM} = \int_{B_{\rm min}}^{B_{\rm cut}} m_p B \frac{dN}{dB} dB. \tag{5.30}$$

$B_{\rm cut}$ is the upper cutoff of AQN mass, due to the constraint on the largest closed axion walls that can eventually evolve into AQNs as we discussed at the end of chapter 5.1.4. Parameters $B_{\rm min}$, $B_{\rm cut}$ and α are not theoretically well constrained, as we have discussed in chapter 5.1. Indeed, while the theoretical analysis predicts the generic power-law behavior of AQN size distribution, the value for the exponent α is expressed in terms of the un-

[40]Note that the definitions of N and N_0 here are slightly different from that defined in chapter 5.1 where N and N_0 are the total numbers there rather than number densities.

known parameter δ according to eq. (5.11) which itself describes the features of bubble's formation between $T_{\rm osc}$ and T_c.

On the other hand, the observational constraints are less trivial and can be used to constrain the unknown parameters in the AQN size distribution. Analysis of nanoflare energy distribution in Ref. [66] shows that the best fit to data is achieved with the exponent $\alpha \simeq 2.5$ and numerous attempts to reproduce the data fails with $\alpha < 2$. Another option advocated in Ref. [67] show that nanoflare energy distribution consists of two exponents: $\alpha \simeq 1.2$ for low energy, $W \leq 10^{24}$ erg, and $\alpha \simeq 2.5$ for $W \geq 10^{24}$ erg. Based on the simple relation between nanoflare energy and AQN size in the AQN framework, $W = 2m_p c^2 B$, $W = 10^{24}$ erg corresponds to $B \simeq 3 \times 10^{26}$. Models of AQN size distribution with different α will be studied in detail in chapter 6 in the context of numerically simulating their annihilation pattern in the Sun.

From eq. (5.30), the average AQN baryon number can be estimated as

$$\langle B \rangle \approx \frac{\alpha - 1}{\alpha - 2} B_{\rm min}, \qquad \alpha > 2. \tag{5.31}$$

Given that eq. (5.24) suggests a lower bound of survival AQNs, $\sim 10^{24}$, we should require $B_{\rm min} \gtrsim 10^{24}$ if we want AQNs to contribute significantly to dark matter. However, there is a large uncertainty on this lower bound, since eq. (5.24) is the number of collisions rather than the number of annihilation events. Interestingly, independent of the theoretical constraint from eq. (5.24), the observational constraints as reviewed in chapter 2 (see eq. (2.5)) put a similar constraint on $\langle B \rangle$, which indicates $\langle B \rangle \gtrsim 3 \times 10^{24}$. Many nanoflare models in Refs. [66, 67] that satisfy this condition (via the relation $W = 2m_p c^2 B$) can simultaneously saturate the energy budget for explaining the solar corona mystery; see Refs. [6, 28, 29]. We consider this phenomenon a nontrivial self-consistency check of the AQN framework that the allowed window for baryon charge B overlaps the nanoflare energy spectrum fitted to explain the corona heating.

5.3 Conclusion

We conclude this chapter as follows. The theoretical calculations based on percolation theory showed that the size distribution of AQNs has a power-law behavior, eq. (5.15). On the other hand, the energy distribution of nanoflares also follows a power law. The AQN size distribution will not be altered by

the subsequent evolution of AQNs after their formation $T_{\rm form} \sim 40$ MeV, as long as $B_{\rm min} > 10^{24}$ is satisfied. This constraint is consistent with the observational constraint eq. (2.5). Furthermore, the allowed window is compatible with the energy window of nanoflares that has been studied independently in Refs. [66, 67], which should be regarded as one self-consistency check of the AQN model. These arguments strongly support the proposal that the AQN model can explain the solar corona mystery with the annihilation events of AQNs hitting the Sun identified as the nanoflares [6, 28, 29]. The exponent α of the AQN size distribution cannot be predicted theoretically, as it depends on another unknown parameter δ sensitive to the pattern of axion domain wall formation during the QCD epoch. But α can be well constrained by the studies of nanoflares [66, 67]. In the following chapter 6, we are going to study the annihilation pattern of AQNs in the Sun in detail using models with different α, to explore the signals induced by the AQN model.

Chapter 6

Observation I: Impulsive Radio Events in Quiet Solar Corona

The Murchison Widefield Array (MWA) recorded impulsive radio events in the quiet solar corona at frequencies 98, 120, 132, and 160 MHz [9]. In this chapter, we are going to demonstrate that these radio events are the direct manifestation of annihilation events of antimatter AQNs that enter the Sun. As we have reviewed in chapter 2, the solar corona heating problem can be resolved in the AQN framework with the solar nanoflares identified as the AQN annihilation events. We further support this claim by demonstrating that observed impulsive radio events, including their rate of appearance, their temporal and spatial distributions, and their energetics are matching the generic consequences of AQN annihilations in quiet corona. This chapter is adapted from Ref. [4].

6.1 The AQN model: application to the solar corona heating

In this part, we overview the basic characteristics of nanoflares, from the AQN viewpoint. The corresponding results will play a vital role in our studies in chapter 6.2, where we interpret the radio events analyzed by Ref. [9] in terms of the AQN annihilation events [6, 28].

6.1.1 The nanoflares: observations and modeling

We start with a few historical remarks. The solar corona is a very peculiar environment. Starting at an altitude of 1000 km above of the photosphere, the highly ionized iron lines show that the plasma temperature exceeds a few 10^6 K. The total energy radiated away by the corona is of the order of $L_{\rm corona} \sim 10^{27}$ erg s^{-1}, which is about 10^{-6}-10^{-7} of the total energy radiated by the photosphere. Most of this energy is radiated at the extreme ultraviolet (EUV) and soft X-ray wavelengths. There is a very sharp transition region, located in the upper chromosphere, where the temperature suddenly jumps from a few thousand degrees to 10^6 K. This transition layer is relatively thin, 200 km at most. This transition happens uniformly over the Sun, even in the quiet Sun, where the magnetic field is small (~ 1 G), away from active spots and coronal holes. The reason for this uniform heating of the corona is not understood.

A possible solution to the heating problem in the quiet Sun corona was proposed in 1983 by Parker [117], who postulated that a continuous and uniform sequence of miniature flares, which he called "nanoflares", could happen in the corona. This became the conventional view. The term "nanoflare" has been used in a series of papers by Benz and coauthors [118–122], and many others, to advocate the idea that these small "micro-events" might be responsible for the heating of the quiet solar corona. We want to mention a few relatively recent studies [66, 67, 123–128] and reviews [129, 130] which support the basic claim of earlier works, i.e., nanoflares play the dominant role in the heating of the solar corona.

In what follows, we adopt the definition suggested in [122] and refer to nanoflares as "micro-events" in quiet regions of the corona, to be contrasted with "microflares", which are significantly larger in scale and observed in active regions. The term "micro-events" refers to a short enhancement of coronal emission in the energy range of about $(10^{24} - 10^{28})$erg. One should emphasize that the lower limit gives the instrumental threshold for observing quiet regions, while the upper limit refers to the smallest events observable in active regions. The list below shows the most important constraints on nanoflares from the observations of the EUV iron lines with Extreme ultraviolet Imaging Telescope (EIT) on board the Solar and Heliospheric Observatory (SoHO):

1. The EUV emission is highly isotropic [119, 121], therefore the nanoflares have to be distributed very "uniformly in quiet regions", in contrast

with microflares and flares which are much more energetic and occur exclusively in active areas [122]. For instance, flares have a highly non-isotropic spatial distribution because they are associated with the active regions.

2. According to Ref. [120], in order to reproduce the measured EUV excess, the observed range of nanoflares needs to be extrapolated from the observed events interpolating between (3.1×10^{24}-1.3×10^{26}) erg to sub-resolution events with much smaller energies; see item 3 below.

3. In order to reproduce the measured radiation loss, the observed range of nanoflares (having a lower limit at about 3×10^{24} erg due to the instrumental threshold) needs to be extrapolated to energies as low as 10^{22} erg and in some models, even to 10^{20} erg (see Table 1 in Ref. [120]).

4. The nanoflares and microflares appear in a different range of temperature and emission measure (see Fig. 3 in Ref. [122]). While the instrumental limits prohibit observations at intermediate temperatures, nevertheless the authors of Ref. [122] argue that "the occurrence rates of nanoflares and microflares are so different that they cannot originate from the same population". We emphasize this difference to argue that the flares originate at sunspot areas, with locally large magnetic fields $\mathcal{B} \sim (10^2 - 10^3)$ G, while the EUV emission (which is observed even in very quiet regions where $\mathcal{B} \sim 1$ G) is isotropic and covers the entire solar surface

5. Time measurements of many nanoflares demonstrate a Doppler shift with typical velocities of (250-310) km/s (see Fig. 5 in Ref. [118]). The observed line width in OV of ± 140 km/s far exceeds the thermal ion velocity, which is around 11 km/s [118].

6. The temporal evolution of flares and nanoflares also appears different. The typical ratio between the maximum and minimum EUV irradiance during the solar cycle does not exceed a factor of 3 between its maximum in 2000 and its minimum in 2009 (see Fig. 1 from Ref. [131]), while the same ratio for flares and sunspots is much larger, of the order of 10^2. If the magnetic reconnection was fully responsible for both the flares and nanoflares, then the variation during the solar cycles should be similar for these two phenomena. It is not what is observed;

the modest variation of the EUV with the solar cycles in comparison to the flare fluctuations suggests that the EUV radiation does not directly follow the magnetic field activity, and that the EUV fluctuation is a secondary, not a primary effect of the magnetic activity.

The nanoflares are usually characterised by the following distribution:

$$dN \propto W^{-\alpha} dW, \quad 10^{21}\ \text{erg} \lesssim W \lesssim 10^{26}\ \text{erg} \tag{6.1}$$

where dN is the number of nanoflare events per unit time, with energy between W and $W + dW$. In formula (6.1), we display the approximate energy window for W as expressed by items 2 and 3, including the sub-resolution events extrapolated to very low energies. The distribution dN/dW has been modeled via magnetohydrodynamics (MHD) simulations [66, 67] in such a way that the Solar observations match the simulations. The parameter α was fixed to fit observations [66, 67] (see the description of the different models below).

6.1.2 The nanoflares as AQN annihilation events

It has been conjectured in Ref. [28] that the nanoflares can be identified with AQN annihilation events. This conjecture was essentially motivated by the fact that the amount of energy available from the dark matter falling on the Sun per second, in the form of mass (mc^2) , is similar to the amount of energy needed to maintain the corona at its observed temperature ($\sim 10^{27}$ erg s^{-1}). The dark matter density in the solar system is estimated to be of the order of $\rho_{\rm DM} \simeq 0.3\ \text{GeV}\,\text{cm}^{-3}$, within a factor ~ 2. From this identification, it follows that the baryon charge distribution (within the AQN framework) and the nanoflare energy distribution (6.1) must be one and the same function [28]:

$$dN \propto B^{-\alpha} dB \propto W^{-\alpha} dW \tag{6.2}$$

where dN is the number of nanoflare events with energy between W and $W + dW$, which occur as a result of the complete annihilation of the antimatter AQN carrying baryon charge between B and $B + dB$.

An immediate self-consistency check of this conjecture is the observation that the allowed window (2.5) for the AQN's baryon charge largely overlaps with the approximate energy window for nanoflares W expressed by eq. (6.1). This is because the annihilation of a single baryon charge produces an energy

of about $2m_pc^2 \simeq 2$ GeV, which can be expressed in terms of the conventional units as follows,

$$1 \text{ GeV} = 1.6 \times 10^{-10}\text{J} = 1.6 \times 10^{-3}\text{erg}, \tag{6.3}$$

such that the nanoflare energy W for the antimatter AQN with baryon charge B can be approximated as $W \simeq 2 \text{ GeV}\cdot B$. One should emphasize that this is a highly nontrivial self-consistency check of the proposal [28], as the acceptable windows (2.5) and (6.1) for the AQNs and nanoflares have been constrained from drastically different physical systems.

Encouraged by this self-consistency check and the highly nontrivial energetic consideration, Ref. [6] used the power-law index α entering eq. (6.1) to describe the baryon number distribution dN/dB for the antimatter AQNs, which represents the direct consequence[41] of the conjecture (6.2). More specifically, in the Monte Carlo (MC) simulations performed in Ref. [6] , the baryon charge distribution of AQNs, as given by eq. (6.6) , is assumed to directly follow the nanoflare distribution dN/dW , with the same index α as the conjecture (6.2) states.

The nanoflare distribution models proposed in [66, 67] have been adapted by [6]. Three different choices for the power-law index α have been considered in [66, 67]:

$$\alpha = 2.5,\ 2.0,\ \text{or} \begin{cases} 1.2 & W \lesssim 10^{24}\text{erg} \leftrightarrow B \lesssim 3 \times 10^{26} \\ 2.5 & W \gtrsim 10^{24}\text{erg} \leftrightarrow B \gtrsim 3 \times 10^{26} \end{cases}. \tag{6.4}$$

In addition to the power-law index α, different models are also characterized by different choices of B_{min}: 10^{23} and 3×10^{24}. Therefore, a total of 6 different models have been discussed in Refs. [66, 67] which we expressed in terms of the baryon charge B rather than in terms of the nanoflare energy W. There is an up cutoff of B due to the properties of initial closed domain walls, which is hard to calculate theoretically, as we have discussed in chapter 5 (where we used the label B_{cut} there). Here, we fix the maximum B as $B_{\text{max}} = 10^{28}$,

[41] As we have argued in chapter 5, the algebraic scaling (6.2) is a generic feature of the AQN formation mechanism based on percolation theory; see eq. (5.15). The phenomenological parameter α is determined by the properties of the domain wall formation during the QCD transition in the early Universe, but it cannot be theoretically computed in strongly coupled QCD. Instead, it will be constrained based on the observations as discussed in the text.

which is consistent with both eq. (2.5) and eq. (6.1).

In this work, we will only use simulations with $\langle B\rangle \gtrsim 10^{25}$ in order to be consistent with eq. (2.5). This means that we are excluding two models considered in Ref. [66, 67]: the models with $B_{\rm min} \sim 10^{23}$ for $\alpha = 2.5$ and $\alpha = 2$. We also exclude the model with $B_{\rm min} \sim 10^{23}$ for $\alpha = (1.2, 2.5)$ to simplify things as it produces results very similar to another model. The remaining three models are labeled as follows:

$$\begin{aligned}
&\text{Group 1}: \ B_{\rm min} = 3\times 10^{24}, \alpha = 2.5 \\
&\text{Group 2}: \ B_{\rm min} = 3\times 10^{24}, \alpha = 2.0 \\
&\text{Group 3}: \ B_{\rm min} = 3\times 10^{24}, \alpha = \begin{cases} 1.2, & B \lesssim 3\times 10^{26} \\ 2.5, & B \gtrsim 3\times 10^{26} \end{cases}
\end{aligned} \tag{6.5}$$

while $B_{\rm max} = 10^{28}$ for all the models. The average baryon number of the distribution is defined as

$$\langle B\rangle = \int_{B_{\rm min}}^{B_{\rm max}} dB\ [B\ f(B)], \qquad \frac{dN}{dB} \propto f(B) \propto B^{-\alpha} \tag{6.6}$$

where $f(B)$ is normalized and the power-law is taken to hold in the range from $B_{\rm min}$ to $B_{\rm max}$. This has also been discussed in chapter 5.2.4.

The above estimate reveals an astonishing coincidence between the energy/mass windows (2.5) and (6.1) for AQNs and nanoflares respectively. This coincidence is a strong support of our proposal [6, 28] that the nanoflares and the AQN annihilation events are the same phenomena (see items 2 and 3 of chapter 6.1.1).

We are now in a position to present several additional arguments in favor of our proposal: item 1 is also naturally explained in the AQN framework as dark matter is expected to be distributed very uniformly over the Sun, making no distinction between quiet and active regions, in contrast with large flares. A similar argument applies to item 4, as the strength of the magnetic field and its localization is absolutely irrelevant for the nanoflare events in the form of the AQNs, in contrast with the conventional paradigm where nanoflares are thought to be scaled down configurations of their larger cousins, which are much more energetic and occur exclusively in active areas and cannot be uniformly distributed.

The existence of a large Doppler shift, with typical velocities (250-310)

km/s, mentioned in item 5, can be understood within the AQN interpretation as the following: the typical velocities of an antimatter AQN entering the solar corona is very high $v \gtrsim 600$ km/s. The Mach number $M_{\rm mach} = v/c_s$ is thus very large. A shock wave will be formed and will push the surrounding material to velocities which are much higher than would normally be present at thermal equilibrium.

Finally, as stated in item 6, the temporal modulation of the EUV irradiance over a solar cycle is very small and does not exceed a factor ~ 3, as opposed to the much dramatic changes in Solar activity, with modulations on the level of 10^2 over the same time scale. This suggests that the energy injection from the nanoflares is weakly related to solar activity, which is in contradiction with the picture where magnetic reconnection modulated by the Sun activity plays an essential role in the formation and dynamics of nanoflares. This is, however, consistent with our interpretation of nanoflares being associated with AQN annihilation events, as an external cause of the main source of the EUV irradiance.

6.2 Confronting the model with the radio observations

We start this part by describing the basic mechanism of the radio emission due to AQN annihilation events in the solar corona. We estimate the event rate in chapter 6.2.2. The role of non-thermal electrons in the generation of the radio signal events is discussed in chapter 6.2.3. Finally, in chapter 6.2.4 we estimate the intensity of the radio signal events.

6.2.1 Mechanism of the radio emission in solar corona

It is generally accepted that the radio emission from the corona results from the interaction of plasma oscillations (also known as Langmuir waves) with the non-thermal electrons which must be injected into the plasma [132]. An important element for the successful emission of radio waves is that a plasma instability must develop. It occurs when the injected electrons have a non-thermal high energy component, with a momentum distribution function characterized by a positive derivative[42] with respect to the electron velocity.

[42] If the derivative has a negative sign, it will lead to the so-called Landau damping.

In this case, a plasma instability develops and radio waves can be emitted.

The frequency of emission ν is mostly determined by the plasma frequency ω_p in a given environment, i.e.,

$$\omega^2 = \omega_p^2 + k^2 \frac{3T}{m_e}, \quad \omega_p^2 = \frac{4\pi\alpha n_e}{m_e}, \quad \nu = \frac{\omega}{2\pi}, \tag{6.7}$$

where n_e is the electron number density in the corona, while T is the temperature at the same altitude and k is the wavenumber. For example, the frequency $\nu = 160$ MHz considered in [9] will be emitted when $n_e \simeq 3.4 \times 10^8 \text{cm}^{-3}$. One should emphasize that the emission of radio waves generically occurs at an altitude which is distinct from the altitude where the AQN annihilation events occur, and where the energy is injected into the plasma. This is because the mean-free path λ of the non-thermal electrons being injected into the plasma is very long $\lambda \sim 10^4$ km. Therefore, these electrons can travel a very long distance before they transfer their energy to the radio wave, as we will discuss in chapter 6.2.3.

We propose that non-thermal electrons are produced by antimatter AQNs entering the solar corona, when the annihilation processes start. It is known that the number density of the non-thermal (suprathermal in terminology [132]) electrons n_s must be sufficiently large $n_s/n_e \gtrsim 10^{-7}$ for the plasma instability to develop, in which case the radio waves will be generated [132]. As the density n_s/n_e approaches the threshold values at some specific frequencies, the intensity increases sharply, which we identify with the observed impulsive radio events. These threshold conditions may be satisfied randomly in space and time, depending on properties of the injected electrons [132]. All these plasma properties are well beyond the scope of this thesis. However, we shall demonstrate that the number density of the non-thermal electrons n_s generated by AQNs can easily be in proper range $n_s/n_e \gtrsim 10^{-7}$ for the plasma instability to develop. To be more specific, in chapter 6.2.3 we shall argue that the ratio $n_s/n_e \sim 10^{-7}$ is always sufficiently large for the plasma instability to develop, which eventually generate the radio waves.

Therefore, our proposal is that the AQN annihilation events (identified with nanoflares as explained in chapter 6.1.2) produce a large number of non-thermal electrons, which, in turn, generate the observed impulsive radio events [9] as a result of plasma instability. In the following text, we will support our proposal by estimating a number of observables analyzed in Ref. [9] and show that our proposal is consistent with all observed data,

including the frequency of appearance, the intensity of radiation, duration, spatial and wait time distributions.

6.2.2 The event rate

We are now in a position to interpret the radio emission data from Ref. [9] in terms of AQN annihilation events. Antimatter AQNs start to lose their baryon charge, due to the annihilation, in close vicinity of the transition region, at an altitude of 2150 km (see Fig. 5 in Ref. [6] and also Fig. 6.5 below). However, the radio emission happens at much higher altitudes, as we will explain in chapter 6.2.3.

In this part, we want to compare the maximum radio event rate (33481 events observed in the 132 MHz frequency band, during 70 minutes) to the expected rate of AQN annihilation events which are identified with nanoflares, and must be much more numerous (according to conventional solar physics modeling). Specific nanoflare models [66, 67] (expressed by eq. (6.5) in terms of the baryon charge B) correspond to an event rate which is at least a few orders of magnitude higher than the observed radio event rate, see Fig. 8 in Ref. [6]. There is no contradiction here because it is likely that the dominant portion of the nanoflare events are too small to be resolved. This point has been mentioned in items 2 and 3 in chapter 6.1.1 with a comment that all models must include small but frequent events which had been extrapolated to sub-resolution region. Therefore, we interpret the low event rate at radio frequencies as the manifestation that only the strongest and the most energetic, but relatively rare, AQN annihilation events can be resolved in radio bands. We define $\bar{B}$ as the minimum baryonic charge an AQN must have in order to generate a resolved radio impulse.

We can compute (in terms of $\bar{B}$) the event rate for the energetic AQNs which are powerful enough to generate the *resolved* radio impulses as recorded in Ref. [9]. The corresponding impact rate can be computed in the same way as Fig. 8 from Ref. [6], the only difference being that the lower bound is determined by $\bar{B}$ instead of $B_{\min}$,

$$\left(\frac{dN}{dt}\right)_{\bar{B}} \propto \int_{\bar{B}}^{B_{\max}} dB\ f(B). \tag{6.8}$$

Since the maximum number of detected radio events in [9] is 33481 at the

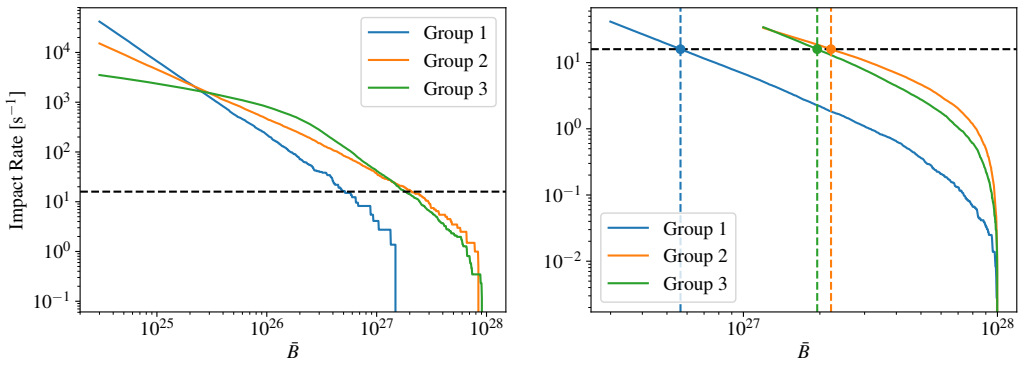

Figure 6.1: Left: the impact rate of AQNs with the size above $\bar{B}$ where $\bar{B}$ varies from $B_{\rm min}$ to $B_{\rm max}$ for different groups of AQNs. The horizontal black dashed line is the observed rate of radio events, eq. (6.9). Right: the result from the second-round simulation where we focus on large AQNs only. Again, the horizontal black dashed line is eq. (6.9). The vertical dashed lines are the corresponding $\bar{B}$ for different groups. More details about the numerical simulations that lead to these two subfigures can be found in Appendix B. This figure is taken from Ref. [4].

132 MHZ band in 70 minutes, the event rate is

$$\frac{dN_{\rm obs.}}{dt} \sim \frac{33481}{70 \text{ minutes} \times 1/2} \sim 16 \text{ s}^{-1}. \tag{6.9}$$

The factor 1/2 accounts for the fact that only half of the Sun's whole surface is visible.

By equalizing eqs. (6.9) and (6.8) we can estimate the parameter $\bar{B}$ when sufficiently large radio events originate from large AQNs with $B \gtrsim \bar{B}$.[43]

The results are presented in Fig. 6.1. It is the intersection of the black dashed line eq. (6.9) and the simulated line of each group given by eq. (6.5). The intersections are shown in the right subfigure, and the corresponding $\bar{B}$ are respectively 5.65×10^{26}, 2.21×10^{27}, and 1.95×10^{27} for the three groups. We expect that only AQNs with masses greater than $\bar{B}$ are sufficiently energetic to generate the observable impulsive radio events.

The parameter $\bar{B}$ obviously depends on the size distribution models listed

[43]This estimate does not include the possibility of "clustering" events with very short time scale discussed in chapter 6.3.2.

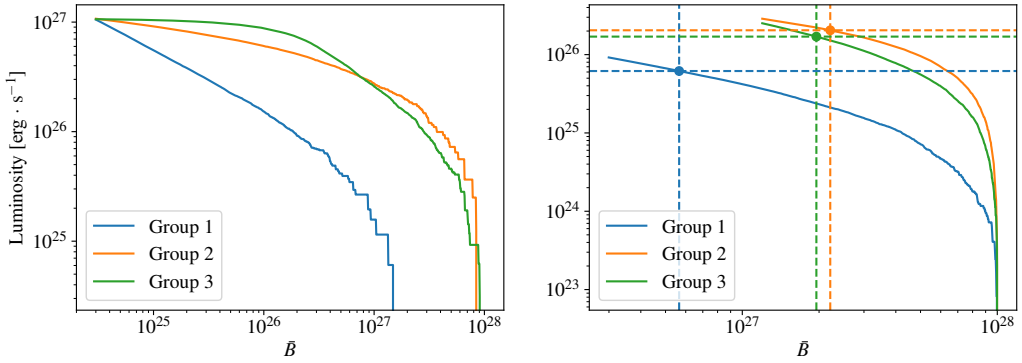

Figure 6.2: Left: the luminosity generated by the annihilation of AQNs with the size above $\bar{B}$ where $\bar{B}$ varies from $B_{\rm min}$ to $B_{\rm max}$ for different groups of AQNs. Right: the result from the second-round simulation where we focus on large AQNs only. The vertical dashed lines correspond to the $\bar{B}$ determined by eq. (6.9) in Fig. 6.1. More details about the numerical simulations that lead to these two subfigures can be found in Appendix B. This figure is taken from Ref. [4].

in eq. (6.5), it corresponds to a detection limit and should not be treated as a fundamental parameter of the theory. An instrument with different resolution and/or sensitivity will affect the radio events selection criteria and therefore change the value of $\bar{B}$, in which case some events from the continuum spectrum would be considered as impulsive events.[44]

Our next task is to estimate the total luminosity $L^{\odot}_{\bar{B}}$ released as a result of the complete annihilation of the large AQNs with $B \gtrsim \bar{B}$. The calculation is similar to the estimation done for Fig. 10 of Ref. [6], with the only difference that the lower bound is determined by $\bar{B}$ rather than $B_{\rm min}$,

$$L^{\odot}_{\bar{B}} \propto \int_{\bar{B}}^{B_{\rm max}} dB\ B^{\frac{2}{3}} f(B). \tag{6.10}$$

The results for the models listed in (6.5) are presented in Fig. 6.2. The corresponding $L^{\odot}_{\bar{B}}$ assume the following values: 6.17×10^{25} erg$\cdot$s^{-1}, $2.05 \times$

[44]It is known that the continuum contribution in the radio emissions is similar in magnitude to the impulses events as we will discuss in chapter 6.2.4. Some of the events from continuum could be treated in future as impulsive events if a better resolution instrument is available. However, this does not drastically modify our estimate for $\bar{B}$.

10^{26} erg $\cdot$ s^{-1} and 1.70×10^{26} erg $\cdot$ s^{-1}, which are approximately an order of magnitude smaller than the luminosity released by all AQNs annihilation. This implies that only about 10% of the total AQN-induced luminosity comes from the large AQNs with $B \gtrsim \bar{B}$, which are the same AQNs assumed to produce the resolved radio events in [9]. Our estimates show that while the strong events with $B \gtrsim \bar{B}$ are very rare with an impact rate approximately 3 orders of magnitude smaller than all AQNs annihilation, their contribution to the luminosity is suppressed only by one order of magnitude. This is, of course, due to the factor $B^{\frac{2}{3}}$ in the expression for the luminosity, eq. (6.10).

The energy flux $\Phi^{\odot}_{\bar{B}}$, observed on Earth, coming from these large AQNs with $B \gtrsim \bar{B}$ is estimated as

$$\Phi^{\odot}_{\bar{B}} \simeq \frac{L^{\odot}_{\bar{B}}}{4\pi (AU)^2} \simeq (1.8 - 6) \cdot 10^{-2} \frac{\text{erg}}{\text{cm}^2 \text{ s}}, \tag{6.11}$$

where we used the range of numerical values for $L^{\odot}_{\bar{B}}$ estimated above. In the following we will establish the physical connection between the energy flux (6.11) generated by large AQNs with $B \gtrsim \bar{B}$ and the flux observed in radio frequency bands observed in Ref. [9]. In order to make this connection, we have to estimate what fraction of the huge amount of energy due to the AQN annihilation is transferred to the tiny portion in the form of radio waves. To compute this efficiency, we need to estimate the relative density of the non-thermal electrons which will be produced as a result of the AQN annihilation. The estimation of this efficiency is the topic of the next subsection.

6.2.3 Non-thermal electrons

The starting point for our analysis is the number of annihilation events per unit length while the AQN propagates through the ionized corona environment:

$$\frac{dN}{dl} \simeq \pi R^2_{\text{eff}} n_p, \tag{6.12}$$

where n_p is the baryon number density of the corona (mostly protons) and the effective radius R_{eff} of the AQNs can be interpreted as the effective size of the AQNs due to the ionization characterized by the AQN's charge Q as explained in Ref. [6]. The enhancement of the interaction range R_{eff} due to

the long range Coulomb force is given by [6]:

$$\left(\frac{R_{\rm eff}}{R}\right)=\epsilon_1\epsilon_2,\qquad \epsilon_1\equiv\sqrt{\frac{8(m_eT_P)R^2}{\pi}},\qquad \epsilon_2\equiv\left(\frac{T_I}{T_P}\right)^{\frac{3}{2}}, \tag{6.13}$$

where T_I is the internal temperature of AQN and T_P is the plasma temperature in the corona. The estimation of the internal thermal temperature T_I is a highly nontrivial and complicated problem which requires an understanding of how the heat, due to the friction and the annihilation events, will be transferred to the surrounding plasma from a body moving with supersonic speed with Mach number $M_{\rm mach}\equiv v/c_s>1$.

It is known that the supersonic motion will generate shock waves and turbulence. It is also known that a shock wave leads to a discontinuity in velocity, density, and temperature due to the large Mach numbers $M_{\rm mach}\gg 1$. It has been argued in Refs. [6, 29] that, for a normal shock, the jump in temperature is given by the Rankine–Hugoniot condition:

$$\frac{T_I}{T_P}\simeq M^2\cdot\frac{2\gamma(\gamma-1)}{(\gamma+1)^2}\gg 1,\qquad \gamma\simeq 5/3, \tag{6.14}$$

and, as a result, all the electrons from the plasma which are on the AQN path within distance $R_{\rm eff}$ will be affected. To be more precise, these electrons will experience elastic scattering by receiving the extra kinetic energy ΔE which lies in the window $\Delta E\in(T_P,T_I)$. It is precisely these non-thermal electrons that will subsequently interact with the plasma and be the source of the plasma instability. These non-thermal electrons will transfer their energy to the emission of radio waves with frequency ν as explained at the end of chapter 6.2.1.

We are now in a position to estimate the parameter $\eta_{\rm energy}$ defined as the ratio between the energy transferred (per unit length l) to the radio waves and the total energy produced by a single AQN (per unit length l) as a result of the annihilation:

$$\eta_{\rm energy}\approx\frac{(\Delta E)\cdot[\pi R_{\rm eff}^2n_e]}{(2m_pc^2)\cdot[\pi R_{\rm eff}^2n_p]}\approx\frac{\Delta E}{2m_pc^2}\sim 10^{-7}, \tag{6.15}$$

where the denominator accounts for the total energy due to the annihilation events with rate (6.12) and the numerator accounts for the kinetic energy received by affected electrons. In our estimate of eq. (6.15), we assume an

approximate local neutrality such that $n_e \approx n_p$. Furthermore, to be on the conservative side, we also assume that $\Delta E \approx 2 \times 10^2$ eV, such that ΔE only slightly exceeds the plasma temperature $\approx T_P$ at high altitudes of order 10^4 km, where radio emission occurs. Finally, we also assume that the dominant portion of the ΔE will be eventually released in the form of radio waves. It is very likely that there are few missing numerical factors of order one on the right-hand side in eq. (6.15) as our assumptions formulated above are only approximations. However, we believe that eq. (6.15) gives a correct order of magnitude estimate for the energy efficiency transfer ratio $\eta_{\rm energy}$. We provide a few numerical estimates in chapter 6.2.4 suggesting that eq. (6.15) is very reasonable and consistent with observed intensities in radio bands [9].

The next step is the estimation of n_s/n_e, which must be sufficiently large $n_s/n_e \gtrsim 10^{-7}$ for the plasma instability to develop [132] (see chapter 6.2.1). As we shall see now, the proposed mechanism indeed satisfies this requirement. We start with the expression of the total number of electrons ΔN_e to be affected while the AQN travels over a distance l:

$$\Delta N_e \sim (\pi R_{\rm eff}^2 l) \cdot n_e(h), \qquad l \simeq v \cdot \Delta t, \tag{6.16}$$

where $n_e(h)$ is the electron number density at the altitude $h \simeq 2000$ km where annihilation events become efficient [6]. These affected electrons will receive extra energy ΔE and extra momentum $m_e v_\perp$ with the very large velocity component $v_\perp$ perpendicular to the AQN path as the shock front due to $M \gg 1$ has a form of a cylinder along the AQN path. A large portion of an AQN trajectory can be viewed as an almost horizontal path with relatively small incident angles toward the Sun (skim trajectories). These non-thermal electrons will have a component $v_\perp$ perpendicular to the AQN path and travel unperturbed up to a distance of the order of the mean-free path $\lambda \sim 10^4$ km (to be estimated below).

After a time Δt, the same non-thermal electrons ΔN_e will have spread over a distance r from the AQN path, estimated as follows:

$$\Delta N_e \sim (2\pi r \Delta r l) \cdot n_s(r), \tag{6.17}$$

where Δr is the width of the shock front measured at distance r. For a non-thermal electron traveling away from the AQN path with perpendicular

velocity $v_\perp$, the distance r is given by:

$$r \sim v_\perp \Delta t, \qquad v_\perp \simeq \sqrt{\frac{2\Delta E}{m_e}} \simeq 10^4 \sqrt{\frac{\Delta E}{2\times 10^2 \text{ eV}}} \frac{\text{km}}{\text{s}}. \tag{6.18}$$

Equalizing eqs. (6.16) and (6.17), we arrive at the following estimate for the ratio n_s/n_e:

$$\left[\frac{n_s(r)}{n_e(h)}\right] \simeq \left(\frac{R^2_{\text{eff}}}{r\Delta r}\right), \qquad r \lesssim \lambda. \tag{6.19}$$

Eq. (6.19) holds as long as $r \lesssim \lambda$. For larger distances $r \gtrsim \lambda$, the non-thermal electrons will eventually thermalize and loose their ability to generate a plasma instability. One should emphasize that $n_s(r)$ entering eq. (6.19) is taken at the distance r from the AQN path, while $n_e(h)$ is taken in the vicinity of the path, i.e., at $r \approx 0$.

We are interested in this ratio when both components are computed at the same location and we now have to check if it is larger than 10^{-7}, the requirement to generate the plasma instability. The relevant configuration for our study corresponds to non-thermal electrons moving upward.[45] In this case the relation (6.19) assumes the form

$$\left[\frac{n_s(r)}{n_e(r)}\right] \simeq \frac{1}{2}\left[\frac{n_e(h)}{n_e(r+h)}\right] \cdot \left(\frac{R^2_{\text{eff}}}{r\Delta r}\right), \quad r \lesssim \lambda, \tag{6.20}$$

where the factor $1/2$ accounts for upward moving electrons and $n_e(r) \equiv n_e(r+h)$ is the electron density computed at distance $\sim r$ above the AQN path ($h \sim 2000$ km).

Eq. (6.20) has a conventional form for a cylindrical geometry with the expected suppression factor r^{-1} at large distances and constant value for Δr. However, it is known that the width of the shock Δr also growths with time[46] as $\Delta r \propto \sqrt{t} \propto \sqrt{r R_{\text{eff}}}$. Therefore, we expect that a proper scaling at

[45] The radio waves emitted at altitudes below h will have much higher frequencies than considered in the present work, and shall not be discussed here.

[46] Such scaling is known to occur, for example, when the meteoroids propagate in Earth's atmosphere where the cylindrical symmetry is also realized. We refer to Ref. [39] (with large list of references on the original literature devoted to this topic) where this scaling specific for the cylindrical geometry has been used in the context of the AQN propagation in Earth's atmosphere.

large r assumes the form:

$$\left[\frac{n_s(r)}{n_e(r)}\right] \sim \frac{1}{2}\left[\frac{n_e(h)}{n_e(r+h)}\right] \cdot \left(\frac{R_{\rm eff}}{r}\right)^{\frac{3}{2}}, \qquad r \lesssim \lambda, \tag{6.21}$$

We will calculate this ratio for large AQNs with $B \gtrsim \bar{B}$ which are capable of generating the resolved radio signals. Using our previous estimates for ϵ_1 and ϵ_2 from Section IV.C of Ref. [6] and using the electron number density in Table 26 of Ref. [8], we arrive at the estimate

$$\left[\frac{n_s(r)}{n_e(r)}\right] \gtrsim 10^{-7} \quad \text{for} \quad r \sim 10^4 \text{ km}. \tag{6.22}$$

The condition (6.22) implies that n_s/n_e is indeed sufficiently large for the plasma instability to develop [132] on distances of order $r \sim 10^4$ km from the AQN path. This implies that the non-thermal electrons can propagate upward to very large distances before they transfer their energy to the radio waves at much higher altitudes, of order $(h+r)$. The scale $r \sim 10^4$ km assumes the same order of magnitude value as the mean-free path λ, which at altitude $h \simeq 10^4$ km can be estimated as follows:

$$\lambda^{-1} \simeq \sigma n_p, \qquad \sigma \simeq \frac{\alpha^2}{(\Delta E)^2}, \qquad \lambda \sim 10^4 \text{ km}, \tag{6.23}$$

where $\Delta E \approx 2 \times 10^2$ eV is the typical kinetic energy of the non-thermal electrons at the moment of emission.

One should emphasize that the estimation given above assumes a constant density n_p along the electron path. This is clearly not the case for the upward-moving non-thermal electrons. One can define an effective mean-free path $\lambda^{-1}_{\rm eff}(h)$ as follows[47]

$$\lambda^{-1}_{\rm eff}(h) \equiv \int_{h_0}^{h} \frac{dh' \sigma n_p(h')}{(h-h_0)}, \qquad h_0 \simeq 2150 \text{km}, \tag{6.24}$$

which accounts for the density variation with altitude. It reduces to the canonical definition (6.23) when n_p is a constant along the electron's path.

[47] We use $h_0 \simeq 2150$ km precisely because AQNs start to annihilate at this altitude (shown in Fig. 6.5) which is the start of the transition region as the density drastically increases (see Table 26 or Fig. 8 of Ref. [8]).

This definition of the effective mean-free path in the context of the present proposal is very convenient as it explicitly shows at what altitude most of the energy will be thermalized, and what portion of the energy can be released in the form of the radio waves.

To be more precise, the portion $f(h)$ of the non-thermal electrons which survive at altitude h can be estimated as follows

$$f(h) = \exp\left(-\int_{h_0}^{h} \frac{dh'}{\lambda_{\text{eff}}(h')}\right), \tag{6.25}$$

where the mean-free path $\lambda_{\text{eff}}(h)$ at altitude h is defined by eq. (6.24). The behavior for $f(h)$ as a function of the altitude h is shown in Fig. 6.3 by the blue line for initial kinetic energy of the non-thermal electrons $\Delta E \approx 2 \times 10^2$ eV. This value for ΔE has been used in all our estimates through the text.

The most important remark here is that the suppression factor $f(h)$ is very modest for altitudes where high frequency waves are emitted, see Fig. 6.4. We emphasize that, in this parameter range, the density of the non-thermal electrons remains sufficiently large to satisfy the crucial condition (6.22) for the plasma instability to develop [132]. Therefore, the dominant portion of the non-thermal electron energy will be released in the form of the radio waves. At the same time, the suppression becomes essential for higher altitudes where low frequency waves are emitted. At higher altitudes the suppression factor $f(h)$ plays the dominant role and non-thermal electrons lose their energy to thermalization. The density of the non-thermal electrons is insufficient to satisfy the crucial condition (6.22) for the plasma instability to develop [132]. At this point, the radio emission stops completely. One should emphasize that such a sharp cutoff for the radio emission at lower frequencies is a very unique and specific prediction of the proposed mechanism.

One should also mention that the density n_p drastically increases at slightly lower altitudes $h \lesssim 2000$ km (in comparison with $h \simeq 2150$ km), such that the mean-free path λ_{eff} decreases correspondingly, and the condition (6.22) breaks down. Therefore, the non-thermal electrons emitted at $h \lesssim 2000$ km cannot propagate to very high altitudes $\sim 10^4$ km where radio emission occurs.

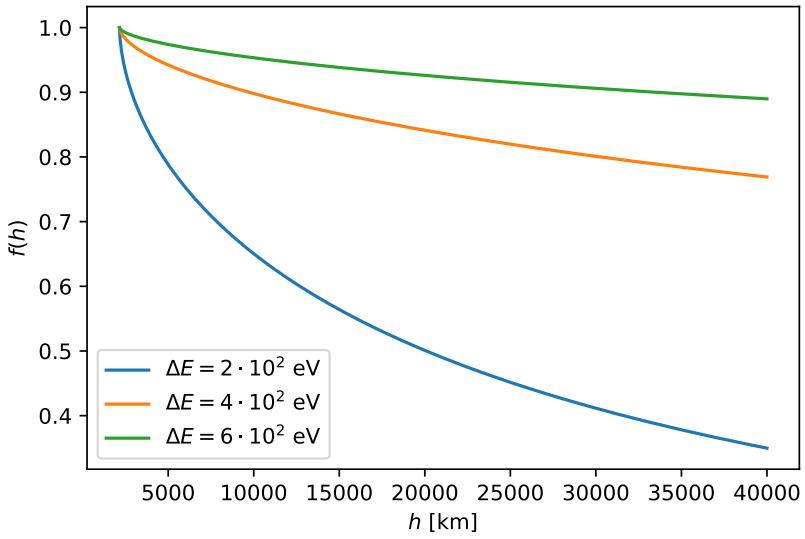

Figure 6.3: Suppression factor $f(h)$ defined by eq. (6.25). This factor describes the remaining portion of the non-thermal electrons at altitude h. The blue line corresponds to the initial kinetic energy $\Delta E \approx 2 \times 10^2$ eV which has been used in all our estimates through the text. For illustrative purposes, we also presented the same suppression factor $f(h)$ for other values of parameter ΔE. Suppression factor becomes essential for $h \gtrsim 4 \times 10^4$ km corresponding to low frequency emission as one can see from Fig. 6.4. In computing eq. (6.25), we have used $n_p(h) \approx n_e(h)$ above h_0 where the profile of $n_e(h)$ is from Ref. [8] (the solar profiles needed in the numerical computations in this chapter are all from [8]). This figure is taken from Ref. [4].

6.2.4 Radio flux intensity

In this part, we estimate the portion of the AQN-induced energy flux which is transferred to the radio waves $\Phi^{\rm radio}$. We express $\Phi^{\rm radio}$ in terms of the energy flux emitted by the AQNs as radio waves:

$$\Phi^{\rm radio} \simeq \Phi^{\odot}_{\bar{B}} \cdot \eta_{\rm energy} \left(\frac{\Delta B}{B}\right) \simeq (0.6{-}6) \times 10^{-10} \frac{\rm erg}{\rm cm^2\ s}, \quad \text{(theoretical prediction)} \tag{6.26}$$

where the first factor $\Phi^{\odot}_{\bar{B}}$, given by eq. (6.11), reflects the contribution of the large AQNs with $B \gtrsim \bar{B}$ to the total AQN-induced luminosity. The fac-

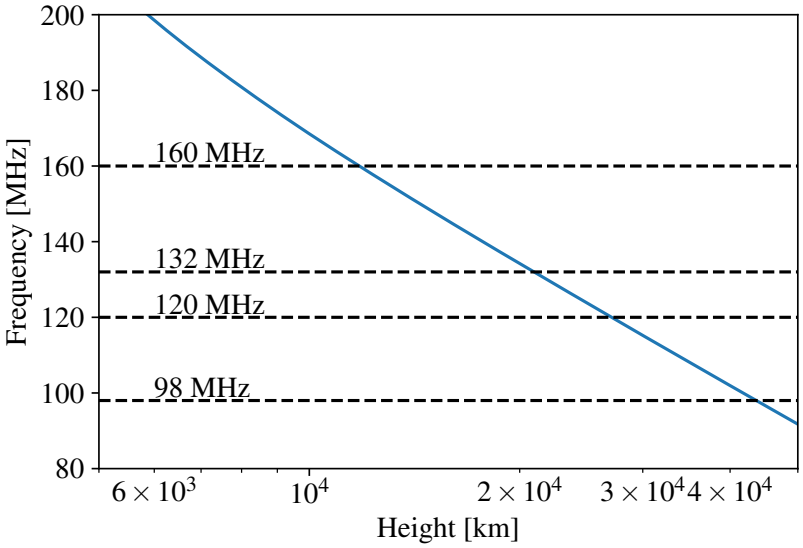

Figure 6.4: Frequency of the emission, $\nu = \omega/2\pi \approx \omega_p/2\pi$ (i.e., eq. (6.7)) as a function of height. Radio emission occurs at the altitudes above 10^4 km while the dominant portion of the AQN annihilation events occur at lower altitudes $h < 2150$ km as shown in Fig. 6.5. This figure is taken from Ref. [4].

tor η_{energy} is given by eq. (6.15) and represents the portion of the energy transferred to the radio frequency bands through the non-thermal electrons leading to the plasma instability. Finally, the factor $\Delta B/B \sim (0.3\text{-}1) \times 10^{-1}$ describes a typical portion of the baryon charge annihilated in the altitude range (2000-2150) km. This is precisely the region where the AQN annihilation events effectively start and where the interactions of AQNs with the surrounding plasma produce the non-thermal electrons which eventually generate the radio waves. The Monte-Carlo simulations for $\Delta B/B$ are presented in Fig. 6.5. One can see that the dominant portion of the annihilation events occur at the lower altitudes $h \lesssim 2000$ km. However, the mean-free path λ at lower altitudes of the affected electrons is too short as our estimations (6.23) suggest. Therefore, the affected electrons from altitudes $h \lesssim 2000$ km cannot reach higher altitudes where the radio waves are generated. This is precisely the source of the suppression expressed in the ratio $\Delta B/B \ll 1$.

We can now compare our estimate (6.26) to the observed intensities mea-

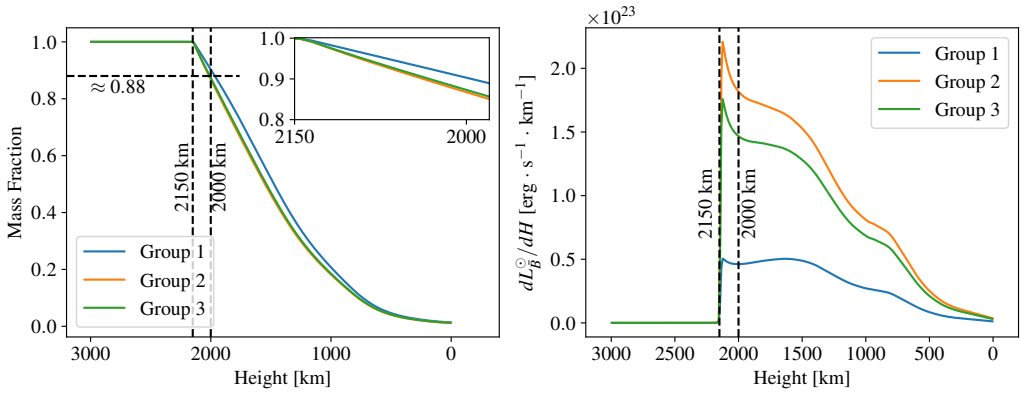

Figure 6.5: Left: mass fraction $1-\Delta B/B$ being annihilated as a function of the altitude. This is plotted by taking the average of the mass loss profiles of the AQNs above $\bar{B}$ (i.e., the AQNs that will generate radio emissions) where $\bar{B}$ has been determined by eq. (6.9). We see that AQNs start to annihilate at about 2150 km. Right: luminosity per unit length as a function of the altitude where the energy is converted from the mass loss according to eq. (6.3). This is also plotted by taking the average of the AQNs above $\bar{B}$, then multiplied by the impact rate of these large AQNs. This figure is taken from Ref. [4].

sured in radio frequency bands by Ref. [9]:

$$\begin{aligned} \frac{d\Phi^{\text{radio}}}{d\omega}(160\text{ MHz}) &\simeq 6\text{ SFU}, \quad \Delta\omega = 2.56\text{ MHz} \\ \frac{d\Phi^{\text{radio}}}{d\omega}(120\text{ MHz}) &\simeq 3\text{ SFU}, \quad \Delta\omega = 2.56\text{ MHz} \end{aligned} \tag{6.27}$$

where

$$\text{SFU} \equiv 10^4\text{Jy} = 10^{-19}\frac{\text{erg}}{\text{Hz cm}^2\text{ s}}. \tag{6.28}$$

The observations [9] were done in twelve frequency bands from 80 MHz to 240 MHz with $\Delta\omega = 2.56$ MHz bandwidth each. It is known [133, 134] that the radio emission occurs in the entire energy band $\sim$ (0-200) MHz, and not specifically in one of the 12 frequency narrow bands. It is also known [133, 134] that the contributions from continuum and impulsive fluxes are approximately the same in all frequency bands. Therefore we estimate the total intensity in radio bands by multiplying eq. (6.27) with ~ 200 MHz to

account for the entire radio emission associated with short impulsive events as well as the continuum:

$$\Phi_{\rm total}^{\rm radio} \simeq (0.6-1.2)\times 10^{-10}\frac{\rm erg}{\rm cm^2\ s}, \quad \text{(observation)}. \tag{6.29}$$

Despite the fact that our calculation involves various steps and approximations, the total measured flux, eq. (6.29), is consistent with our order-of-magnitude estimate, eq. (6.26). We consider this as a highly non-trivial consistency check for our proposal as it includes a number of very different elements which were studied previously for a completely different purpose in a different context.

We conclude this section with few important remarks. The occurrence probability shown in Fig. 4 in Ref. [9] suggests that the power-law index α is always large, with $\alpha > 2$. As explained in chapter 5, we cannot predict this index theoretically, but all the nanoflare models used in our studies as expressed by eq. (6.5) are consistent with the observed power-law index α because the AQNs generating the resolved radio impulses must be sufficiently large with $B > \bar{B}$, in which case the index α is always large (index $\alpha = 1.2$ for one of the models from eq. (6.5) describes the distribution of small AQNs with $B < \bar{B}$ which do not produce the resolved radio signals).

The basic picture for the radio emission advocated here is that one and the same AQN may generate the emissions in different frequency bands because the non-thermal electrons produced by the AQN and moving in an upward direction can emit the radio waves at different altitudes with different plasma frequencies as long as non-thermal electron density is sufficiently high and satisfies the condition, eq. (6.22). As an illustration, we show the frequency of emission, eq. (6.7), as a function of height on Fig. 6.4. In this example, all the radio emissions must be correlated within time over seconds, which is considerably shorter than the typical mass-loss timescale which is about 10-20 seconds, see Figs. 5 and 6 in Ref. [6].

This generic picture also suggests that the emission at higher frequencies ν must be more intense due to a number of reasons. First, the upward moving non-thermal electrons are much more numerous at lower altitude (corresponding to higher ν) in comparison with higher altitudes (corresponding to lower ν) because n_s/n_e ratio scales as $r^{-3/2}$. When this scaling reaches a ratio below the required rate (6.22), the radio wave emission cannot occur as the density of the non-thermal electrons is not sufficient for the plasma instability to develop [132]. Furthermore, the effective mean-free path determined

by eq. (6.24) essentially determines the highest altitudes where non-thermal electrons may reach; see Fig. 6.3. After this height the non-thermal electrons will thermalize and cannot be the source of the radio waves.

Second, according to eq. (6.26), the lower the altitude, the higher the annihilation rate. This is because the portion of the annihilated baryon charge $\Delta B/B$ drastically increases when altitude decreases; see Fig. 6.5. When the frequency of the radio emission becomes too high, the radiation becomes a subject of absorption too strong to be detectable above the quiet Sun background. Such suppression with higher frequency radiation has indeed been observed for frequencies $\nu \gtrsim 240$ MHz; see Ref. [134].

The same line of arguments may also explain the observed huge difference between the number of observed events (4748) at the smallest frequency band (98 MHz) in comparison to the rate at larger frequency bands where the recorded number of events is almost one order of magnitude higher [9]. These arguments suggest that counting rate at even lower frequencies (such as 80 and 89 MHz bands recorded by MWA) should be even lower than 4748 events recorded at 98 MHz [9].

6.3 Wait time distribution

The goal here is to understand the wait time distribution reported by Ref. [9]. The main observation was that the impulsive events are non-Poissonian in nature. This non-Poissonian feature is shown in Fig. 7 of Ref. [9] where the occurrence probability at small wait times (below 10 seconds) is linearly growing instead of approaching a constant, which is what is expected for a Poissonian distribution.

We shall argue below that, in the AQN model, such behavior could be explained by the presence of "effective" clustering of events when one and the same AQN in flight may generate a cascade of seemingly independent events in short time scales. These events, however, are not truly independent, as they result, in fact, from one and the same AQN when the typical mass loss time is measured in 10-20 seconds; see Fig. 6 in Ref. [6]. Few short radio pulses on scales of few seconds could be easily generated during this long flight time. Such "clustering" will violate the assumption of the Poissonian distribution of independent events.

In what follows we develop an approach which can incorporate such "clustering" at small time scales, while the distribution remains Poissonian at

larger time scales, i.e., the time scale of distinct AQNs entering the Corona. The corresponding approach is known as a non-stationary Poissonian process which results in Bayesian statistics.

6.3.1 Overview of the non-Poissonian processes

We start with an overview of the non-Poissonian processes and outline the conventional technique to describe them, as given in [135–137]. In the case of a conventional random stationary Poissonian process, the waiting time distribution $P(\Delta t)$ is expressed as an exponential distribution:

$$P(\Delta t) = \lambda e^{-\lambda \Delta t}, \qquad \int P(\Delta t) d\Delta t = 1, \tag{6.30}$$

where λ in this section (chapter 6.3) is the mean event occurrence rate. For a constant λ, this distribution describes a stationary Poissonian process. When $\lambda(t)$ depends on time, one can generalize eq. (6.30) and introduce the probability function of waiting times which becomes itself a function of time [135]:

$$P(t, \Delta t) = \lambda(t + \Delta t) \exp\left[- \int_t^{t+\Delta t} \lambda(t') dt' \right]. \tag{6.31}$$

If observations of a non-stationary Poisson process are made during a time interval $[0, T]$, then the distribution of waiting times $P(\Delta t)$ will be, weighted by the number of events $\lambda(t)dt$ in each time interval $(t, t + dt)$, given by:

$$P(\Delta t) = \frac{1}{N} \int_0^T \lambda(t) P(t, \Delta t) dt, \quad N = \int_0^T \lambda(t) dt. \tag{6.32}$$

If λ varies adiabatically, one can subdivide non-stationary Poisson processes into piecewise stationary Poisson processes (Bayesian blocks), take the continuum limit, and represent the distribution of waiting times as follows [135–137]:

$$P(\Delta t) = \frac{\int_0^T \lambda^2(t) e^{-[\lambda(t)\Delta t]} dt}{\int_0^T \lambda(t) dt}. \tag{6.33}$$

One can check that eq. (6.33) reduces to its original Poissonian expression, eq. (6.30), when λ is time independent. It is convenient to introduce $f(\lambda)$

which describes the adiabatic changes of λ as follows:

$$f(\lambda) \equiv \frac{1}{T}\frac{dt(\lambda)}{d\lambda}, \qquad f(\lambda)d\lambda = \frac{dt}{T}, \qquad \int d\lambda f(\lambda) = 1. \tag{6.34}$$

In terms of $f(\lambda)$, eq. (6.33) assumes the form

$$P(\Delta t) = \frac{\int_0^\infty \lambda^2 f(\lambda) e^{-[\lambda \Delta t]} d\lambda}{\int_0^\infty \lambda f(\lambda) d\lambda}. \tag{6.35}$$

The stationary Poissonian distribution corresponds to $f(\lambda) = \delta(\lambda - \lambda_0)$ such that eq. (6.35) reduces to the original expression, eq. (6.30), with constant λ_0 as it should.

6.3.2 Clustering events

We are now in a position to describe the physics of "effective" clustering events using non-stationary Poisson distribution framework, eq. (6.35), as outlined above. As previously mentioned several, short radio pulses on scales of few seconds could be easily generated during a single AQN "relatively" long flight time of the order of 10-20 seconds (see Fig. 6 in Ref. [6]).

With this picture in mind, we introduce the following $\lambda(t)$ dependence to describe non-stationary Poisson processes. At long time scales $t > t_0$, we keep the constant λ_0 corresponding to the stationary Poisson distribution:

$$\lambda = \lambda_0, \qquad f(\lambda) \sim \delta(\lambda - \lambda_0) \quad \text{for} \quad t > t_0, \tag{6.36}$$

while for shorter time scales $t < t_0$, we parameterize $f(\lambda)$ as follows:

$$f(\lambda) = c\lambda^\beta, \qquad \lambda = \lambda_0 \left[\frac{t}{t_0}\right]^{\frac{1}{\beta+1}} \quad \text{for} \quad t < t_0, \tag{6.37}$$

where the parameters β, λ_0 and t_0 should be fitted to match the observational signal distribution. The parameterization for non-stationary Poisson processes (6.37) is a generic power law behavior which satisfies the condition $\lambda(t \to 0) \to 0$ when $t \to 0$. It has been used previously [135–137] for many different systems, including the solar flares.[48] In comparison with pre-

[48] In particular, a more general expression for $f(\lambda) = c\lambda^\beta \exp(-\gamma\lambda)$ was considered which also includes the exponential tail $\exp(-\gamma\lambda)$ [137]. We do not include this exponential factor

vious studies, we consider the superposition of two terms, eqs. (6.36) and (6.37), which allows us to quantitatively characterize (by taking an appropriate limit) the level of non-stationary Poisson processes and the extent of deviation from the stationary Poisson distribution. As we shall argue below, the non-stationary Poisson processes play the dominant role in our studies, which is the main claim of the present section.

We start by explaining the physical meaning of the parameters entering eqs. (6.36) and (6.37). As we discuss below, t_0 will enter the observables in the form of the dimensionless parameter (t_0/T). The physical meaning of this parameter is clear: it determines the time-portion of the clustering events. In case when $(t_0/T) \ll 1$ the clustering events play a very minor role, while for $(t_0/T) \sim 1$ the clustering events become essential. In the limit $t_0/T \to 0$, the physical mean value $\langle\lambda\rangle$ approaches its unperturbed magnitude λ_0 corresponding to the stationary Poisson distribution. However, in case when $(t_0/T) \sim 1$ (which will be the case as we discuss below), the dimensionless parameter $(\langle\lambda\rangle/\lambda_0)$ must be smaller than one as it accounts for non-stationary Poisson processes. The parameter $(\langle\lambda\rangle/\lambda_0) \to 1$ approaches identity if non-stationary Poisson processes play the minor role. The deviation of this parameter from $(\langle\lambda\rangle/\lambda_0) \neq 1$ is a precise quantitative characteristic of the non-stationary Poisson processes in the dynamics of the system.

From the basic features of the AQN model one should expect (t_0/T) to be large, of order one. This is because a single AQN event could produce a number of radio emission events which should correspond to the clustering events, since they are not independent. Furthermore, we also expect that $(\langle\lambda\rangle/\lambda_0)$ strongly deviates from the identity, which represents a quantitative characteristic of a contribution due to the clustering events as the Poissonian distribution is characterized by a single parameter λ_0 with $\langle\lambda\rangle = \lambda_0$.

With this preliminary remarks on physical meaning of the parameters we can now proceed with computations with the main goal to analyze the role of non-stationary Poisson processes in the radio wave emission as a result of the AQN annihilation events. One can combine eqs. (6.36) and (6.37) to represent $f(\lambda)$ as follows:

$$f(\lambda) = \left[\left(\frac{T-t_0}{T}\right)\delta(\lambda-\lambda_0)\right] + \left[\frac{\beta+1}{\lambda_0}\frac{t_0}{T}\left(\frac{\lambda}{\lambda_0}\right)^{\beta}\theta(\lambda_0-\lambda)\right], \qquad (6.38)$$

as it simply shifts the definition for $\Delta t \to (\Delta t + \gamma)$ as one can see from eq. (6.35).

where factor $(T-t_0)/T$ is inserted in front of the delta function $\delta(\lambda-\lambda_0)$ to preserve the normalization, Ref. (6.34). One should emphasize that λ_0 is not the mean event occurrence rate $\langle\lambda\rangle$ anymore. Instead, the proper value for $\langle\lambda\rangle$ reads:

$$\langle\lambda\rangle \equiv \int \lambda f(\lambda) d\lambda = \lambda_0 \left[1 - \frac{1}{\beta+2}\left(\frac{t_0}{T}\right)\right]. \tag{6.39}$$

Now we are in a position to compute $P(\Delta t)$ as defined by (6.35):

$$P(\Delta t) = \frac{1}{\langle\lambda\rangle}\int_0^\infty \lambda^2 f(\lambda) e^{-[\lambda\Delta t]} d\lambda, \tag{6.40}$$

with $f(\lambda)$ as given by eq. (6.38). The result can be represented as follows:

$$P(\Delta t) = \frac{\lambda_0^2}{\langle\lambda\rangle} e^{-[\lambda_0\Delta t]} \cdot \left(\frac{T-t_0}{T}\right) + \frac{(\beta+1)\lambda_0^2}{\langle\lambda\rangle} \cdot \left(\frac{t_0}{T}\right) \left[\int_0^{\lambda_0} \frac{d\lambda}{\lambda_0} \left(\frac{\lambda}{\lambda_0}\right)^{\beta+2} e^{-[\lambda\Delta t]}\right], \tag{6.41}$$

where the first term describes the stationary Poisson distribution while the second term describes the deviation from Poisson distribution at small time scales. The second term in distribution (6.41) can be expressed in terms of the lower incomplete $\gamma(s,x)$ function defined as follows:

$$\gamma(s,x) \equiv \int_0^x u^{s-1} e^{-u} du, \quad \gamma(s,x) = \Gamma(s) - \Gamma(s,x), \tag{6.42}$$

where $\Gamma(s)$ is the gamma function and $\Gamma(s,x)$ is the upper incomplete gamma function. We identify the parameters from the integrand entering eq. (6.41) as follows:

$$u = \lambda\Delta t, \qquad x \equiv \lambda_0\Delta t, \qquad s = \beta+3 \tag{6.43}$$

to arrive at the following expression for $P(\Delta t)$ in terms of the lower incomplete $\gamma(s,x)$ function:

$$P(\Delta t) = \frac{\lambda_0^2}{\langle\lambda\rangle} e^{-[\lambda_0\Delta t]} \cdot \left(\frac{T-t_0}{T}\right) + \frac{\lambda_0^2(\beta+1)}{\langle\lambda\rangle} \cdot \left(\frac{t_0}{T}\right) \cdot \left(\frac{1}{\lambda_0\Delta t}\right)^{\beta+3} \cdot \gamma\left[\beta+3, \lambda_0\Delta t\right]. \tag{6.44}$$

This expression is correct for any value of t_0/T. However, it is very instructive to see explicit dependence on Δt when $t_0/T \ll 1$ is small, and the Poisson distribution is restored.

With this purpose in mind, we simplify eq. (6.44) by expanding the in-

complete gamma function, which can be simplified as follows:

$$P(\Delta t) \approx \frac{\lambda_0^2}{\langle\lambda\rangle} e^{-[\lambda_0 \Delta t]} \left(\frac{T-t_0}{T}\right) + \frac{\lambda_0^2(\beta+1)\Gamma(\beta+3)}{\langle\lambda\rangle} \cdot \left(\frac{t_0}{T}\right) \cdot \left(\frac{1}{\lambda_0 \Delta t}\right)^{\beta+3}, \tag{6.45}$$

where we use the identity (6.42) and ignored the exponentially small contribution coming from incomplete upper gamma function:

$$\Gamma(s, x \to \infty) \to x^{s-1} \exp(-x). \tag{6.46}$$

In the limit $(t_0/T) \to 0$, we recover the conventional Poisson distribution, while $(t_0/T) \neq 0$ describes the deviation from Poisson statistics in this simplified setting.

We are now ready to analyze the non-Poisson distribution given by eq. (6.45). The important point here is that this distribution is a superposition of two parts: the first term describes the Poisson distribution with small correction in normalization. The most important part for us is the second term which is parametrically small at $(t_0/T) \ll 1$. However, it could become the dominant part of the distribution $P(\Delta t)$ at small $\Delta t \to 0$ due to a high power $(\Delta t)^{-(\beta+3)}$ in the denominator (6.45).

It is interesting to note that Ref. [9] noticed that their data can be fitted as a superposition of two terms which have precisely the form of two terms entering eq. (6.45). However, Ref. [9] fitted the observed signal to an expression that represents the product of two terms rather than in the form of sum of two terms entering eq. (6.45) with a well-defined physical meaning of the relevant parameters such as (t_0/T). Next, we fit that data from Ref. [9] using exact eq. (6.41) and simplified eq. (6.45) for $P(\Delta t)$. Our main conclusion of this fit is that the clustering events play the dominant role in the distribution $P(\Delta t)$.

6.3.3 Wait time distribution: theory confronts the observations

The occurrence probability is presented in Fig. 7 in Ref. [9]. First, we have to comment that the occurrence probability plotted in Fig. 7 in Ref. [9] is different from the wait time distribution $P(\Delta t)$ defined here. It is convenient to explain the difference using the description in terms of the discrete bins $[\Delta t_i, \Delta t_{i+1}]$. In these terms, Fig. 7 of Ref. [9] is a histogram, where the

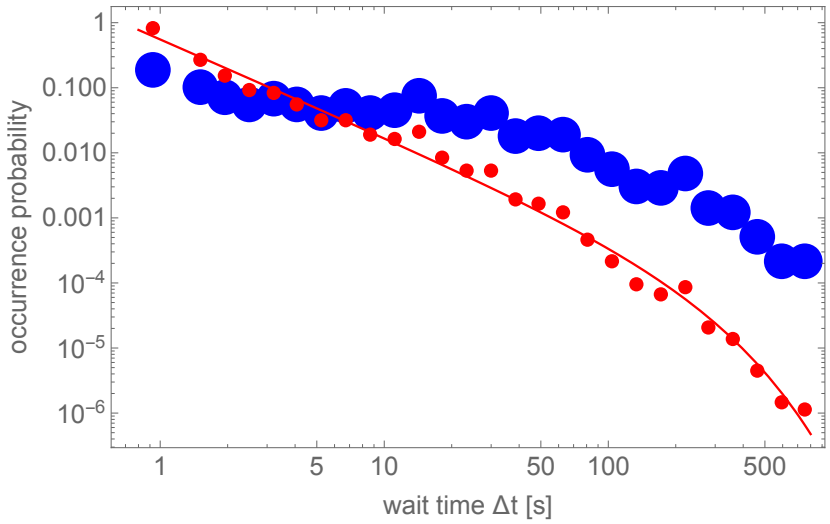

Figure 6.6: The blue points are extracted from Fig. 7 in Ref. [9] (132 MHz). Dividing the blue points by the corresponding bin width, we get the red points (i.e., the values of $P(\Delta t_i)$ in eq. (6.47)). The red line is fitted by eq. (6.48) with $A = 0.56 s^{-1}, n \simeq 1.5, \lambda \simeq 0.0049 s^{-1}$. This figure is taken from Ref. [4].

blue points represent the values of n_i/N where n_i is the number of events with wait-time located in the bin $[\Delta t_i, \Delta t_{i+1}]$ and N is the total number of events. However, by definition, the wait time distribution $P(\Delta t_i)$ is obtained by dividing n_i/N by the bin width $[\Delta t_{i+1} - \Delta t_i]$ for proper normalization of $P(\Delta t_i)$. Indeed,

$$\begin{aligned} P(\Delta t_i) &\equiv \frac{n_i}{N} \frac{1}{[\Delta t_{i+1} - \Delta t_i]}, \\ \sum_i P(\Delta t_i)[\Delta t_{i+1} - \Delta t_i] &= \sum_i \frac{n_i}{N} = 1. \end{aligned} \tag{6.47}$$

As noticed by Ref. [9], the data can be nicely fitted using the following function

$$P(\Delta t) = A(\Delta t)^{-n} \exp(-\lambda \Delta t), \tag{6.48}$$

where the continuum limit is already assumed. We confirm that the good match can indeed be achieved, and the corresponding fit is shown by the red line in Fig. 6.6.

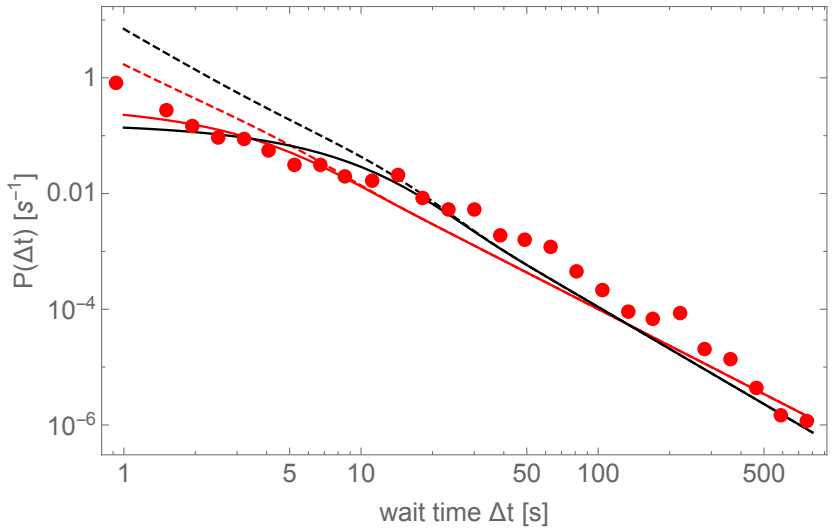

Figure 6.7: The red points are the same as those in Fig. 6.6 (i.e., the values of $P(\Delta t_i)$ in eq. (6.47)). The solid lines are fitted by the full expression of $P(\Delta t)$ given by eq. (6.41). The solid red line gives $\beta = -0.9$, $t_0 = 4000$ s, $\lambda_0 = 0.5$ s^{-1}. Other choices around this group of parameters can also give similar result. For example, the solid black line corresponds to $\beta = -0.6$, $t_0 = 3000$ s, $\lambda_0 = 0.2$ s^{-1}. In comparison, the dashed lines are the simplified $P(\Delta t)$ given by eq. (6.45), with the same group of parameters chosen correspondingly. This figure is taken from Ref. [4].

We are now ready to interpret the results obtained above in terms of the two dimensionless parameters (t_0/T) and $(\langle\lambda\rangle/\lambda_0)$ introduced in eq. (6.37) as the generic way to parameterize non-stationary Poisson processes. First of all, the acceptable fit shown in Fig. 6.7 always produces the relatively large value for (t_0/T). Indeed, the first solution corresponds to $(t_0/T) \simeq 0.95$, while the second solution assumes the value $(t_0/T) \simeq 0.71$. We remind that this parameter (t_0/T) describes the portion of time when clustering events occur. In case of stationary Poisson processes, $(t_0/T) = 0$. Fit in both cases suggests that non-stationary Poisson processes occur for most of the time, which unambiguously implies that non-stationary Poisson processes play the dominant role in radio wave emission. This is consistent with the proposed AQN mechanism when the non-stationary Poisson distribution is expected and anticipated.

Another quantitative characteristic which describes the deviation from

conventional Poisson distribution is the dimensionless parameter $(\langle\lambda\rangle/\lambda_0)$. The acceptable fit shown in Fig. 6.7 always produces a strong deviation of the parameter $(\langle\lambda\rangle/\lambda_0)$ from identity. Indeed, $(\langle\lambda\rangle/\lambda_0) \approx 0.14$ for the first solution while $(\langle\lambda\rangle/\lambda_0) \approx 0.5$ for the second solution. This represents another strong evidence supporting our claim that non-stationary Poisson processes play the dominant role in radio wave emission.

One should note that the quantitative estimates of the parameters from the first principles within the AQN framework are hard to carry out. We could only anticipate a large deviation from conventional Poisson distribution as explained above, while any quantitative estimates of these parameters are not feasible at the moment. The problem is that the radio emission by non-thermal electrons is a random process, which strongly depends on surrounding plasma features. Furthermore, the emission spectrum of the non-thermal electrons also represents a challenging theoretical problem, as emission occurs in the system which is moving with a very large Mach number when the turbulence, shock waves and other non-equilibrium processes dominate the dynamics of the non-thermal electron emission.

Our first quantitative prediction is that the parameters (t_0/T) and $(\langle\lambda\rangle/\lambda_0)$ must be very similar for different frequency bands. Our second quantitative prediction, is that the emission between radio events observed at different frequencies must be correlated with time delays measured in seconds. This correlation is very specific to the AQN mechanism.

It is interesting to note that the data from Ref. [9] can be nicely fitted using the function (6.48), which exhibits structures similar to our formula (6.45). The important difference here is that our formula was derived with well-defined parameters (t_0/T) and $(\langle\lambda\rangle/\lambda_0)$, which quantitatively characterize the non-stationary Poisson processes, while the extraction of A, λ, n from the fitting (6.48) represented on Fig. 6.6 does not allow to arrive at any quantitative conclusion.

As clustering events play a major role, one may wonder if our estimate of $\bar{B}$ in chapter 6.2.2 may be modified as a result of these events. We think that the corresponding variation is numerically mild, and does not modify the picture advocated in this work.[49] Therefore, we ignore the corresponding

[49]Indeed, even if each AQN event generates a cluster consisting on average, let us say, three radio events, it would change the event rate (6.9) by the same factor three. We note, that a much larger number of events within the same cluster would be inconsistent with total energy estimate eq. (6.26) which agrees with observations eq. (6.29). The scaling parameter $\alpha \simeq 2.5$ defined by eq. (6.5) implies that the corresponding variation in $\bar{B}$ does

modifications in $\bar{B}$ in the present study.

We have discussed at length that the presence of clustering events is a generic feature of the mechanism for impulsive radio events. We interpret the fit shown in Fig. 6.7 of the data from Ref. [9] with our expression eq. (6.41) as an additional strong support for our proposal when radio emissions always accompany nanoflare events.

One should emphasize that nanoflares are introduced as generic events, producing an impulsive energy release at small scale (see the review papers Refs. [129, 130]). The fact that nanoflares are the consequence of AQN annihilation events accompanied by the clustering of radio events is a highly nontrivial consistency check of the entire framework . Such clustering events supported by data in Ref. [9] are clearly related to a non-Poissonian character of distribution, and the AQN model provides a natural solution for this feature.

6.4 Conclusion

We demonstrated that AQN annihilation events in the Sun could be accompanied by radio events. This proposal is consistent with the observations reported by Ref. [9], including the frequency of appearance, the temporal and spatial distributions, their intensity, and other related observables. There are several direct consequences of this proposal which future observations will be able to support or refute:

1. The proposed mechanism suggests that a considerable portion of radio events recorded at different frequencies, might be emitted by a single AQN continuously generating radio signals, as a result of different plasma frequencies at different altitudes. This picture suggests that there must be a spatial correlation between radio events in a given local patch (within size 10 km), in different frequency bands. Observations of correlated clustering events as discussed in chapter 6.3.2 and chapter 6.3.3, are the direct manifestation of correlations observed in the same frequency band. We advocate the idea that similar spatial correlations, from different frequency bands, can also exist. There can also be similar temporal correlations; see item 4 below.

not exceed a factor $\sqrt[2.5]{3} \approx 1.5$. These changes are much smaller than the difference in $\bar{B}$ between distinct acceptable models (6.5) , as one can see from Fig. 6.1.

2. Lower frequencies waves could be emitted from higher altitudes. The intensity of emission depends on the altitude highly non-trivially. First, the upward-moving non-thermal electrons are much more numerous at lower altitude (corresponding to higher ν) because n_s/n_e scales as $r^{-3/2}$. The radio emission cannot occur when the ratio becomes below the required rate (6.22). Second, the mean-free path defines the highest altitudes the non-thermal electrons may reach. Above this altitude, the non-thermal electrons will thermalize and cannot be a source of radio waves. As a result of these suppression factors, we expect that the low frequency emissions should be in general suppressed. Of course, the radio emission is related to random processes, highly sensitive to some specific local features of the plasma and non-thermal electrons, as discussed in chapter 6.2.1. Therefore, our prediction of suppression is subject to possible fluctuations within small frequency bands.

   This tendency has been indeed observed for the 98 MHz band, where the recorded number of resolved events is at least one order of magnitude smaller than for the three other higher frequencies bands. We predict that the emission rate at 80 MHz and 89 MHz, which have been recorded, but are not yet published by Ref. [9], should be even lower (even in comparison with 98 MHz emission).

3. In contrast with the low frequency bands, the event rate for higher frequency bands should be higher than the rate recorded for the 160 MHz band. This prediction can be directly tested in future analysis by studying emissions with $\nu \gtrsim 160$ MHz, since some of their observations were done in the 179, 196, 217 and 240 MHz bands [9]. One should comment here that at higher frequencies ($\nu \gtrsim 240$ MHz), radio emission is subject to a strong absorption, and that the observed intensity will experience suppression [134], limiting our perspectives to study higher frequency emissions.

4. The proposed AQN mechanism of radio emission predicts the presence of correlations between the emissions in different frequency bands. These correlations emerge due to the upward motion of the non-thermal electrons, with typical velocities $v_\perp \simeq 10^4$km/s according to eq. (6.18). The delay in arrival time at different heights is measured in seconds, when the height varies at the scale of 10^4 km, according to Fig. 6.4. As a result of upward motion, the low frequency emissions should be

delayed in comparison to the high frequency emissions.

5. Solar Orbiter recently observed so-called "campfires" in the extreme UV frequency bands. It is tempting to identify such events with the annihilation of large AQNs, as they are capable of generating radio signals sufficiently strong to be resolved. We therefore suggest to search for a cross-correlation between MWA radio signals and recordings of the extreme UV photons by Solar Orbiter.

Chapter 7

Observation II: X-ray Annual Modulation Observed by XMM-Newton

The XMM-Newton observatory show evidence with an 11σ confidence level for seasonal variation of the X-ray background in the near-Earth environment in the 2-6 keV energy range [10]. The observed seasonal variation suggests that the signal could have a dark matter origin, since it is very difficult to explain with conventional astrophysical sources. In this chapter, we are going to show that the observed seasonal variation can be explained by the AQN model. This chapter is adapted from Ref. [5].

7.1 Motivation

The main motivation of this chapter is to explore the seasonal variation of the near-Earth X-ray background found in the XMM-Newton data by Ref. [10]. A seasonal variation with a confidence level of 11σ was detected in the 2-6 keV energy range (see Fig. 7.1 which is adapted from Ref. [10]). The authors argue that conventional astrophysical sources have been ruled out, so they propose an explanation based on the assumption that keV axions are emitted by the Sun and convert to X-rays in the Earth's magnetosphere. These X-rays would be subsequently elastically scattered, on average, through a right angle to reach the telescope. This interpretation should be contrasted with the original idea proposed by Ref. [138–140] which views the axion-emitting

solar core through the solid Earth with an X-ray telescope. The original idea by Ref. [138] does not work as an explanation of the effect found by Ref. [10] because the XMM-Newton's operations exclude pointing at the Sun and at the Earth directly. Some of the major criticism of the Ref. [10] interpretation include the following (see Ref. [141]): a) Due to conservation of momentum, in conventional cases, the X-ray photons generated in the magnetic field should be collinear with the parent axions. Therefore, since XMM-Newton never directly points towards the Sun, it should not see any solar axions; b) Only in the case of a highly inhomogeneous component of the magnetic field with a fluctuation in the keV scale would the photons be non-collinear with the parent axions. Such a fast fluctuating component is very unlikely to be a dominant portion of a geomagnetic field. Even if non-collinear effects are generated in the geomagnetic field and we assume that the photon flux converted from axions would be totally isotropic, the geometric factor $\xi = \Omega_{\rm XMM}/4\pi$ (where $\Omega_{\rm XMM}$ is the aperture of XMM-Newton) is very small, $\xi \simeq 10^{-5}$. This is in strong disagreement with the requirement of $\xi \simeq 1$ for the interpretation of the observed seasonal variation as proposed by Ref. [10]. Other issues with this interpretation were also discussed in Ref. [141].

Although the explanation given by Ref. [10] turns out to be untenable, the phenomenon of a seasonally varying X-ray background around the Earth detected with an 11σ confidence level remains a mystery (see Fig. 7.1). The seasonal variation pattern is clearly related to the Earth's revolution around the Sun, which strongly indicates that dark matter galactic wind could play a central role. The motivation of this chapter is to interpret the seasonally varying X-ray background as a natural result of the annually modulating dark matter wind[50] in the context of the AQN framework. In our framework, the AQNs emit X-rays isotropically and can propagate in any direction. The radiated X-rays are automatically subject to seasonal variation, since the AQNs are the dominant contributor to dark matter. Our proposal is therefore

[50]There are subtle points here related to XMM-Newton's position and its view angle as it orbits the Earth. This complication does not allow an immediate interpretation of the data in terms of the conventional annual modulation, which is normally attributed to dark matter wind with its maximum on June 1 and minimum on December 1 (see the original paper Ref. [142] and the review Ref. [143] for more information). The maximum and minimum values will obviously get shifted as a function of the satellite's position with respect to the Earth's surface. We will make a few comments on these complications later in the text.

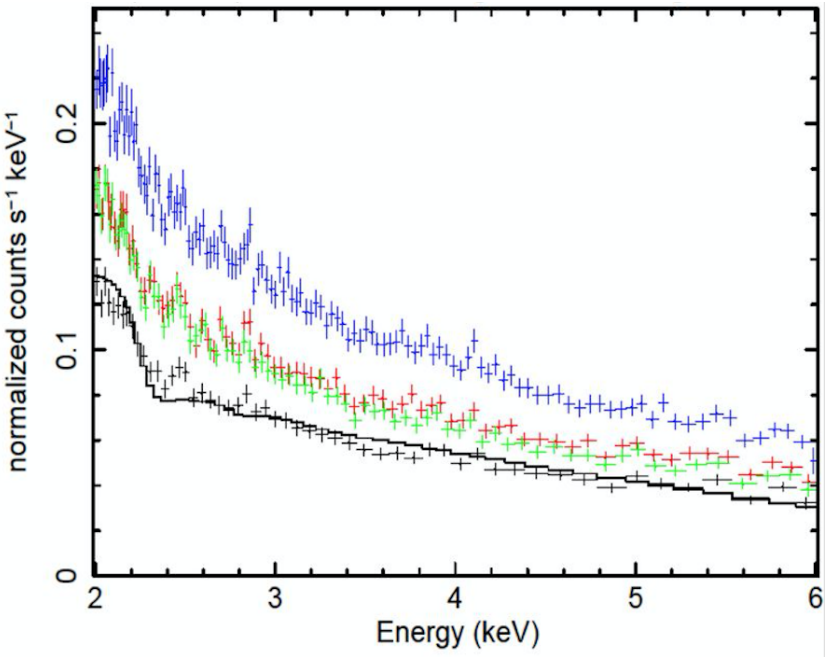

Figure 7.1: 2-6 keV X-ray background spectra detected by the EPIC pn camera carried by XMM-Newton (the data are integrated from 2000 to 2012) for each of the four spacecraft seasons: Winter (black), Summer (green), Spring (red), and Fall (blue). This figure is taken from Ref. [5] where it was adapted from Figure 14(a) in Ref. [10].

very different from Refs. [10, 138–140] which consider axions as the dominant source of dark matter.

The basic idea in our proposal follows from the fact that antimatter AQNs will hit the Earth at a low rate. These AQNs will lose some of their mass from annihilation, and they will also lose some momentum [36]. The AQNs are not completely destroyed. At the moment of their exit, they are very hot objects as a result of friction and annihilation events occurring in the Earth's deep underground layers. At the exit point, their temperature can be as high as $T_0 \sim$ 200-500 keV (this is discussed in chapter 7.2). The AQNs slowly cool down while they continue their trajectory away from the Earth's surface and emit radiation. At this stage, the AQNs continue to lose their accumulated heat and slowly decrease their internal temperature. On average, when AQNs reach distances of the order $r \gtrsim 8R_{\oplus}$, their temperature remains very high,

$T \gg 10$ keV. The XMM-Newton operates precisely at such distance and can easily observe these X-rays emitted by AQNs. AQNs represent the dominant form of dark matter in this model, and the velocities of AQNs hitting the Earth are different for different seasons. We call this the annual modulation of the dark matter wind (see footnote 50 for a comment on this terminology). As a result, the flux of AQNs that leave the Earth also depends on seasons, which consequently leads to a seasonal varying X-ray background. The objective of this chapter is to calculate if the model is consistent with the observations by Ref. [10]. We will show that the amplitude of the seasonal variations, which is on the level of 20-25%, and the energy spectrum are both consistent with Ref. [10].

Note that it is not the goal of this chapter to match the observed seasonal variation presented in Fig. 7.1 with our proposed mechanism. Our goal is limited to the generic computation of the energy spectrum (which is almost the same for all seasons) and the demonstration that the seasonal variation could potentially be very large. The reproduction of Fig. 7.1 can only be attempted with the precise knowledge of the satellite position and orientation, which is well beyond the scope of this work.

As we have reviewed in chapter 2, there are several excesses of emissions in different frequency bands contained in the galactic spectrum of the Milky Way, which seem to be consistent with the moderate emission processes inherent to the AQN model [53–58]. The best-known example is the strong galactic 511 keV line. Several of these diffuse emissions could be explained within the AQN framework if the AQNs carry a baryon charge of order $\langle B \rangle \sim 10^{25}$; see Refs. [53–58] for further details with explicit computations in different frequency bands. In all of these cases, the emitted photons are generated in the electrosphere which is the outer layer of AQNs; see also chapter 5.2 for a brief discussion about the formation of the electrosphere which is an outer layer of an AQN, consisting of electrons in case of matter AQNs (positrons in case of antimatter AQNs).

The X-ray emission in the near-Earth environment, which is the subject of this chapter, also originates from the electrosphere. Therefore the thermal properties of the electrosphere play a crucial role. The relevant thermal features of the electrosphere have been analyzed previously in Ref. [57] in the context of galactic emission, where the AQN's internal temperature turns out to be very low, being around $T \sim$ eV. This temperature is determined by the requirement that the rate of the energy emission is equal to the rate of energy deposition due to the annihilation processes between the

baryons from the surrounding material with the antiquarks from the AQN's core. As the density of the material in the center of a galaxy is quite low, $n_b \sim 10^2$ cm^{-3}, the corresponding rate of collisions of baryons with the AQNs is also very low. This eventually determines an AQN's low internal temperature, around $T \sim$ eV. Note that the heat exchange inside the AQN, between the electrosphere and the AQN core, is extremely efficient. Consequently, the temperature of both are the same, T.

In this chapter, we are interested in the AQNs crossing the Earth's interior with a very high density of the surrounding material, $n_b \sim 10^{24}$ cm^{-3}, and even higher in the Earth's core. As a result, the AQNs crossing the Earth's interior will acquire very high temperatures, reaching up to $T \simeq$ 200-500 keV, as argued in chapter 7.2. For such high temperatures, several new phenomena related to ionization, plasma frequency, and other many-body effects, which had been previously neglected in Ref. [57], become very important and have to be explicitly incorporated into the computational framework. The corresponding modifications of the dynamics of the electrosphere accounting for all of these effects will be the subject of the following chapter 7.2. We use these results in chapter 7.3 to calculate the spectrum accumulated by XMM-Newton from the hot AQNs based on the observatory's configuration and orbit information, and compare it with the observations.

7.2 AQN-induced X-rays

In order to theoretically calculate the spectrum received by XMM-Newton from the radiation of hot AQNs that have crossed the Earth's interior, the first step is to know the radiation spectrum from the electrosphere of an AQN characterized by a high temperature $T \sim$ 200-500 keV, which represents the topic of chapter 7.2.1. In chapter 7.2.2, we examine the cooling process of AQNs in space after they leave the Earth. Since the AQN's radiation features change as its temperature drops, we need to know the temperature, intensity, and spectrum of AQNs when they reach the region $r \sim 10R_\oplus$, where the XMM-Newton is operational.

7.2.1 AQN emissivity

The properties of thermal emission from the electrosphere of an AQN have been discussed in Ref. [57]. First, we will briefly summarize the previous

results here. After that, we will discuss a number of complications which are relevant for our present work (when the temperature is very high $T \sim$ 200-500 keV). These were ignored in previous studies with $T \sim$ eV in the context of galactic emission.

The spectral surface emissivity is denoted as $dF/d\omega = dE/dtdAd\omega$, representing the energy emitted by a single AQN per unit time, per unit area of the AQN's surface, and per unit frequency. It has the following expression [57]:

$$\frac{dF}{d\omega}(\omega) = \frac{1}{2}\int_0^\infty dz\ \frac{dQ}{d\omega}(\omega, z) \tag{7.1}$$

where

$$\frac{dQ}{d\omega} = n^2(z) \cdot \frac{4\alpha}{15}\left(\frac{\alpha}{m_e}\right)^2 2\sqrt{\frac{2T}{m_e\pi}}\left(1+\frac{\omega}{T}\right)\mathrm{e}^{-\omega/T} h\left(\frac{\omega}{T}\right). \tag{7.2}$$

$n(z)$ is the local density of positrons at distance z from the AQN's surface, which has the following expression:

$$n(z) = \frac{T}{2\pi\alpha}\frac{1}{(z+\bar{z})^2}, \tag{7.3}$$

with

$$\bar{z}^{-1} = \sqrt{2\pi\alpha}\cdot m_e \cdot \left(\frac{T}{m_e}\right)^{1/4}, \quad n(z=0) \simeq (m_e T)^{3/2}, \tag{7.4}$$

where $n(z=0)$ reproduces an approximate formula for the plasma density in the Boltzmann regime at temperature, T. The function $h(x)$ in eq. (7.2) is a dimensionless function computed in Ref. [57] (see Appendix C for details). The important features of the spectrum will be discussed in detail later, but we would like to emphasize that the spectrum is qualitatively different from conventional black body radiation, despite of the fact that the electrosphere is characterized by a specific temperature, T. The reason is that the size of the system is much smaller than the photon's mean free path and, as a result, the photons cannot thermalize in this system.

The thermal properties presented above were applied to the study of the emission from AQNs from the galactic centre, where an AQN's internal temperature is very low, $T \sim$ eV, as already mentioned in chapter 7.1. When an AQN propagates in the Earth's atmosphere, its internal temperature starts to rise to $\sim$ 40 keV or so [39]. When the AQN enters the Earth's surface, it is further heated to $\sim$ 200 keV, due to the much higher density of the Earth's

interior (see the Appendix of Ref. [39] for more details). These processes and the corresponding emission spectrum are very complicated to compute because in this high temperature regime, a number of many-body effects in the electrosphere that were previously ignored become important. In what follows, we explain the physics of these effects, while all of the technical details are developed in Appendix C.

1. The modification of the positron density $n(z)$ in the electrosphere. The most important modification due to high temperature occurs as a result of the ionization of the system. Loosely bound positrons leave the system, and strongly bound positrons change their positions and momenta to adjust to the corresponding modifications of the system. Indeed, the neutrality of the AQN will be lost due to the ionization at $T \neq 0$, in which case the antimatter AQNs will acquire a negative electric charge due to the ionized positrons. The corresponding charge, Q, can be estimated as follows [28]:

$$Q \simeq 4\pi R^2 \int_{z_1}^{\infty} n(z) dz \sim \frac{4\pi R^2}{2\pi\alpha} \cdot \left(T\sqrt{2m_e T} \right), \tag{7.5}$$

where $n(z)$ is the density of the positrons eq. (7.3), in the electrosphere. In this estimate, it is assumed that the weakly bound positrons, with binding energy $\epsilon \lesssim T$, will be stripped off of the electrosphere as a result of high temperature, T. These loosely bound positrons are localized mostly at the outer region of the electrosphere, at distances $z > z_1(T) \approx (2m_e T)^{-1/2}$, which motivates the cutoff in our estimate (7.5).

Since the temperature of the AQN's core becomes very high due to the large number of annihilation events in the Earth's interior, a large number of weakly bound positrons will be stripped off of the AQN, and the number density of remaining positrons will drastically decrease. The corresponding changes in the electrosphere are determined by nontrivial non-equilibrium dynamics, which shall not be discussed in the present work. Instead, we introduce a phenomenological suppression factor, κ, which effectively accounts for the relevant physics:[51]

$$n(z) = \kappa \cdot \frac{T}{2\pi\alpha} \frac{1}{(z+\bar{z})^2}. \tag{7.6}$$

[51] Note that the meaning of κ here is completely different from the same symbol κ defined in chapter 4 which accounts for completely different physics.

Although the computations of the coefficient κ from first principles are very difficult and saved for a future study, it is expected that it depends on temperature, T, and z, since different z-shells will be affected by the annihilation processes differently. However, we ignore these complications in the remainder of the paper and will treat κ as a constant parameter in the range $0 < \kappa < 1$.

2. Ionization of loosely bound positrons. Eq. (7.6) is a simplification which does not take into account the fact that loosely bound positrons will be completely stripped off by high temperature, while more strongly bound positrons will be less affected and stay bound. One can easily add this feature to our simplified analysis by describing κ as a step function:

$$\kappa(z,T) = \begin{cases} 0 \quad \text{if} \quad z \geq z_1 \\ \kappa(T) \quad \text{if} \quad z < z_1 \end{cases} , \tag{7.7}$$

where $z_1(T)$ is defined as

$$z_1(T) \simeq \frac{1}{\sqrt{2m_e T}}. \tag{7.8}$$

In this way, we preserve the crucial feature of the system that loosely bound positrons from the outer region of the electrosphere are stripped from the AQN and do not participate in the cooling of the system.

3. The role of the plasma frequency. The plasma frequency ω_p characterizes the propagation of photons in a plasma. It can be thought of as an effective mass for the photons: only photons with an energy larger than this mass can propagate outside of the system, while photons with $\omega < \omega_p$ can only propagate for a short time and distance $\sim \omega_p^{-1}$ before being absorbed back. For our estimates, we will use a conventional non-relativistic expression for ω_p:

$$\omega_p^2(z) = \frac{4\pi\alpha n(z)}{m_e}; \quad \omega_p(z) \simeq \sqrt{\frac{2T}{m_e}} \frac{\sqrt{\kappa}}{(z+\bar{z})}, \tag{7.9}$$

where we substituted eq. (7.6). The important implication of the plasma frequency $\omega_p(z)$ is that the densest regions of the electrosphere stop emitting photons because the plasma frequency is too high, since $\omega_p^2 \sim n$ according to eq. (7.9). This implies that the emissivity, eq. (7.2), from the dense regions will be exponentially suppressed at the plasma frequency [57]:

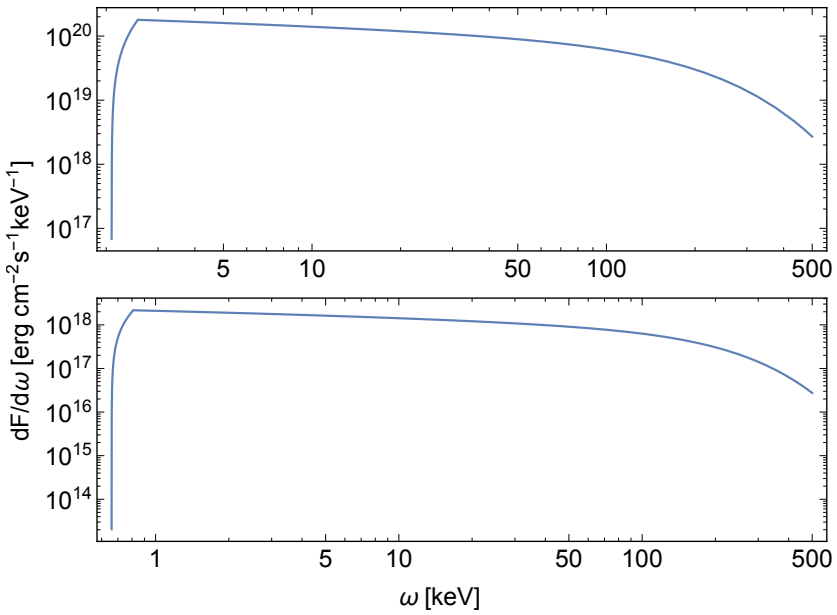

Figure 7.2: The spectral surface emissivity of an AQN with all of the effects discussed in this chapter 7.2.1 included, see eq. (C.8) in Appendix C. $\kappa = 10^{-2.5}$ in the top subfigure and $\kappa = 10^{-3.5}$ in the bottom subfigure. The two subfigures are plotted with $T = 100$ keV as an example. This figure is taken from Ref. [5].

$$\frac{d\tilde{Q}}{d\omega}(\omega, z) \sim \mathrm{e}^{-\omega_p(z)/T} \cdot \frac{dQ}{d\omega}(\omega, z). \tag{7.10}$$

With all of these effects taken into account, the spectral surface emissivity (7.1) can now be numerically computed. We refer the reader to Appendix C for technical details of the computations. Two examples are shown in Fig. 7.2 for $T = 100$ keV and $\kappa(T) = 10^{-2.5}, 10^{-3.5}$. Fig. 7.2 reveals some important features. First of all, the spectrum is almost flat in the region $\omega \lesssim T$. This is a direct manifestation of a very generic property of emission by charged particles when the energy of the emitted photon is much smaller than all of the other scales of the problem, the so-called "soft Bremsstrahlung" emission or "soft photon theorem." In this case, the emission is known to show a $d\omega/\omega$ behavior for the probability to emit a soft photon with frequency ω. This property implies that the intensity of radiation, $dF/d\omega \sim$ constant, must be

flat for soft photons. As we will discuss in chapter 7.3, this unique property of the spectrum will play a key role in our interpretation of the spectrum observed by XMM-Newton. On the other hand, for large $\omega \gg T$, the exponential suppression, $\exp(-\omega/T)$, becomes the most important feature of the spectrum. The complete suppression of the emission at very small $\omega \ll T$ is an artifact of our simplification of the density, $n(z) \sim \kappa(z)$, in the form of a step function (7.7). There is another cusp behavior also at $\omega \ll T$ (the peak in Fig. 7.2). This results from our simplified treatment of the plasma frequency, ω_p, when $dF/d\omega$ is approximated by a piecewise function (when the emission with $\omega \geq \omega_p$ from a high density region occurs with no suppression, while emission with $\omega \leq \omega_p$ from the same region is completely dropped). In reality, both of these effects leading to the cusps should be described by a smooth function. However, this part of the spectrum with $\omega \ll T$ will not play any role in our analysis which follows.[52]

The next step is the computation of the cooling rate, done in chapter 7.2.2. For this purpose, we need the total surface emissivity $F_{\rm tot}(T, \kappa)$ which is a function of T and κ. This is done by integrating $dF/d\omega$ over ω. The technical details of the calculations can be found in Appendix C, eq. (C.13). We parameterize the final formula for the emissivity, which will be used in chapter 7.2.2, as follows:

$$F_{\rm tot}(T) \simeq \frac{\alpha}{15\pi^{5/2}} \frac{T^5}{m_e} \cdot c_1(\kappa) \left(\frac{T}{10 \text{ keV}} \right)^{c_2(\kappa)} \tag{7.11}$$

with

$$c_1(\kappa) = 4\kappa^2, \quad c_2(\kappa) = -0.89. \tag{7.12}$$

7.2.2 AQN cooling

While passing through the Earth, an AQN will be heated up by friction and annihilation events. Its temperature when exiting the Earth's surface is denoted by T_0. The AQN will be heated up in a fraction of a second because

[52] An important consequence of the strong suppression at small $\omega \ll T$ is that the intensity of the visible light emission with $\omega \sim 1$ eV is strongly suppressed in comparison to the X-ray emission. It could play a dramatic role in the identification of AQN annihilation events in the atmosphere with the so-called skyquakes. They occur when a sonic boom is not accompanied by any visible light which would normally be expected for any meteors-like events; see Ref. [39] for details.

of the very efficient energy transfer between the AQN and its surrounding dense material. However, it is expected that T_0 cannot become much higher than $\sim$ 500 keV because of different processes. These include e^+e^- pair production and black body radiation, which start to dominate the AQN's emission deep underground, and become much more important than the Bremsstrahlung radiation, eq. (7.2). The lower bound on T_0 is at the order of $\sim$ 200 keV, as shown by Ref. [39]. Calculating T_0 precisely from first principles remains very difficult because the energy transfer in the Earth's interior includes complicated processes, and it is not part of the present work. For this reason, we will treat T_0 as a phenomenological parameter.

Fortunately, these complications do not affect our analysis once the AQNs exit the surface and start to travel in empty space. After exiting Earth, the energy loss from the AQN into space is entirely determined by eq. (7.11). In this case, the initial condition for the cooling is simply characterized by T_0. One can completely ignore any new annihilation events at this point because the density of the material in Earth's atmosphere drops very quickly with height. Therefore, the AQNs are assumed to be travelling in empty space immediately after they exit the Earth's surface, with initial temperature $T(r = R_\oplus) = T_0$.

Our goal now is to calculate the energy loss rate of the heated AQN while it travels through space, away from Earth, with a typical dark matter speed of ~ 220 km/s. The total initial energy accumulated by the AQN is determined by its exit temperature, T_0, and specific heat, c_V. The corresponding expression for unpaired quark matter is known [51] and it is given by:

$$c_V = \frac{N_c N_f}{3}\mu^2 T, \tag{7.13}$$

where μ is the chemical potential, and N_c, N_f are the number of colors and flavors in the system. There are many different CS phases with drastically different expressions for c_V. In particular, in 2SC (two flavor superconducting phase), the expression for the specific heat [51] assumes the form :

$$c_V \simeq \frac{1}{3}T(\mu_d^2 + \mu_u^2), \tag{7.14}$$

where chemical potentials in CS phases are in the range $\mu_u \simeq \mu_d \simeq 500$ MeV. This numerical value is perfectly consistent with our studies of the typical value of the AQN's chemical potential at the moment of its formation as we

have studied in chapter 3.3. For our numerical analysis in what follows, we use expression (7.14).

The energy of the AQN decreases when its temperature decreases, according to the conventional formula

$$dE = c_V \cdot V \cdot dT, \tag{7.15}$$

where V is the AQN volume. The energy emitted by an AQN per unit time has been computed in the previous section and it is given by eq. (7.11):

$$-dE/dt = F_{\rm tot}(T) \cdot 4\pi R^2, \tag{7.16}$$

where sign minus implies that the energy of the AQN is decreasing with time as a result of emission. Combining eqs. (7.15) and (7.16), we arrive at the desired equation describing the change of the temperature, T, with time, t, while the AQN is moving away from the Earth and emitting photons:

$$\frac{dT}{dt} = -\frac{4\pi R^2}{V}\frac{1}{c_V(T)}F_{\rm tot}(T). \tag{7.17}$$

The solution of this differential equation, with initial condition $T(t=0) = T_0$, is given by:

$$\begin{aligned}\left(\frac{t}{1\ \text{sec}}\right) \simeq & \frac{0.34}{c_1(\kappa)[c_2(\kappa)+3]}\left(\frac{R}{10^{-5}\ \text{cm}}\right)\left(\frac{\mu_{u,d}}{500\ \text{MeV}}\right)^2 \\ & \times\left[\left(\frac{T}{10\ \text{keV}}\right)^{-[c_2(\kappa)+3]} - \left(\frac{T_0}{10\ \text{keV}}\right)^{-[c_2(\kappa)+3]}\right],\end{aligned} \tag{7.18}$$

where $T(t) = T_0$ at $t = 0$, when the AQN exits the Earth's surface. We refer the readers to Appendix D for the details on the derivation.

Fig. 7.3 shows T as a function of time, t, for different values of κ and T_0. We choose $R = 2.25 \times 10^{-5}$ cm, which has been previously used in axion emission studies [36]. Fig. 7.3 illustrates a very important result: after $t \approx 100$ seconds, when the AQN is at distance $r \geq 3R_\oplus$, the temperature $T(t)$ is not very sensitive to the initial temperature T_0 for a given coefficient κ. This is because AQNs with higher initial temperature T_0 emit more radiation and cool down more quickly. As a result, $T(t)$ is much more sensitive to κ than T_0, as shown by the blue and black lines in Fig. 7.3. This is because a smaller

value of κ leads to a drastic reduction of the emission. As a consequence of this suppressed emission for a sufficiently small κ, the temperature remains close to its initial value, T_0, for a long period of time, $t \sim 10^3$ seconds. Ref. [10] selected observations such that XMM-Newton would always point away from the Earth and Sun. Therefore, we expect that their signal will be weakly sensitive to T_0 and strongly sensitive to κ.

Another important quantity is the AQN energy loss rate. It can be computed as follows: the total energy stored in an AQN at the moment of exit is

$$E_0 = \int_0^{T_0} c_V(T) V dT. \tag{7.19}$$

The energy lost due to thermal emission to space is given by

$$E(t) = 4\pi R^2 \int_0^t dt F_{\rm tot}[T(t)], \tag{7.20}$$

where $F_{\rm tot}[T]$ is determined by eq. (7.11) and $T(t)$ by eq. (7.18). The stored energy $[1 - E(t)/E_0]$ as function of time for different values of κ and T_0 is shown in Fig. 7.4. This function describes the fraction of energy remaining in the AQN core at time t, which vanishes when $t \to \infty$. Fig. 7.4 shows that a smaller κ corresponds to a reduced emission and therefore a much slower energy loss rate. For instance, for $\kappa = 10^{-3.5}$, the stored energy in the AQN core is almost unaltered up to $t \simeq 10^2$ seconds.

We conclude this part with a few comments on our choice of the parameters T_0 and κ, which appear in the computations and provide a benchmark for our numerical estimates. As we shall see in the following text, the spectrum of the emission depends on these parameters in a very nontrivial way. Our goal here is to give a few simple order-of-magnitude estimates supporting our choice of T_0 and κ being used in the present work.

As already mentioned at the beginning of this section, the exit temperature is expected to be in the range $T_0 \sim$ 200-500 keV. This results from the very high rate of annihilation events in the dense environment,[53] and that the heat loss from e^+e^- pair production and black body radiation prevents T_0 from going beyond $\sim$ 500 keV.

[53]Indeed, according to eq. (7.19), the energy, $E_0 \simeq \frac{1}{2} c_V V T_0^2$ with $T_0 \simeq 500$ keV, is achieved when the AQN travels a distance of order $L \sim 0.5$ km, at which the accumulated annihilation energy, (2 GeV)$n_b \pi R^2 L$ with $n_b \sim 10^{24}$cm^{-3}, becomes the same order of magnitude as E_0.

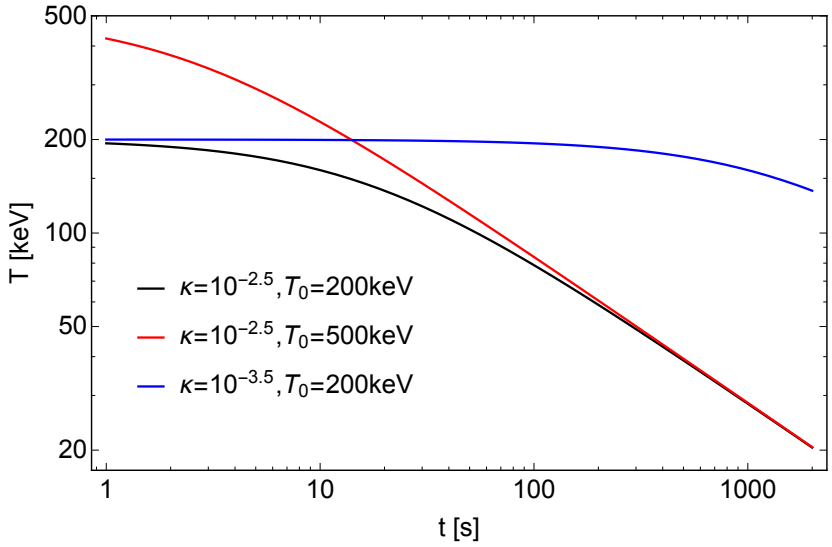

Figure 7.3: T vs. t for different values of κ and T_0. $T = T_0$ at $t = 0$. An important feature here is that the behavior $T(t)$ at $t \gtrsim 100$ s (when XMM-Newton becomes operational) is not sensitive to the initial value of T_0 for a given κ; see text for explanations. This figure is taken from Ref. [5].

The other parameter which enters our computations is the suppression factor, κ, defined by eq. (7.6). This was introduced to account for the drastic decrease of the positron number density from the electrosphere, which can emit photons. This strong suppression is a direct consequence of high internal temperature, T_0, when a large number of weakly bound positrons are expanded over much larger distances order of R rather than distributed over much shorter distances of order $\bar{z}$ defined by eq. (7.4). This leads to the following estimate for suppression factor[54]

$$\kappa \sim \left(\frac{\bar{z}}{R}\right)^{\frac{1}{2}} \sim \frac{1}{\sqrt{mR}} \frac{1}{\sqrt[4]{2\pi\alpha}} \sim 2 \times 10^{-3}. \tag{7.21}$$

[54] A simplified procedure for the estimate of κ, as mentioned in the text is not a proper way of computation. This is because the positron's density will be adjusting when T_0 varies. The consistent procedure would be a mean-field computation of the positron density by imposing the proper boundary conditions relevant to nonzero temperature and nonzero charge, similar to the $T \approx 0$ computations carried out in Ref. [57, 58]. The corresponding computations have not been done yet, and we keep parameter κ as a phenomenological free parameter.

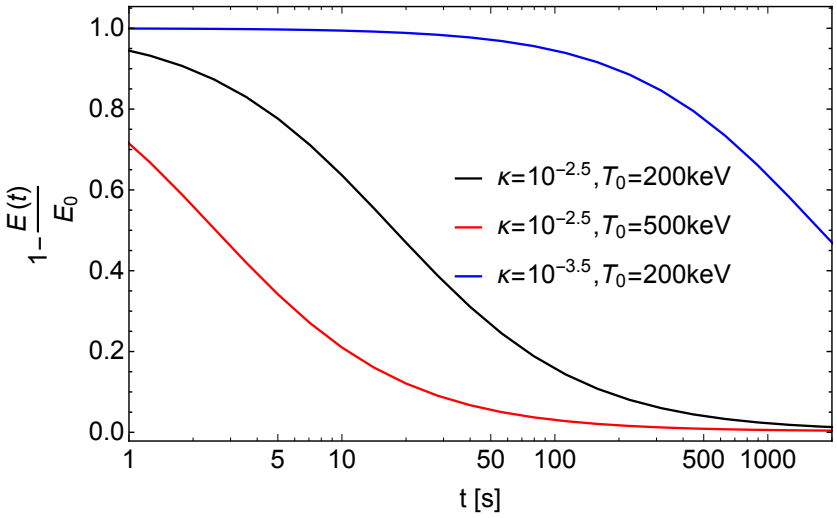

Figure 7.4: The relative stored energy $[1 - E(t)/E_0]$ vs. t, for different values of κ and T_0. An important feature here is that a smaller $\kappa = 10^{-3.5}$ corresponding to a reduced emission leads to a much slower decay rate. In this case, the AQN keeps its initial energy value up to $t \lesssim 10^2$ s. This figure is taken from Ref. [5].

This is only an order-of-magnitude estimate, and as emphasized in footnote 54, κ will be treated as a free phenomenological parameter in the rest of this chapter.

7.3 Computation of the spectrum and comparison with XMM-Newton data

This is the central part of this chapter, as we are in a position to compute the spectrum and intensity received by XMM-Newton from the thermal emission of AQNs computed above. The obtained results can be directly compared with the observations from Ref. [10].

We start with the simplified assumption that the AQNs are *uniformly* distributed around the Earth. We will also assume that the AQNs exit the Earth *radially*. As we shall see below, we are able to reproduce the spectrum observed by XMM-Newton with the AQN framework. The spectrum shape (but not the intensity) is insensitive to the free parameters of the model,

as our result represents a very generic consequence of the system when the spectrum is essentially determined by the "soft photon theorem" which we already mentioned at the end of chapter 7.2.1.

With these simplifications in mind, the number density of AQNs that have passed through the Earth is

$$n_{\rm AQN}(s) = \frac{1}{4\pi(R_\oplus + s)^2} \cdot \frac{\mathcal{F}}{v_{\rm out}}, \tag{7.22}$$

where Fig. 7.5 shows the geometry of the configuration. In eq. (7.22), s denotes the distance from the Earth's surface. $v_{\rm out}$ is the AQN velocity leaving the Earth's surface, which is assumed to be the same for all AQNs and independent of s. For simplicity, we approximate $v_{\rm out} \simeq v_{\rm in}$ where $v_{\rm in}$ is the AQN velocity when it hits the Earth, although the AQN may be slowed down by the interactions with their surroundings inside the Earth. This approximation is good enough for our analytical treatment here. The effect of the velocity difference between $v_{\rm out}$ and $v_{\rm in}$ will be discussed in chapter 7.4. We denote $\mathcal{F}$ as the total AQN flux (number per unit time) that hits the Earth. It has been estimated as follows [36]:

$$\mathcal{F} \simeq 0.67\ {\rm s}^{-1} \left(\frac{\rho_{\rm DM}}{0.3\ {\rm GeV/cm}^3}\right) \left(\frac{v_{\rm in}}{220\ {\rm km/s}}\right) \left(\frac{10^{25}}{\langle B\rangle}\right). \tag{7.23}$$

We adopt the following values for our numerical estimates: $v_{\rm out} \simeq v_{\rm in} \simeq 220$ km/s; average baryon charge, $\langle B\rangle = 10^{25}$ (which corresponds to an average size of the AQN, $\langle R\rangle = 2.25 \times 10^{-5}$ cm). This corresponds to a total flux of $\mathcal{F} \simeq 0.67\ {\rm s}^{-1}$ [36].

Fig. 7.5 shows the positions of the Earth and the XMM-Newton observatory. It also shows how the XMM-Newton observatory receives the radiation from a large number of AQNs, with number density $n_{\rm AQN}$, surrounding the Earth. Various configuration parameters are defined in the caption of Fig. 7.5. The following geometric relations are useful:

$$\begin{aligned} &s_{\rm mid}(\theta) = \frac{L}{-\cos\theta} - R_\oplus, \quad y_{\rm mid}(\theta) = -L\tan\theta, \\ &r_{\rm mid}(\theta) = (y_{\rm mid} + L)\tan\alpha_c. \end{aligned} \tag{7.24}$$

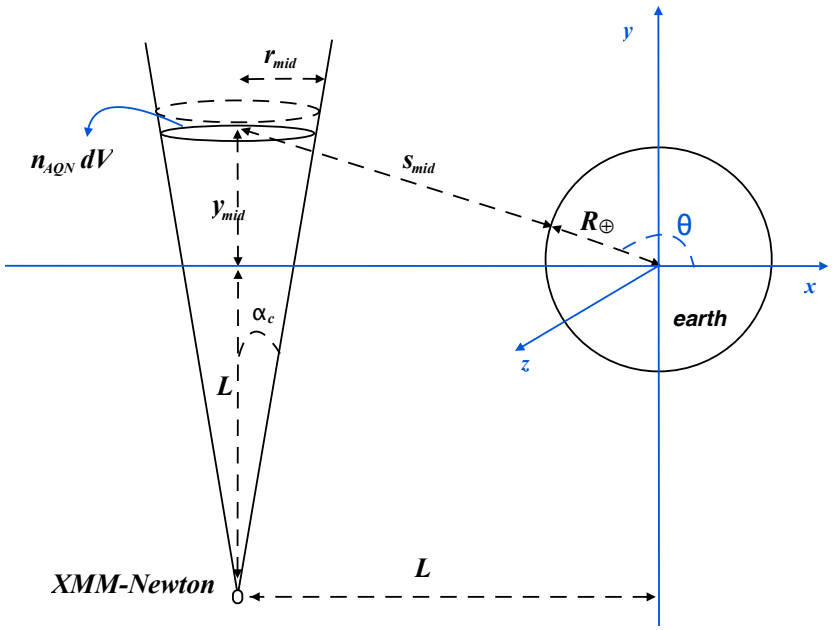

Figure 7.5: The XMM-Newton observatory is assumed to be located at the position $(-L, -L, 0)$. The cone is the field of view of the EPIC pn camera carried by XMM-Newton. In our present work, we focus on this camera (see footnote 57 for details). The cone points in the direction $+y$. dV is the volume of the thin disk, and the number of AQNs contained inside is $n_{\rm AQN}dV$. $r_{\rm mid}$ is the radius of the thin disk. Since the opening angle of the cone is very small, $\alpha_c = 0.25\,{\rm deg}$, it is a good approximation that all AQNs inside dV are located at the same point $(-L, y_{\rm mid}, 0)$. $y_{\rm mid}$ could be negative, so they have the same distance, $s_{\rm mid}$, to the Earth's surface. The range of θ is apparently $[\pi/2, 5\pi/4]$. This figure is taken from Ref. [5].

The number of AQNs inside the thin disk of the cone (shown in Fig. 7.5) is

$$dN(\theta) = n_{\rm AQN}dV = n_{\rm AQN}[s_{\rm mid}(\theta)] \cdot \pi r_{\rm mid}^2(\theta) dy_{\rm mid}(\theta). \tag{7.25}$$

The distance, $s_{\rm mid}$, and the time, t, are connected by the AQN velocity, $v_{\rm out}$ that $s_{\rm mid} = v_{\rm out}t$. The spectrum received by the XMM-Newton observatory

can be calculated as:

$$\begin{aligned}\frac{dF_r}{d\omega} &= \int_{\text{cone}} \frac{dF}{d\omega}\left(T_{\text{mid}},\omega\right) \frac{R^2}{[y_m(\theta)+L]^2}\; dN(\theta) \\ &= \int_{\frac{\pi}{2}}^{\frac{5\pi}{4}} d\theta\; \left\{ \frac{dF}{d\omega}\left(T_{\text{mid}},\omega\right) \frac{R^2}{[y_m(\theta)+L]^2} \right. \\ &\left. \cdot n_{\text{AQN}}[s_{\text{mid}}(\theta)] \cdot \pi r_{\text{mid}}^2(\theta) \frac{L}{\cos^2\theta} \right\},\end{aligned} \tag{7.26}$$

where $dF/d\omega\left(T_{\text{mid}},\omega\right)$ is the spectral surface emissivity computed at the moment $t_{\text{mid}} = s_{\text{mid}}(\theta)/v_{\text{out}}$ with the corresponding temperature T_{mid}. The computations of $dF/d\omega(T,\omega)$ for arbitrary T have been carried out in chapter 7.2.1; see Fig. 7.2 for $dF/d\omega(T,\omega)$ computed at $T = 100$ keV as an example. R in eq. (7.26) is the AQN radius, $R \simeq 2.25 \times 10^{-5}$cm, corresponding to $\langle B\rangle = 10^{25}$. For numerical estimates, we choose $L = 7R_\oplus$, where $R_\oplus$ is the Earth's radius.[55]

The radiation spectrum $dF_r/d\omega$ given by eq. (7.26) is the energy received by the observatory per unit time, per unit area, and per unit frequency. In order to make a precise comparison between our calculations and the observations [10], we convert $dF_r/d\omega$ to $f^{(\text{theory})}$, the *number of photons* received by the observatory per unit time, per unit area, per unit frequency, and *per unit solid angle*, which is defined as follows:

$$f^{(\text{theory})} \equiv \frac{1}{\Omega_c}\frac{1}{\omega}\frac{dF_r}{d\omega}, \tag{7.27}$$

where $\Omega_c = 2\pi(1-\cos\alpha_c) \approx 5.98 \times 10^{-5}$ sr ≈ 0.196 deg^2 is the solid angle of the cone. The corresponding theoretical prediction is plotted in Fig. 7.6, for several typical values of the parameters of the system, κ, T_0, as discussed in chapter 7.2.

In order to compare with observations from XMM-Newton in the 2-6 keV energy band, we use the power-law fit of the observations (see eq. (11) from

[55] The orbit of XMM-Newton is highly elliptical, with an apogee altitude of ~ 115000 km and a perigee altitude of ~ 6000 km. The orbit period is ~ 48 hr. The orbit changes with time, due to several perturbations. We refer the readers to the XMM-Newton Users Handbook [144] for details. The observatory only works at altitudes above the Earth's radiation belts ~ 46000 km; see e.g., Refs. [144, 145]. Therefore, in this section, we choose $L = 7R_\oplus$, which implies that the altitude of the observatory is $\sqrt{2}L - R_\oplus \approx 57000$ km.

Ref. [10]):[56]

$$f^{(\mathrm{obs})} = N_0 \left(\frac{\omega}{\mathrm{keV}}\right)^{-\Gamma} \frac{1}{\mathrm{cm}^2 \cdot \mathrm{s} \cdot \mathrm{keV} \cdot \mathrm{sr}}. \tag{7.28}$$

The normalization factor N_0 is dimensionless, while f is measured in the unit of $[\mathrm{cm}^{-2}\mathrm{s}^{-1}\mathrm{keV}^{-1}\mathrm{sr}^{-1}]$. For the EPIC pn camera carried by XMM-Newton,[57] the values of the numerical parameters (N_0, Γ) are:

$$\begin{aligned} \mathrm{Winter}(N_0,\Gamma) &= \quad (6.66, 0.97); \\ \mathrm{Spring}(N_0,\Gamma) &= \quad (9.08, 0.98); \\ \mathrm{Summer}(N_0,\Gamma) &= \quad (9.60, 1.06); \\ \mathrm{Fall}(N_0,\Gamma) &= \quad (12.09, 0.97), \end{aligned} \tag{7.29}$$

see Table 3 in Ref. [10]. These numbers are obtained by fitting the data observed by the EPIC pn camera (from Fig. 7.1) showing the seasonal variation of the X-ray background with 11σ significance. The maximum amplitude of the seasonal variation from these data occurs between Winter and Fall, rather than between Winter and Summer. It has been discussed in Ref. [10] and will be discussed in the context of the AQN model in chapter 7.4.2.

Fig. 7.6 shows our theoretical prediction (the solid lines from Eq. (7.27)) against the observed spectra (the dotted lines from Eq. (7.28)) for four seasons. The similarity between the observations and theoretical computations is impressive, considering that the shape of the predicted radiation spectrum is only slightly sensitive to the parameters κ and T_0. This result is a direct consequence of the AQN framework.[58] The basic reason for the robustness of our prediction is that the spectrum shape is essentially determined by the very fundamental "soft photon theorem," with a specific behavior, $d\omega/\omega$, for

[56] The symbols in eq. (11) of Ref. [10] conflict with ours, so we rewrite eq. (11) as eq. (7.28), using our own symbols to avoid confusion.

[57] XMM-Newton carries three cameras that are relevant to us: EPIC pn, EPIC MOS1, and EPIC MOS2. The three cameras all clearly show the seasonal variation of the X-ray background with similar values of (N_0,Γ) listed in the main text, which can be seen in Table 3 of Ref. [10]. Therefore, we only need to focus on one camera, which is enough for our purpose to compare the AQN-based calculations with the observations. We choose the EPIC pn camera because it has the largest photon grasp (effective area × aperture), which is a key parameter in studying the background of X-ray radiation, and because it has better counting statistics than the two EPIC MOS cameras [10].

[58] A cusp behavior in the region ω = 1-2 keV in Fig. 7.6 has no physical significance. Rather, it is a reflection of our simplified treatment of the regions with small ω, which results in such a cusp singularity, see comments on this cusp behavior in chapter 7.2.1.

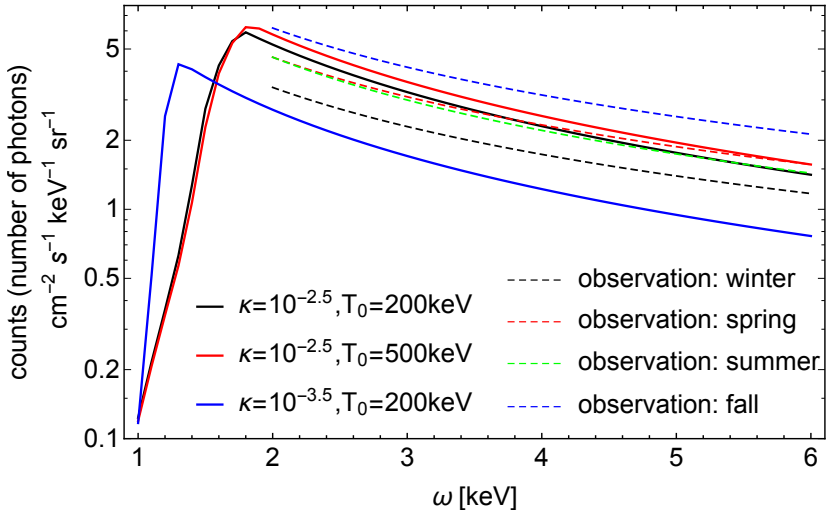

Figure 7.6: The relation f vs. ω, eq. (7.27), for $(\kappa, T_0) = (10^{-2.5}, 200 \text{ keV})$, $(10^{-2.5}, 500 \text{ keV})$, and $(10^{-3.5}, 200 \text{ keV})$ respectively. The x-axis represents frequency. The y-axis represents the values of $f^{(\text{theory})}$, given by eq. (7.27), which is the number of photons received by the XMM-Newton observatory (camera EPIC pn) per unit time, per unit area, per unit frequency, and per unit solid angle in the AQN framework, shown by solid lines. In comparison, we also plot $f^{(\text{obs})}$, given by eq. (7.28), representing the data observed by the EPIC pn camera for four seasons, shown by the four dashed lines respectively. This figure is taken from Ref. [5].

$\omega \ll T$, as we already emphasized earlier at the end of chapter 7.2.1. The slope, Γ, as seen in eq. (7.28), is indeed very close to $\Gamma \simeq 1$ for all seasons. This shows very strong support for our AQN framework.

The amplitude of the spectrum, on the other hand, is sensitive to the parameters (κ, T_0). It is also sensitive to the dark matter distribution, AQN size distribution, velocity distribution, etc., as one can see from eq. (7.23) for the AQN flux. The distance and orientation of the XMM-Newton will also play a role in the seasonal variation. Some of these effects will be discussed in chapter 7.4. We can use our analytical predictions to explore the (κ, T_0) parameter range that is consistent with the observations shown in Fig. 7.1.

For this purpose, we calculate the maximum likelihood $\mathcal{L}(\kappa, T_0)$ defined

as:

$$\mathcal{L}(\kappa, T_0) = \exp\left[-\frac{1}{2}\left(\frac{d - f(\kappa, T_0)}{\sigma}\right)^2\right], \tag{7.30}$$

where the data, d, and the model, $f(\kappa, T_0)$, are estimated at one particular frequency, ω. We choose $\omega = 3$ keV, but any frequency would work, since the model and the observations show a very similar frequency dependence. The value of d in eq. (7.30) is chosen as the middle of the four observed spectra, which is defined as the average of the top spectrum (Fall) and bottom spectrum (Winter), i.e., $d \equiv \frac{1}{2}[f^{(\mathrm{obs,F})} + f^{(\mathrm{obs,W})}]$. The variance, σ, is chosen as $\sigma \equiv \frac{1}{2}[f^{(\mathrm{obs,F})} - f^{(\mathrm{obs,W})}]$, which represents the maximum signal variation between the four seasons. Note that we are not in a position to calculate a full likelihood function over all frequencies, since we do not know the correlation for different ω, and the resulting likelihood would be difficult to interpret. Nevertheless, our approach should provide a reasonable order-of-magnitude estimate of the region of the parameter space, (κ, T_0), consistent with the observations. We are not trying to interpret $\mathcal{L}(\kappa, T_0)$ in a probabilistic way because our error estimate is only approximate. However, the maximum of $\mathcal{L}(\kappa, T_0)$ at 1 is still a valid indicator of where the (κ, T_0) degeneracies lie. Fig. 7.7 shows the iso-contours of $\mathcal{L}(\kappa, T_0)$, where a lighter color represents a better match. The allowed parameter space is represented by two branches in Fig. 7.7. The right vertical branch is essentially independent of T_0, and it matches the observations for $\kappa \sim 10^{-2.5}$. This "insensitivity" to T_0 is consistent with the red and black lines in Fig. 7.3, which illustrates the fact that AQN cooling is independent of T_0 when κ is high enough. On the other hand, the left branch is strongly dependent on both κ and T_0. The next step is to investigate the seasonal variation in the context of our model. From the qualitative arguments given in chapter 7.2.2, the physically preferred values for κ and T_0 are in the right branch. However, for completeness, we will also calculate the seasonal variations for a lower value of κ. In the following chapter 7.4, the calculations will be restricted to the three sets of parameter values represented by the big solid dots in Fig. 7.7.

We conclude this part with the following comment. Our computation of the spectrum and intensity is robust and can be used to plan future experiments to perform the annual modulation studies in the near-Earth environment. However, a signal modulation is usually expected for any dark matter detection experiment. In the following text, we discuss the impact of the Earth position (chapter 7.4.1) and the possible complications due to the

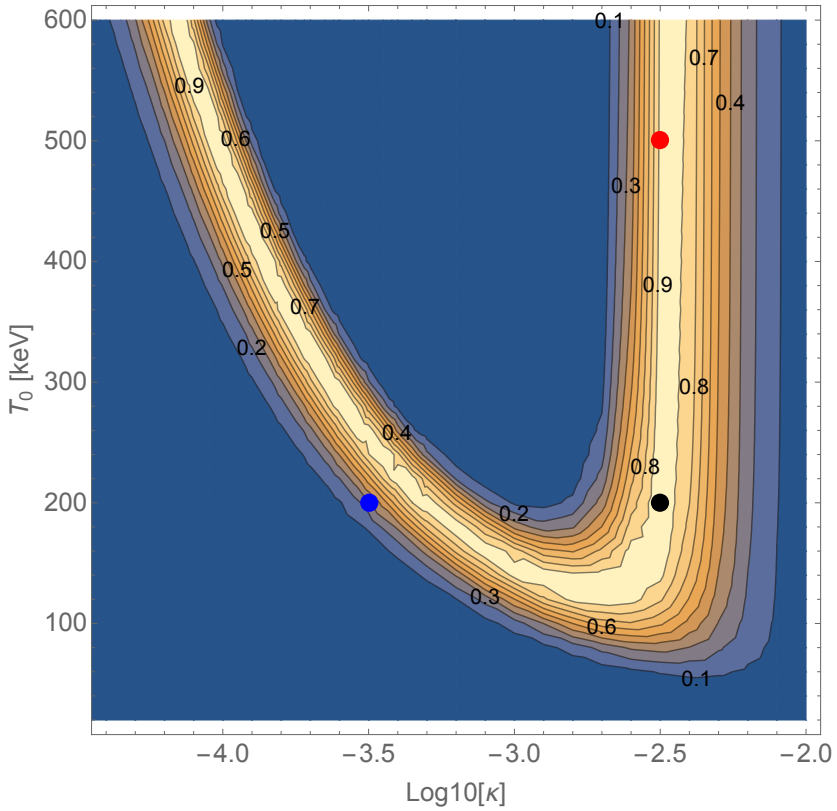

Figure 7.7: The contour plot of $\mathcal{L}(\kappa, T_0)$. The numbers labelled on the contour lines are the values of $\mathcal{L}$. The three points marked on the plot are the three sets of (κ, T_0) that we have chosen in all of our previous plots: $(10^{-2.5}, 200 \text{ keV})$, $(10^{-2.5}, 500 \text{ keV})$, and $(10^{-3.5}, 200 \text{ keV})$. This figure is taken from Ref. [5].

telescope altitude and orientation (chapter 7.4.2).

7.4 Seasonal variation

Up to this part, our focus was on the calculation of the average intensity of the AQN radiation spectrum, ignoring the seasonal variations. However, the seasonal variation was the most important feature discovered by Ref. [10]. The authors claimed an 11σ confidence level detection of the seasonal variation in the 2-6 keV energy band, after removing all possible instrumental

contamination and known astrophysical sources. They argued that known conventional astrophysical sources had been ruled out as a possible explanation of their signal. The main goal of this section is to explain how the seasonal variation might occur in the AQN framework. We will find that an annual amplitude modulation at the order of 20-25% is expected. Interestingly, with conventional dark matter models (e.g., WIMPs), any seasonal variation is expected to be at a much lower level, at the order of 1-10% (see, e.g., Refs. [142, 143]).

7.4.1 Effect of the Earth's position on its orbit

In chapter 7.3, we introduced $v_{\rm in}$, the speed of an AQN hitting the Earth. However, the Earth's motion around the Sun leads to a seasonal variation of $v_{\rm in}$, which will affect the AQN signal represented by eq. (7.26). In this part, we will calculate the amplitude of the seasonal effect, using the analytical prediction, eq. (7.26), and a realistic model of an AQN's incoming speed, $v_{\rm in}$, which is different in the Winter and Summer.

The Sun is moving in the galactic plane, on a nearly circular orbit with velocity, $v_{\rm DM_G}$, with respect to the galactic center. The rotation of the dark matter halo is negligible compared to the rotation of the Sun. Therefore, the entire solar system is facing a dark matter wind with an average velocity of approximately $v_{\rm DM_G}$. The tilt of the ecliptic plane relative to the dark matter wind is approximately 60°. This configuration is shown in Figure 7.8, along with the positions of the four seasons on the Earth's orbit.

We proceed as follows. The dark matter velocity with respect to the Sun is $\vec{v}_{\rm DM_G}$, with $v_{\rm DM_G} \simeq 220$ km/s. The velocity of the Earth around the Sun is $\vec{v}_{\rm E}$, with $v_E = 30$ km/s. Consequently, the dark matter velocity with respect to the Earth is given by

$$\vec{v}_{\rm in} = \vec{v}_{\rm DM_G} - \vec{v}_{\rm E}, \tag{7.31}$$

and the magnitude is

$$v_{\rm in} = \sqrt{v_{\rm DM_G}^2 + v_{\rm E}^2 - 2v_{\rm DM_G} \cdot v_{\rm E} \cdot \cos\theta}, \tag{7.32}$$

where θ is the angle between $\vec{v}_{\rm E}$ and $\vec{v}_{\rm DM_G}$. θ is 60° in the Winter, 120° in the Summer, and 90° in the Spring and Fall. Noting that $\vec{v}_{\rm DM_G} \gg \vec{v}_{\rm E}$, eq. (7.32) can be simplified via Taylor expansion as

$$v_{\rm in} \simeq v_{\rm DM_G} - v_E \cos\theta. \tag{7.33}$$

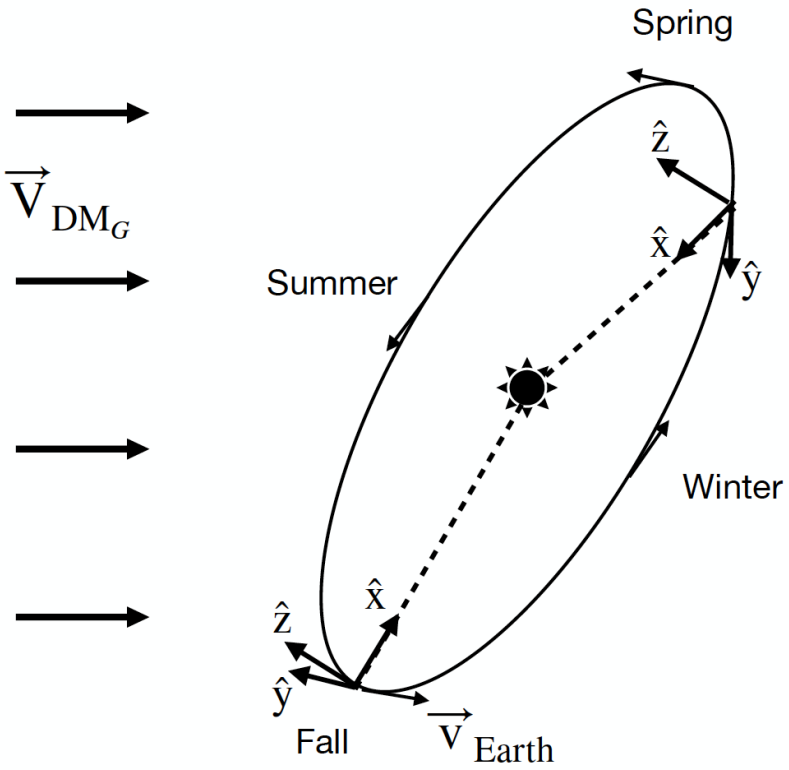

Figure 7.8: Motion of dark matter relative to the Solar System, which is taken as the fixed reference frame. The Earth moves in a nearly circular orbit, with a velocity, $\vec{v}_{\rm E}$, relative to the Sun. The location of the seasons relative to the orientation of the ecliptic plane and dark matter wind, $v_{\rm DM_G}$, is important for the effect discussed in chapter 7.4. This figure is taken from Ref. [5].

Using this approximation, the magnitudes of the dark matter velocities (with respect to the Earth) in the four seasons are:

$$\begin{aligned} v_{\rm in}^{\rm (Sp)} &= v_{\rm in}^{\rm (F)} \simeq v_{\rm DM_G}, \\ v_{\rm in}^{\rm (W)} &\simeq v_{\rm DM_G} - \Delta v, \\ v_{\rm in}^{\rm (S)} &\simeq v_{\rm DM_G} + \Delta v, \end{aligned} \tag{7.34}$$

where $\Delta v = \cos(60^\circ) \cdot v_E = 15$ km/s. Δv is the deviation from 220 km/s,

caused by the Earth's revolution around the Sun. The result is that the dark matter velocity is different for different seasons, which is apparent in Eq. (7.34), and this leads to the seasonal variation of the X-ray background.

There are two specific features which are not shared by conventional WIMP models. The first one is related to the fact that the $v_{\rm in}$ and $v_{\rm out}$ velocities are different in the AQN model, but not in conventional dark matter. The second one is related to the fact that the intensity of the radiation explicitly depends on the number of AQNs which can be seen by the detector at each given moment, as shown in Fig. 7.5 and computed in eq. (7.26). As we will see below, this leads to a feature unique to the AQN framework that is not shared by conventional dark matter.

The first effect, related to $v_{\rm out} \neq v_{\rm in}$, can be explained as follows. The passage of the AQN through the Earth is accompanied by friction and annihilation events with the surroundings, leading to $v_{\rm out} < v_{\rm in}$. We used $v_{\rm out} = v_{\rm in} = 220$ km/s in chapter 7.3, a simplification that was sufficient to estimate the average of the AQN-induced spectrum. However, in this section, the fact that $v_{\rm out}$ is smaller than $v_{\rm in}$ may have an important impact on the seasonal variation. The reason is that as $v_{\rm out}$ gets closer to Δv, the seasonal variation becomes relatively more important. Different AQNs have different paths through the Earth, which results in different $v_{\rm out}$ even for the same $v_{\rm in}$. The precise distribution of $v_{\rm out}$ can only be obtained by numerical simulations, which is left for future studies. The speed change can be quantified by a parameter γ:

$$\gamma = \frac{v_{\rm out}}{v_{\rm in}}. \tag{7.35}$$

Combining eq. (7.34) with eq. (7.35), we obtain the following expressions for $v_{\rm out}$ in the four seasons:

$$\begin{aligned} v_{\rm out}^{\rm (Sp)} &= v_{\rm out}^{\rm (F)} \simeq \gamma v_{\rm DM_G}, \\ v_{\rm out}^{\rm (W)} &\simeq \gamma(v_{\rm DM_G} - \Delta v), \\ v_{\rm out}^{\rm (S)} &\simeq \gamma(v_{\rm DM_G} + \Delta v). \end{aligned} \tag{7.36}$$

The second effect is that the intensity measured by XMM-Newton depends on the number of AQNs passing through the detection cone of the detector which further depends on $v_{\rm out}$. Using eq. (7.26), the *average* $dF_r/d\omega$

measured by the detector is given by:

$$\frac{dF_r}{d\omega} \simeq n_{\rm AQN}(\bar{s}) V \cdot \frac{dF}{d\omega}[T(\bar{s})], \tag{7.37}$$

where $\bar{s}$ denotes the *average* distance of the AQNs inside the cone, as viewed from the Earth's surface. The quantity $n_{\rm AQN}(\bar{s})$ is the number density of AQNs at distance $\bar{s}$, while $dF/d\omega[T(\bar{s})]$ is the spectrum emitted by a single AQN at distance $\bar{s}$, determined by the temperature $T(\bar{s})$. The volume, V, is the effective volume of the cone, which is a constant, inside which the AQNs contribute to the total spectrum received by XMM-Newton. This means that we do not consider AQNs that are too far away from the detector. The detailed calculation of eq. (7.37) is shown in Appendix E, where we obtain an expression of $dF_r/d\omega$ as a function of $v_{\rm out}$:

$$\frac{dF_r}{d\omega} \propto \left(\frac{K_1}{v_{\rm out}} + K_2\right)^{-\frac{3.22}{c_2(\kappa)+3}}, \tag{7.38}$$

where K_1 and K_2 are functions of κ and T_0 (see Appendix E for details).

The maximum seasonal difference is expected between Summer and Winter, because they have the maximum velocity difference, $2\gamma\Delta v$, as seen from eq. (7.36). We define the ratio

$$r \equiv \frac{\left(\frac{dF_r}{d\omega}^{(\rm S)}\right)}{\left(\frac{dF_r}{d\omega}^{(\rm W)}\right)} \tag{7.39}$$

as the difference between the Summer and Winter spectra. Using eqs. (7.36) and (7.38), we get

$$r \simeq \left[\frac{\gamma^{-1}K_1/(v_{\rm DM_G} + \Delta v) + K_2}{\gamma^{-1}K_1/(v_{\rm DM_G} - \Delta v) + K_2}\right]^{-\frac{3.22}{c_2(\kappa)+3}}, \tag{7.40}$$

where $v_{\rm DM_G} = 220$ km/s and $\Delta v = 15$ km/s, as discussed above.

The functions K_1 and K_2 play a very important role in our study. If the temperature T, strongly deviates from its initial value T_0, such that $T \ll T_0$ at the moment of observation, then the second term with T_0 in the brackets in eq. (D.1) can be ignored, which drastically simplifies all equations. In

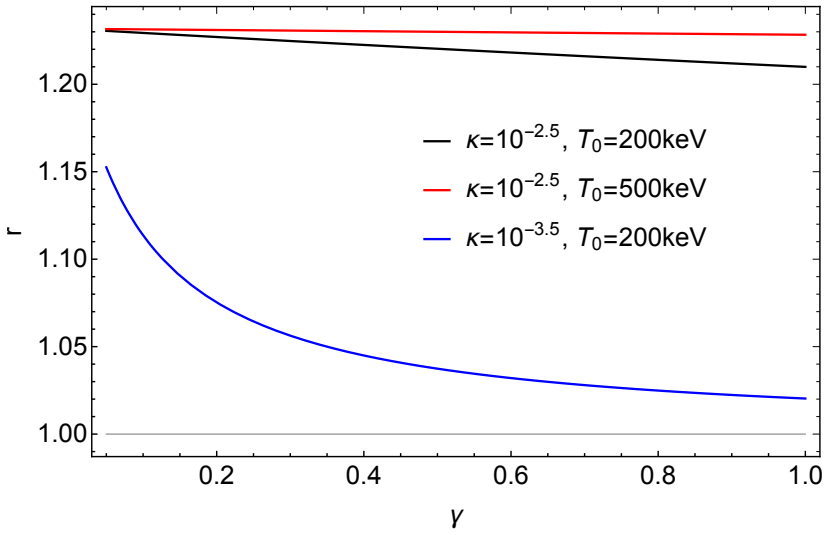

Figure 7.9: The ratio r as a function of γ for different groups of κ and T_0. The solutions from the right branch from Fig. 7.7 (red and black lines) will always produce $r \approx 20\%$ irrespective of the value of γ, while the solution from the left branch from Fig. 7.7 (blue line) will generate a small value of r. This figure is taken from Ref. [5].

particular, the term $K_2 \sim T_0^{-[c_2(\kappa)+3]}$ in eq. (E.6) and further in eq. (7.38) can be ignored. Thus, eq. (7.40) can be simplified to

$$r \simeq \left(\frac{v_{\mathrm{DM_G}} + \Delta v}{v_{\mathrm{DM_G}} - \Delta v}\right)^{\frac{3.22}{c_2(\kappa)+3}} \approx 1.23, \tag{7.41}$$

which does not depend on γ, nor any other features of the system, such as the absolute values of the temperature, T_0, or value of κ, as long as condition $T \ll T_0$ is satisfied. This is a very solid and robust consequence of the AQN model. One should also emphasize that the condition $T \ll T_0$ is always satisfied for all solutions on the right branch shown in Fig 7.7. Indeed, the temperature, T, drastically drops for any value of T_0 with $\kappa \simeq 10^{-2.5}$, as shown in Fig. 7.3.

Eq. (7.41) is a very important result. It shows that for solutions from the right branch of Fig. 7.7, the seasonal variation could be large, up to $\sim$ 20-25%, relatively insensitive to the exact value of κ, T_0, and γ. Fig. 7.9 shows the results of the exact computation from eq. (7.40) supporting this

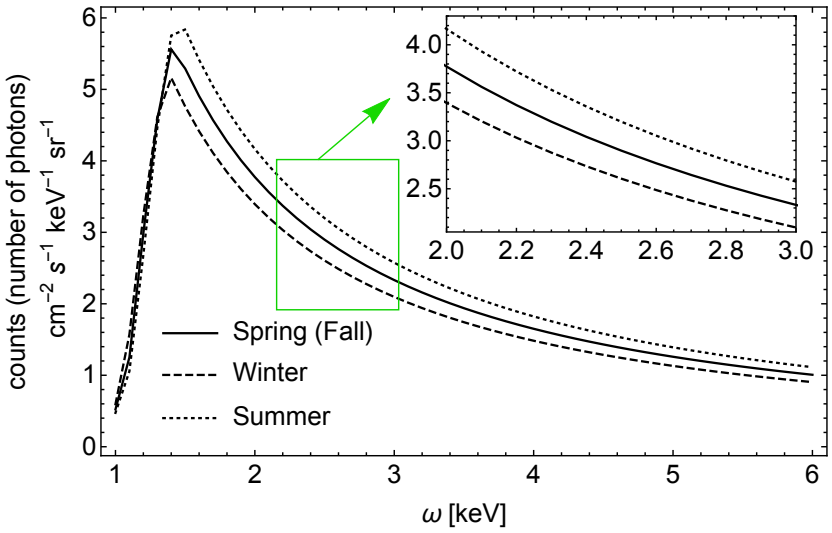

Figure 7.10: Demonstration of the seasonal variation with specific parameters $(\kappa, T_0, \gamma) = (10^{-2.5}, 200 \text{ keV}, 0.5)$ as an example. A small portion of the spectrum, $\omega \in$ 2-3 keV, is zoomed in to demonstrate a large seasonal variation on the level of $\approx 20\%$. This figure is taken from Ref. [5].

claim, where the red and black lines remain relatively flat at $r \approx 1.23$ for all values of γ. The solutions from the left branch lead to a considerably smaller amplitude of the seasonal variation for any values of γ, as illustrated by the blue line in Fig. 7.9. In the context of the AQN framework, the result (7.41) provides a strong argument in favour of a solution in the right branch of Fig. 7.7, because only the right one is capable of leading to seasonal variations in agreement with Ref. [10].

As an example of seasonal variation, Fig. 7.10 shows the spectrum $f^{(\text{theory})}$, which is defined as eq. (7.27) with $dF_r/d\omega$ given by eq. (7.26), for four seasons. For this plot, we choose $\kappa = 10^{-2.5}, T_0 = 200$ keV, and $\gamma = 1/2$. However, as we have shown previously, the radiation spectrum is not very sensitive to parameters T_0 and γ, as long as we choose a solution from the right branch of Fig. 7.7. A sample of the spectrum with $\omega \in$ 2-3 keV shows a large seasonal variation at the level of $\sim$ 20-25%.

The maximal seasonal variation observed by Ref. [10] can be estimated from the normalization factors N_0 (which are given in eq. (7.29) for different

seasons) as follows:

$$\frac{N_0(\text{Fall}) - N_0(\text{Winter})}{N_0(\text{Fall}) + N_0(\text{Winter})} \approx 0.29, \tag{7.42}$$

which is a very large effect. One should emphasize that the seasonal variation (7.42) cannot be directly compared with our estimate of parameter r which was computed for Summer-Winter modulation (7.41). This is due to the satellite's positions and the orientations of the detector, which will be discussed in chapter 7.4.2. The main lesson of our computations is that the annual modulation effect is very large, much larger than conventional WIMP models can predict [142, 143] which is normally on the level of 1-10%.

7.4.2 Effect of the satellite's position and orientation on its orbit

The previous calculations show that we should expect a seasonal modulation of the signal, which should be strongest in Summer, weakest in Winter, and equally half-way for Fall and Spring. This effect is entirely driven by the strength of the local dark matter wind speed. Compared to Fig. 7.1, one can see that this does not quite agree with the seasonal modulation measured by Ref. [10], as given by eq. (7.29). In their measurement, the Fall amplitude is the highest, and Summer and Spring are equal. However, as noted by Ref. [10], there are two additional factors which can change the seasonal modulation of the X-ray background significantly: the altitude of the telescope and the direction of the field-of-view (or beam). These factors are particularly important in the context of our model. Firstly, the altitude plays a role because, as shown by Eq. (7.37), an AQN's temperature upon exiting Earth decreases quickly with altitude. Therefore, if the telescope observes from a high altitude out, the X-ray background should be lower than if observed from a lower altitude. Secondly, the orientation of the telescope beam is also important. The X-ray background will indeed be stronger in the direction opposite to the incoming dark matter wind. This is caused by the fact that, on average, more heated AQNs will emerge from the side of the Earth opposite to the side where they preferentially entered from. Consequently, depending on the telescope position and orientation, the seasonal variation of the X-ray background can be altered. Fortunately, these are effects which can be completely accounted for, as long as the telescope's or-

bital parameters are known exactly. This is what Ref. [10] have done in their study for their specific solar-axion model. While their model has a number of fundamental major problems, as mentioned in chapter 7.1, the main point is that the seasonal variations as observed by XMM-Newton do not follow the standard annual modulation with a simple $\cos(\Omega t + \phi_0)$ form, as is normally expected [142, 143]. In particular, Fig. 5 from Ref. [10] shows that the seasonal variation predictions differ for different observing epochs, because of the particular telescope positions and orientations at those epochs. The resulting effect can significantly change the phase of the seasonal variation and the amplitude by approximately a factor of two.

The reason that this effect can be so strong is that the XMM-Newton is placed on a Highly-elliptical Earth Orbit (HEO), with an inclination of 40° relative to the ecliptic plane, a southern apogee altitude of ~ 115000 km, and a perigee of ~ 6000 km, with an orbital period of 48 hours. At apogee, it points towards the Sun in Summer and away from it in Winter. The exact prediction of the X-ray background becomes a highly non-trivial task, which requires precise knowledge of the telescope position and orientation for every data point being taken, which is beyond the scope of the present work.

At the same time, the obtained spectrum represents a very solid and robust result, which is not sensitive to the telescope's position and orientation. Furthermore, a strong seasonal variation (difference between maximum and minimum intensity) represented by eq. (7.41) is also a very solid and robust property of the AQN framework, not sensitive to any specific details of the model. The comparison of our prediction in X-ray to the signal measured by Ref. [10] strongly constrains the parameter κ, and very mildly constrains the initial temperature, $T_0 \in$ 200-500 keV. This is because AQNs with very different temperatures behave in a very similar way after the long journey of $t \geq 10^2$s, where XMM-Newton is operational at distances of $r \gtrsim 8R_\oplus$, as one can see from Fig. 7.3. The most important message here is that the intensity, spectrum, and magnitude of the seasonal variation on the level of 20-25%, measured by Ref. [10], can be naturally accommodated within the AQN framework, as argued in this chapter.

7.5 Conclusion

In this chapter, we computed the emission spectrum and intensity of AQNs after they leave the Earth in the region where XMM-Newton is operational.

The obtained results are consistent with the observations by [10]. The important point is that the shape of the spectrum is not sensitive to any details of the model, and this represents very solid and robust predictions of the AQN framework. In addition, we also computed the parameter r which represents the maximal range of seasonal variation. We found that $r \approx$ 20-25%, and it is not sensitive to the model parameters. However, r cannot be literally compared with observations by Ref. [10], due to the reasons explained in chapter 7.4.2.

In this chapter, we did not explore all of the possible sizes that AQNs can have. In contrast to the uniform size R and the uniform velocity $v_{\mathrm{DM_G}}$ of AQNs used in this chapter, the more realistic case is that the AQN size follows a distribution based on percolation theory (as we have studied in chapter 5), and the AQN velocity follows a Gaussian distribution [36] (see also Appendix B). These two distributions can be taken into consideration in future studies with the help of Monte Carlo simulations, similar to what we have done in chapter 6. The main points of the present work are expected to be further confirmed by the detailed numerical simulations at that time.

Another very important aspect of the work presented in this chapter is to open the possibility to make a robust prediction for near-Earth seasonal variations at higher energies. Such a prediction could provide a decisive test of the AQN model. As shown in this paper, the radiation spectrum extends well beyond 6 keV, and we are in a position to make a prediction in the γ-ray range. The Gamma-ray Burst Monitor (GBM) instrument on the Fermi Telescope has multi-year archival data of γ-ray background measurements in the near-Earth environment [146]. This would constitute the ideal data set to test our model because we are able to predict uniquely the X-ray background, as seen by XMM-Newton, and the γ-ray background, as seen by GBM. According to the AQN model, the two backgrounds, separated by two orders of magnitude in frequency, should share very similar properties, once the instrumental and astrophysical sources are removed. This exciting project is left for future work.

Chapter 8

Conclusions

In this thesis, we have discussed the recent developments in AQN model building and some potential observational evidence of AQNs based on the papers, Refs. [1–5]. In chapter 3, we focused on the AQN formation. We have studied the AQN formation in the background of the nonzero oscillating axion field. It is assumed that the PQ phase transition occurs before inflation (pre-inflationary scenario), so the axion field is coherent over the scale of the entire Universe. The coherent nonzero oscillating axion field can generate many CP-violating effects, which will finally lead to a disparity between matter and antimatter AQNs. We have analytically and numerically shown that the magnitude of the disparity is of order one, and it is insensitive to many model parameters. This result is important because it verifies that the basic relation $\Omega_{\rm DM} \sim \Omega_{\rm visible}$ is a natural result in the AQN model where the conventional baryogenesis process is replaced by the CP-violating charge separation process. In addition, we have obtained the real-time evolution of an AQN from its initial state (a closed axion domain wall with baryon charge induced on the wall) to its final stable CS state. To achieve this, we have overcome the so-called multi-scale problem ($\omega_R \tau_R \sim \Lambda_{\rm QCD}/m_a \sim 10^{10}$) that arises in numerically computing the AQN formation, with the help of envelope-following method. With an example, the result of real-time evolution has verified the basic features of the AQN model with $T_{\rm form} \sim 40$ MeV and $\mu_{\rm form} \gtrsim 450$ MeV. Such a large $\mu_{\rm form}$ is consistent with the formation of CS phase. The temperature scale ~ 40 MeV is related to the formation of the baryon-to-photon ratio observed today, eq. (2.2), based on completely different arguments (see e.g., Ref. [50]).

Next, in chapter 4, we have discussed the abundances of different com-

ponents of dark matter in the AQN framework. In particular, we have taken into consideration the contribution of free axion abundance from the misalignment mechanism along with the contribution of the AQN abundance. In addition, to describe the AQN abundance more precisely, we have incorporated several corrections to the AQN mass: the energy of the closed axion domain wall as the shell and the correction from the energy difference between CS and hadronic phases. As a consequence, we have obtained a quantitative expression of the parameter c that describes the disparity between matter and antimatter AQNs, based on the relations of different components of dark matter. Within the most region of available constraints on model parameters, $c \equiv B_+/B_-$ is an order-of-one quantity (roughly 0.4-0.6). This is consistent with chapter 3 which has studied the disparity from a different point of view, focusing on how the disparity builds during the process of AQN formation. For the most part of parameter space of m_a, θ_0, and H_I, we have found that the free axion abundance only accounts for a small portion of dark matter, while the AQN abundance dominates dark matter with an order-of-one c insensitive to model parameters, m_a, θ_0, and H_I. Again, this supposes the natural realization of the relation $\Omega_{\rm DM} \sim \Omega_{\rm visible}$ in the AQN model.

In chapter 5, we have studied the size distribution of AQNs. The AQN size at $T_{\rm form}$ depends on its initial conditions, R_0 and T_0. Based on percolation theory, we have found that the size distribution of AQNs follows of power-law, $dN/dB \sim B^{-\alpha}$. Furthermore, we have demonstrated that the size distribution can survive the subsequent evolution during pre-BBN, post-BBN, and post-recombination epochs after $T_{\rm form} \sim 40$ MeV, as long as $B_{\rm min} \gtrsim 10^{24}$. The exponent α can be expressed in terms of the parameter δ which is sensitive to the pattern of the formation of axion domain walls between $T_{\rm osc}$ and T_a, and cannot be predicted theoretically. On the other hand, the energy distribution of solar nanoflares also follows a power-law distribution. The match between the AQN size distribution and nanoflare energy distribution supports the claim that the "solar corona mystery" could be resolved by the AQN model with the nanoflares identified as the annihilation events of AQNs hitting the Sun [6, 28, 29].

In chapter 6, we have simulated AQNs impacting the Sun and the corresponding annihilation events using the Monte Carlo method. We have demonstrated that the impulsive radio events in quiet solar corona recorded by MWA [9] can be induced by the annihilation events of AQNs that enter the Sun. The frequency of appearance, the temporal and spatial distribu-

tions, the intensity, clustering events, etc., of the recorded impulsive radio events are consistent with the generic predictions of the AQN model. Furthermore, the AQN model predicts several features of the recorded impulsive radio events that could be tested in future studies. The clustering events discussed in chapter 6 have demonstrated the existence of correlation of radio events in the same frequency band. We predict that similar spatial correlations between radio events in different frequency bands also exist. The AQN model also predicts that in general the event rate is higher (lower) for emissions in higher (lower) frequency bands (but no higher than ~ 240 MHz because such emissions will be strongly absorbed [135]), but this prediction is subject to possible fluctuations due to specific local features of plasma and non-thermal electrons.

In chapter 7, we have calculated the emissivity of the AQN electrosphere in the high temperature range 200-500 keV acquired by AQNs due to the friction and annihilation events when they cross the Earth. When the hot AQNs leave the Earth, they emit photons in the space that can be detected by space telescopes such as XMM-Newton. We have shown that the corresponding spectrum generated by AQNs matches the observations by XMM-Newton [10]. Furthermore, the annual modulation of the speed of AQNs with respect to the Earth will finally lead to a seasonal variation of the near-Earth X-ray background. We have shown that the magnitude of the AQN-induced seasonal variation is large, on the level of 20-25%, which could potentially explain the observed seasonal variation of the near-Earth X-ray background in energy range 2-6 keV by XMM-Newton [10]. However, we have also demonstrated that our result of seasonal variation cannot be literally compared with the observations in Ref. [10]. This is because in our calculations we have fixed the position and orientation of XMM-Newton for simplicity, but in reality both the satellite's position and orientation vary on its orbit, which could greatly change the phase of seasonal variation. Nevertheless, the shape (not the magnitude) of the AQN-induced spectrum is robust, insensitive to the details of the satellite's position and orientation. The consistency between it and the observed spectra by XMM-Newton [10] indicates that the AQN model might be able to resolve the observed seasonal variation completely.

The AQN model was initially proposed to resolve the two basic problems: the nature of dark matter and the observed matter-antimatter asymmetry in the Universe, which could naturally answer why the dark matter and visible matter have similar abundances, $\Omega_{\rm DM} \sim \Omega_{\rm visible}$. In addition, the AQN model could potentially explain many puzzles and mysteries observed in astronomy

and cosmology, as we have listed in chapter 2, including the two cases that we have discussed in detail in chapter 6 and chapter 7. Finally, we want to emphasize that the AQN model could be tested by future observations or even current available data. In addition to the four frequency bands (98, 120, 132 and 160 MHz) of impulsive radio events that have been analyzed in Ref. [9], there are higher and lower frequency bands recorded by MWA at the same time, which could be used to test the feature of event rate predicted by the AQN model. The correlations of radio events in different frequency bands predicted by the AQN model could also be tested by current data or future observations. In addition, the AQN model could be tested by analyzing whether and how the MWA observations in radio frequency bands and Solar Orbiter observations in EUV frequency bands ("campfires", which might be explained as the annihilation events of large AQNs) correlate with each other. A different test is from our discussions in chapter 7. Our AQN-based calculations have shown that the seasonal-variation signal could extend up to ~ 100 keV of photon frequency, which could be tested by the archival data recorded by space telescopes such as the GBM on the Fermi telescope, NuSTAR, INTEGRAL, etc.

Bibliography

[1] S. Ge, X. Liang, and A. Zhitnitsky, "Cosmological CP-odd axion field as the coherent Berry's phase of the universe," *Physical Review D*, vol. 96, no. 6, p. 063514, 2017.

[2] S. Ge, X. Liang, and A. Zhitnitsky, "Cosmological axion and a quark nugget dark matter model," *Physical Review D*, vol. 97, no. 4, p. 043008, 2018.

[3] S. Ge, K. Lawson, and A. Zhitnitsky, "Axion quark nugget dark matter model: Size distribution and survival pattern," *Physical Review D*, vol. 99, no. 11, p. 116017, 2019.

[4] S. Ge, M. S. R. Siddiqui, L. Van Waerbeke, and A. Zhitnitsky, "Impulsive radio events in quiet solar corona and axion quark nugget dark matter," *Physical Review D*, vol. 102, no. 12, p. 123021, 2020.

[5] S. Ge, H. Rachmat, M. S. R. Siddiqui, L. Van Waerbeke, and A. Zhitnitsky, "X-ray annual modulation observed by XMM-Newton and axion quark nugget dark matter," *arXiv preprint arXiv:2004.00632*, 2020.

[6] N. Raza, L. van Waerbeke, and A. Zhitnitsky, "Solar corona heating by axion quark nugget dark matter," *Physical Review D*, vol. 98, no. 10, p. 103527, 2018.

[7] X. Liang and A. Zhitnitsky, "Axion field and the quark nugget's formation at the QCD phase transition," *Physical Review D*, vol. 94, no. 8, p. 083502, 2016.

[8] E. H. Avrett and R. Loeser, "Models of the solar chromosphere and transition region from SUMER and HRTS observations: formation of the extreme-ultraviolet spectrum of hydrogen, carbon, and oxygen,"

The Astrophysical Journal Supplement Series, vol. 175, no. 1, p. 229, 2008.

[9] S. Mondal, D. Oberoi, and A. Mohan, "First radio evidence for impulsive heating contribution to the quiet solar corona," *The Astrophysical Journal Letters*, vol. 895, no. 2, p. L39, 2020.

[10] G. W. Fraser, A. M. Read, S. Sembay, J. A. Carter, and E. Schyns, "Potential solar axion signatures in X-ray observations with the XMM–Newton observatory," *Monthly Notices of the Royal Astronomical Society*, vol. 445, no. 2, pp. 2146–2168, 2014.

[11] G. Bertone and T. M. Tait, "A new era in the search for dark matter," *Nature*, vol. 562, no. 7725, pp. 51–56, 2018.

[12] N. Aghanim *et al.*, "Planck 2018 results-VI. Cosmological parameters," *Astronomy & Astrophysics*, vol. 641, p. A6, 2020.

[13] A. R. Zhitnitsky, "'Nonbaryonic' dark matter as baryonic color superconductor," *Journal of Cosmology and Astroparticle Physics*, vol. 0310, p. 010, 2003.

[14] R. D. Peccei and H. R. Quinn, "CP conservation in the presence of pseudoparticles," *Physical Review Letters*, vol. 38, no. 25, p. 1440, 1977.

[15] R. D. Peccei and H. R. Quinn, "Constraints imposed by CP conservation in the presence of pseudoparticles," *Physical Review D*, vol. 16, no. 6, p. 1791, 1977.

[16] R. D. Peccei, "The strong CP problem and axions," in *Axions*, pp. 3–17, Springer, 2008.

[17] L. Di Luzio, M. Giannotti, E. Nardi, and L. Visinelli, "The landscape of QCD axion models," *Physics Reports*, 2020.

[18] S. Weinberg, "A new light boson?," *Physical Review Letters*, vol. 40, no. 4, p. 223, 1978.

[19] F. Wilczek, "Problem of strong p and t invariance in the presence of instantons," *Physical Review Letters*, vol. 40, no. 5, p. 279, 1978.

[20] J. E. Kim, "Weak-interaction singlet and strong CP invariance," *Physical Review Letters*, vol. 43, no. 2, p. 103, 1979.

[21] M. A. Shifman, A. Vainshtein, and V. I. Zakharov, "Can confinement ensure natural CP invariance of strong interactions?," *Nuclear Physics B*, vol. 166, no. 3, pp. 493–506, 1980.

[22] A. R. Zhitnitsky, "On possible suppression of the axion hadron interactions. (In Russian)," *Sov. J. Nucl. Phys.*, vol. 31, p. 260, 1980. [Yad. Fiz.31,497(1980)].

[23] M. Dine, W. Fischler, and M. Srednicki, "A simple solution to the strong CP problem with a harmless axion," *Physics letters B*, vol. 104, no. 3, pp. 199–202, 1981.

[24] D. J. Marsh, "Axion cosmology," *Physics Reports*, vol. 643, pp. 1–79, 2016.

[25] P. Sikivie, "Axion cosmology," in *Axions*, pp. 19–50, Springer, 2008.

[26] P. Sikivie, "Invisible axion search methods," *Reviews of Modern Physics*, vol. 93, no. 1, p. 015004, 2021.

[27] D. H. Oaknin and A. Zhitnitsky, "Baryon asymmetry, dark matter, and quantum chromodynamics," *Physical Review D*, vol. 71, no. 2, p. 023519, 2005.

[28] A. Zhitnitsky, "Solar Extreme UV radiation and quark nugget dark matter model," *Journal of Cosmology and Astroparticle Physics*, vol. 1710, no. 10, p. 050, 2017.

[29] A. Zhitnitsky, "Solar flares and the axion quark nugget dark matter model," *Physics of the Dark Universe*, vol. 22, pp. 1–15, 2018.

[30] A. Zhitnitsky, "DAMA/LIBRA annual modulation and axion quark nugget dark matter model," *Physical Review D*, vol. 101, no. 8, p. 083020, 2020.

[31] K. Lawson and A. Zhitnitsky, "The 21 cm absorption line and the axion quark nugget dark matter model," *Physics of the Dark Universe*, vol. 24, p. 100295, 2019.

[32] H. Fischer, X. Liang, A. Zhitnitsky, Y. Semertzidis, and K. Zioutas, "New mechanism producing axions in the aqn model and how the CAST can discover them," *Physical Review D*, vol. 98, no. 4, p. 043013, 2018.

[33] L. Van Waerbeke and A. Zhitnitsky, "Fast radio bursts and the axion quark nugget dark matter model," *Physical Review D*, vol. 99, no. 4, p. 043535, 2019.

[34] X. Liang and A. Zhitnitsky, "Gravitationally bound axions and how one can discover them," *Physical Review D*, vol. 99, no. 2, p. 023015, 2019.

[35] V. V. Flambaum and A. R. Zhitnitsky, "Primordial lithium puzzle and the axion quark nugget dark matter model," *Physical Review D*, vol. 99, no. 2, p. 023517, 2019.

[36] K. Lawson, X. Liang, A. Mead, M. S. R. Siddiqui, L. Van Waerbeke, and A. Zhitnitsky, "Gravitationally trapped axions on Earth," *Physical Review D*, vol. 100, no. 4, p. 043531, 2019.

[37] X. Liang, A. Mead, M. S. R. Siddiqui, L. Van Waerbeke, and A. Zhitnitsky, "Axion quark nugget dark matter: Time modulations and amplifications," *Physical Review D*, vol. 101, no. 4, p. 043512, 2020.

[38] D. Budker, V. V. Flambaum, X. Liang, and A. Zhitnitsky, "Axion quark nuggets and how a global network can discover them," *Physical Review D*, vol. 101, no. 4, p. 043012, 2020.

[39] D. Budker, V. V. Flambaum, and A. Zhitnitsky, "Infrasonic, acoustic and seismic waves produced by the axion quark nuggets," *arXiv preprint arXiv:2003.07363*, 2020.

[40] A. Zhitnitsky, "The mysterious bursts observed by telescope array and axion quark nuggets," *Journal of Physics G: Nuclear and Particle Physics*, vol. 48, no. 6, p. 065201, 2021.

[41] X. Liang, E. Peshkov, L. Van Waerbeke, and A. Zhitnitsky, "A proposed network to detect axion quark nugget dark matter," *Physical Review D*, vol. 103, no. 9, p. 096001, 2021.

[42] X. Liang and A. Zhitnitsky, "Telescope array bursts, radio pulses and axion quark nuggets," *arXiv preprint arXiv:2101.01722*, 2021.

[43] E. Witten, "Cosmic separation of phases," *Physical Review D*, vol. 30, no. 2, p. 272, 1984.

[44] E. Farhi and R. L. Jaffe, "Strange matter," *Physical Review D*, vol. 30, no. 11, p. 2379, 1984.

[45] A. De Rújula and S. L. Glashow, "Nuclearites—a novel form of cosmic radiation," *Nature*, vol. 312, no. 5996, pp. 734–737, 1984.

[46] J. Madsen, "Physics and astrophysics of strange quark matter," in *Hadrons in dense matter and hadrosynthesis*, pp. 162–203, Springer, 1999.

[47] J. Preskill, M. B. Wise, and F. Wilczek, "Cosmology of the invisible axion," *Physics Letters B*, vol. 120, no. 1-3, pp. 127–132, 1983.

[48] L. F. Abbott and P. Sikivie, "A cosmological bound on the invisible axion," *Physics Letters B*, vol. 120, no. 1-3, pp. 133–136, 1983.

[49] M. Dine and W. Fischler, "The not-so-harmless axion," *Physics Letters B*, vol. 120, no. 1-3, pp. 137–141, 1983.

[50] E. W. Kolb and M. S. Turner, "The early universe," *Nature*, vol. 294, no. 5841, pp. 521–526, 1981.

[51] M. G. Alford, A. Schmitt, K. Rajagopal, and T. Schäfer, "Color superconductivity in dense quark matter," *Reviews of Modern Physics*, vol. 80, pp. 1455–1515, 2008.

[52] A. Zhitnitsky, "Cold dark matter as compact composite objects," *Physical Review D*, vol. 74, p. 043515, 2006.

[53] D. H. Oaknin and A. R. Zhitnitsky, "511-KeV photons from color superconducting dark matter," *Physical Review Letters*, vol. 94, p. 101301, 2005.

[54] A. Zhitnitsky, "The width of the 511-kev line from the bulge of the galaxy," *Physical Review D*, vol. 76, p. 103518, 2007.

[55] M. M. Forbes and A. R. Zhitnitsky, "Diffuse x-rays: Directly observing dark matter?," *Journal of Cosmology and Astroparticle Physics*, vol. 0801, p. 023, 2008.

[56] K. Lawson and A. R. Zhitnitsky, "Diffuse cosmic gamma rays at 1–20 MeV: a trace of the dark matter?," *Journal of Cosmology and Astroparticle Physics*, vol. 2008, no. 01, p. 022, 2008.

[57] M. M. Forbes and A. R. Zhitnitsky, "WMAP haze: Directly observing dark matter?," *Physical Review D*, vol. 78, p. 083505, 2008.

[58] M. M. Forbes, K. Lawson, and A. R. Zhitnitsky, "The electrosphere of macroscopic 'quark nuclei': A source for diffuse MeV emissions from dark matter," *Physical Review D*, vol. 82, p. 083510, 2010.

[59] M. G. Aartsen *et al.*, "Search for non-relativistic magnetic monopoles with IceCube," *The European Physical Journal C*, vol. 74, no. 7, p. 2938, 2014. [Erratum: Eur.Phys.J.C 79, 124 (2019)].

[60] P. W. Gorham, "Antiquark nuggets as dark matter: New constraints and detection prospects," *Physical Review D*, vol. 86, no. 12, p. 123005, 2012.

[61] D. M. Jacobs, G. D. Starkman, and B. W. Lynn, "Macro dark matter," *Monthly Notices of the Royal Astronomical Society*, vol. 450, no. 4, pp. 3418–3430, 2015.

[62] E. T. Herrin, D. C. Rosenbaum, and V. L. Teplitz, "Seismic search for strange quark nuggets," *Physical Review D*, vol. 73, no. 4, p. 043511, 2006.

[63] D. Cyncynates, J. Chiel, J. Sidhu, and G. D. Starkman, "Reconsidering seismological constraints on the available parameter space of macroscopic dark matter," *Physical Review D*, vol. 95, no. 6, p. 063006, 2017.

[64] J. S. Sidhu, R. J. Scherrer, and G. Starkman, "Antimatter as macroscopic dark matter," *Physics Letters B*, vol. 807, p. 135574, 2020.

[65] J. S. Sidhu, R. Scherrer, and G. Starkman, "Death and serious injury from dark matter," *Physics Letters B*, vol. 803, p. 135300, 2020.

[66] A. Pauluhn and S. K. Solanki, "A nanoflare model of quiet Sun EUV emission," *Astronomy & Astrophysics*, vol. 462, p. 311, 2007.

[67] Bingert, S. and Peter, H., "Nanoflare statistics in an active region 3D MHD coronal model," *Astronomy & Astrophysics*, vol. 550, p. A30, 2013.

[68] E. Witten, "Large N chiral dynamics," *Annals of Physics*, vol. 128, p. 363, 1980.

[69] E. Witten, "Theta dependence in the large N limit of four-dimensional gauge theories," *Physical Review Letters*, vol. 81, pp. 2862–2865, 1998.

[70] S. Coleman, "Quantum sine-Gordon equation as the massive Thirring model," *Physical Review D*, vol. 11, pp. 2088–2097, 1975.

[71] S. Mandelstam, "Soliton operators for the quantized sine-Gordon equation," *Physical Review D*, vol. 11, pp. 3026–3030, 1975.

[72] P. Sikivie, "Axions, domain walls, and the early universe," *Physical Review Letters*, vol. 48, no. 17, p. 1156, 1982.

[73] A. Vilenkin and A. E. Everett, "Cosmic strings and domain walls in models with Goldstone and pseudo-Goldstone bosons," *Physical Review Letters*, vol. 48, no. 26, p. 1867, 1982.

[74] M. M. Forbes and A. R. Zhitnitsky, "Domain walls in QCD," *Journal of High Energy Physics*, vol. 2001, no. 10, p. 013, 2001.

[75] G. Gabadadze and M. Shifman, "Vacuum structure and the axion walls in gluodynamics and QCD with light quarks," *Physical Review D*, vol. 62, no. 11, p. 114003, 2000.

[76] D. Son, M. A. Stephanov, and A. Zhitnitsky, "Domain walls of high-density QCD," *Physical Review Letters*, vol. 86, no. 18, p. 3955, 2001.

[77] T. W. B. Kibble, "Topology of cosmic domains and strings," *Journal of Physics A: Mathematical and General*, vol. 9, pp. 1387–1398, 1976.

[78] W. H. Zurek, "Cosmological experiments in superfluid helium?," *Nature*, vol. 317, pp. 505–508, 1985.

[79] S. Borsanyi *et al.*, "Calculation of the axion mass based on high-temperature lattice quantum chromodynamics," *Nature*, vol. 539, no. 7627, pp. 69–71, 2016.

[80] T. Vachaspati and A. Vilenkin, "Formation and evolution of cosmic strings," *Physical Review D*, vol. 30, no. 10, p. 2036, 1984.

[81] S. Chang, C. Hagmann, and P. Sikivie, "Studies of the motion and decay of axion walls bounded by strings," *Physical Review D*, vol. 59, no. 2, p. 023505, 1998.

[82] K. Rajagopal and F. Wilczek, "The condensed matter physics of QCD," in *At The Frontier of Particle Physics: Handbook of QCD (In 3 Volumes)*, pp. 2061–2151, World Scientific, 2001.

[83] M. M. Forbes and A. Zhitnitsky, "Primordial galactic magnetic fields from domain walls at the QCD phase transition," *Physical Review Letters*, vol. 85, no. 25, p. 5268, 2000.

[84] M. M. Forbes and A. R. Zhitnitsky, "Primordial galactic magnetic fields: An application of QCD domain walls," *arXiv preprint hep-ph/0102158*, 2001.

[85] J.-W. Chen and E. Nakano, "Shear viscosity to entropy density ratio of QCD below the deconfinement temperature," *Physics Letters B*, vol. 647, no. 5-6, pp. 371–375, 2007.

[86] O. Wantz and E. Shellard, "Axion cosmology revisited," *Physical Review D*, vol. 82, no. 12, p. 123508, 2010.

[87] O. Wantz and E. Shellard, "The topological susceptibility from grand canonical simulations in the interacting instanton liquid model: chiral phase transition and axion mass," *Nuclear physics B*, vol. 829, no. 1-2, pp. 110–160, 2010.

[88] P. Arnold, G. D. Moore, and L. G. Yaffe, "Transport coefficients in high temperature gauge theories (i): leading-log results," *Journal of High Energy Physics*, vol. 2000, no. 11, p. 001, 2000.

[89] P. Kovtun, D. T. Son, and A. O. Starinets, "Viscosity in strongly interacting quantum field theories from black hole physics," *Physical Review Letters*, vol. 94, no. 11, p. 111601, 2005.

[90] L. Fleury and G. D. Moore, "Axion dark matter: strings and their cores," *Journal of Cosmology and Astroparticle Physics*, vol. 2016, no. 01, p. 004, 2016.

[91] V. B. Klaer and G. D. Moore, "The dark-matter axion mass," *Journal of Cosmology and Astroparticle Physics*, vol. 2017, no. 11, p. 049, 2017.

[92] M. Gorghetto, E. Hardy, and G. Villadoro, "Axions from strings: the attractive solution," *Journal of High Energy Physics*, vol. 2018, no. 7, p. 151, 2018.

[93] L. R. Petzold, "An efficient numerical method for highly oscillatory ordinary differential equations," *SIAM Journal on Numerical Analysis*, vol. 18, no. 3, pp. 455–479, 1981.

[94] D. Baumann, "University lecture notes," *http://cosmology.amsterdam/education/cosmology/*.

[95] T. Hiramatsu, M. Kawasaki, K. Saikawa, and T. Sekiguchi, "Production of dark matter axions from collapse of string-wall systems," *Physical Review D*, vol. 85, no. 10, p. 105020, 2012.

[96] M. Kawasaki, K. Saikawa, and T. Sekiguchi, "Axion dark matter from topological defects," *Physical Review D*, vol. 91, no. 6, p. 065014, 2015.

[97] M. Buschmann, J. W. Foster, and B. R. Safdi, "Early-universe simulations of the cosmological axion," *Physical Review Letters*, vol. 124, no. 16, p. 161103, 2020.

[98] L. Visinelli and P. Gondolo, "Dark matter axions revisited," *Physical Review D*, vol. 80, no. 3, p. 035024, 2009.

[99] T. Kojo, P. D. Powell, Y. Song, and G. Baym, "Phenomenological QCD equation of state for massive neutron stars," *Physical Review D*, vol. 91, no. 4, p. 045003, 2015.

[100] G. G. Raffelt, "Astrophysical axion bounds," in *Axions*, pp. 51–71, Springer, 2008.

[101] A. Arvanitaki, M. Baryakhtar, and X. Huang, "Discovering the QCD axion with black holes and gravitational waves," *Physical Review D*, vol. 91, no. 8, p. 084011, 2015.

[102] P. W. Graham, I. G. Irastorza, S. K. Lamoreaux, A. Lindner, and K. A. van Bibber, "Experimental searches for the axion and axion-like particles," *Annual Review of Nuclear and Particle Science*, vol. 65, pp. 485–514, 2015.

[103] P. A. R. Ade *et al.*, "Joint analysis of BICEP2/Keck Array and Planck data," *Physical Review Letters*, vol. 114, no. 10, p. 101301, 2015.

[104] A. D. Linde, "Generation of isothermal density perturbations in the inflationary universe," *Physics Letters B*, vol. 158, no. 5, pp. 375–380, 1985.

[105] D. Seckel and M. S. Turner, ""Isothermal" density perturbations in an axion-dominated inflationary universe," *Physical Review D*, vol. 32, no. 12, p. 3178, 1985.

[106] M. P. Hertzberg, M. Tegmark, and F. Wilczek, "Axion cosmology and the energy scale of inflation," *Physical Review D*, vol. 78, no. 8, p. 083507, 2008.

[107] J. Hamann, S. Hannestad, G. G. Raffelt, and Y. Y. Wong, "Isocurvature forecast in the anthropic axion window," *Journal of Cosmology and Astroparticle Physics*, vol. 2009, no. 06, p. 022, 2009.

[108] T. Kobayashi, R. Kurematsu, and F. Takahashi, "Isocurvature constraints and anharmonic effects on QCD axion dark matter," *Journal of Cosmology and Astroparticle Physics*, vol. 2013, no. 09, p. 032, 2013.

[109] D. Stauffer, "Scaling theory of percolation clusters," *Physics Reports*, vol. 54, no. 1, pp. 1 – 74, 1979.

[110] D. Stauffer and A. Aharony, *Introduction to percolation theory: revised second edition*. CRC press, 2014.

[111] K. Bauchspiess and D. Stauffer, "Use of percolation clusters in nucleation theory," *Journal of Aerosol Science*, vol. 9, no. 6, pp. 567 – 577, 1978.

[112] M. B. Isichenko, "Percolation, statistical topography, and transport in random media," *Reviews of Modern Physics*, vol. 64, no. 4, p. 961, 1992.

[113] P. Grinchuk, "Large clusters in supercritical percolation," *Physical Review E*, vol. 66, no. 1, p. 016124, 2002.

[114] T. Lubensky and A. McKane, "Cluster size distribution above the percolation threshold," *Journal of Physics A: Mathematical and General*, vol. 14, no. 5, p. L157, 1981.

[115] T. Vachaspati, "Lunar mass black holes from QCD axion cosmology," *arXiv preprint arXiv:1706.03868*, 2017.

[116] N. Yoshida, K. Omukai, L. Hernquist, and T. Abel, "Formation of primordial stars in a lambda-CDM universe," *The Astrophysical Journal*, vol. 652, pp. 6–25, 2006.

[117] E. N. Parker, "Nanoflares and the solar X-ray corona," *The Astrophysical Journal*, vol. 330, pp. 474–479, 1988.

[118] S. Krucker and A. O. Benz, "Are heating events in the quiet solar corona small flares? multiwavelength observations of individual events," *Solar Physics*, vol. 191, pp. 341–358, 2000.

[119] A. O. Benz and S. Krucker, "Heating the quiet corona by nanoflares: Evidence and problems," in *Recent Insights into the Physics of the Sun and Heliosphere: Highlights from SOHO and Other Space Missions* (P. Brekke, B. Fleck, and J. B. Gurman, eds.), vol. 203 of *IAU Symposium*, p. 471, 2001.

[120] U. Mitra-Kraev and A. O. Benz, "A nanoflare heating model for the quiet solar corona," *Astronomy & Astrophysics*, vol. 373, pp. 318–328, 2001.

[121] A. O. Benz and S. Krucker, "Energy distribution of microevents in the quiet solar corona," *The Astrophysical Journal*, vol. 568, pp. 413–421, 2002.

[122] A. O. Benz and P. C. Grigis, "Micro-events in the active and quiet solar corona," *Advances in Space Research*, vol. 32, pp. 1035–1042, 2003.

[123] I. G. Hannah, S. Christe, S. Krucker, G. J. Hurford, H. S. Hudson, and R. P. Lin, "RHESSI microflare statistics. II. X-ray imaging, spectroscopy, and energy distributions," *The Astrophysical Journal*, vol. 677, pp. 704–718, 2008.

[124] S. Terzo, F. Reale, M. Miceli, J. A. Klimchuk, R. Kano, and S. Tsuneta, "Widespread nanoflare variability detected with Hinode/X-ray telescope in a solar active region," *The Astrophysical Journal*, vol. 736, p. 111, 2011.

[125] S. J. Bradshaw, J. A. Klimchuk, and J. W. Reep, "Diagnosing the time-dependence of active region core heating from the emission measure. I. low-frequency nanoflares," *The Astrophysical Journal*, vol. 758, p. 53, 2012.

[126] D. B. Jess, M. Mathioudakis, and P. H. Keys, "Nanoflare activity in the solar chromosphere," *The Astrophysical Journal*, vol. 795, p. 172, 2014.

[127] A. S. Kirichenko and S. A. Bogachev, "Plasma heating in solar microflares: Statistics and analysis," *The Astrophysical Journal*, vol. 840, p. 45, 2017.

[128] C. Mac Cormack, A. M. Vásquez, M. López Fuentes, F. A. Nuevo, E. Landi, and R. A. Frazin, "Energy input flux in the global quiet-Sun corona," *The Astrophysical Journal*, vol. 843, p. 70, 2017.

[129] J. A. Klimchuk, "On solving the coronal heating problem," *Solar Physics*, vol. 234, pp. 41–77, 2006.

[130] J. A. Klimchuk, "Nanoflare heating: Observations and theory," *arXiv preprint arXiv:1709.07320*, 2017.

[131] S. Bertolucci, K. Zioutas, S. Hofmann, and M. Maroudas, "The Sun and its Planets as detectors for invisible matter," *Physics of the Dark Universe*, vol. 17, pp. 13–21, 2017.

[132] G. Thejappa, "A self-consistent model for the storm radio emission from the Sun," *Solar Physics*, vol. 132, no. 1, pp. 173–193, 1991.

[133] R. Sharma, D. Oberoi, and M. Arjunwadkar, "Quantifying weak non-thermal solar radio emission at low radio frequencies," *The Astrophysical Journal*, vol. 852, p. 69, jan 2018.

[134] D. Oberoi, R. Sharma, and A. E. E. Rogers, "Estimating solar flux density at low radio frequencies using a sky brightness model," *Solar Physics*, vol. 292, p. 75, 2017.

[135] M. S. Wheatland, P. A. Sturrock, and J. M. McTiernan, "The waiting-time distribution of solar flare hard X-ray bursts," *The Astrophysical Journal*, vol. 509, pp. 448–455, dec 1998.

[136] M. J. Aschwanden and J. M. McTiernan, "Reconciliation of waiting time statistics of solar flares observed in hard X-rays," *The Astrophysical Journal*, vol. 717, pp. 683–692, jun 2010.

[137] C. Li, S. J. Zhong, L. Wang, W. Su, and C. Fang, "Waiting time distribution of solar energetic particle events modeled with a non-stationary Poisson process," *The Astrophysical Journal*, vol. 792, p. L26, aug 2014.

[138] L. Dilella and K. Zioutas, "Observational evidence for gravitationally trapped massive axion(-like) particles," *Astroparticle Physics*, vol. 19, pp. 145–170, 2003.

[139] H. Davoudiasl and P. Huber, "Detecting solar axions using earth's magnetic field," *Physical Review Letters*, vol. 97, p. 141302, 2006.

[140] H. Davoudiasl and P. Huber, "Feasibility study for measuring geomagnetic conversion of solar axions to X-rays in low earth orbits," *Journal of Cosmology and Astroparticle Physics*, vol. 0808, p. 026, 2008.

[141] M. Roncadelli and F. Tavecchio, "No axions from the sun," *Monthly Notices of the Royal Astronomical Society: Letters*, vol. 450, no. 1, pp. L26–L28, 2015.

[142] K. Freese, J. A. Frieman, and A. Gould, "Signal modulation in cold dark matter detection," *Physical Review D*, vol. 37, pp. 3388–3405, 1988.

[143] K. Freese, M. Lisanti, and C. Savage, "Colloquium: Annual modulation of dark matter," *Reviews of Modern Physics*, vol. 85, pp. 1561–1581, 2013.

[144] ESA:XMM-NewtonSOC, "XMM-Newton users' handbook," *http://xmm-tools.cosmos.esa.int/external/xmm_user_support/documentation/uhb/XMM_UHB.pdf*, Issue 2.17, 2019.

[145] M. Santos-Lleó *et al.*, "The life cycle of XMM-Newton's 'Targets of Opportunity'," *ESA Bulletin*, vol. 107, pp. 54–62, 2001.

[146] C. Meegan *et al.*, "The Fermi Gamma-ray Burst Monitor," *The Astrophysical Journal*, vol. 702, no. 1, pp. 791–804, 2009.

Appendix A

Calculation of the baryon charge distribution dN/dB

This appendix is adapted from Ref. [3]. In this appendix, we will show the details of calculating eq. (5.6) and eq. (5.12), to support the results in chapter 5.1.4. We first rewrite eq. (5.6) as

$$N(B) = N_0 P \int_{T_c}^{T_c \cdot \left[B/(K\xi_{\min}^3 T_c^3)\right]^{1/[3(\beta+1)]}} dT_0 \int_{\xi(T_0)}^{\left[B/(KT_0^3)\right]^{1/3}} dR_0 \; f \qquad \text{(A.1)}$$

with the limits of integration written explicitly, which can be explained as follows. The integral (A.1) is performed over the region $KR_0^3T_0^3 \leq B$ with the constraints $T_c \lesssim T_0 \lesssim T_{\rm osc}$ and $R_0 \gtrsim \xi(T_0)$ from the model of T_0 and R_0 distributions. We show the region of integration in Fig. A.1, where the parameter space enclosed by $T_c \lesssim T_0 \lesssim T_{\rm osc}$ and $R_0 \gtrsim \xi(T_0)$ is represented by the colored region. The green lines are the contour lines of B with $KR_0^3T_0^3 = B$ for different values of B. The region of integration is the area enclosed by the solid black lines and one of the green lines (to the left of the green line), from which we can obtain the limits of integration. The lower limit of R_0 is $R_{\rm lower} = \xi(T_0)$; the upper limit of R_0 is on the green line, $R_{\rm upper} = [B/(KT_0^3)]^{1/3}$; the lower limit of T_0 is T_c. The upper limit of T_0 is a little complicated: it could either be the intersection of the line $\xi(T_0)$ and the green line, $T_{\rm upper} = T_c \cdot [B/(K\xi_{\min}^3 T_c^3)]^{1/3(\beta+1)}$, or simply $T_{\rm upper} = T_{\rm osc}$, depending on different values of B. However, we are not likely to have the chance to use the latter case that $T_{\rm upper} = T_{\rm osc}$ as the upper limit of T_0, which is explained as follows.

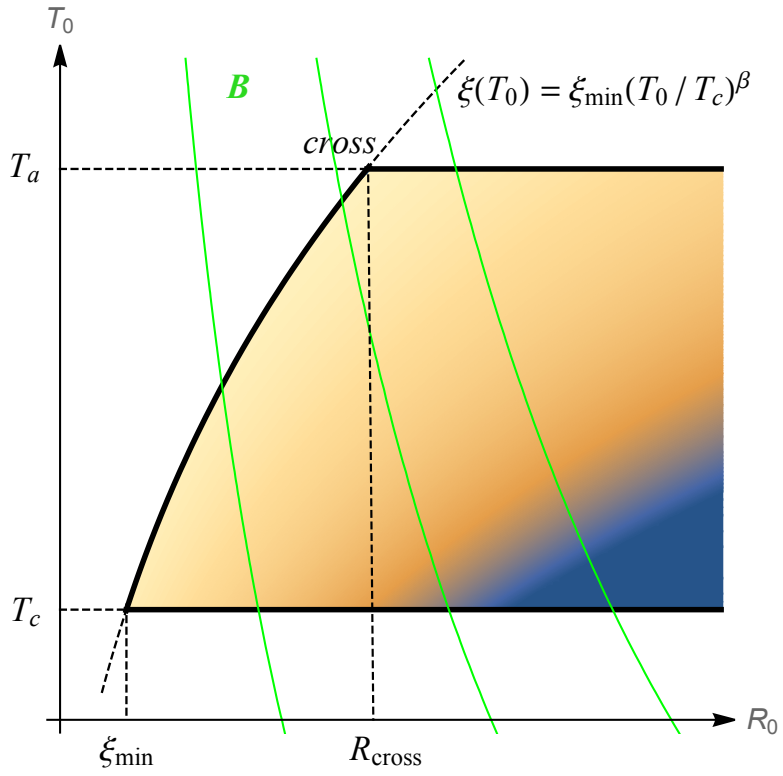

Figure A.1: Parameter space of R_0 and T_0. The colored region represents the initially allowed (R_0, T_0) for the formation of closed domain walls. Different colors represent different magnitudes of $f(R_0, T_0)$ which decreases from the light yellow part to the deep blue part (gradually away from the correlation length $\xi(T_0)$). The green lines are the contour lines of B, i.e., each line corresponds to the same value of B, with B increasing from left to the right. $T_a \equiv T_{\text{osc}}$. This figure is taken from Ref. [3].

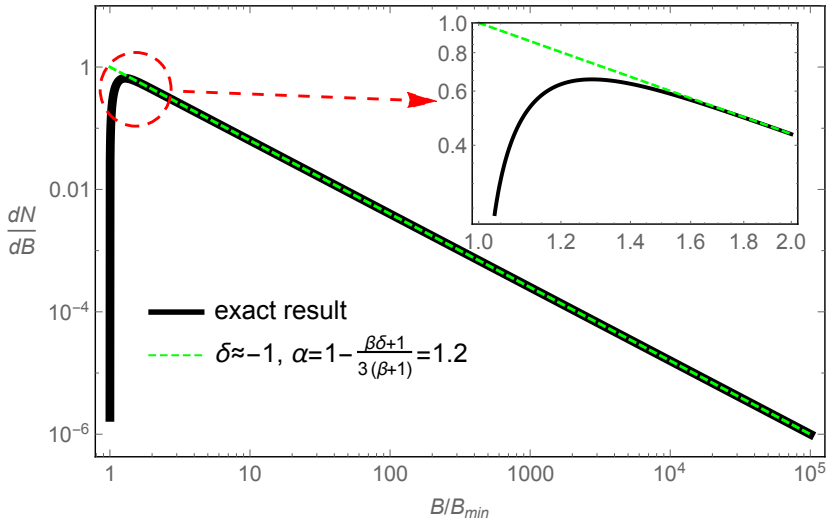

(a)

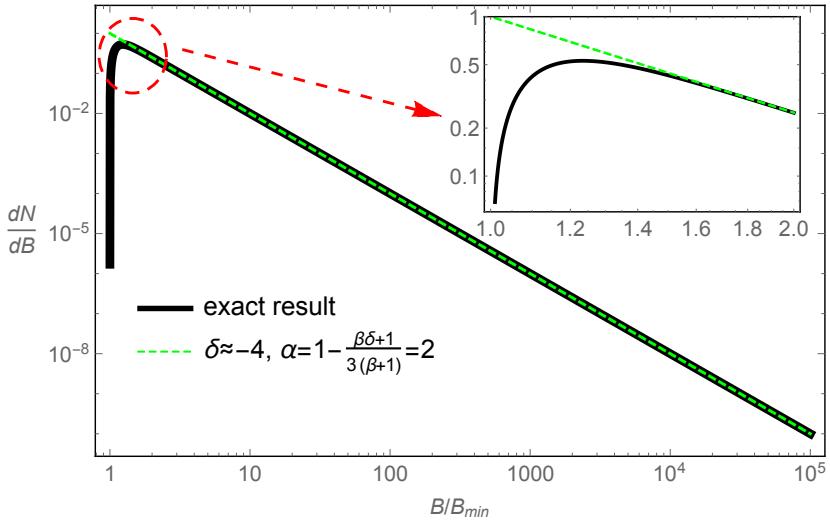

(b)

Figure A.2: The relation between dN/dB and $b \equiv B/B_{\rm min}$. We choose $\tau = 2$, $\lambda = 10$ and $\beta = 3.925$ for both panels. The difference between (a) and (b) is the values of δ. In panel (a), $\delta \approx -1$ and thus $\alpha = 1.2$; in panel (b), we choose $\delta \approx -4$ to make $\alpha = 2$. The solid black dashed green lines in each panel represent eq. (A.5) and eq. (A.8) respectively (the prefactor $N_0 P/B_{\rm min}$ in the two equations is rescaled to completely show dN/dB in the range from 0 to 1 for illustrative purposes). This figure is taken from Ref. [3].

If we want the upper limit of T_0 in the integration to be $T_{\rm osc}$, B has to be larger than $B_{\rm cross} = K\xi^3(T_{\rm osc})T_{\rm osc}^3$ which is the value of B at the crossing point where the line $\xi(T_0)$ intersects the horizontal line $T_0 = T_{\rm osc}$. We should compare $B_{\rm cross}$ with the minimal baryon charge $B_{\rm min} = K\xi_{\rm min}^3 T_c^3$ which corresponds to the closed domain wall formed at $T_0 = T_c$ with $R_0 = \xi_{\rm min}$. We get

$$B_{\rm cross} = \left(\frac{T_{\rm osc}}{T_c}\right)^{3(\beta+1)} B_{\rm min} \simeq 10^{15} B_{\rm min} \tag{A.2}$$

where we approximate it using $T_{\rm osc}/T_c \simeq 10$ and $\beta \simeq 3.925$. We see that the range is 15 orders of magnitude wide, which is large enough for us to match the baryon charge distribution of AQNs with the energy distribution of solar nanoflares. Therefore, we choose T_0 as $T_{\rm upper} = T_c \cdot [B/(K\xi_{\rm min}^3 T_c^3)]^{1/[3(\beta+1)]}$ for the upper limit in eq. (A.1).

Next, we are going to calculate eq. (A.1). Using the definitions $r = R_0/\xi_{\rm min}$ and $u = T_0/T_c$, we rewrite eq. (5.12) in a more concise way

$$f(r,u) = \frac{1}{\xi_{\rm min} T_c} \cdot u^{3\beta(\tau-1)+\beta\delta} \cdot r^{2-3\tau} \cdot {\rm e}^{-\lambda r^2 u^{-2\beta}}. \tag{A.3}$$

Substituting $f(r,u)$ into eq. (A.1) and using the definition $b = B/B_{\rm min}$, we arrive at

$$\begin{aligned} N(b) &= N_0 P \cdot T_c \xi_{\rm min} \int_1^{b^{\frac{1}{3(\beta+1)}}} du \int_{u^\beta}^{u^{-1} b^{\frac{1}{3}}} dr \; f(r,u) \\ &= N_0 P \int_1^{b^{\frac{1}{3(\beta+1)}}} du \int_{u^\beta}^{u^{-1} b^{\frac{1}{3}}} dr \; \left[u^{3\beta(\tau-1)+\beta\delta} \cdot r^{2-3\tau} \cdot {\rm e}^{-\lambda r^2 u^{-2\beta}}\right], \end{aligned} \tag{A.4}$$

from which we further get

$$\frac{dN}{dB} = \frac{1}{B_{\rm min}} \frac{dN}{db} = \frac{N_0 P}{3 B_{\rm min}} \cdot b^{-\tau} \int_1^{b^{\frac{1}{3(\beta+1)}}} du \; u^{3(\beta+1)(\tau-1)+\beta\delta} \cdot {\rm e}^{-\lambda b^{\frac{2}{3}} u^{-2(\beta+1)}}. \tag{A.5}$$

This can be further simplified using the relation

$$\int_1^{b^{\frac{1}{3(\beta+1)}}} dt\ u^m \mathrm{e}^{-\lambda b^{2/3} u^{-n}} = \frac{1}{n}(\lambda b^{2/3})^{\frac{1+m}{n}} \cdot \Gamma(-\frac{1+m}{n}, \lambda b^{\frac{2}{3}} u^{-n})\Big|_{u=1}^{u=b^{\frac{1}{3(\beta+1)}}}$$
$$\simeq \frac{1}{n}(\lambda b^{2/3})^{\frac{1+m}{n}} \cdot \Gamma(-\frac{1+m}{n}, \lambda), \qquad \text{for } b \gg 1, \tag{A.6}$$

where $m \equiv 3(\beta+1)(\tau-1)+\beta\delta$ and $n \equiv 2(\beta+1)$; $\Gamma(s,x) = \int_x^\infty t^{s-1}\mathrm{e}^{-t}dt$ is the *incomplete gamma function*. To obtain the last approximate equality, we neglect the term $\Gamma(-\frac{1+m}{n}, \lambda b^{2/3})$ since it is far smaller than the term $\Gamma(-\frac{1+m}{n}, \lambda)$ for $b \gg 1$. The condition $b \gg 1$ is satisfied in a wide range of B values, which are generally several orders larger than $B_{\min}$. Substituting (A.6) into (A.5), we arrive at

$$\frac{dN}{dB} = \frac{N_0 P}{3B_{\min}} \frac{1}{n} \lambda^{\frac{1+m}{n}} \Gamma(-\frac{1+m}{n}, \lambda) \cdot b^{-1+\frac{\beta\delta+1}{3(\beta+1)}}, \qquad b \gg 1. \tag{A.7}$$

We see that dN/dB follows a power-law distribution,

$$\frac{dN}{dB} \propto b^{-\alpha}, \text{ with } \alpha = 1 - \frac{\beta\delta+1}{3(\beta+1)}, \qquad b \gg 1 \tag{A.8}$$

which verifies the relation (5.15). The finite-cluster parameters τ (contained in m) and λ that we have discussed in chapter 5.1.2 only affect the relative magnitude of dN/dB, but not the slope of the power-law distribution $-\alpha$.

The parameter β describing the relation between axion mass and cosmological temperature is well calculated; see eq.(3.37). The other parameter δ from the model of T_0 distribution eq. (5.11) is relatively adjustable, which can result in different slopes of the power-law distribution dN/dB. This parameter (which may have any sign) describes the distribution of the bubble formation. As we explained in the main text, the positive sign of δ corresponds to the preference of the bubble formation close to $T_{\rm osc}$, while the negative δ corresponds to the preference for bubble formation close to T_c with a much stronger tilt of the axion potential.

We plot the baryon charge distribution of AQNs in Fig. A.2. We choose $\tau = 2$, $\lambda = 10$ and $\beta = 3.925$ for both panels. The difference between them is the value of δ which is highly underdetermined. In Fig. A.2a, we choose $\delta \approx -1$ to make $\alpha = 1.2$. The solid black line is the plot of eq. (A.5), which

represents the exact result of the distribution. As a comparison, we also plot the approximate relation (A.8) represented by the dashed green line, which is straight in the log-log scale. We see that the approximate relation (A.8) matches the exact result eq. (A.5) pretty well after the turning point where the condition $b \gg 1$ becomes valid. In Fig. A.2b, we consider the case $\delta \approx -4$ which corresponds to $\alpha = 2$. All other ingredients are the same as the first panel.

Appendix B

Simulation of AQNs in the Solar Atmosphere

This appendix is adapted from Ref. [4]. The appendix shows the details of the MC simulation for AQNs (to be specific, antimatter AQNs) hitting the Sun and their evolution in the solar atmosphere before getting completely annihilated, which aims to support the discussions in chapter 6.

B.1 Simulation setup

The setup of the simulation in the present work follows that in Ref. [6], which can be divided into three steps. The first step is to use the MC method to generate a large number of dark matter particles in the solar neighborhood and collect the ones that will eventually impact the Sun. The second step is to assign AQN masses to the particles. We will use different models of the AQN mass distributions (as shown in (6.5)). The third step is to solve the multiple differential equations that dominate the annihilation process of AQNs in the solar atmosphere.

Step 1. In this step, we simulate the positions and velocities of dark matter particles in the solar neighborhood. The velocity distribution of the dark matter particles, with respect to the solar system frame, follows a Maxwellian distribution:

$$f_{\vec{v}}(\vec{v})d^3\vec{v} = \frac{d^3\vec{v}}{(2\pi\sigma^2)^{3/2}} \exp\left[-\frac{v_x^2 + v_y^2 + (v_z - v_\odot)^2}{2\sigma^2}\right] \tag{B.1}$$

where the velocity dispersion is $\sigma \simeq 110$ km/s, and the velocity shift $v_\odot \simeq 220$ km/s is due to the relative motion between the Sun and the dark matter halo.

The positions of particles are generated in such a way that they initially *uniformly* populate in a spherical shell around the Sun. The inner and outer boundaries of the spherical shell are respectively $R_{\rm min} = 1$ AU and $R_{\rm max} = 10$ AU. Note that our choice of $R_{\rm min}$ is different from Ref. [6] where $R_{\rm min} = R_\odot$ there. Choosing a larger $R_{\rm min}$ is to reduce the effect of the Sun's gravity on the *initial* velocity distribution (B.1). The solar escape velocity at 1 AU is $v_e \approx 42$ km/s, so when a particle moves from infinity with the typical velocity $v_0 = 220$ km/s to this distance, the velocity increment due to the Sun's gravity is $\Delta v = \sqrt{v_0^2 + v_e^2} - v_0 \approx 4$ km/s which is very small compared with v_0. Similar to Ref. [6], we generated $N_{\rm sample} = 2 \times 10^{10}$ such particles. The particles then move following Newton's gravity, attracted by the Sun, using the classical two-body orbit dynamics. The criteria to determine whether or not a particle will impact the Sun are also the same as in [6]. For a given particle, if the perihelion of the hyperbolic trajectory is smaller than $R_\odot$ (and also if the velocity direction is inward), then it will impact the Sun. It turns out that from the initial sample of 2×10^{10}, the number of particles that will impact the Sun is $N_{\rm imp} = 30457$.[59] The trajectory and impact properties of these impacting particles are shown in Fig. B.1.

The expression of the impact parameter b is

$$b = r_p \sqrt{1 + \frac{2GM_\odot}{r_p v_0^2}} \tag{B.2}$$

where r_p is the perihelion distance. v_0 is the particle velocity at infinity that can be extrapolated from the initial velocity and position simulated, i.e., $v_0 = \sqrt{v_i^2 - 2GM_\odot/r_i}$. The impacting requires $0 \le r_p \le R_\odot$. If we take $r_p = R_\odot$, we get the maximum impact parameter $b_{\rm max}$. The distribution of the impact parameter (in the form of $b/b_{\rm max}$) is shown in the subplot (b) of

[59] In comparison, the number obtained in Ref. [6] is 36123. The difference is beyond the statistical fluctuation. This difference occurs not only due to our choice of a larger $R_{\rm min}$, the inner boundary of the initially simulated region, but also a technical detail that a different method (more appropriate) is chosen in determining the perihelion. However, all of these changes have no significant effects on the results as we can see in Fig. B.1 by comparing it with Ref. [6].

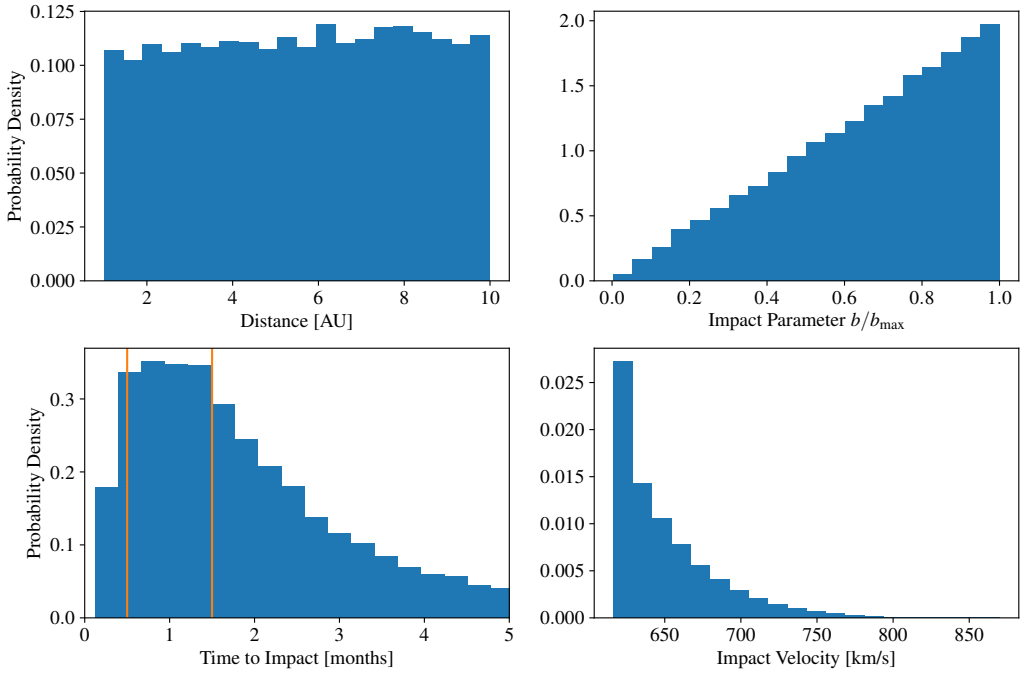

Figure B.1: Probability density distributions of the trajectory and impact properties for the $N_{\text{imp}} = 30457$ impacting particles. The plots represent (a) the initial distance distribution of these impacting particles, (b) the impact parameter distribution, (c) the impact time distribution and (d) the velocity distribution when they impact the Sun. This figure is taken from Ref. [4].

Fig. B.1.

From the distribution of impact time as shown in the subplot (c) of Fig. B.1, we can calculate the impact rate. Following the logic in Ref. [6], we should only use the time window where the rate is constant. We choose it as $t_{\text{imp}} \in [0.5, 1.5]$ months where the boundaries are denoted as two vertical lines in the plot. The rate in the time window is constant because the dominant part of particles impacting the Sun are the particles from the spherical shell between R_{min} and R_{max}. Outside the time window, we see the rate drops because we did not simulate the particles outside the spherical shell. The impact rate is $N(\Delta t_{\text{imp}})/\Delta t_{\text{imp}}$ where $N(\Delta t_{\text{imp}})$ is the number of particles impacting the Sun in the time window chosen above. Note that this impact rate is not the true impact rate because the number of AQNs simulated, $N_{\text{sample}} = 2 \times 10^{10}$, is not the true number of AQNs inside the spherical shell.

To convert the impact rate to the true impact rate, we need to multiply it by the scaling factor f_S which is the ratio of the true number of AQNs in the spherical shell to $N_{\rm sample}$:

$$f_S = \frac{\frac{4}{3}\pi(R_{\rm max}^2 - R_{\rm min}^2)\cdot n_{\rm nugget}}{N_{\rm sample}} \tag{B.3}$$

where $n_{\rm nugget}$ is the number density of antimatter AQNs in the solar system:

$$n_{\rm nugget} = \left(\frac{2}{3}\cdot\frac{3}{5}\cdot\rho_{\rm DM}\right)\cdot\frac{1}{m_P\langle B\rangle}. \tag{B.4}$$

and $\rho_{\rm DM} \simeq 0.3$ GeV cm^{-3} is the dark matter density in the solar system. 3/5 of the dark matter is in the form of antimatter AQNs; $\sim 2/3$ mass of an AQN is in the form of baryons (the remaining $\sim 1/3$ is in the form of axion domain wall as the AQN shell; see Ref. [6] or chapter 4 for more details). m_P is the proton mass. $\langle B\rangle$ is the average baryon number carried by an AQN. It depends on different models of AQN mass distribution that will be discussed in Step 2. Thus, the true rate of (antimatter) AQNs impacting the sun is

$$\frac{dN}{dt} = \frac{N(\Delta t_{\rm imp})}{\Delta t_{\rm imp}}\cdot f_S, \quad t_{\rm imp}\in[0.5, 1.5]\text{ months}. \tag{B.5}$$

Step 2. We are now assigning masses (baryon numbers) to all the AQNs collected in Step 1 that will impact the Sun. For each AQN, its mass is assigned randomly with the probability following one of the three models of power-law distribution, (6.5). Thus, we have three copies of all the impacting AQNs with different mass distributions.

Step 3. The evolution of an AQN in the solar atmosphere is described by a system of differential equations, including the kinetic energy loss due to friction and the mass loss due to the annihilation events of the antibaryons carried by AQN with the baryons in the atmosphere. We refer the reader to Ref. [6] for a complete list of the differential equations needed here, and their derivation. In order to solve these equations numerically, the density and temperature profiles of the solar atmosphere above the photosphere are also needed. In this work, we adopt the profiles presented in Ref. [8] which are more accurate than those used in Ref. [6].

The mass loss varying with time (or equivalently, height above the solar photosphere) for the $N_{\rm imp}$ AQNs is then computed numerically.

B.2 Results

The results obtained from the numerical simulations are presented in the main text. Additional details are given here.

Fig. 6.1 shows the rate of AQNs in the mass range $[\bar{B}, B_{\rm max}]$ impacting the Sun. The rate is calculated as eq. (B.5) but with only large AQNs $B \geq \bar{B}$ taken into account. By varying the value of the cutoff $\bar{B}$ from $B_{\rm min}$ to $B_{\rm max}$, we quantify how the impact rate depends on $\bar{B}$, as shown in the figure. The rate at $\bar{B} = B_{\rm min}$ is the total impact rate. For the three groups, the total impact rates are respectively 4.17×10^4 s^{-1}, 1.52×10^4 s^{-1} and 3.52×10^3 s^{-1} which match well Ref. [6] (see Fig. 8 there).

In addition, the luminosity $L^{\odot}$ can be calculated as $L^{\odot} = 2 \langle \Delta m \rangle c^2 \cdot dN/dt$ where Δm is an AQN's mass loss along its trajectory through the solar atmosphere before entering the dense region, the photosphere. Similarly, we can compute the luminosity $L^{\odot}_{\bar{B}}$ by counting large AQNs ($B \geq \bar{B}$) only, and the result is shown in Fig. 6.2 for different groups of mass distribution. The total luminosity is obtained at $\bar{B} = B_{\rm min}$. For the three groups, the total luminosity are respectively 1.05×10^{27} erg $\cdot$ s^{-1}, 1.07×10^{27} erg $\cdot$ s^{-1} and 1.06×10^{27} erg $\cdot$ s^{-1} which match well Ref. [6] (see Fig. 10 there).

One may notice that in the two left subfigures of Figs. 6.1 and 6.2, the simulated lines become zigzag at large baryon numbers. This is because the proportion of large AQNs is actually very small. Despite the number of all the impacting AQNs is as large as 30457, the power-law index $\alpha \sim (2 - 2.5)$ makes the hit rate with large B very tiny when assigning masses to AQNs randomly in Step 2. For example, our statistical result shows that in Group 1, the number of AQNs with $B \geq 5 \times 10^{26}$ is only 12, and the number of AQNs with $B \geq 10^{27}$ is only 3. Such tiny numbers cause large statistical fluctuation, so we see the zigzags in the two left subfigures. We have to generate enough large AQNs to remove the large statistical fluctuation.

We resolve this technical problem as follows. We simulate *another* 10^{10} AQNs by redoing the three steps in the setup as described above. We call this procedure the second-round simulation. We get 15019 AQNs that will finally impact the Sun out of the total 10^{10} AQNs. The masses (baryon numbers) assigned to these 15019 impacting AQNs are constrained in the range $B \in [B_L, B_{\rm max}]$. B_L for each group should be chosen well above $B_{\rm min}$ to ensure that enough large AQNs can be generated, but B_L should not exceed the start of the zigzags. Although we did not simulate all AQNs in this second-round simulation, we can extrapolate the "number" of impacting

AQNs in the *full* mass range by looking at the proportion of large AQNs ($B \in [B_L, B_{\max}]$) in the full mass range.[60] Furthermore, we can calculate the extrapolated N_{sample} and the extrapolated scaling factor f_S. Finally, we obtain the true impact rate of these large AQNs simulated in the second-round simulation. Similarly, we obtain the luminosity. The results are shown in the two right subfigures of Figs. 6.1 and 6.2, where we see that the large statistical fluctuation disappears.

[60]The advantage of assigning AQNs masses only in the range of $[B_L, B_{\max}]$ is that we do not repeat generating a huge amount of small AQNs which are far more than needed and only to make the simulations extremely time-consuming.

Appendix C

Calculation of $dF/d\omega$ and $F_{\rm tot}$

This appendix is adapted from Ref. [5]. This Appendix shows the details of how we derive the expression of the spectral surface emissivity, eq. (C.8), which is shown in Fig. 7.2, and the expression of the total surface emissivity, eq. (7.11), presented in chapter 7.

We start with the spectral surface emissivity, eq. (7.1), with all of the extra effects discussed in chapter 7.2.1 included. Only photons with an energy larger than the plasma frequency, $\omega_p(z)$, can propagate outside of the system. The largest plasma frequency, $\omega_p(z=0)$, occurs in the deepest region of the electrosphere, where the positron density is the largest. Therefore, photons with an energy, $\omega > \omega_p(z=0)$, created anywhere in the electrosphere, $(z \geq 0)$, can propagate outside of the system. For $\omega < \omega_p(z=0)$, there is a cutoff determined by eq. (7.9):

$$z_0(\omega) = \frac{1}{\omega}\sqrt{\kappa}\sqrt{\frac{2T}{m_e}} - \bar{z}. \tag{C.1}$$

Photons with an energy, $\omega < \omega_p(z=0)$, can propagate outside of the system only if they are created in the regime, $z > z_0(\omega)$. Therefore, eq. (7.1) becomes a piecewise function with $\omega_p(z=0)$ as the turning point.

We should also notice that when ω is small enough, the lower cutoff, $z_0(\omega)$ in eq. (C.1), could be larger than the upper cutoff, z_1 in eq. (7.8), defined by the ionization effect. We can then get a critical frequency by equating $z_0 = z_1$:

$$\omega_{z_0=z_1}(T) = \sqrt{\kappa}\sqrt{\frac{2T}{m_e}}[z_1(T) + \bar{z}(T)]^{-1}. \tag{C.2}$$

We see that $z_0 < z_1$ for $\omega > \omega_{z_0=z_1}$, while $z_0 > z_1$ for $\omega < \omega_{z_0=z_1}$. Only photons with $\omega > \omega_{z_0=z_1}$ can be generated. The low frequency photons with $\omega < \omega_{z_0=z_1}$ cannot be generated because the region of the electrosphere that could generate them is ionized (see eq. (7.7)). Therefore, $dF/d\omega$ should be written as:

$$\frac{dF}{d\omega}(\omega) = \begin{cases} \frac{1}{2}\int_{z_0(\omega)}^{z_1} dz\ \frac{d\tilde{Q}}{d\omega}(\omega, z), & \text{if } \omega_{z_0=z_1} < \omega < \omega_p(z=0); \\ \\ \frac{1}{2}\int_{0}^{z_1} dz\ \frac{d\tilde{Q}}{d\omega}(\omega, z), & \text{if } \omega > \omega_p(z=0). \end{cases} \tag{C.3}$$

Integrating $d\tilde{Q}/d\omega$ (7.10) over z gives:

$$\begin{aligned} \int dz \frac{d\tilde{Q}}{d\omega}(\omega, z) &= \int dz\ n^2(z) \mathrm{e}^{-\omega_p(z)/T} G(\omega) \\ &= \kappa^2 \left(\frac{T}{2\pi\alpha}\right)^2 G(\omega) \int dz\ \frac{\mathrm{e}^{-\sqrt{\kappa}\sqrt{\frac{2}{m_e T}}\frac{1}{z+\bar{z}}}}{(z+\bar{z})^4} \\ &= \kappa^2 \left(\frac{T}{2\pi\alpha}\right)^2 G(\omega) H(z), \end{aligned} \tag{C.4}$$

with

$$H(z) = \mathrm{e}^{-\sqrt{\frac{2\kappa}{m_e T}}\frac{1}{z+\bar{z}}} \left[\frac{1}{\sqrt{\frac{2\kappa}{m_e T}}} \frac{1}{(z+\bar{z})^2} + \frac{2}{\left(\sqrt{\frac{2\kappa}{m_e T}}\right)^2} \frac{1}{(z+\bar{z})} + \frac{2}{\left(\sqrt{\frac{2\kappa}{m_e T}}\right)^3} \right]. \tag{C.5}$$

$G(\omega)$ in eq. (C.4) is a function defined for convenience to collect the terms that do not depend on z:

$$G(\omega) \equiv \frac{4\alpha}{15} \left(\frac{\alpha}{m_e}\right)^2 2\sqrt{\frac{2T}{m_e \pi}} \left(1 + \frac{\omega}{T}\right) \mathrm{e}^{-\omega/T} h\left(\frac{\omega}{T}\right). \tag{C.6}$$

The expression for $h(x)$ is:

$$h(x) = 17 + 12 \left[\ln 2 + \left(1 + \mathrm{e}^x \int_1^\infty \frac{\mathrm{e}^{-xy}}{y} dy \right) (1+x)^{-1} \right], \tag{C.7}$$

which is a function derived in Ref. [57] (we refer the readers to Appendix A2

of Ref. [57] for further details). Plugging eq. (C.4) into eq. (C.3), we get:

$$\frac{dF}{d\omega}(\omega) = \begin{cases} \frac{1}{2}\kappa^2 \left(\frac{T}{2\pi\alpha}\right)^2 \cdot G(\omega) \cdot [H(z_1) - H(z_0(\omega))], \\ \qquad\qquad \text{if } \omega_{z_0=z_1} < \omega < \omega_p(z=0); \\ \\ \frac{1}{2}\kappa^2 \left(\frac{T}{2\pi\alpha}\right)^2 \cdot G(\omega) \cdot [H(z_1) - H(0)], \\ \qquad\qquad \text{if } \omega > \omega_p(z=0). \end{cases} \tag{C.8}$$

We plot $dF/d\omega$ vs. ω in Fig. 7.2 in chapter 7, with $T = 100$ keV as an example, and $\kappa = 10^{-2.5}, 10^{-3.5}$ respectively.

Now, we are ready to calculate the total surface emissivity, $F_{\rm tot}(T)$, by integrating $dF/d\omega$ over ω:

$$\begin{aligned} F_{\rm tot}(T) =& \int_{\omega_{z_0=z_1}(T)}^{\infty} d\omega \ \frac{dF}{d\omega}(\omega) \\ =& \left[\int_{\omega_{z_0=z_1}(T)}^{\omega_p(z=0)} d\omega \ \frac{1}{2}\int_{z_0(\omega)}^{z_1} dz \frac{dQ}{d\omega}(\omega, z)\right] \\ &+ \left[\int_{\omega_p(z=0)}^{\infty} d\omega \ \frac{1}{2}\int_{0}^{z_1} dz \frac{dQ}{d\omega}(\omega, z)\right] \\ =& \frac{\alpha}{15\pi^{5/2}} \frac{T^5}{m_e} \kappa^2 \left[I_1(T) + I_2(T)\right], \end{aligned} \tag{C.9}$$

with

$$\begin{aligned} I_1(T) =& \frac{1}{T}\sqrt{2}(m_e T)^{-3/2} \\ &\times \int_{\omega_{z_0=z_1}(T)}^{\omega_p(z=0)} d\omega \ \left(1 + \frac{\omega}{T}\right) \mathrm{e}^{-\frac{\omega}{T}} h\left(\frac{\omega}{T}\right) \cdot [H(z_1) - H(z_0(\omega))], \\ I_2(T) =& \frac{1}{T}\sqrt{2}(m_e T)^{-3/2} \\ &\times \int_{\omega_p(z=0)}^{\infty} d\omega \ \left(1 + \frac{\omega}{T}\right) \mathrm{e}^{-\frac{\omega}{T}} h\left(\frac{\omega}{T}\right) \cdot [H(z_1) - H(0)]. \end{aligned} \tag{C.10}$$

The two dimensionless functions $I_1(T)$ and $I_2(T)$ can be solved numerically.

In Fig. C.1, we plot $[I_1(T) + I_2(T)]$ vs. T in the range 1 keV $\leq T \leq$ 1000 keV, for $\kappa = 10^{-2.5}, 10^{-3.5}$ respectively. We see that the two lines of $[I_1(T) + I_2(T)]$, with $\kappa = 10^{-2.5}$ and $10^{-3.5}$, almost overlap with each other,

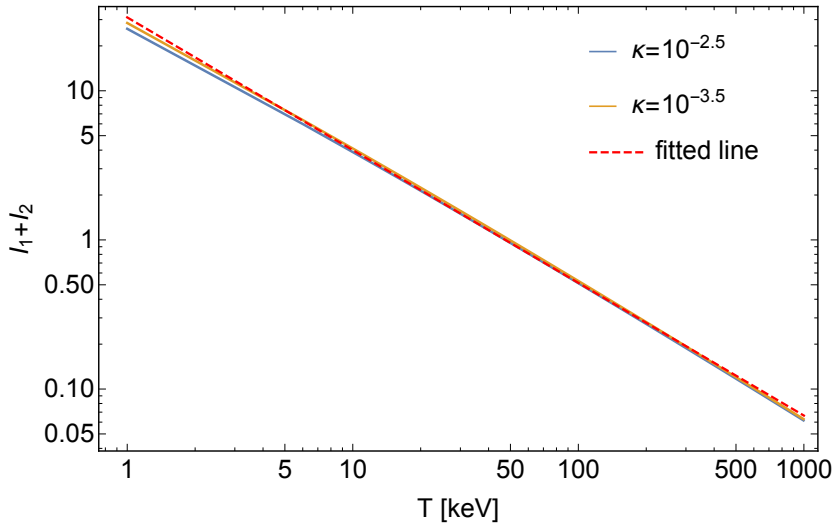

Figure C.1: $[I_1(T)+I_2(T)]$ as a function of T, for $\kappa = 10^{-2.5}, 10^{-3.5}$. We see that the two lines almost overlap with each other, and that they are fitted to the red dashed line. This figure is taken from Ref. [5].

and that they are nearly a linear function of T in the log-log scale. Then, we fit $[I_1(T)+I_2(T)]$ to a simple function (the red dashed line in Fig. C.1):

$$[I_1(T)+I_2(T)] = c_1' \left(\frac{T}{10\ \text{keV}}\right)^{c_2'}, \tag{C.11}$$

with the two fitting parameters

$$c_1' = 4, \quad c_2' = -0.89. \tag{C.12}$$

This is a good approximation for $\kappa = 10^{-2.5}, 10^{-3.5}$. Then, plugging eqs. (C.11) and (C.12) into eq. (C.9), we get:

$$F_{\text{tot,fit}}(T) = \frac{\alpha}{15\pi^{5/2}} \frac{T^5}{m_e} \kappa^2 \cdot c_1' \left(\frac{T}{10\ \text{keV}}\right)^{c_2'}. \tag{C.13}$$

To see how good the fitted result (C.13) is, we plot it together with the exact F_{tot}, eq. (C.9), in the top subfigure of Fig. C.2 for $\kappa = 10^{-2.5}, 10^{-3.5}$. In the bottom subfigure of Fig. C.2, we also plot the relative error $(F_{\text{tot}} - F_{\text{tot,fit}})/F_{\text{tot}}$. We see that the relative error is within 10% for $T \gtrsim 10$ keV.

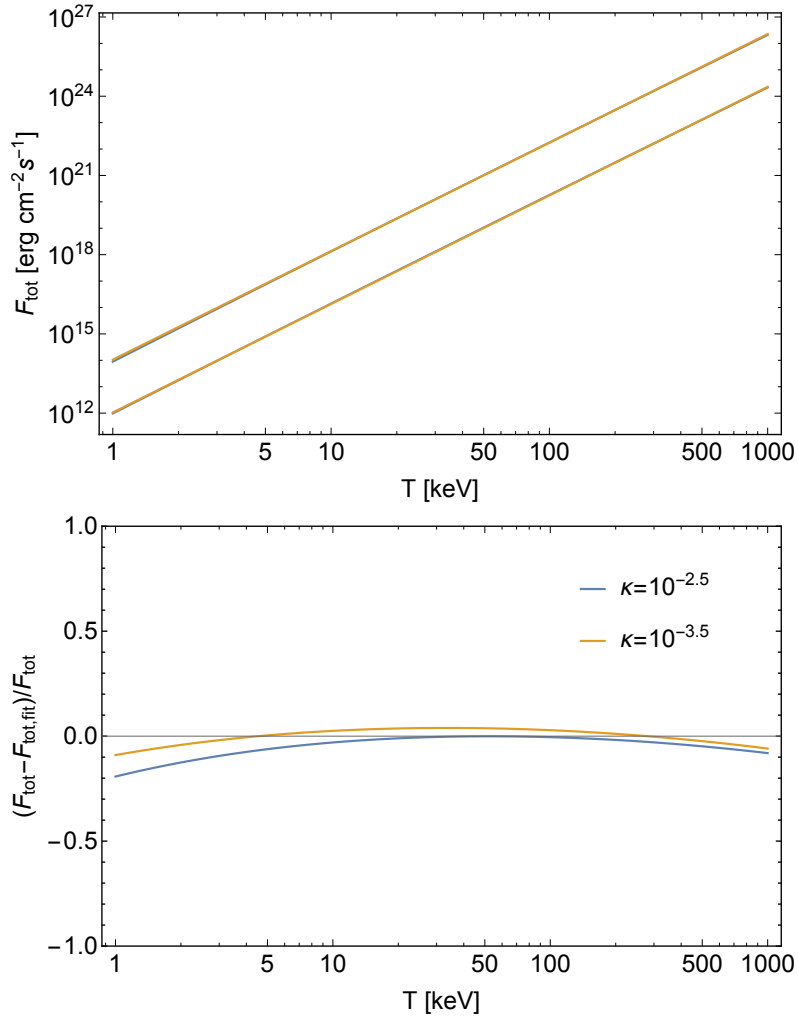

Figure C.2: Top subfigure: the relation $F_{\rm tot}$ vs. T, for $\kappa = 10^{-2.5}, 10^{-3.5}$ (top and bottom respectively). The blue lines are the exact $F_{\rm tot}$, eq. (C.9); the yellow lines are the fitted result, eq. (C.13). We see that for each given κ, the blue line almost overlaps with the corresponding yellow line. Bottom subfigure: the relative error. This figure is taken from Ref. [5].

Appendix D

Calculation of AQN cooling

This appendix is adapted from Ref. [5]. This appendix shows more details of an AQN cooling process in the space, T vs. t, when it exits the earth after hitting, which aims to support the discussions in chapter 7.2.2.

Solving the differential equation (7.17) gives:

$$\begin{aligned}\frac{t}{1\text{ sec}} &\simeq \frac{R_{\rm AQN}}{1\text{ sec}}\frac{5\pi^{5/2}}{3\alpha c_1(\kappa)[c_2(\kappa)+3]}\frac{m_e(\mu_u^2+\mu_d^2)}{(10\text{ keV})^3}\\ &\quad\cdot\left[\left(\frac{T}{10\text{ keV}}\right)^{-[c_2(\kappa)+3]}-\left(\frac{T_0}{10\text{ keV}}\right)^{-[c_2(\kappa)+3]}\right]\\ &\simeq \frac{0.34}{c_1(\kappa)[c_2(\kappa)+3]}\left(\frac{R_{\rm AQN}}{10^{-5}\text{ cm}}\right)\left(\frac{\mu_{u,d}}{500\text{ MeV}}\right)^2\\ &\quad\cdot\left[\left(\frac{T}{10\text{ keV}}\right)^{-[c_2(\kappa)+3]}-\left(\frac{T_0}{10\text{ keV}}\right)^{-[c_2(\kappa)+3]}\right],\end{aligned} \tag{D.1}$$

or equivalently:

$$\begin{aligned}T(t) \simeq 10\text{ keV}\cdot\Bigg[&\frac{t}{1\text{ sec}}\left(\frac{R_{\rm AQN}}{10^{-5}\text{ cm}}\right)^{-1}\left(\frac{\mu_{u,d}}{500\text{ MeV}}\right)^{-2}\\ &\cdot\left(\frac{0.34}{c_1(\kappa)[c_2(\kappa)+3]}\right)^{-1}+\left(\frac{T_0}{10\text{ keV}}\right)^{-[c_2(\kappa)+3]}\Bigg]^{-\frac{1}{c_2(\kappa)+3}}.\end{aligned} \tag{D.2}$$

Appendix E

Calculation of $dF_r/d\omega$ as a function of $v_{\rm out}$

This appendix is adapted from Ref. [5]. This appendix shows the details of how we derive eq. (7.38) that is presented in chapter 7.

We are going to calculate eq. (7.37) to find out the relation between $dF_r/d\omega$ and $v_{\rm out}$. First, we analyze the factor $dF/d\omega$ that occurs in eq. (7.37). The expression of $dF/d\omega$ is given in (C.8). We focus the second branch ($\omega > \omega_p(z=0)$) of the piecewise function (C.8), which is the location of the frequencies that we are interested in.

As we can see from Fig. 7.3, the AQNs are still very hot when they enter the XMM-Newton's cone. We have $T \gg \omega$, where $\omega \sim$ 2-6 keV is the frequency range that we are interested in. This results in the pattern of the "soft photon theorem", as explained in chapter 7.3. We can drop the terms suppressed by ω/T, so the second branch of eq. (C.8) is approximated as:

$$\frac{dF}{d\omega} \propto T^{5/2} \cdot P(\omega, T), \tag{E.1}$$

where

$$P(\omega, T) \equiv h\left(\frac{\omega}{T}\right)\left[H(z_1(T), T) - H(0, T)\right]. \tag{E.2}$$

In Fig. E.1, we plot the relation $P(\omega,T)$ vs. T, for $\kappa = 10^{-2.5}, 10^{-3.5}$. We see that $P(\omega,T)$ can be well fitted to the red dashed line, which represents the function [constant $\times\, T^{0.72}$]. So we have:

$$P(\omega, T) \propto T^{0.72}. \tag{E.3}$$

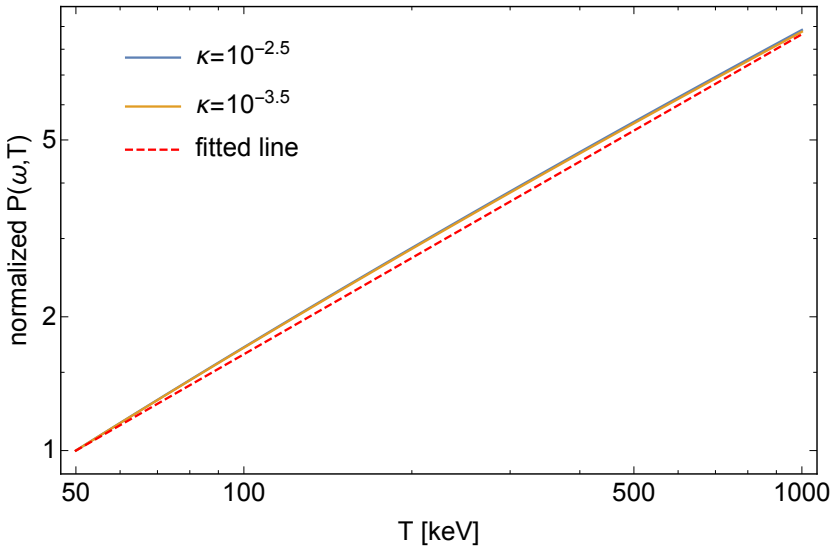

Figure E.1: The relation between the normalized $P(\omega,T)$ and T, for $\kappa = 10^{-2.5}$, $10^{-3.5}$. The two lines almost overlap with each other. We use the function [constant $\times T^{0.72}$] (red dashed line) to fit the two lines. The two lines are plotted at $\omega = 3$ keV. Changing the value of ω only slightly affects the relation between $P(\omega,T)$ and T. Since we do not care about the magnitude of $P(\omega,T)$, it is actually plotted in the normalized form, $P(\omega,T)/P(\omega,50\text{ keV})$. This figure is taken from Ref. [5].

Note that $P(\omega,T)$ is also a function of ω which is only contained in $h(\omega/T)$. In plotting Fig. E.1, ω is chosen to be 3 keV. Since $\omega/T \ll 1$, changing the value of ω only slightly affects the value of $P(\omega,T)$. Thus, to study the relation between $P(\omega,T)$ and T, we can fix ω at a certain value. This is good enough for our approximate analysis in this appendix. Combining eqs. (E.1) and (E.3), we get:

$$\frac{dF}{d\omega} \propto T^{3.22}. \tag{E.4}$$

The relation between T and v_{out} is given in eq. (D.2). We can rewrite eq. (D.2) as:

$$T \simeq 10\text{ keV} \cdot \left[\frac{K_1(\kappa)}{v_{\text{out}}} + K_2(\kappa,T_0)\right]^{-\frac{1}{c_2(\kappa)+3}}, \tag{E.5}$$

where

$$K_1(\kappa) \equiv \frac{s}{1\ \text{sec}} \cdot \left(\frac{0.34}{c_1(\kappa)[c_2(\kappa)+3]}\right)^{-1} \left(\frac{R_{\text{AQN}}}{10^{-5}\ \text{cm}}\right)^{-1} \left(\frac{\mu_{u,d}}{500\ \text{MeV}}\right)^{-2},$$
$$K_2(\kappa, T_0) \equiv \left(\frac{T_0}{10\ \text{keV}}\right)^{-[c_2(\kappa)+3]}. \tag{E.6}$$

Next, we check on possible variations of the factor, n_{AQN}, that occurs in eq. (7.37). From eq. (7.22), we know that:

$$n_{\text{AQN}} \propto \frac{\mathcal{F}}{v_{\text{out}}} \propto \frac{\mathcal{F}}{v_{\text{in}}} \frac{v_{\text{in}}}{v_{\text{out}}} \propto \frac{v_{\text{in}}}{v_{\text{out}}} = \gamma^{-1}, \tag{E.7}$$

where we have used the relation that $\mathcal{F}/v_{\text{in}}$ is a constant (see eq. (7.23)). γ is the ratio between v_{out} and v_{in}, which is defined in chapter 7.4. For simplicity, we assume that the loss of AQN velocity inside the Earth is proportional to the magnitude of the entry velocity, v_{in}, so γ and thus n_{AQN} are seasonally invariant, despite the fact that v_{in} changes with seasons.

Plugging eqs. (E.4) and (E.5) into eq. (7.37), we finally arrive at:

$$\frac{dF_r}{d\omega} \propto \left(\frac{K_1}{v_{\text{out}}} + K_2\right)^{-\frac{3.22}{c_2(\kappa)+3}}. \tag{E.8}$$